Chemical Analysis of Cells and Tissues with Time-of-Flight Secondary Ion Mass Spectrometry

Michael A. Robinson

A dissertation

submitted in partial fulfillment of the

requirements for the degree of

Doctor of Philosophy

University of Washington

2013

Reading Committee:

David G. Castner, Chair

Lara Gamble

Jim Pfaendtner

Program Authorized to Offer Degree:

Department of Chemical Engineering

Table of Contents

List of Figures……..……..…vii
List of Tables……..…...…ix
List of Abbreviations……..……...…….……...x
Acknowledgements……...xi
Abstract…….....xii

1. Introduction……..1
1.1. Motivation……1
1.2. Objective…...……...2
1.3. Organization of this Document……5

2. Background……..6
2.1. Introduction……..6
2.2. ToF-SIMS Theory……..……..7
2.2.1. ToF-SIMS Equations……7
2.2.2. Proposed Models for Sputtering……...9
2.2.2.1. Linear Cascade Theory……11
2.2.2.2. Precursor Model……..…..……11
2.2.3. Matrix Effects……..…13
2.2.4. Simulations……13
2.3. ToF-SIMS Instrumentation…….……..…..14
2.3.1. Liquid Metal Ion Guns…….……...14
2.3.2. Electron Impact Sources……15
2.3.3. Comparison of Primary Ion Sources…….……..15
2.3.4. Time-of-Flight Analyzer…….……18
2.3.5. Custom-built Instrumentation for Biological Sample Analysis….……19
2.4. Literature Review…….……..…20
2.4.1. Biological Cells……..……20
2.4.2. Biological Tissues…….……..21
2.4.3. Lipids…….……....22
2.4.4. Proteins…….……..23
2.4.5. DNA……..24
2.4.6. Multivariate Analysis…….…….24
2.5. Other Techniques for Biological Sample Analysis of Cells and Tissues……..25
2.5.1. Matrix-assisted Laser Desorption Ionization…….25
2.5.2. Desorption Electrospray Ionization……26
2.5.3. Raman Spectroscopy……..26

3. Materials and Methods……28
3.1. Materials……28
3.1.1. Non-biological Materials……28
3.2.2. Cell Lines Used in these Studies……....28
3.2. Methods……29
3.2.1. Silicon Substrate Preparation……29
3.2.2. Cell Growth……29

3.2.3. Ammonium Acetate Rinsing Solution……29
3.2.4. Liquid Ethane Formation……30
3.2.5. Cryofixation by Plunge Freezing ……..30
3.2.6. Chemical Fixation……..……30
3.2.7. Freeze-drying……..……31
3.2.8. Frozen-hydrated analysis of cell with ToF-SIMS……..……31
3.2.9. ToF-SIMS……...……32
3.2.10. Atomic Force Microscopy……33
3.2.11. Principal Component Analysis……33

4. Characterization of sample preparation methods of NIH/3T3 fibroblasts for ToF-SIMS analysis……..……..36

4.1. Abstract……..37
4.2. Background……38
4.3. Experimental Methods……..……..42
4.3.1. Cell Seeding……42
4.3.2. Ammonium Acetate Rinsing Solution……43
4.3.3. Rinsing, Plunge Freezing, and Lyophilization of Cells……..43
4.3.4. Chemical Fixation……...44
4.3.5. Frozen-Hydrated: Preparation and Analysis of Cells……44
4.3.6. ToF-SIMS……...45
4.4. Results…….…….....46
4.4.1. Proper Rinsing of Cells…….……..46
4.4.2. Spectra from Cell Surfaces……...……..47
4.4.3. Comparing the Depth Profiles of freeze-dried and formaldehyde-fixed cells……...…50
4.4.4. Comparing the Depth Profiles of freeze-dried and frozen-hydrated cell....55
4.5. Conclusion……...……..60
4.6. Supporting Information……62

5. ToF-SIMS Depth Profiling of Cells: Z-correction, 3D Imaging, and Sputter Rate of Individual NIH/3T3 Fibroblasts……...77

5.1. Abstract……..78
5.2. Introduction……79
5.3. Materials and Methods……...…82
5.3.1. Cell Culture……82
5.3.2. Chemical Fixation……...…83
5.3.3. Lyophilization……83
5.3.4. ToF-SIMS……...84
5.3.5. Atomic Force Microscopy…..……84
5.3.6. Data Handling/ ZcorrectorGUI……...……85
5.4. Results and Discussion……..87
5.4.1. ZcorrectorGUI……87
5.4.2. Sputter Rate of Single Cells……89
5.5. Conclusion……94

5.6. Supporting Information……96

6. **Chemical Analysis of eight human breast cancer cell lines with ToF-SIMS**……..100
6.1. Abstract……101
6.2. Introduction……102
6.3. Materials and Methods……106
6.3.1. Cell Line Growth and Preparation……106
6.3.2. ToF-SIMS……107
6.3.3. Principal Component Analysis……108
6.3.4. Normalized Peak Intensity Histograms……108
6.4. Results……108
6.4.1. Comparison of Triple Negative and Receptor Positive Cell Lines Using Positive Ions……...113
6.4.2. Normalized Peak Intensities (Positive Ions)……116
6.4.3. Comparison of Triple Negative and Receptor Positive Cell Lines Using Negative Ions……...119
6.4.4. Normalized Peak Intensities (Negative Ions)……...……121
6.5. Conclusion……..……124
6.6. Supporting Information……..125

7. Analysis of Breast Cancer Tumors with TOF-SIMS……129
7.1. Abstract……130
7.2. Introduction……..131
7.3. Materials and Methods……132
7.3.1. Tissue Preparation……132
7.3.2. ToF-SIMS……133
7.3.3. Principal Component Analysis……135
7.4. Results……..137
7.4.1. PCA Applied to Spectra Acquired from Tissue Slices……....137
7.4.2. PCA Applies to Images Acquired from Tissue Slices……..143
7.4.3. Relating Chemical Images to Biological Structures……148
7.4.4. Mapping Unique Distribution of Fatty Acids……...…150
7.5 Conclusion……153

8. Conclusions and Future Directions……157
8.1. Conclusions……..157
8.2. Future Directions……158

Appendix……161

Appendix A. ToF-SIMS 3D Imaging of HeLa Cells……..162
A.1. Abstract……..163
A.2. Introduction……164
A.3. Materials and Methods……167
A.3.1. ToF-SIMS……....167
A.3.2. Data Handling/3D Imaging Reconstruction……169

A.3.3. Atomic Force Microscopy……...…169
A.3.4. HeLa Cells and Sample Preparation……170
A.4. Results and Discussion……....170
A.4.1. C_{60} Etching to Reveal Molecular Structures……170
A.4.2. Burst mode and 3D Imaging of Single Cells……...172
A.5. Conclusions……181
A.6. Supplemental Information……...183

Appendix B. Miscellaneous Projects/Work……..……..186
B.1. 3D imaging of Gold Nanoparticles in NIH/3T3 Fibroblasts……...186
B.2. 3D imaging of complex materials with non-uniform sputter rates: onion skin cell……..…193
B.3. Chemical mapping of lactating mouse breast tissue……...199

Bibliography…….……..205

List of Figures

2.1. Schematic of a monatomic primary ion impacting a solid surface……....11
2.2. Energy on a surface resulting from a primary ion impact……12
2.3. A diagram of a time-of-flight detector…….….19

4.1. A schematic of several methods used to prepare biological cells for ToF-SIMS analysis…39
4.2. Harsh rinsing can damage the plasma membrane of NIH/3T3 fibroblasts……...…….47
4.3. Spectra from the surface of cells that were prepared using various methods……48
4.4. Plot comparing secondary ion intensities from cells prepared using chemical fixation or freeze-drying……..52
4.5. Comparison of select negatively charged secondary ions from cells prepared in several ways……...……54
4.6. Plot comparing secondary ion intensities from cells prepared using frozen-hydrated or freeze-drying…….58
S.4.1. Na^+ and $^{41}K^+$ peaks and intensities……63

5.1. A flow diagram of the z-correction process……..86
5.2. Visualization options provided by the ZcorrectorGUI……88
5.3. Visualization of the m/z 58^+ signal from a single NIH/3T3 fibroblast…….89
5.4. A comparison of corrected ToF-SIMS and AFM data from the same cell……91
TOC Graphic……..95
S.5.1. A comparison of AFM and corrected ToF-SIMS data of a chemically fixed NIH/3T3 fibroblast……97
S.5.2. Residual signals after depth profiling a cell……...…98
S.5.3. AFM topography images of cells before and after C_{60} etching……99

6.1. PCA of eight breast cancer cell lines using the High Mass peak list and positive ions…...113
6.2. Normalized intensities of selected positively charged ions…….117
6.3. PCA of eight breast cancer cell lines using the High Mass peak list and negative ions…..120
6.4. Normalized intensities of selected negatively charged ions……123
S.6.1. PCA of eight breast cancer cell lines using the Large Positive Ion peak list……..126
S.6.2. Additional normalized intensities of selected positively charged ions……127
S.6.3. Additional normalized intensities of selected negatively charged ions……128

7.1. Optical images of H&E-stained, adjacent tissue slices from all four tissue blocks…….135
7.2. PCA using Large Negative Ion Peak list……..……..139
7.3. Comparison of PCA using High Mass and High Mass (cell) peak lists using negative ions……...141
7.4. PC1 vs. PC3 using High Mass (cell) Negative Ion peak list……...142
7.5. PCA using High Mass Positive Ion Peak list……...143
7.6. PCA imaging results for PC1-4 using positive ions……144
7.7. PCA imaging results for PC1-5 using negative ions……...145
7.8. Comparison of PCA, H&E and optical images of breast cancer tumor tissue……150
7.9. Distributions of fatty acids in area from the tumor tissues……..152

A.1. Three Bi_3^+ analysis modes used for ToF-SIMS data acquisition……167
A.2. Positive burst alignment (HSR) ion images of the HeLa cells prepared by a simple wash-and-dry method……171
A.3. ToF-SIMS images of HeLa cells using Burst and HMR modes……174
A.4. Submicron spatial resolution is demonstrated using single HeLa cells……..176
A.5. Z-corrected XZ images of HeLa cells with incorporated BrdU……179
A.6. Z-corrected 3D images of BrdU localized within cells using two different LMIG operating modes……..……180
S.A.1. AFM images of HeLa cells before and after C_{60} etching……185
S.A.2. Plot of sputtered depth vs. C_{60} dose density……...……185

B.1. AuNPs imaged within NIH/3T3 fibroblasts by ToF-SIMS……190
B.2. A 3D reconstruction of AuNPs within NIH/3T3 fibroblasts, imaged by ToF-SIMS dual-beam depth profiling……...191
B.3. Optical images of the same onion cell in the AFM and in the TOF-SIMS……195
B.4. Comparison of AFM and z-corrected 3D ToF-SIMS image of onion cell……196
B.5. Cross-section comparison of AFM and ToF-SIMS data from onion cell……...198
B.6. Optical image of H&E-stained lactating mouse breast tissue……200
B.7. Three color overlay of lactating mouse breast tissue using ToF-SIMS data……..202
B.8. A second three color overlay of lactating mouse breast tissue using ToF-SIMS data……203
B.9. Comparing the structrues in the ToF-SIMS chemical image with those in the H&E-stained section……..204
B.10. Comparison of spectra from three regions of interest from mouse tissue……204

List of Tables

2.1. A comparison of ToF-SIMS primary ion sources……...……...16

S.4.1. All positive secondary ions detected from both the freeze-dried and formaldehyde-fixed cells……..…..64
S.4.2. Positive secondary ions that were detected from the frozen-hydrated cells but not the freeze-dried cells…….……..….72
S.4.3. All positive secondary ion detected from both the frozen-hydrated cells and the freeze-dried cells……..….75

6.1. The cell lines used in the Chapter 6 study with ER, PR and Her2 receptor status……..110
6.2. Key positive ion m/z and fragment ID for peaks that show the largest variance in PC 1, 2 and 4……110
6.3. Key negative ion m/z and fragment ID for peaks that show the largest variance in PC 1, 2 and 3…….112

7.1. Key negatively charged secondary ions from PCA analysis.....153
7.2. Key positively charged secondary ions from PCA analysis.....155

A.S.1. The list of positive and negative secondary ions used in Figures 3, 4, 5…….184

List of Abbreviations

AA: Ammonium acetate
AFM: Atomic force microscope
AuNP: Gold nanoparticle
BC: Breast cancer
DAG: Diacylglyceride
DESI: Desorption electrospray ionization
DFA: Discriminant function analysis
DLPC: 1,2-dilauroyl-sn-glycero-3-phosphocholine
DPPC: Dipalmitoylphosphatidylcholine
ER: Estrogen receptor
FD: Freeze-dried
FF: Formaldehyde-fixed
FH: Frozen-hydrated
GCIB: Gas cluster ion beam
H&E: Hematoxylin and eosin
HER2: Human epidermal growth factor receptor 2
HMR: High mass resolution
HSR: High spatial resolution
LMIG: Liquid metal ion gun
LN_2: Liquid nitrogen
MAG: Monoacylglyceride
MALDI: Matrix-assisted laser desorption ionization
MVA: Multivariate analysis
PC: Phosphocholine
PCA: Principal component analysis
POPC: 1-palmitoyl-2-oleoyl-sn-glycero-3-phosphocholine
PR: Progesterone receptor
PLS-DA: Partial least squares discriminant analysis
RP: Receptor positive
SI: Secondary ion
SM: Sphingomyelin
TN: Triple negative
ToF-SIMS: Time-of-flight secondary ion mass spectrometry
UHV: Ultra-high vacuum

Acknowledgements

I want to thank a lot of people for helping me and supporting me through this journey. First and foremost, I want to thank my family. My mom, dad, sister and stepmom never stopped encouraging me. Without you guys, I wouldn't have been able to finish this thing. I love you all and I can't wait to see more of everyone, assuming I live close!

A close second, I want to thank some special people with last names other than Robinson: the Petti's and Di Spaltros. There are really too many people to name, so if you aren't mentioned here, please don't hold it against me. I am writing this with hours left to turn it in. Dan, Alison, Ron, Amy, Nick, Ryan, Nanci, Sam, and Amanda are all very important people to me and I appreciate everything that they did to help me through this. The Daggets, the Malones, I can't wait to see more of you.

I would also like to thank all of the great people I have met and put up with me in Seattle. I believe that my class of graduate students, 2008, was the best one. Five years later many of us are still hanging around each other on a regular basis. The new students are also great and I wish them the best. OK time to turn this in!

Abstract

In this work the chemical analysis of biological cells and tissues with time-of-flight secondary ion mass spectrometry (ToF-SIMS) was explored. ToF-SIMS has the ability to obtain a mass spectrum with submicron spatial resolution for imaging and is extremely surface sensitive. ToF-SIMS for biological sample analysis is still an emerging field, so the development and characterization of novel sample preparation and analysis methods is key to acquiring useable information. In this work, three different methods to prepare NIH/3T3 fibroblasts were investigated: chemically fixed, freeze-dried and frozen-hydrated. Chemical fixation followed by rinsing removed a majority of intracellular Cl^-, improving the secondary ion yields of all organic positively charged secondary ions an average of 2.6x. Damage cross sections were reduced during frozen-hydrated analysis, improving the secondary ion yields of higher mass organic fragments. In a separate experiment, accurate 3D reconstructions of NIH/3T3 fibroblasts were produced. A simple z-correction was applied to the data cube, and the biggest assumption for that correction was validated. An intracellular lipid-rich region surrounding the nucleus was visualized.

ToF-SIMS applied to two different breast cancer systems. In the first, eight human breast cancer cell lines were distinguished form one another using mass spectra and principal component analysis (PCA). Not only was PCA to distinguish the cell lines form one another, it also highlighted the largest sources of variance between the cells. Phosphocholine, fatty acids, cholesterol and diacylglycerols (DAGs) were identified as key peaks. The identification of these species indicate that differences in lipid metabolism play an important role in separating the cell types from one another. Breast cancer tumor tissues were also investigated. Data from four tumors was collected. PCA applied to the spectra distinguished the four tissues from one

another. Imaging PCA determined the largest sources of variance within an analysis area. Structures were identified by PCA that matched structures observed in serial-sectioned, conventionally-stained slices, and other domains that were not visible in the conventionally-stained slices. As with the breast cancer cell lines, phosphocholine, fatty acids, DAGs, cholesterol and vitamin were found to be large sources of variance, indicating lipid metabolism plays in important role in tumor differentiation.

1. Introduction

1.1 Motivation

The accurate identification and localization of distinct regions and components of biological cells and tissues is important for obtaining a complete understanding of biological systems. While knowledge of the organization of structures within cells and tissues is essential to the understanding of biological processes, it is often insufficient. Chemical information is also very important, but is not afforded by most conventional analysis techniques For example, histological staining is used to determine the location, type and grade of tumors, which has a high prognostic value, but still is subjective and not fully predictive of chemotherapeutic response or patient outcome. No chemical information is provided by conventional histological methods. In addition to established methods, obtaining the representative biochemical fingerprints from tumors could lead to an improved ability to predict chemotherapeutic response and patient outcome. Furthermore, the identification and distribution of small, intracellular molecules such as metabolites and pharmaceutical agents within cells and tissues is crucial to determine modes of action and mechanisms, but difficult to ascertain using conventional methods.

A variety of instruments can probe the structural organization of biological cells and tissues with high spatial resolutions (optical [1, 2] and electron microscopies [3]), although few are capable of acquiring complementary chemical information with similarly high spatial resolution. Time-of-flight secondary ion mass spectrometry (ToF-SIMS) is an ultra-high vacuum (UHV) surface analytical tool capable of obtaining chemical information from biological samples with sub-micron spatial resolution [4] and high chemical specificity.

Advances in instrumentation have driven ToF-SIMS to the forefront of biological research. State-of-the-art liquid metal ion guns (LMIGs) [5, 6] can produce focused ion beams capable of generating images with 100 nm spatial resolution on non-ideal biological samples [4], along with continuously improving secondary ion (SI) yields [7]. New sputter ion sources [8, 9] provide added functionality by allowing the removal of organic material with less and less damage accumulation [10], opening the door for obtaining more relevant chemical information from depth profiling [11] and three-dimensional chemical imaging [12] experiments. Time-of-flight analyzers can simultaneously detect all desorbed ions [13], with current instruments capable of achieving mass resolutions ($m/\Delta m$) of 10,000.

The improvements to ToF-SIMS instrumentation allow for improved secondary ion yields and high mass fragments to be obtained from biological samples, so their examination has become more prevalent. Now that cells and tissues are being analyzed more frequently, there are a number of issues that must be addressed. For example, the preparation methods for cells so they can enter the UHV environment still needs to be carefully studied. Different methods may yield different results due to changes to the cells. Although three dimensional representations of data sets from cells and tissues are possible, there is still a need to improve upon these approaches. Last, cancer is a complex, heterogeneous malignancy, and the chemical signatures provided by ToF-SIMS may help understand cancer metabolism and improve the ability predict the chemotherapeutic response of patients.

1.2 Objective

The objective of this dissertation is to explore the chemical composition of single cells and tissues with ToF-SIMS, and to continue the development of the technique to be able to

successfully obtain relevant information from these complex samples. This includes the development and characterization of novel sample preparation methods for the analysis of single eukaryotic cells, and to improve the 3D chemical imaging capabilities of ToF-SIMS on complex organic samples. To pursue novel applications, the mechanisms underlying the chemotherapeutic resistance of certain human breast cancer cell lines and tumors are investigated. Specific chemical biomarkers that will aid in this investigation are explored. The objectives are broken up into several specific aims that are described below.

Specific Aim #1: Characterization of sample preparation methods of NIH/3T3 fibroblasts for ToF-SIMS analysis.

Hypothesis: The surface spectra, as well as secondary ion yields generated from depth profiles of NIH/3T3 fibroblasts will vary depending on how the cells are prepared for analysis.

Methodology: The preparation methods investigated were plunge-freezing in ethane with frozen-hydrated analysis, plunge freezing followed by freeze-drying, and chemical fixation with 4% formaldehyde and air drying. Surface spectra and the accumulated secondary ion yields from depth profiles were investigated.

Specific Aim #2: Accurately map a single cell in three dimensions using ToF-SIMS. Specifically, apply a z-correction, first described by Breitenstein *et al.* [14] to the entire 3D data cube. Additionally, determine if the key assumption of the z-correction, a constant sputter rate, is a valid one for NIH/3T3 fibroblasts. *Hypothesis*: NIH/3T3 fibroblasts, although very complex, will have a uniform sputter rate when etched with C_{60}^{++} in x, y and z. By having a uniform sputter rate, the relatively simple z-correction first described by Breitenstein *et al.* can be applied to an entire data cube, producing a more accurate 3D reconstruction of the original data. We

hypothesize that the sputter rate will not change drastically during etching and that it will be homogeneous in x and y for a single fibroblast cell.

Methodology: AFM was used to map the height of several NIH/3T3 fibroblasts. 3D depth profiles were acquired from the same cells. The sputter rate was calculated by dividing the known height of the cells by the C_{60} etching dose. The ZcorrectorGUI, an in-house software was created and used to compare the AFM data and the ToF-SIMS data.

Specific Aim #3: Chemical analysis of eight breast cancer cell lines using ToF-SIMS.

Hypothesis: Different human breast cancer cell lines have unique metabolic signatures. Variations in the mass spectra produced by ToF-SIMS and the cells may be separated using MVA techniques, providing unique information about each cell line. This information may be related to distinct metabolic patterns between the cell lines. Lipid metabolism is of particular interest because of the increasing importance of lipogenesis on cancer onset and progression, and because of the efficiency with which lipids are ionized during the SIMS process.

Methodology: Cells were fixed with formaldehyde and air dried prior to analysis with ToF-SIMS. Positive and negative polarity surface spectra were acquired following a small dose of C_{60} sputtering to remove surface contaminants. PCA was used to distinguish the different cell types.

Specific Aim #4: ToF-SIMS analysis of human breast cancer biopsy tissue.

Hypothesis: Relevant spatially mapped chemical information can be obtained from human breast cancer biopsy samples that will be complementary to standard histological staining and PET imaging. Lipid species and small, molecular fragments derived from metabolites can be

identified that may help determine the susceptibility of one tumor to be chemoresistant relative to other tumors.

Methodology: Human breast cancer tumors were biopsied, flash frozen, sectioned and placed on silicon chips. One set of samples analyzed by ToF-SIMS, the other set by conventional histology techniques. Spectra were acquired from multiple 1 mm x 1 mm areas per sample. Multivariate analysis was performed on both the spectra and chemical images to determine the most significant differences between the samples and within an analysis spot. These differences may be related to metabolic differences between the samples.

1.3 Organization of this Document

Chapter one provides a motivation this dissertation and the topics covered within.

Chapter two includes an extended background on ToF-SIMS theory and current instrumentation, as well as providing a small literature review on the analysis of biological cells and tissues.

Chapter three provides an overview of the materials and methods used in the above studies.

Chapter four explores the effects that various sample preparation methods have on single cells prior to ToF-SIMS analysis. The results include comparing surface spectra from frozen hydrated and dried cells, as well as the accumulated ion signal from selected positive organic fragments stemming from lipids, proteins and DNA obtained during depth profiles.

Chapter five further develops the 3D imaging capabilities of ToF-SIMS applied to single cells. A key assumption is validated, that is the question on the uniformity of the sputter rate of an entire NIH/3T3 fibroblast. Once validated, a complete 3D data set is presented following a z-correction with newly developed, in-house software (developed by Dr. Dan Graham). Chapter

six investigates how eight human breast cancer cell lines differ in metabolic processes by comparing the unique chemical signatures obtained with ToF-SIMS. The cell lines were distinguished from one another using the ToF-SIMS spectra and multivariate analysis.

Chapter seven discusses the analysis of human breast cancer tumor tissues. Freeze-fixed tissue slices from four patients were analyzed in what is an initial study from this group. The effects of multivariate analysis, both on the spectra and images were explored. The tissues had varied lipid signatures, which may be an indication of metabolic differences.

Chapter eight is the conclusion to this thesis. It is a perspective on the current work and contemplates future experiments.

Appendix A is a recent paper on 3D imaging of bromodeoxyuridine (BrdU) in single HeLa cells. This paper is an extension of the work in Chapter 5 in that it is one of the only examples of mapping a non-native, intracellular chemical species in an accurate, 3D fashion. This paper also investigates multiple operating modes of the LMIG analysis gun, determining that simultaneous high mass and spatial resolution is necessary for the best results.

Appendix B is a compilation of work that merits discussion, but at present time is not ready for publication. Included here is work on lactating mouse breast tissue, imaging gold nanoparticles in NIH/3T3 fibroblasts, and 3D imaging of a single plant cell (an onion cell).

2. Background

2.1 Introduction

The following topics are covered in this chapter:

- Theory and governing equations of ToF-SIMS.
- A literature review that encompasses the necessary background for a grounded understanding of this thesis. This is not meant to be an exhaustive literature review.
- An overview of several other analytical tools that can provide chemical information, with a comparison to ToF-SIMS.

Time-of-flight secondary ion mass spectrometry (ToF-SIMS) is an ultra-surface sensitive, ultra-high vacuum (UHV) analytical technique capable of probing the top 1-2 nanometers of a sample's surface [15]. An ion (the primary ion) is accelerated towards the surface of interest, and as a result of the impact of the ion with that surface, a large number of particles are ejected into the vacuum (e.g. neutral atoms, ions, electrons, and molecules). A small portion of these particles are ions (secondary ions), which are collected and separated in a time-of-flight analyzer. The secondary ions are representative of the species that make up the surface, and so ToF-SIMS is a technique that is capable of acquiring chemical information from a surface. For imaging, spatial resolution below 100 nm is attainable with current liquid metal ion guns (LMIGs) [4]. Secondary ion yields have been greatly enhanced through the adoption of polyatomic ion sources [5, 8]. These capabilities and ongoing improvements are discussed in more detail below, and are the principal reasons why ToF-SIMS is now a viable tool for solving problems related to biological cells and tissues.

2.2 ToF-SIMS Theory

2.2.1 Governing ToF-SIMS equations

The essential SIMS equation for positive secondary ions is [16]:

$$I_m = I_p Y_m \alpha_m^+ \theta_m \eta \quad \text{(Eq. 1)}$$

I_m: SI current of species m

I_p: primary ion particle flux

Y_m: sputter yield of species m

α_m^+: ionization probability of positive ion m

θ_m: fractional concentration of m in the surface layer

η: transmission of the system

Positive and negative secondary ions of species m (I_m) are desorbed from a surface as a result of the bombardment by energetic primary ions. The SI current of m depends largely on two intrinsic properties of the system: the sputter yield, Y_m, and the ionization probability of species m, α_m^+. The sputter yield may be defined as:

$$Y_m = N_m / N_p \quad \text{(Eq. 2)}$$

N_m: the number of sputtered particles of species m

N_p: the number of primary ion particles that impact the surface

The ionization probability depends heavily on the sample and is discussed in more detail below in Section 2.2.4. Two other important parameters are the damage cross-section, σ, and the efficiency, E. σ can be thought of qualitatively as the average surface area that is damaged during a single primary ion collision, and can be quantitatively related to the SI ion current of species m as:

$$I_m = I_{m,0} * e^{(-\sigma I_p)} \quad \text{(Eq. 3)}$$

I_m: SI current of species m

$I_{m,0}$: initial SI current of species m

σ: damage cross-section

I_p: primary ion particle flux

Additionally, the efficiency, E, can be defined as:

$$E = Y_m / \sigma \quad \text{(Eq. 4)}$$

Y_m: sputter yield

σ: damage cross-section

The damage cross-section and efficiency are useful parameters for comparing the performance of primary ion sources, which can be found in Section 2.3.3.

2.2.2 Proposed models for sputtering mechanisms

When an energetic primary ion impacts a sample, a portion of that ion's energy is transferred to the surface region. This energy transfer causes particle types to be ejected. Less than 1% of the emitted particles are secondary ions. Multiple theories have been developed to model the sputtering processes, two of which are presented here.

2.2.2.1 Linear cascade theory

Sigmund's linear cascade theory models a monatomic (for example, Ar^+) primary ion impacting a solid surface [17, 18]. The primary ion imparts a portion of its momentum to the atoms in the top few monolayers of the surface through inelastic collisions. Collision cascades are initiated, similar to billiard balls colliding with one another, some of which conclude with a secondary ion being ejected from the surface. A schematic of this process is shown in Figure 2.1. This model is more accurate describing a high energy monatomic primary ion impacting a polycrystalline surface, and less accurate in describing lower energy, polyatomic primary ions impacting complex organic surfaces like cells and tissues.

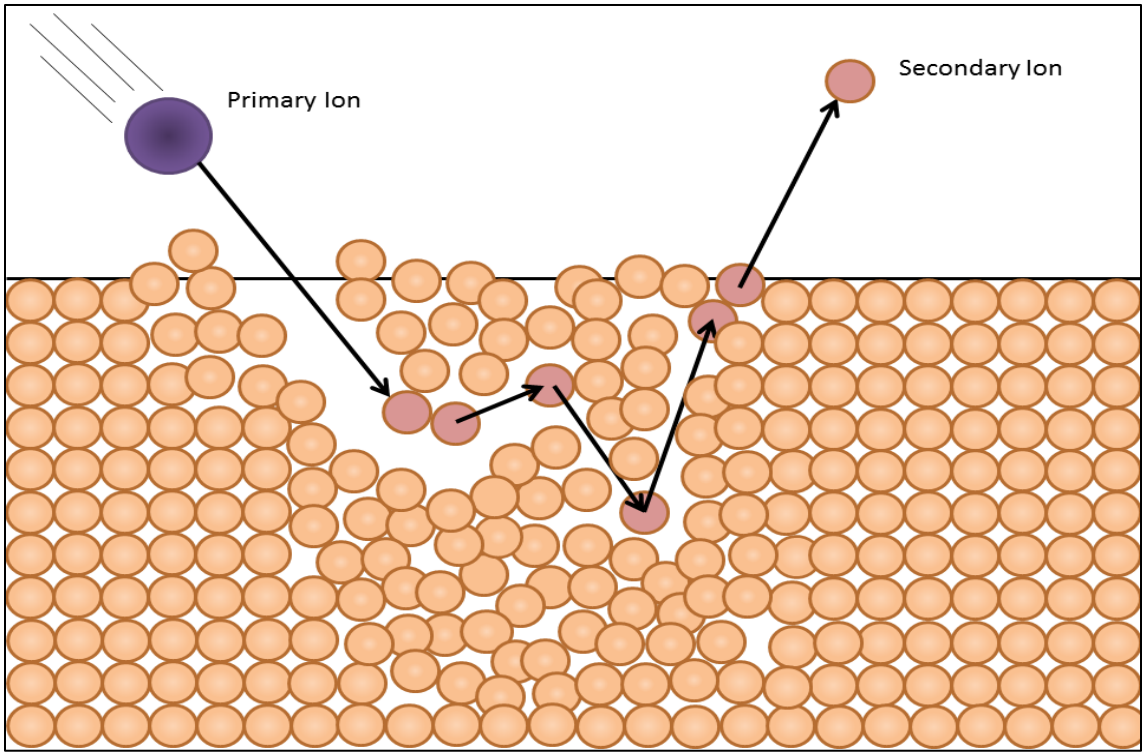

Figure 2.1. A schematic of a monatomic primary ion impacting a solid surface. The primary ion imparts a portion its energy on surface atoms via inelastic collisions, which act like billiard balls in a series of "collision cascades". There is a probability that through these collisions a secondary ion will be ejected.

2.2.2.2 Precursor model

An alternative model was developed by Benninghoven *et al.* that describes the energy distribution, E(r), that a keV primary ion imparts on a surface during impact [19]. This model was originally developed to describe a monolayer of organic molecules on a metal surface, but is viable for thicker organic samples [20]. A schematic of the energy distribution following a primary ion impact on a surface is shown in Figure 2.2. The highest energy density (red area) is found at the point of impact and dissipates as the distance from the impact site increases. In the high energy zone, fragmentation is highest and only small SI and atomic species are ejected. At some distance from the collision point, the energy density is not sufficient to break all of the covalent bonds within the sample (yellow area). As a result, larger SI fragments are ejected.

The qualitative energy density distributions as a function of distance from the impact position for monatomic and polyatomic primary ions are plotted on the top half of Figure 2.2 (adapted from Ref. 4). The energy profile produced by a monatomic ion has a high maximum and quickly decays. In contrast, the energy density profile produced a polyatomic ion collision has a lower maximum and decays much less rapidly as distance from the impact site increases. E_B is the binding energy that must be exceeded for intact molecules to be ejected.

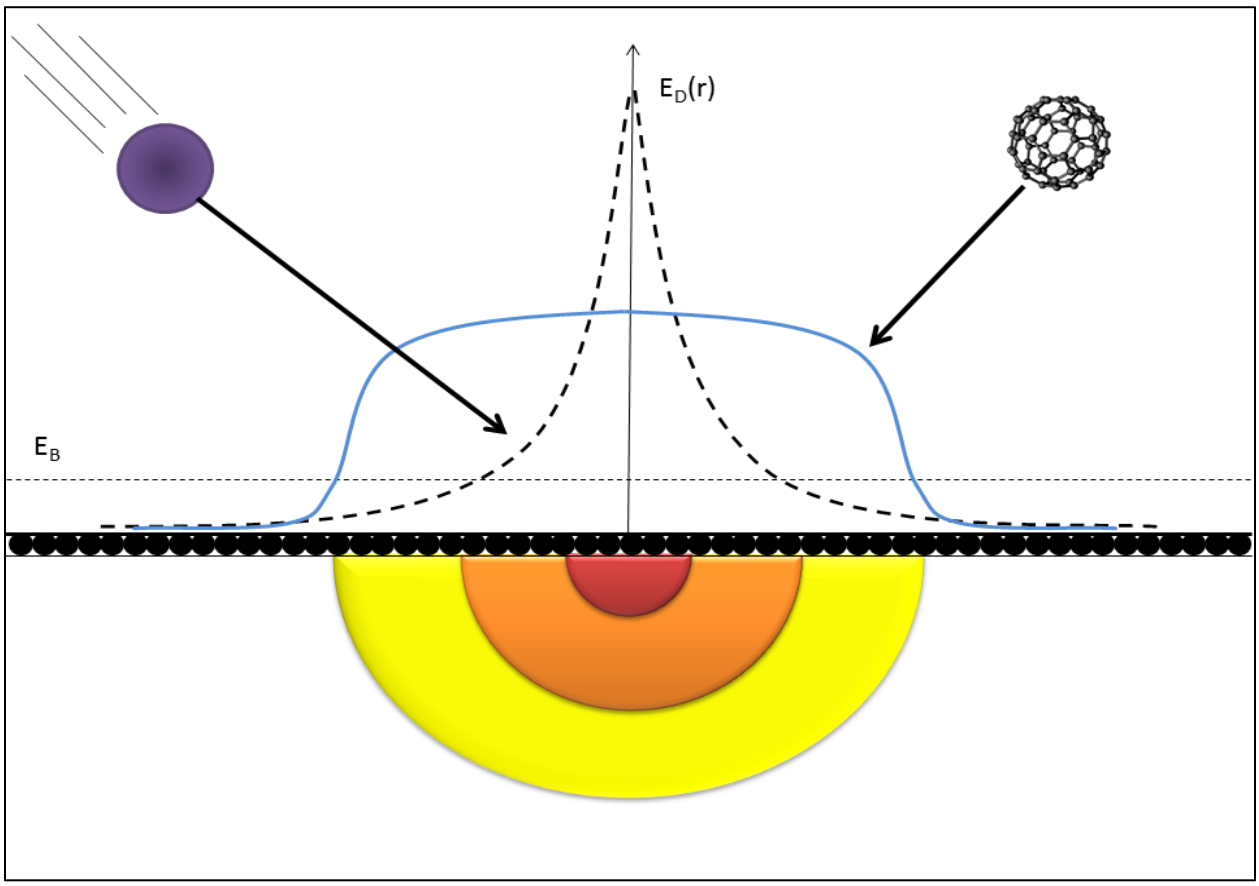

Figure 2.2. The energy density on the surface of a sample that has been transferred from an impinging primary ion is plotted. The red color represents the area of highest energy density, where mostly monatomic secondary ions will be ejected. The yellow area represents the area with the lowest energy density, where the largest secondary ions will be ejected. The qualitative energy density distribution from impacts by monatomic and polyatomic primary ions as a function of distance from the impact site is plotted on the top half of the figure (adapted from Ref. 4).

2.2.3 Matrix Effects

ToF-SIMS is considered "semi-quantitative" because quantities of components on a surface or within a material typically cannot be accurately determined (for example, in ng/cm^2). Each ion has an ionization probability (α^+) which partially depends on the surrounding environment (the matrix) [21]. The same compound in two different matrices, all other parameters being equal, may have different secondary ion yields. This is known as the *matrix effect*. There are studies that were performed with rigorous standards that were able to quantify the amount of a substance in a material [22], although this is very difficult to do accurately for a wide range of samples. Using a Cs^+ primary ion can significantly reduce matrix effects within some systems [23].

Matrix effects often prevent the absolute determination of concentrations of lipids, drugs or biomarkers within biological cells and tissues. This is one of the major limitations of ToF-SIMS. Relative comparisons can be made if the samples' matrices are similar, i.e. the relative amount of a particular lipid species in the plasma membranes of multiple cell types prepared the same way. Salts decreased the SI yields of organic fragments in peptide films [24], cells [25] tissues [26]. The presence of salts in biological cells and its effect on the SI yield of organics is a major topic of Chapter 4. There are methods that have been successful in reducing the negative effects salts have on SI yields, the most successful being analysis at cryogenic temperatures [24, 27].

2.2.4 Simulations of ToF-SIMS phenomena

Computer modeling has been a great complement to experiments and has created a better understanding of fundamental processes underlying ToF-SIMS. Some recent simulation studies

include the examination of the lateral displacement of Si atoms after multiple C_{60} impacts on a silicon surface [28]. The results indicate that the movement of atoms in the topmost layer of the silicon surface is isotropic, and that surface atoms can be laterally repositioned up to 100 angstroms prior to sputter removal. The development of surface topography on an Ag surface as a result of Ar_{872}, Au_3 and C_{60} bombardment was examined by simulating over 1000 successive primary ion impacts [29]. The results predict that surface roughness will increase until a saturation roughness is reached. In addition, the roughest surface was produced by Au_3 impacts, followed by C_{60} at normal incidence, then Ar_{872} at normal incidence, and the smoothest surface was produced by C_{60} at 70° normal to the surface. As computer hardware continues to improve and simulations can include more and more primary ion impacts, a better understanding of SIMS processes will be achieved.

2.3 ToF-SIMS Instrumentation

2.3.1 Liquid metal ion gun (LMIG)

LMIGs were initially developed decades ago for microfabication and analytical purposes [30], and their usefulness for SIMS has been explored for some time [31]. LMIGs produce an ion beam by covering a small tip with liquid metal and applying a large electric field. Ions are extracted from the resulting Taylor cone and focused in a downstream column. The focused beam can then be rastered precisely across the sample's surface. Current LMIGs have typical spatial resolutions around 100 nm in the pulsed mode [4], although this number will continue to be reduced. The development of the current generation of Au_n^{q+} LMIGs for use on ToF-SIMS instruments was presented by Davies *et al.* in 2003 [6]. Reports of Bi_n^{q+} LMIGs for use on ToF-

SIMS instruments was first presented by Touboul *et al.*, who demonstrated the efficacy of this new source by analyzing biological tissue [5].

2.3.2 Electron impact sources

Electron impact sources ionize a neutral gas phase molecule by bombarding it with energetic electrons. C_{60} sources produce ions this way [8], as do the "next-generation" argon gas cluster ion beams (GCIBs) [32]. C_{60} has been used to sputter depth profiling experiments of organic films [33], biological cells [34] and tissues [26] due to its high efficiency [8, 35]. C_{60} has been employed in a dual-beam approach [11, 36], where C_{60} was used as a sputtering source, and a LMIG was used during analysis cycles. C_{60} can also be used for both sputtering and analysis [7, 37]. GCIB argon sources are being increasingly utilized in experiments, as they are able to successfully sputter a larger amount of materials than C_{60}.

2.3.3 Comparison of primary ion sources

Kersting *et al.* compared the SI emission behavior caused by bombarding Irganox 1010 with monatomic (Ga^+, Cs^+, Au^+) and polyatomic primary ion sources (Au_2^+, Au_3^+, SF_5^+, C_{60}^+) [35]. The major conclusions were that heavier monatomic primary ions are more efficient than lighter ones and that all polyatomic ions are more efficient than any monatomic ion. C_{60} at 20 keV had the highest efficiency of the sources that were examined (for an explanation of efficiency see Eq. 4). Touboul *et al.* compared Bi_n^{q+} to Au_n^{q+} and determined they had very similar secondary ion yields, damage cross sections, efficiencies, and useful spatial resolutions during imaging of rat brain tissue [5]. Bi_3^+ had a beam current at least five times larger than Au_3^+ in similar experiments [38], and thus was preferred by the authors for biological tissue imaging experiments. A summary of these values is shown in Table 2.1.

Primary Ion (ref #)	Sample	Secondary ion	Y	σ	E
Au^+ [37]	Rat brain tissue	Cholesterol (m/z 385)	$2.13x10^{-5}$	$3.92x10^{-13}$	$5.43x10^{7}$
Au_3^+ [37]	Rat brain tissue	Cholesterol (m/z 385)	$6.60x10^{-4}$	$6.36x10^{-13}$	$1.04x10^{9}$
Bi^+ [5]	Rat brain tissue	Cholesterol (m/z 385)	8.36×10^{-5}	2.75×10^{-13}	3.04×10^{8}
Bi_3^+ [5]	Rat brain tissue	Cholesterol (m/z 385)	7.06×10^{-4}	4.14×10^{-13}	1.71×10^{9}
Au^+ [34]	Irganox 1010	$C_{73}H_{107}O_{12}^-$	$4.4x10^{-5}$	$3.0x10^{-13}$	$1.5x10^{8}$
Au_3^+ [34]	Irganox 1010	$C_{73}H_{107}O_{12}^-$	$2.0x10^{-3}$	$1.1x10^{-12}$	$1.8x10^{9}$
C_{60}^+ [34]	Irganox 1010	$C_{73}H_{107}O_{12}^-$	$3.2x10^{-3}$	$2.1x10^{-13}$	$1.5x10^{10}$

Table 2.1. A comparison of primary ion sources. Y is secondary ion yield, σ is damage cross section, E is efficiency.

C_{60} was the most efficient primary ion in these studies because of the lower energy per atom in a C_{60} molecule compared to the energy per atom of the other ions [39]. For example, 10 keV Bi has an energy per atom of 10 keV, while the energy of one carbon atom in 10 keV C_{60} is 167 eV. Whereas a C_{60} ion imparts most of its energy to the near-surface region, a monatomic Bi primary ion can penetrate 25 nm into the sample [15, 40, 41], disrupting and damaging subsurface layers. One explanation is that the C_{60} molecule breaks up upon impact [42, 43], creating an effect similar to 60 individual, low-energy carbon atoms impacting the surface. As more energy is deposited in the near-surface region, sputter and SI yields increase and less damage is caused to the region immediately below the impact zone [44].

Argon GCIBs reduce the energy per atom even farther. Typical cluster sizes for these sources range from Ar_{500} to Ar_{3000}, while impact energies remain at 10-20 keV, producing energy per atom values between 3 – 40 eV [45, 46]. Several initial studies on the performance of Ar GCIBs concluded that they produced a larger sputtering volume than C_{60} on the NPL Irganox reference material [9, 33]. Ar clusters also generated less sputter induced roughness, with values of R_q typically 1-2 nm, compared to 10 nm for C_{60} [47]. The reduction in sputter-induced topography by Ar clusters on organic materials is not fully understood. Both for Ar [9] and C_{60} [39], the sputter yield was more dependent on the total impact energy than on the energy per atom.

A recent report compared the use of C_{60} and Ar GCIBs for analyzing biological samples [48]. Depth profiles of cholesterol films with C_{60} and Ar reached similar steady state SI intensities of the characteristic m/z 369.3 fragment. C_{60} and Ar GCIB were compared as sputtering and analysis sources on cancer cell and tumor sections [49]. This study found that Ar clusters were able to better preserve the signals from intact molecular phospholipid ions after etching, and reduced the accumulation of the chemical background noise compared to C_{60}^+.

A well characterized advantage of GCIBs over C_{60} as a sputtering beam is the ability of Ar clusters to sputter "Type I" polymers. There are two commonly accepted classes of polymers, Type I and Type II. Type I polymers crosslink when irradiated, while Type II mostly degrade due to a random chain scission process. Type I polymers are often not highly branched, and most contain aromatic groups. C_{60} has been historically very ineffective at successfully sputtering Type I polymers, which cross link under bombardment. A comprehensive list of Type I and II polymers is found in the 2009 review by Mahoney [50]. Ar GCIBs have been

much more successful in sputtering Type I polymers, as well as complex, highly aromatic organic polymers like those commonly found in organic light emitting diodes (OLED) [46].

The increased SI yields and efficiencies of modern polyatomic ion sources, during analysis and sputtering, are major reasons why ToF-SIMS is a viable tool for exploring complex biological samples. The recent addition of Ar GCIB to the arsenal of available ion sources should prove to be very beneficial, as it has been shown to reduce damage caused by sputtering and best preserves chemical information compared to the others source used to date.

2.3.4 Time-of-flight analyzer

Most current static SIMS instruments use a "time-of-flight" (ToF) analyzer [13]. There are multiple types of ToF analyzers present on SIMS instruments. That which is installed on the ION-TOF V is depicted in Figure 2.3. The ToF analyzer's predecessor, the quadrupole mass analyzer [51, 52], is still widely used today. Some dynamic SIMS instruments utilize a magnetic sector mass analyzer [53]. The advantages of a ToF analyzer are its ability to detect all of the collected secondary ions in parallel, high mass resolution ($m/\Delta m$ ~10,000), and is capable of detected ions in a theoretically unlimited mass range. Prior to entering the analyzer, secondary ions are ejected from a surface and accelerated at a fixed voltage to the entrance of the analyzer. The collected ions enter a field-free zone, and as they have different masses and the same energies, travel through the analyzer with different velocities. They then impact the detector, where the ion's travel time is related to its mass by:

$$t = d*(m/2zV)^{1/2} \quad \text{(Eq. 5)}$$

t: flight time

d: flight distance, length of detector

m: mass of the ion

z: charge of the ion

V: accelerating potential

A schematic of SIs traveling through a ToF analyzer is shown in Figure 2.3. The green molecule is the lightest, so it travels through the field-free region with the highest velocity and arrives at the detector first. The red molecule is the heaviest, so it is detected last. Typical lengths for analyzers are 1-2 meters. Many modern ToF analyzers incorporate a reflectron (or ion mirror), which improves mass resolution by correcting the flight times of ions with the same mass that have an initial energy spread entering the analyzer.

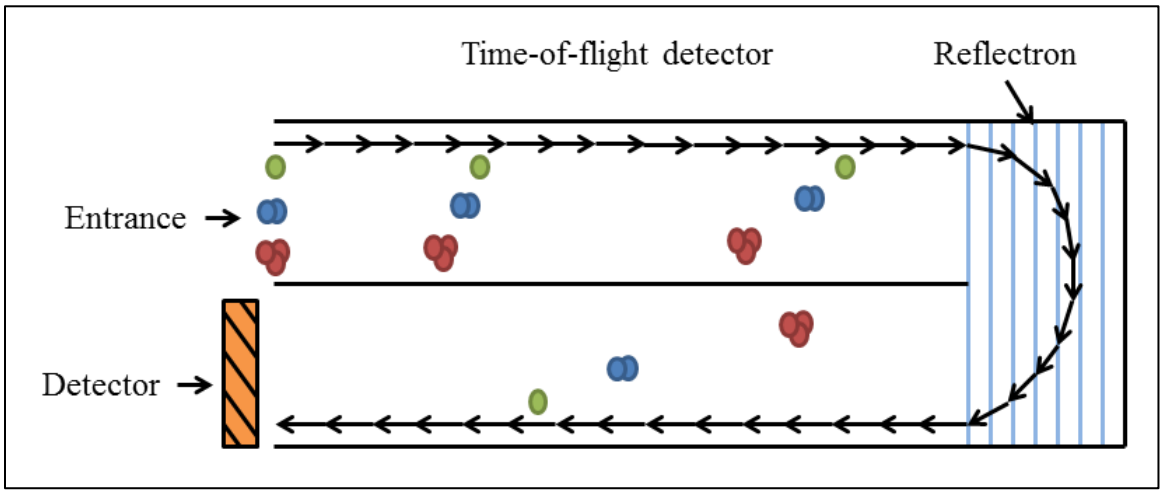

Figure 2.3. A diagram of a time-of-flight analyzer. Secondary ions are accelerated to the entrance of the analyzer, where they enter a field-free zone. Smaller fragments will travel faster than larger fragments and reach the detector first, producing a mass spectrum. The reflectron improves mass resolution by correcting the flight distance of ions of the same mass that enter the analyzer with slightly different energies.

2.3.5 Custom-built instrumentation for biological sample analysis

There have been a number of instrumentation developments that specifically address improving the examination of biological cells and tissues. Ionoptika's J105 allows for the *in-situ* freeze-fracturing of a frozen cells under vacuum [54], while the Arlinghaus group has incorporated a cryomicrotome into a ToF-SIMS to serial section frozen tissue and analyze the fresh face of a tissue block multiple times on the same sample [55]. An *in-situ* freeze fracture device has been adapted from the J105 freeze fracture system to work on an Ion-ToF IV cold stage [56, 57].

2.4 Literature Review

2.4.1 Biological cells

The early investigations of cells with SIMS were carried out in the dynamic regime. Many were performed by Chandra *et al.*, who imaged the intracellular distributions of atomic ions (i.e. K^+, Na^+, Mg^+, Ca^+). Freeze-fracturing was introduced, and is still used, as a method to prepare cells for ion microscopy analysis [58-60]. Mentre *et al.* explored how the presence of water affects intracellular diffusible cations [61]. A number of early reviews detailing the potential role of ion microscopies in the biomedical fields focus on mapping intracellular drug distributions, localizing intracellular radioactive isotopes, and mapping chemical elements relevant to metabolic activities [62-65].

The first study on biological cells with ToF-SIMS was in 1997. Colliver *et al.* developed an early frozen-hydrated sample preparation protocol for cells for ToF-SIMS analysis [66]. While SI yields were low (due to the monatomic Ga^+ primary ion), this work proved the feasibility of a cellular molecular information with ToF-SIMS. Soon after, lipid fragments from the plasma membranes of frozen-hydrated red blood cells were successfully collected [67, 68].

The number of papers focused on probing cell chemistry with ToF-SIMS began to rise more rapidly at this point (~2002), due to the advent of the Au_n^{q+} and Bi_n^{q+} ion sources. Some highlights include a 2004 paper where chemical images showed that the low-curvature lipid phosphatidylcholine (PC) is reduced in the membrane regions between fusing *Tetrahymena* cells, where large amounts of highly curved fusion pores are located [69]. A follow-up study showed that the decrease in PC concentration follows, not precedes, structural changes in the plasma membrane [38]. In 2007 Fletcher *et al.* produced 3D chemical maps of various several biological components of a *Xenopus laevis* oocyte using C_{60}^+ as both the sputtering and analysis beam [12] Breitenstein *et al.* reconstructed z-corrected 3D views of animal cells (gluteraldehyde-fixed epithelium-like normal rat kidney cells) for the first time [14, 70]. A correction was introduced to the 3D data stack that shifted pixels along the z-axis to their correct position. The intracellular adenine signal from frozen-hydrated HeLa cells was presented in a three dimensional, corrected format [27]. Ostrowski *et al.* compared macrophages that had been grown in culture media supplemented with cholesterol versus those that had no supplementation. They found that the macrophages grown in the cholesterol-supplemented media contained over double the amount of cholesterol in the outer leaflet of the plasma membrane than the control cells [71]. Brison *et al.* evaluated different methods to prepare cells prior to analysis and mapped the intracellular Br^- signal uptaken by HeLa cells from media-supplemented 5-bromodeoxyuridine [34].

2.4.2 Biological tissues

A majority of the research on biological tissues has been lipid-related, as these provide high SI yields. As with cells, an increase in the number of research articles that focused on biological tissues increased around 2002 upon the introduction of polyatomic ion sources.

One of the earliest ToF-SIMS investigations of tissue was completed by John et al. in 1997 [72], which focused on collecting spectra of different drug species in tissue-like films (Matrigel®) and rat brain tissue. Since then, there have been investigations on ocular tissues [73, 74], lipid distributions in the aortic wall [75], lipid mapping of zebra finch brain [76], cardiac tissue in hypertensive rats [77], Fabry disease biomarkers [78], dystrophic muscle tissue [79], lipids near skeletal muscle [80]. Wood tissue and fibers have also been characterized, showing the broad impact ToF-SIMS can have [81-83]. These are just some examples of the types of tissues that have been examined.

2.4.3 Lipids

Lipids have garnered a lot of attention by the ToF-SIMS community due to their high ionization efficiencies. A comprehensive list of lipid fragments obtained from mammalian cells, tissues, bacteria and microbes was included in a recent review by Passarelli and Winograd [84]. A detailed list of lipid fragments less than m/z 300 was created to assist peak assignment in cell and tissue analysis [85], The peak list was generated analyzing 1,2-dilauroyl-*sn*-glycero-3-phosphocholine (DLPC) and ^{15}N-DLPC model films.

The investigation of model membrane systems plays an important role in furthering the understanding of lipid behavior in more complex biological samples. Prinz *et al* compared three structurally different phospholipid assemblies, finding that the 1-palmitoyl-2-oleoyl-sn-glycero-3-phosphocholine (POPC) molecular ion (m/z 760^+) was detected with the highest intensity in the most well-ordered of the three [86]. Different orientations of dipalmitoylphosphatidylcholine (DPPC) molecules showed changes in the mass spectra, most notably of the PC headgroup at m/z 184^+ and a characteristic alkyl tail fragment at m/z 311^+. In a heads up orientation the PC headgroup signal intensity was high while the peak representing the tail was low. This was

reversed in samples that had DPPC in a tails up configuration, and for an unordered film both peaks were detected [68]. There are numerous studies that have mapped lipid distributions in many types of cells and tissues, which are covered in more detail in the sections 2.4.1 and 2.4.2.

2.4.4 Proteins

Proteins make up a large amount of the material in cells and tissues. Since large biomolecules are broken up during the SI emission process, the spectra from different proteins often look similar, especially in the low mass (m/z <150) region. The mass spectral fingerprints of the 20 naturally occurring amino acids have been previously characterized [87, 88]. Within cells and tissues, it is not possible to determine the relative amounts of individual proteins. There are too many present, combined with insufficient quantity and intensity of unique mass fragments. However, three different types of human breast cancer cell lines have been distinguished based on the relative difference in known amino acid peak intensities and multivariate analysis methods [89]. Two small, hydrophobic proteins have been mapped in relation to lipid species in a model lung surfactant system [90].

Adsorbed proteins can be differentiated from one another based on unique peaks, the relative intensities of similar peaks and multivariate analysis methods [91, 92]. Additionally, complex multicomponent protein films have been examined. In binary and tertiary films, the outermost surface composition was quantitatively measured [93-95]. It has proven difficult, thus far, to test adsorbed protein films more complex than this.

The exceptional surface sensitivity of ToF-SIMS allows a protein's conformation and orientation on surfaces to be probed. Because the sampling depth is 1-2 nm [15], and since many adsorbed proteins have dimensions larger than this, different conformations and orientations will

generate different mass spectra. Baio *et al.* examined the orientation of a surface immobilized variant of the humanized anti-lysozyme [96], as well as how the structure of bovine serum albumin (BSA) changed upon adsorption onto three different calcium phosphate phases [97].

2.4.5 DNA

The components of deoxyribonucleic acid (DNA) were examined by May *et al.* using XPS and ToF-SIMS [98]. DNA microarrays have been probed with ToF-SIMS because of its shallow sampling depth and imaging capabilities [99-101]. Due to the above studies, the characteristic fragments of DNA are well known and are detectable within cells. Fletcher *et al.* mapped the adenine molecular ion in a three dimensional image of HeLa-M cells [27].

2.4.6 Applications using multivariate analysis

Multivariate analysis (MVA) methods can reduce the complexity of very large data sets, like those that are generated with ToF-SIMS. Principal components analysis (PCA) is a MVA technique which reduces the number of variables (the peaks selected from the spectra) from many hundreds to a few new variables that capture the greatest variance (principal components). The outputs of PCA are the scores, which relate the samples to one another, and loadings, which relate the selected peaks to the samples. PCA has been useful in a number of studies that attempt to find significant differences between similar samples. Often in studies of cells and tissues, PCA is used to help distinguish one cell or tissue type from another and display the largest sources of variance between the samples. This is often necessary, as the spectra from cells and tissues are often extremely complicated and difficult to interpret.

Wagner *et al.* used PCA to differentiate between 13 different types of adsorbed proteins [102], and PCA is widely used for generating useful information. [92]. Jungnickel *et al.*

successfully discriminated between four yeast strains from two species [103]. In this study, 34 ions out of 1200 detected were determined to distinguish between the strains. The intracellular compartments of three human breast cancer cell lines, as well as the cells themselves were distinguished one another with the help of PCA [104]. Prostate cancer cells have been distinguished from malignant cells [105, 106].

Partial least squares discriminant analysis (PLS-DA) has been used in combination with desorption electrospray ionization mass spectrometry (DESI) to classify the disease state of human bladder carcinoma tissue sections with a 12% misclassification rate. PCA and PLS-DA were used to identify rat esophageal epithelial cells and NIH/3T3 fibroblasts in heterogeneous culture. Unknown regions of cells otherwise unidentifiable by ToF-SIMS could be classified based on the PLS-DA model [34].

2.5 Other techniques for chemical analysis of biological cells and tissues

2.5.1 Matrix-assisted laser desorption ionization (MALDI) mass spectrometry

MALDI utilizes an ultra-violet (UV) laser to desorb large biomolecules from surfaces. An organic matrix is deposited on the surface of interest which absorbs UV light. When the laser is directed at the matrix, UV light is adsorbed and creates a plasma, of sorts, of the top micron of material. The advantage of MALDI is that entire biomolecules may be detected. This includes very large lipid species, whole proteins, etc. Whereas in SIMS “high mass” fragments are typically between m/z 700-2000, in MALDI the mass of detected species can reach m/z 200,000.

State-of-the-art MALDI instruments are capable of imaging biologically relevant samples with spatial resolution that are increasingly improving, with groups now claiming 3-5 μm spatial resolutions [107-109], although many commercial instruments have a minimum resolution of

30-80 μm [110]. Single cell imaging was shown to be possible [111]. A thorough comparison of ToF-SIMS and MALDI-ToF imaging was completed by Hammond *et al* [112].

ToF-SIMS and MALDI-ToF are complementary methods. ToF-SIMS provides higher spatial resolution in imaging, although has a much a lower mass range. Alternatively, MALDI is able to desorb very high masses (sometimes with m/z > hundreds of thousands), although at lower spatial resolutions. Studies that have utilized both ToF-SIMS and MALDI mass spectrometry include the analysis of rat brain tissue [113], and the examination of Fabry disease biomarkers [78].

2.5.2 Desorption electrospray ionization (DESI) mass spectrometry

DESI is an atmospheric mass spectral analytical technique. Ionized liquid droplets are directed at surface. There are multiple proposed mechanisms of ionization [114]. In one mechanism, the solvent hits the surface, dissolves the molecule of interest, and leaves the surface. On its path to the analyzer, the solvent is evaporates, leaving only an ion to be detected. Current DESI instrumentation is capable of imaging biological tissue with a 100-500 μm spatial resolution [115], over a mass range similar to ToF-SIMS. Some examples of DESI analyses of biological samples include investigating bovine blastocytes [116], and probing oocytes and pre-implant mouse embryos [116].

2.5.3 Raman spectroscopy

Raman spectroscopy is based on the inelastic scattering of photons after they interact with a molecule [117]. Some of the impinging laser light is inelastically scattered (~ 1 photon in 10^7), providing information regarding the vibrational modes within the sample. Variations on classical Raman spectroscopy include surface-enhanced Raman spectroscopy (SERS) [118] and

coherent anti-stokes Raman spectroscopy (CARS)[119]. A particular advantage of Raman spectroscopy is the ability to non-invasively image living subjects [120].

3. Materials and Methods

3.1 Materials

3.1.1 Non-biological materials

Silicon chips were used as substrates for all cell and tissue for all experiments. Silicon wafers (Silicon Quest Intl., Santa Clara, CA) were diced into 1x1 cm^2 chips and cleaned before being used for the cell experiments. Ethane gas was purchased from Praxair (Dansbury, CT), part number ET 5.0RS, 99.999% purity. Total weight of the gas and cylinder was 36 lbs. The smallest available ethane bottle was purchased so that it could fit in a fume hood. The ethane bottle should be stored in a fume hood at all times for safety considerations.

For chemical fixation, 16% ethanol-free formaldehyde (Thermo Scientific, Erie, PA) was purchased in packs of 10, 20 ml ampules. 20 mL 4% formaldehyde solutions were created by adding 5 mL of 16% formaldehyde to 2 mL of 10x PBS and 13 mL of 18 ΩM H_2O.

Ammonium acetate (AA) (Sigma, St. Louis, MO) was used to create isotonic rinsing solutions for the cell studies.

3.1.2 Cells lines used in these studies

NIH/3T3 fibroblast cells were used in Chapters 4 and 5. Originally, a small number of cells were graciously given as a gift from Prof. Buddy Ratner's lab, and those were passaged for the experiments used in these chapters.

Eight breast cancer lines were studied in the Chapter 6 study. These were provided by Prof. David Hockenbery's lab at the Fred Hutchison Cancer Research Center (FHCRC). The four triple-negative (TN) lines were MDA-MB-231, BT-549, HS578t, and HCC1395. The four receptor positive (RP) cell lines that were examined were T47-D, MCF-7, BT-474, and

HCC1428. Details about these cell lines can be found on the American Type Culture Collection website, http://www.atcc.org.

3.2 Methods

3.2.1 Silicon substrate preparation

1 cm x 1 cm chips were soaked in water overnight, then cleaned with 2x five minute sonications in dichloromethane, acetone and methanol. They were dried with purified N_2, then stored in a laminar hood until use.

3.2.2 Cell growth

NIH/3T3 fibroblasts were grown in a 37 °C and 5% CO_2 environment. Cells were seeded at densities between 40,000–100,000 onto silicon chips and were allowed to grow for 2-3 days, depending on the desired cell density. The cells were grown in a typical cell culture laboratory facility following established best practices for cell culture. 1 cm x 1cm silicon chips were placed in 24 well plates and then seeded with the appropriate number of cells. First, ~1.5 mL of cell growth media was pipetted into a well with a silicon chip within it. The cell solution was diluted such that 0.5 mL was added to the well to produce a final volume of 2 mL and the appropriate number of cells. Cells were counted with a hemocytometer.

The human breast cancer cell lines were grown in a 37 °C and 5% CO_2 environment. Cells were seeded onto silicon chips and were allowed to grow for 1-2 days.

All cells were grown in the correct media. Individual media compositions are presented in the Methods section of each chapter.

3.2.3 Ammonium acetate rinsing solution

Ammonium acetate (Sigma, St. Louis, MO) was dissolved in 18 MΩ H_2O to form a 150 mM solution and was bought to pH 7.4 with 1M ammonium hydroxide (Sigma, St. Louis, MO).

3.2.4 Liquid ethane formation

Liquid ethane was used as the cryogen for plunge freezing. Liquid nitrogen (LN_2) does not have a high enough cooling rate to freeze intracellular water without creating large ice crystals. The cryogens that are typically used are either liquid ethane or a mixture of isopentane and propane.

Liquid ethane was produced by leaking purified ethane gas into a LN_2 cooled plastic beaker. The beaker was partially submerged in LN_2, but not so much that LN_2 was able to flow into the beaker. First, a very low flow rate was used, and then at increased flow rates when liquid is initially formed. After the first bit of ethane is formed, a bubbling noise will be audible. By slowly increasing the gas flow rate with time, the gaseous ethane is condensed into enough liquid ethane to plunge freeze the silicon chips. 40-50 ml of liquid ethane was produced for plunge freezing. With the plastic beaker that was used, this equated to a volume that was roughly 1.5 inches deep.

3.2.5 Cryofixation by plunge freezing

Cells seeded onto silicon chips were plunge frozen in liquid ethane using the following procedure. Liquid ethane was produced using the process described in Section 3.2.4. Silicon chips that had been previously seeded with cells were removed from their media and rinsed in the ammonium acetate rinsing solution. A Kimwipe removed excess liquid by touching it to the edge of the silicon chip. The chip was plunged into liquid ethane and held under for 10 seconds, and then quickly placed under liquid nitrogen until further use.

3.2.6 Chemical fixation

20 mL 4% formaldehyde solutions were created by adding 5 mL of 16% formaldehyde to 2 mL of 10x PBS and 13 mL of 18 MΩ H_2O. Cells seeded onto silicon were

rinsed for 1 second in an ammonium acetate rinsing solution to remove excess media and then placed in 2 mL of 4% formaldehyde for 30 minutes. The samples were taken out of the fixing solution, rinsed with H_2O to remove excess buffer solution, and dried overnight.

3.2.7 Freeze-drying

Freeze-drying was performed using Dr. Cecilia Giachelli's manifold type-freeze drier (SP Scientific, Warminster, PA) in Foege N315B. The samples were frozen as described above, and quickly transferred to LN_2. While under LN_2, the chips were placed into small glass test tubes, and the tops were covered with aluminum foil with a small hole. These test tubes were placed into a pre-cooled freeze-dry flask (−80°C freezer overnight), while the chips were still submerged in LN_2. The test tubes were removed from under LN_2, then LN_2 was poured out of the flask until the silicon chip was just barely submerged. It is important to try and minimize the amount of LN_2 that the freeze drier pump has to remove. Then, the flask was attached to the freeze drier and a vacuum was quickly established. The samples dried overnight.

3.2.8 Frozen-hydrated analysis of cells with ToF-SIMS

The heating/cooling stage ("cold stage") for the ION-TOF V instrument is capable of heating or cooling a single sample using temperature controls within the FPanel software. There are separate controls for the load lock temperature and the analysis chamber temperature. It is important to set both controls to the desired temperature, otherwise the sample, and possibly the instrument, will be harmed.

There are two ways to use the stage. In the first, the sample does have to rapidly frozen before entering the loading chamber. This is the more typical way to use the cold stage. In the second, which is the method used in this work, the sample must be rapidly frozen before it is put onto the cold stage, and it must be kept cold during the entire preparation/analysis workflow.

For the first method, place the sample onto the cold stage and screw down the mask on top of it. The thermocouple must be inserted between the mask and the stage and also screwed down. Place the stage in the loading chamber. Add LN_2 to the vacuum dewer (evacuated the night before). Set the desired temperature of the stage in the FPanel; -130 °C < -160 °C is normal here. Bring the cold finger into contact the cold stage. The temperature of the stage will lower. At -100 °C, begin to pump down the loading chamber. Once the desired temperature has been reached and the pressure in the loading chamber is below 5E-7, transfer the stage into the analysis chamber. Remember to set the temperature in the analysis chamber as well. If this is not done, the sample will rapidly heat up and the pressure will spike in the analysis chamber.

For the second method, the sample is frozen before it is put onto the cold stage. The cold stage is precooled in the loading chamber to -160 °C. The sample is rapidly placed onto the cold stage and held down with a clip instead of the mask. The thermocouple is screwed down by the mask on the edge of the portion of the stage where the sample is placed. The cold finger is rapidly put into contact with the cold stage and the loading chamber is pumped down. The temperature is allowed to decrease to ~ -150 °C, the then it is ramped up at a rate of 5 °C/min to -80 °C to sublimate excess water ice. After sublimation, the temperature is reduced to -160 °C, and then the stage is transferred to the analytical chamber.

3.2.9 ToF-SIMS

Detailed ToF-SIMS experimental setups are presented in each chapter. The information presented below are general settings that were similar for all experiments.

Positive and negative secondary ion spectra were collected with an ION-TOF TOF SIMS 5-100 instrument (ION-TOF, Münster, Germany), using a pulsed 25 keV Bi_3^+ primary ion beam. Samples were sputtered with a 20 keV C_{60}^{++} beam. Both the Bi and C_{60} beams are oriented 45°

to the surface normal. The spectra were calibrated using peaks of known mass, and these peaks are presented in each chapter. Low energy electrons were flooded onto the sample to compensate for charge buildup on the surface.

High mass resolution (HMR) spectra ("bunched" mode) were acquired using Bi^{3+}. The Bi_3^+ current was typically 0.15 pA to avoid saturation of lower mass peaks. The high spatial resolution (HSR) mode ("burst alignment" mode) was used to collect high spatial resolution images, always using Bi_3^+. The current was between 0.03-0.06 pA, typically using an 80.1 ns pulse width. In this mode, the spectra have nominal mass resolution (that is, the "peaks" look like step functions).

Some data was collected in the .RAW format using the IONTOF Version 4 software and subsequently converted into the .itm format used by SurfaceLab 6 at a later time. All data was subsequently analyzed using the IONTOF SurfaceLab 6 software.

Regions of interest (ROI's) of the cells have been chosen in some analyses by thresholding the "total counts" image. For these areas the signal from the cells was significantly higher than from the substrate. ROI's were also chosen for the tissue experiments, but this typically based on the distribution of a specific secondary ion or a set of secondary ions.

3.2.10 Atomic force microscopy

To measure the height of the dried cells before ToF-SIMS analysis, a Dimension ICON (Bruker, Santa Barbara, CA) atomic force microscope (AFM) was used in ScanAsyst® mode in air with a silicon nitride, ScanAsyst-Air tip. Raw AFM data was imported into the NanoScope Analysis software and a second order plane fit was applied to all images. No further modifications were applied to the images.

3.2.11 Principal component analysis (PCA)

Due to the complexity of ToF-SIMS spectra, it is often useful to use multivariate analysis methods to "simplify" the data. One popular method is principal component analysis (PCA). PCA is an unsupervised multivariate analysis technique that determines the largest sources of variance within a data set and replots the data on new axes, or principal components. The two outputs of PCA are the scores, which relate the data points to one another, and the loadings, which relate the variable (the peaks) to the data points. A recent review on multivariate analysis methods applied to ToF-SIMS data was written by Graham and Castner [121].

All PCA analyses were performed using the SpectraGUI software (Dan Graham, NESAC/BIO, University of Washington) within MATLAB (Mathworks, Natick, MA). In all instances, the data were normalized by the sum of the selected peaks and square root mean centered.

For the spectral PCA of the tissue data, the most efficient way to extract .txt files with peak intensities is described here. The data were collected as 1 mm x 1 mm "patches", each containing 25 200 μm x 200 μm "tiles". All of the desired peaks were selected manually in the SurfaceLab 6 spectrum software and an .ita file was constructed. Then, in the SurfaceLab 6 image software, a .bif6 file containing all of the images was exported. The .bif6 files can be imported into the ImageGUI (Dan Graham, NESAC/BIO, University of Washington). When the proper "tile resolution" is input into the GUI (256 pixels x 256 pixels), the "cut up stage raster" function was used. A .txt file is generated that has the peak intensities of each of the tiles. The .txt from multiple patches and samples can be combined later to perform PCA. It must be noted that is method is a very efficient way of exporting the necessary peak intensities into the .txt files needed for the SpectraGUI if it is desired to change the region from which the intensities are being extracted. To clarify, to use the *same peak list* but on a different region (e.g. a region of

interest), then this is an efficient method for stitched images. If it is desired to export the intensities of a *new* peak list from the same region, the method described above is not the most efficient. In that case, simply using the "statistics" page in the SurfaceLab6 spectra software is faster.

4. Characterization of sample preparation methods of NIH/3T3 fibroblasts for ToF-SIMS analysis

Michael A. Robinson[1, 3], and David G. Castner[1-3, §]

National ESCA and Surface Analysis Center for Biomedical Problems[1] Departments of Bioengineering[2] and Chemical Engineering,[3] University of Washington, Seattle, WA 98195

§ Corresponding author

David G. Castner

1-206-543-8094 (phone)

1-206-543-3778 (fax)

castner@uw.edu (e-mail)

Keywords

ToF-SIMS, Cells, Depth profile, Sample preparation

4.1 Abstract

The information that is obtained from single cells during time-of-flight secondary ion mass spectrometry (ToF-SIMS) analysis is influenced by the method that was used to prepare the cells. The removal of extracellular media before analysis is necessary, but the rinsing technique should not damage the plasma membrane of the cell. The presence of intracellular salts reduced the secondary ion yield an average of 2.6-fold during Bi_3^+/C_{60}^{++} depth profiles. Chemical fixation followed by rinsing removed a majority of the intracellular salts, "recovering" the positive secondary ion yields. The formaldehyde-fixation process removed a majority of the intracellular Cl^-, but other key anions were not removed in significant amounts. The data presented here is consistent the anion neutralization mechanism largely responsible for the lower ion yields. All of the organic secondary ions that were detected in the freeze-dried cells were also detected in the formaldehyde-fixed cells, suggesting that the fixation process did not remove any molecular species to an extent that is detectable by ToF-SIMS. Compared to freeze dried cells, well preserved, frozen-hydrated cells showed little increase, or a decreased yield, for most low mass ions, but an increased yield for larger mass fragments. This is consistent with a reduced damage cross section at cryogenic analysis temperatures, although proton donation from water and reduction the salt effects in the presence of water likely also play roles. Numerous ions detected from the frozen-hydrated cells were not detected from the freeze dried cells, however many of these ions were attributed to chemical combinations of water, salts and the ammonium acetate rinsing solution.

4.2 Background

Time-of-flight secondary ion mass spectrometry (ToF-SIMS) is a powerful tool that has been used to explore a wide range of biologically relevant samples including: cells and tissues [34, 122-124], lipids [125], proteins on surfaces [92, 126], DNA [100, 101], drug eluting stents [127, 128], explanted biomaterials [129] and decellularized matrix [130]. The unique abilities of ToF-SIMS to acquire a mass spectrum with high mass resolution, as well as produce chemical maps with submicron spatial resolution [4] provides an effective method to probe biological cells and tissues. These strengths, along with the capacity to sputter etch organic material [131, 132], may enable the 3D visualization of sub-cellular features including drug, metabolite or nanoparticle behavior within single cells. There is a continuing need to characterize how diverse sample preparation methods influence the information that is acquired from biological cells [133].

The methods to prepare cells for SIMS analysis can be organized in several ways. A schematic that outlines the most common techniques is shown in Figure 1. They can be separated into one of two fundamental categories: either the cells are dehydrated prior to analysis, or the intracellular water is conserved and the cells are analyzed frozen-hydrated. The methods may also be organized by the mechanism that removes the culture media from a cells' surface before analysis. Either the media is removed with an isotonic rinsing solution, or the cells are freeze-fractured, removing a portion of the cell and all of the media above it, creating a pristine surface for analysis [134, 135].

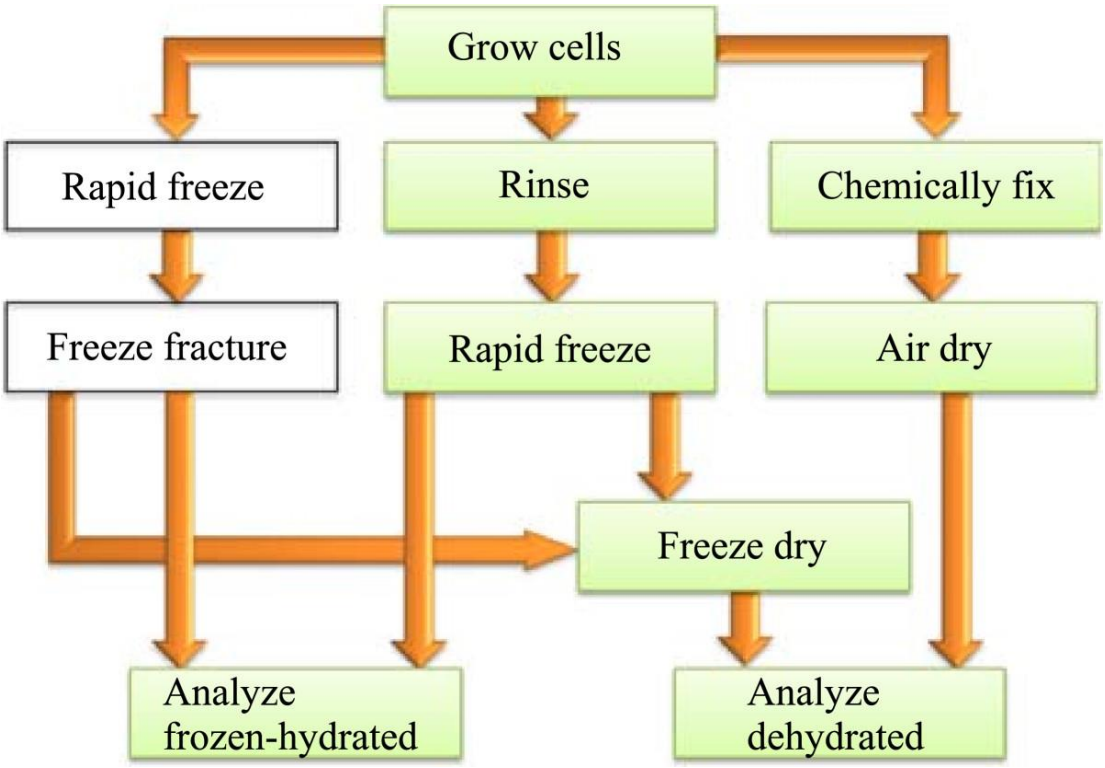

Figure 4.1. A schematic of several of the methods used to prepare biological cells for ToF-SIMS analysis. Cells can either be analyzed following dehydration, or can be analyzed frozen-hydrated with incorporated water still present. Cells can be dried either by chemical fixation and air drying, or plunge-frozen and freeze-dried. Additionally, frozen cells can either be analyzed whole, or following freeze-fracture. The green boxes represent methods that were evaluated in this work.

One of the most common constituents in biological specimens are salts, particularly Na, K and Cl, which greatly lowered the organic SI yields in rat brain tissue and DPPC films [24], as well as bovine serum albumin and polypeptide films [26]. SI yields were "recovered" by rinsing these samples, which removed most of the salts. On single cells, several rinsing solutions were compared, and it was determined that an isotonic solution (150 mM) of ammonium acetate (AA) best removed extracellular growth medium salts and best preserved cell morphology [136]. Ammonium formate (AF) has worked similarly on cells [137] and tissues [26, 138, 139].

Interference reflection microscopy determined the volume change of cells immersed in an AF rinsing solution. At 1 minute of immersion time there was a roughly 1.4x volume increase and at 16 minutes the cells had experienced a 2x volume increase. The swelling amount was not sufficient to rupture the plasma membrane and many cells were viable after a 16 minute immersion [138].

Breitenstein *et al.* used gluteraldehyde-fixation to image single NRK cells in 3D and argued the merits of chemical fixation as a method to prepare cells for ToF-SIMS analysis [14, 70]. The key conclusions included gluteraldehyde-fixation did not cause significant shrinkage of the cell, that cellular compartments remained intact following fixation, and that the distribution of most molecular chemical components (proteins, DNA, lipids) was conserved.

The effects of cryofixation and freeze-drying, as well as various chemical fixations on the morphology and SI yields from the plasma membrane of human fibroblasts were compared by Malm *et al.* [138]. While the cells' extracellular fine structure was better preserved using chemical fixation, the native intracellular K^+/Na^+ ratio was not maintained. The permeability of the plasma membrane to mobile ions was also utilized in early ion microprobe experiments which tested practical ion yields [59]. Intracellular K^+/Na^+ ratios have been used as one indicator to determine the quality of cell preservation. Popularized in the SIMS community by Chandra *et al.*, this ratio has been used to identify healthy cells from damaged ones [56, 134, 140], where a healthy cell has a high K^+/Na^+ ratio. Membrane damage, caused by either the freezing or drying processes resulted in increased permeability to diffusible ions and the loss of this natural gradient. Many of these issues were discussed by Clerc *et al.* with an emphasis on mapping intracellular drugs and nuclear medicine compounds [64]. A major assertion was that

cryofixation methodologies are required when examining highly mobile ions and chemical fixation should only be employed when studying molecules fixed to cell structures.

The investigation of frozen-hydrated (FH) cells with ToF-SIMS may be beneficial for several reasons. First, it allows a cell to be studied in its most native state. Rapid freezing provides a "snapshot" of the cell at a given instant, arresting all biological activity on a millisecond time scale [141]. Dehydration may cause cells to shrink or crack, may redistribute membrane lipids and/or cause plasma membranes to rupture [27, 136, 138]. However shrinking was not reported [70] and membrane lipid distributions were preserved using gluteraldehyde-fixation [142]. At cryogenic temperatures, depth resolution and SI yield were improved in depth profiling polymers, partly by reducing sputter-induced topography. [143, 144]. Several studies have reported increased SI yields in FH analyses, and suggested that the increased yield resulted from proton donation from incorporated water molecules to neutral species [145, 146]. Incorporated water during FH analysis has also alleviated the reduction of SI yields caused by KCl-doped arginine films, restoring yields to those that were acquired on undoped films [24]. Cryogenic analysis reduced the damage cross section of primary ions, which improved the SI yields of larger molecular weight ions in polypeptide films [145].

When cells are analyzed FH with ToF-SIMS, a majority of surface water must be removed due to the 1-2 nm surface sensitivity it provides. A practical method to remove this surface water is *in situ* sublimation [146-148]. This is generally achieved by slowly warming the sample stage from cryogenic temperature to -80 °C, effectively freeze-drying the sample for a short period of time. With FH cell analysis, sublimation is often a necessary step to remove any rinsing solution left over from the removal of the culture media.

Instrumentation developments that specifically addressed improving FH SIMS experiments include Ionoptika's J105, which allows for the *in-situ* freeze fracturing of a frozen cells under vacuum [54]. A cryomicrotome was attached to a ToF-SIMS instrument to serial section frozen tissue *in situ* and analyze the fresh face of sequential tissue slices [55]. Also, recently an *in-situ* freeze fracture device was adapted from the J105 freeze fracture system to work on an ION-TOF IV cold stage [149].

As summarized above, there is significant interest and challenges in using different sample preparation procedures for ToF-SIMS imaging of biological cells. The current study provides a comprehensive comparison of the mass spectral information that was obtained from formaldehyde-fixed cells, cryofixed and dehydrated cells, and frozen-hydrated cells. The surface spectra were obtained from cells that were prepared using each preparation method and examined. The secondary ion yields from depth profiles of the chemically fixed cells were compared to freeze-dried cells. A second SI yield comparison was made between freeze-dried cells and frozen-hydrated cells. All organic ions in all depth profiles were investigated. While there have been studies in the past that have examined SI yields as a function of cell preparation method [27, 138], this is the most complete analysis to date. Additionally, several peaks from the frozen-hydrated analyses were identified that were not detected from the dried cells. This work offers additional insight into which are the primary mechanisms of SI yield enhancement and degradation during ToF-SIMS depth profiling of biological cells.

4.3 Experimental Methods

4.3.1 Cell seeding

NIH/3T3 fibroblasts were seeded onto 1 cm x 1cm silicon chips [150] at densities between 40,000-100,000 cells and grown for 24–48 hours in Eagle's Dubelco's Modified Essential Medium (Invitrogen, San Diego, CA) supplemented with 10% fetal bovine serum (Thermo Scientific, Erie, PA) and 1% antibiotic/antimyotic (Invitrogen, San Diego, CA). Prior to cell seeding the silicon chips were cleaned with 2x sequential five-minute sonications in dichloromethane, acetone and methanol and stored in a laminar hood until cell seeding.

4.3.2 Ammonium acetate rinsing solution

Ammonium acetate (AA) (Sigma, St. Louis, MO) was dissolved in 18 MΩ water to form a 150 mM solution, and was brought to pH 7.4 with 1M ammonium hydroxide [136].

4.3.3 Rinsing, plunge freezing and freeze-drying of cells

Cells on silicon chips were gently rinsed in 150 mM AA for 30 seconds by slowly dipping the silicon chip in the solution followed by minimal movement of the sample in the rinsing solution. Excess liquid was removed by touching the edges of the chip with a Kimwipe. The sample was then rapidly submerged in liquid ethane (produced by leaking ethane gas into a liquid nitrogen cooled plastic beaker) and quickly transferred to liquid nitrogen (LN_2). While under LN_2, the chips were placed into small glass test tubes, and the tops were covered with aluminum foil with a small hole. These test tubes were placed into a pre-cooled freeze-dry flask (−80 °C freezer overnight), while the chips were still submerged in LN_2. The flask was attached to a manifold freeze drier (SP Scientific, Warminster, PA) and a vacuum was established. The samples dried overnight, and then were immediately placed into the ToF-SIMS instrument for analysis.

4.3.4 Chemical fixation

Cells on silicon chips were rinsed briefly in the AA solution and placed into a 4% formaldehyde (Thermo Scientific, Erie, PA) in PBS buffer (EDS Chemicals) solution at room temperature for 30 minutes. The samples were removed and rinsed for 60 seconds in water. Excess liquid was removed from the samples by touching the edges with a Kimwipe, and then they were air dried overnight in a laminar flow hood. The samples were analyzed the following morning.

4.3.5 Frozen-hydrated: preparation of cells and analysis

Samples were prepared in a manner similar to that described in Piwowar *et al*. [151]. Cells on silicon chips were rinsed and plunge frozen as described above. Prior to freezing, it is important to reduce the thickness of the liquid layer to a minimum in order to ensure the best freezing results. After cryofixation in liquid ethane, the samples were transferred to LN_2 until placement onto the ToF-SIMS cold stage. The cold stage was pre-cooled to −160 °C at 10^{-7} mbar in the loading chamber, then vented to atmosphere to allow for the placement of the sample. The sample was rapidly transferred from under liquid nitrogen onto the cold stage, where it was held onto the stage by a clip. The cold finger was immediately brought into contact with the cold stage and the loading chamber was immediately pumped down to $5x10^{-7}$ mbar. The maximum temperature of the cold stage was −85 °C during the entire process, as measured by a thermocouple mounted to the surface of the stage. After the loading chamber was evacuated the sample stage was cooled to −130 °C before warming at a rate of 5 °C/min to −80 °C [38]. The stage was held at −80 °C for 30 minutes to sublimate the excess water from the surface of the cells. After the sublimation, the stage was cooled to −160 °C and transferred into the analysis

chamber. All analyses were performed with the stage temperature at −130 °C. Cells maintained a high K^+/Na^+ ratio, as shown in Additional file 1, Figure S1.

4.3.6 ToF-SIMS

Positive and negative secondary ion spectra were collected with an ION-TOF TOF SIMS 5–100 instrument (ION-TOF, Münster, Germany), using a pulsed 25 keV Bi_3^+ primary ion beam. Samples were sputtered using a 20 keV C_{60}^{++} beam. The Bi and C_{60} beams were oriented 45° to the surface normal. Depth profiles were acquired using the high mass resolution mode ($m/\Delta m$ = 7000 at m/z 27) in the interlaced mode (one analysis scan per sputter cycle) with a Bi_3^+ current of 0.15 pA and an analysis area of 500 x 500 μm^2. The C_{60}^{++} current was kept between 0.3-0.35 nA and a sputter area of 700 x 700 μm^2 was used for all depth profiles. All depth profiles were acquired for 1000 seconds, one shot/pixel and contained 128x128 pixels. Positive ion spectra were mass calibrated using the CH_3^+, $C_2H_3^+$, $C_3H_5^+$, $C_3H_3O^+$, and $C_7H_7^+$ peaks. Negative ion spectra were mass calibrated using the CH^-, OH^-, PO_2^-, and PO_3^- peaks. Secondary ions were collected over a range of 0–860 m/z. Low energy electrons were flooded onto the sample to compensate for charge buildup on the surface. Some data was collected in the .RAW format using the IONTOF Version 4 software and subsequently converted into the .itm raw data format (IONTOF Surface Lab 6). All data was analyzed using the IONTOF Surface Lab 6 software.

Regions of interest (ROI's) for the cells were chosen in all analyses by thresholding the "totalcounts" image. The signal from the cells was significantly higher than from the substrate. Regions were chosen so that a minimum of substrate would be analyzed during the depth profiles. The SI intensities from the depth profiles were normalized by the primary ion dose to allow direct comparison. Peak lists were created by overlaying representative spectra from each

of the preparation methods and using manual peak selection. Known substrate, salt and salt adduct peaks were excluded from the peak lists.

4.4 Results and discussion

The purpose of these experiments was to examine how various methods of sample preparation affected the chemical information obtained from single cells, with an emphasis on SI yields from depth profiles. This work compares cells that were prepared by formaldehyde-fixation (FF), plunge freezing and freeze-drying (FD), and plunge freezing with frozen-hydrated analysis (FH). This is important for 3D ToF-SIMS imaging, where SI intensities of organic species often quickly decrease due to sputtering induced damage [7].

4.4.1 Proper rinsing of cells

The removal of excess media from the surface of cells prior to analysis is an important step in the preparation protocol for ToF-SIMS analysis [136, 138]. An improper rinsing technique can stress the plasma membrane such that it is damaged, as depicted in Figure 2. In an effort to completely remove extracellular media salts from the surface of the cells prior to cryofixation, the sample was immersed in a rapidly stirred AA solution. The cells were submerged for 30 seconds, plunge frozen and freeze dried. An optical image from the analytical chamber of the ToF-SIMS instrument is shown in Figure 4.2A, where a group of fibroblasts is displayed. A high spatial resolution image of the characteristic phosphocholine (PC) head group fragment at m/z 86 ($C_5H_{12}N^+$) is shown in 4.2B, and 4.2C is a zoomed-in area of a subset of cells from 4.2B (blue square). Comparing the lipid distribution from 2C to the optical image from 4.2A, the plasma membranes appear “smeared”. Shear stress on the membrane from the rapidly

moving fluid may have caused this disruption. In Figure 4.2D a cluster of cells from a separate sample are shown that were gently dipped into a stagnant rinsing solution for 30 seconds and then plunge frozen and freeze dried. No smearing of the cell membrane is visible and sufficient salts have been removed to acquire a meaningful spectrum. Thus, to rinse cells without causing plasma membrane smearing, samples should be gently dipped into a rinsing solution for 30–60 seconds. Vigorous stirring should be avoided.

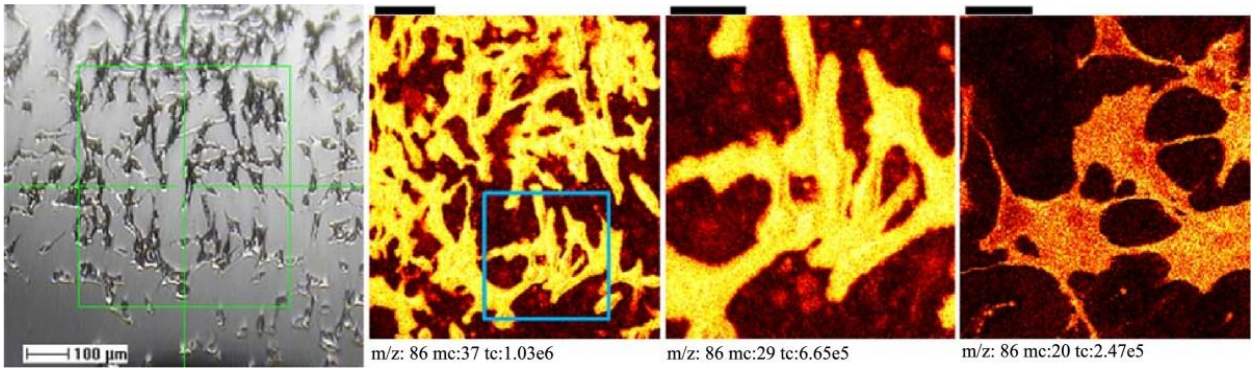

Figure 4.2. Excessively harsh rinsing can damage a cell's plasma membrane. NIH/3 T3 fibroblasts adhered to a silicon chip were rinsed vigorously for 30 seconds in a 150 mM ammonium acetate solution (A) Optical image from the analysis chamber of a group of NIH/3 T3 fibroblasts. (B) Ion image of m/z 86^+, corresponding to $C_5H_{12}N^+$, a characteristic phosphocholine head group fragment. Scale bar is 100 µm. (C) Higher magnification view of the area inside the box shown in (B). The lipid bilayer looks to have ruptured causing some lipid to spread into the area around the cells. Scale bar is 50 µm. (D) An image of the m/z 86^+ fragment of a group of cells on a separate sample that was more gently rinsed. There is no such damage to the cells' outer membrane. Scale bars are 50 µm.

4.4.2 Spectra from cell surfaces

Figure 4.3 shows the positive SI spectra between m/z 660–810, collected from the surface of NIH/3 T3 fibroblasts that were analyzed after the following preparation methods: A) FH, B) FD, C) FF with a light rinse after fixation and D) FF with a heavy rinse after fixation. Each spectrum was normalized to the total counts detected and plotted on the same y-scale. The ions at

m/z 703, 732, 734 and 760 were detected in the spectra from cells using each of the preparation methods. These ions were identified as sphingomyelin SM(34:1) [79], glycerophosphocholine PC(32:1), PC(32:0) [84], and PC(34:1) [152]. The peak at m/z 762.5 was identified as PC(34:0). An unidentified peak at m/z 720.5 was present in each of the spectra. An unidentified peak at m/z 706.5 was present in all but the FH spectrum. The K^+ adducts of SM(34:1), PC(32:1), PC(32:0) and PC (34:1) were detected at m/z 741, 770, 772 and 798, whereas the Na^+ adducts of these lipids were detected at m/z 725, 754, 756 and 782, respectively [139]. The K^+ adducts were not detected in high levels in either of the FF samples, consistent with previous experiments that showed a majority of K^+ was removed during the fixation process [138]. The FF sample that was not rinsed well after fixation had the highest intensity of Na^+ adduct ions, as expected since Na^+ is a major component of the PBS fixation buffer.

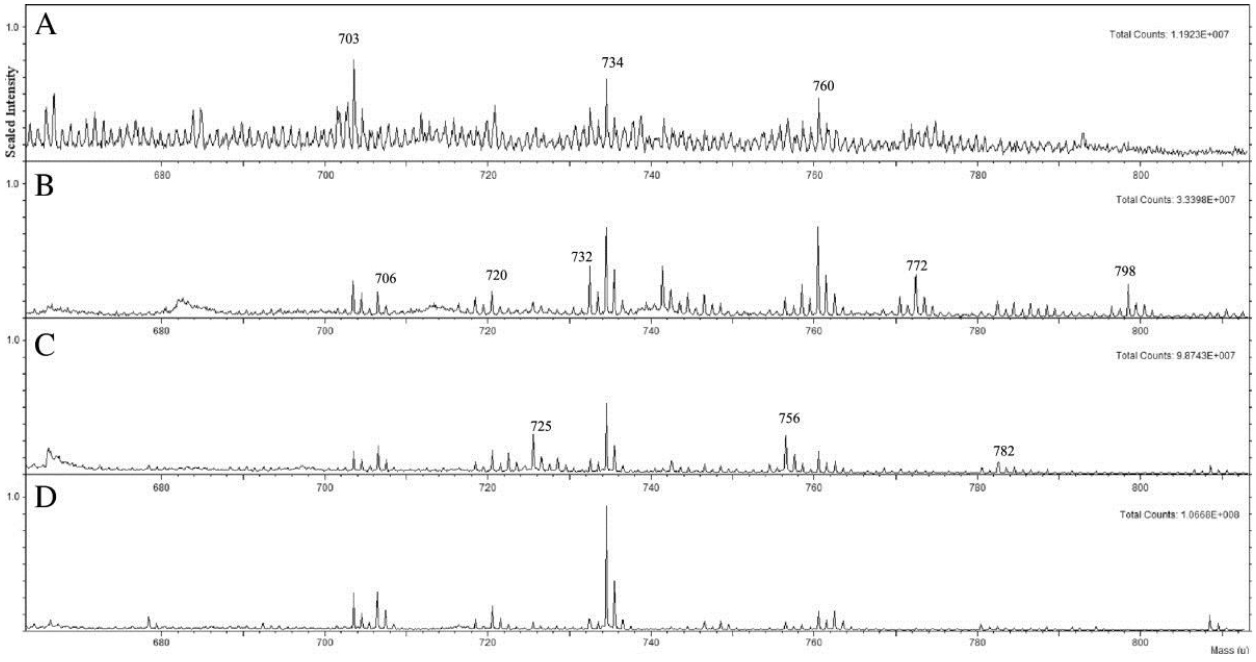

Figure 4.3. Spectra from the surface of cells that were analyzed (A) frozen-hydrated, (B) freeze-dried, (C) formaldehyde-fixed followed by a light rinse and (D) formaldehyde-fixed followed by a heavy rinse. Each spectrum was normalized to the total ion intensity, and all spectra were plotted with the same y-scale. All spectra were acquired with a 250 μm x 250 μm analysis area and to a primary ion dose density of 1.0×10^{12} ions/cm^2. Peaks assignments are given in the text.

The FH and FD spectra were more similar to one another than to the FF spectra, however all four spectra contained the same major peaks. The largest differences between the spectra from the FD (3B) and FF (3D) cells were the lowered intensity of PC(34:1) and PC(32:1), and the increased intensity of PC(32:0) in the FF spectrum. This is consistent with previous results where the normalized intensity of PC(34:1) was lower in gluteraldehyde-fixed cells compared to cryofixed and FD cells [138]. The SM(34:1) ion had a comparable intensity to the PC(32:0) and PC(34:1) peaks in the FH spectrum, whereas in all three spectra of dried cells the SM(34:1) intensity was lower than the PC peaks. These differences in the spectra may have been caused by the increased disorganization of the plasma membrane as the cells shifted from fully hydrated (most native), to freeze dried, to formaldehyde-fixed (least native).

The spectrum from the FH cells was similar to that of the FD cells likely because the FH cells were subjected to a −80 °C environment for a short time to sublime excess surface water. Although a thin layer of water was redeposited onto the surface after this sublimation period (Additional file 5, Figure S.2C), this would likely not reverse any re-organization of the membrane caused by the initial freeze-drying, although it likely would increase ion yields. An ideal preparation to study the plasma membrane would stop the sublimation process with a 1 nm water layer on the sample surface [153]. Perhaps an easier method, although one that was not explored in this work, would be to stop the sublimation with a surface water layer between 10 – 100 nm, and then use cluster sputter etching (C_{60} or large argon clusters) to remove the remaining water to reach the plasma membrane. The sublimation step is not necessary for freeze-fracture experiments on single cells because a pristine intracellular surface is produced by the

fracture process [57, 134]. Due to the difficulty of producing a uniform, thin ice layer, freeze-fracturing may be a better choice for the FH analysis of cells.

Chemical fixation has caused the plasma membrane to become disorganized in some instances, but not in others. Recent work that imaged the sphingomyelin domains in NIH/3 T3 cells used gluteraldehyde-fixation and observed that the plasma membrane was not disorganized [142]. A gluteraldehyde-fixed hTERT-BJ1 fibroblast cell did not show signs of membrane rupture in the m/z 184^+ signal [138]. Cells that were fixed with formalin and freeze dried [27], as well as NIH/3 T3 fibroblasts fixed with formaldehyde [154] did show evidence of plasma membrane rupture. Gluteraldehyde can cross-link the free amine group in phosphoserine and phosphoethanolamine, prominent components of the inner leaflet of the plasma membrane, while formaldehyde cannot. This may be the explanation for the disorganized plasma membranes seen when formaldehyde was used as the fixating agent.

4.4.3 Comparing the depth profiles of FD and FF cells

One of the most exciting prospects of biological sample analysis with ToF-SIMS is depth profiling and the accurate 3D reconstruction of mass-spectral data sets [27, 154]. Low ion yields are the largest hurdle to overcome when acquiring 3D images [155], as there often isn't enough signal intensity for most organic ions of interest to produce a meaningful reconstruction. Salts played a significant role in the suppression of SI yields obtained from depth profiles of rat brain tissue [26] and polypeptide films [24]. To test the extent to which positive SI intensities could be "recovered" by the removal of a majority of intracellular salts (Na^+, K^+, and Cl^-), NIH/3 T3 fibroblasts were prepared using two methods and depth profiles were acquired. In the first method, cells were plunge-frozen in liquid ethane and freeze dried, which preserved the native

intracellular gradients of mobile species. In the second method, cells were fixed with formaldehyde, rinsed to remove buffer salts, and air dried. Chemical fixation will disrupt the native concentration gradients of mobile ions [64, 138], and as such, with heavy rinsing, can be used a as sample preparation method that produces single cells with minimal intracellular salts.

The possibility that intracellular molecules were removed during FF process was examined. The membrane is permeabilized to small molecules during the fixation procedure. Therefore, it is possible some of the intracellular molecules could pass through the permeabilized membrane and be removed during the rinsing step. However, all of the positive ions detected from the FD cells were also detected in the FF cells. Thus, for the instrument parameters and the preparation methodologies used in this study, no removal of intracellular organic ions was detected.

311 common ions were present in the spectra obtained from the two preparation methods. The fold difference in the average, normalized intensity (FF/FD) for each ion is shown in Figure 4.4. The horizontal red line at 1 indicates the same normalized intensity was collected for a given ion from both preparation methods. The normalized intensities of the selected SIs were higher from the depth profiles of FF cells compared to the FD cells. Of the 311 peaks, 14.6% of the ions had an increase in intensity of less than 2x, 56.3% increased between 2x and 3x, and 29.1% increased greater than 3x compared to the FD cells. For the entire peak set, the FF cells had an average increased intensity of 2.6 fold compared to the FD cells. The numerical values of the fold differences of all 311 SIs are shown in Additional file 2, Table S.4.1. Two-tail student's *t*-tests assuming unequal variance were conducted to determine if the intensity differences were statistically significant. The results are shown in Table S.4.1. Using a *p*-value threshold of 0.05,

309 of the 311 ions had statistically significant intensity differences. The two ions that did not exhibit a significant intensity difference were $C_4H_{12}N^+$ and $C_5H_{14}NO^+$ at m/z 74.10^+ and 104.11^+.

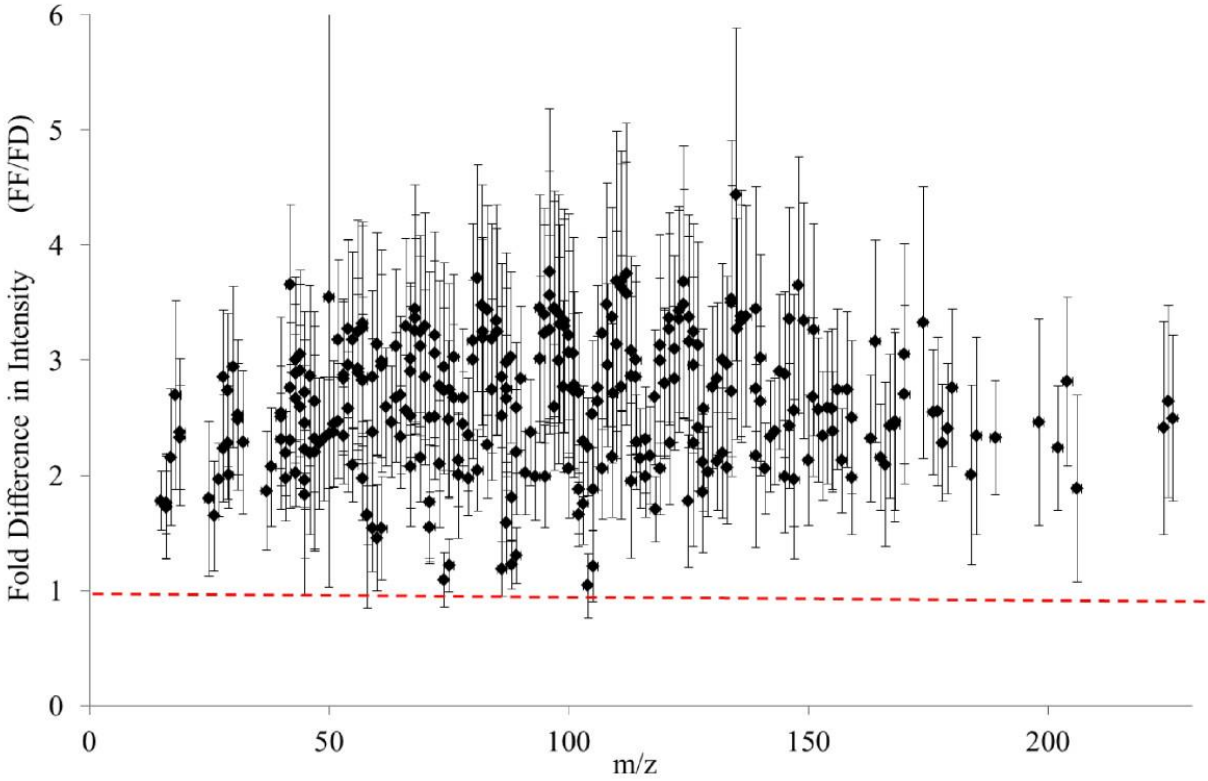

Figure 4.4. Depth profiles were acquired from cells that were freeze-dried (FD) and from those that were formaldehyde-fixed (FF). 311 ions were selected that were detected in the spectra of both sample types. The intensity of each ion was summed over the entire depth profile. Intensity values for each ion were averaged and normalized to the total ion dose. For a given ion, the average intensity from the FF cells was divided by the average intensity from the FD cells. The fold difference is plotted on the y-axis as a function of m/z. The red dotted line signifies a (FF/FD) intensity of 1. Error bars signify one standard deviation. All depth profiles were acquired for 1000 seconds, with a 500 μm x 500 μm analysis area and a 700 μm x 700 μm sputter area. For the FD cells, n = 10, from four total samples and three separate data acquisition sessions. For the FF cells, n = 7, from three total samples and three separate data acquisition sessions.

The intensities of the characteristic PC fragments at m/z 58^+, 86^+, 104^+, 125^+, and 184^+ [85, 156] were among the ions with the lowest fold increase. They had fold increases at or below 2.1 (color-coded yellow in Table S.4.1) compared to the 2.6 fold average increase, and include

the ions with the lowest (m/z 104.11^{+}) and third lowest increase (m/z 86.06^{+}). The intensity of hydrocarbon fragments (color-coded blue) generally increased less than nitrogen- and oxygen-containing fragments. The SIs associated with proteins [87, 88], were often nitrogen-containing (color-coded green) and generally had a larger fold increase than the hydrocarbon and lipid-associated ions. SIs containing oxygen, but not nitrogen (color-coded red) did not display a clear trend, however they also generally had higher fold increase than the lipid and hydrocarbon ions. Despite the nitrogen and/or oxygen content, the fragments originating from PC did not exhibit a large increase. A similar finding was reported when the m/z 86^{+} SI intensity did not change appreciably in depth profiles of rat brain tissue that had been rinsed versus not rinsed, whereas the m/z 184 did have in increased intensity when the tissue was rinsed [26].

It was previously hypothesized that the neutralization of positive SIs by Cl^{-} anions in KCl-doped polypeptide films was the major mechanism of the lowered observed SI yields versus un-doped films [24]. The strongest piece of evidence that supported this mechanism over the others that were proposed was the decreased yield of *all* observed organic ions from the films in the presence of Cl^{-} containing salts. In this work, a similar decrease in all organic SI yields was observed in the FD cells compared to the FF cells. The relative, normalized SI signals from the OH^{-}, CN^{-}, Cl^{-}, CNO^{-}, PO_2^{-} and PO_3^{-} anions are plotted in Figure 4.5. These were examined to determine if they could explain the trend observed in Figure 4.4. The Cl^{-} anion had a statistically significant, higher SI intensity in the FD cells compared to the FF cells. The other five anions except Cl^{-} did not have a statically different SI intensity between the FD and FF cells, although all of the anions except PO_3^{-} had higher mean intensities. This suggests that the anion neutralization mechanism hypothesized by Piwowar *et al*. is the underlying mechanism that

caused the decreased SI intensities acquired from the FD cells, and that the removal of the intracellular Cl^- by fixation and rinsing can improve SI yields.

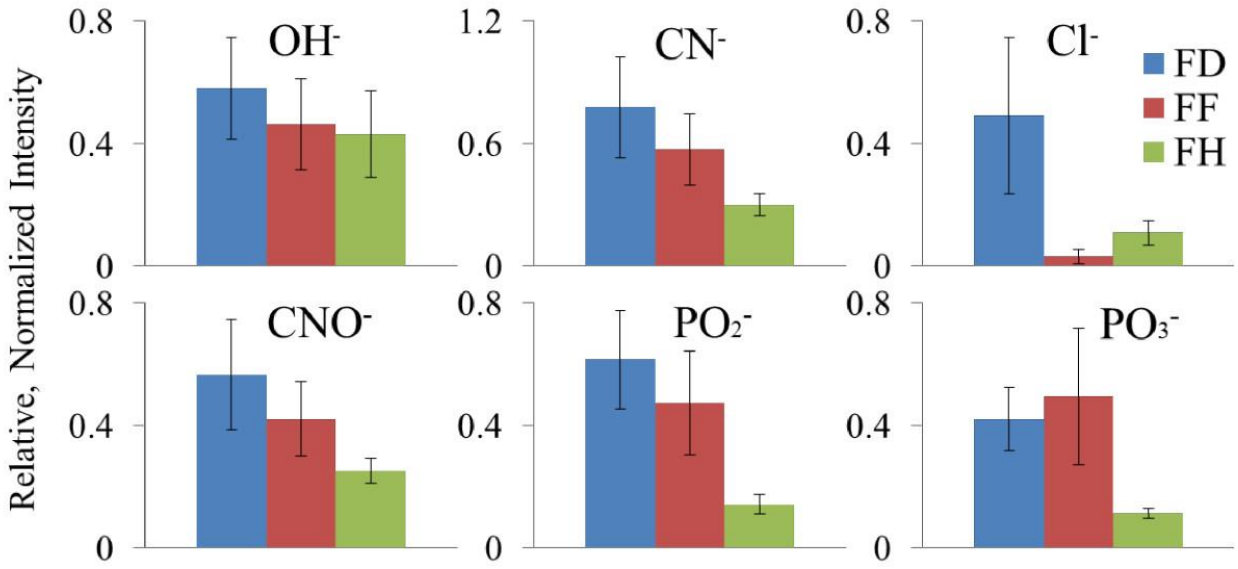

Figure 4.5. Depth profiles were acquired from cells that were freeze-dried (FD, blue bars), formaldehyde-fixed (FF, red bars) and frozen-hydrated (FH, green bars). The average, normalized intensity of the OH^-, CN^-, Cl^-. CNO^-, PO_2^-, and PO_3^- ions were summed over the entire depth profile and plotted. Intensity values for each ion were normalized to the total ion dose. Error bars signify one standard deviation. All depth profiles were acquired for 1000 seconds, using a 500 μm x 500 μm analysis area and a 700 μm x 700 μm sputter area. For the FD cells, n = 10, from four total samples and three separate data acquisition sessions. For the FF cells, n = 7, from three total samples and three separate data acquisition sessions. For the FH cells, n = 11, from three total samples and three separate data acquisition sessions.

Depth profiles from freeze-dried and formaldehyde fixed cells are shown Figure 4.S.2A and B, respectively, depicting the Poisson-corrected intensity of selected secondary ions as a function of C_{60}^{++} sputter time. The depth profiles were normalized to the Bi_3^+ ion dose. The NH_4^+, Na^+, K^+, $C_3H_8N^+$, $C_4H_8N^+$, $C_5H_{12}N^+$ and $C_5H_{15}PNO_4^+$ ions are displayed. For the organic molecules, the line shapes from the two depth profiles look qualitatively similar. In both cases, the initial intensities of the organic molecules were the highest, followed by a quick decay with

increasing sputter dose. The normalized intensities of the organic molecules are also all higher throughout the depth profile of the formaldehyde-fixed cells, consistent with the data presented in Figure 4.4.

4.4.4 Comparing the depth profiles of FD and FH cells.

There was a larger difference between the summed depth profile spectra of the FH cells and the FD cells than between the FF and FD cells. It was more difficult to compare the spectra of the FH cells to the FD cells than the spectra of the FD to the FF. The mass resolution was, generally, worse in the spectra of FH cells than the dried cells, which made the selection of peaks present in both types of spectra difficult. One explanation is that the Bi_3^+ analysis source was optimally tuned in between analyses of the dry samples, whereas the Bi_3^+ source could only be tuned 2–3 hours before the analysis of the FH samples began, and not during the data acquisition. A second possible explanation focuses on the dehydration effect of cells. Full dehydration can collapse cells, reducing the height of dried cells compared to the hydrated form. The mass resolution obtained by the ION-TOF V instrument is sensitive to height variations, and since the hydrated cells were taller than the dried cells (AFM micrographs, data not shown), the mass resolution in the spectra of the FH cells may have been reduced compared to the flatter, dehydrated cells.

There were numerous peaks in the spectra from FH cells that were not detected, or detected in very low amounts, in the spectra of the FD cells. These ions are listed in Table S.4.2 with possible chemical identifications. No peak assignments indicate that a rational identification was not determined. A majority of these “new” peaks were assigned combinations of water, the ammonium acetate rinsing solution, and intracellular salt ions. In depth profiles of FH samples,

water clusters such as $H_3O\text{-}H_2O^+$ and $H_3O\text{-}(H_2O)_2^+$ at m/z 37 and 55 initially decreased in intensity and then increased with time (data not shown). The initial decrease was attributed to the removal of surface water, which adsorbed after the initial sublimation step. Water clusters with Na^+ and K^+ adducts were also detected, e.g. $K\text{-}H_2O^+$. Many of the ions detected in the FH but not FD spectra included NH_3^+ or NH_4^+ in their compositions, which can be attributed at least in part due to the AA rinsing solution. Examples include the ions detected at m/z 52.09^+ and 53.07^+, which were identified as $(NH_3)_2\text{–}NH_4^+$ and $(NH_3)_2\text{–}H_3O^+$. The intensity of the m/z 53.07^+ fragment decreased rapidly initially, in a similar fashion to the other water clusters. Since not all of the ions could be identified with reasonable certainty, it is possible that some of them are more biologically relevant than simply being water- or salt-containing.

The fold difference between the normalized intensities of the 137 SIs detected from both the FH and FD samples are shown in Figure 4.6. The SIs with a higher intensity from the FH cells were plotted in the top half of Figure 4.6 using a positive fold increase (FH/FD > 1), whereas the SIs with a higher intensity from the FD cells were plotted in the bottom half of Figure 4.6 using a negative fold increase (FH/FD < −1). The red, dashed lines at 1 and −1 indicate a ratio of 1, and thus no intensity difference. The numerical values of the fold difference of all ions are shown in Table S.4.3. Two-tail student's *t*-tests were performed assuming unequal variance to determine if the intensity differences were statistically significant. A majority of SIs with m/z < 80 had higher intensities from the FD cells. The low mass SIs that had a statistically significant increased intensity in the FH spectra were CH_3^+, CH_4N^+, CH_3O^+, CH_5N^+, $C_2H_2O^+$, CH_4NO^+, $C_2H_8N^+$, $C_3H_7N^+$, $C_3H_5O^+$, and possibly $C_3H_3Na^+$. All of these ions except CH_3^+ possibly contain an NH_4^+, H_2O^+ or H_3O^+ group. An increased SI intensity was obtained for larger masses in FH samples compared to the FD samples. An increase in the FH/FD ratio with

increasing mass of the fragment was observed for the PC fragments at m/z 86^+, 104^+, 125^+, 166^+, 184^+ and 224^+ (labeled with red arrows in Figure 4.6). The m/z 86 fragment had the lowest fold difference (−1.9) for FD/FH. This value increased for the larger fragments at m/z 104^+ and 125^+, although the intensities from the FD cells were still higher than from the FH cells. Of the PC-related ions, the m/z 166 fragment had a SI yield higher in the FH cells, and the m/z 224^+ had the greatest fold increase. In fact, all selected SIs above m/z 89^+ except the m/z 104^+ and 125^+ (both PC fragments) had an increased intensity from the FH cells compared to the FD cells.

The SI yield results described above are in agreement with previous findings from cryogenic depth profiling experiments of polypeptide films. An increased [M + H^+] intensity in the peptide films was observed when they were cooled from room to cryogenic temperatures during analysis, although there was little to no increase in lower molecular weight fragments [145]. The increased molecular ion signal was attributed to a decreased damage cross-section, produced by the presence of surface water and cryogenic temperatures. More recent work compared the spectra following C_{60} sputter etching from within chemically-fixed, freeze-dried HeLa-M cells to FH cells and observed higher yields for the characteristic DNA peaks at m/z 136^+, 152^+, as well as the PC peak at m/z 184^+ [27]. In that study case, lower mass peaks were not investigated. The results presented in Figure 6 from depth profiles of NIH/3 T3 fibroblasts support the hypothesis that the primary mechanism of increased molecular SI signals result from a decreased damage cross section produced by cryogenic temperatures. The other mechanisms that have been proposed as a source of increased yields from FH analysis, namely proton donation [157] and amelioration of anion neutralization [24] by water, may also be playing a role, but from the data presented in Figure 4.6, it is unclear to what extent.

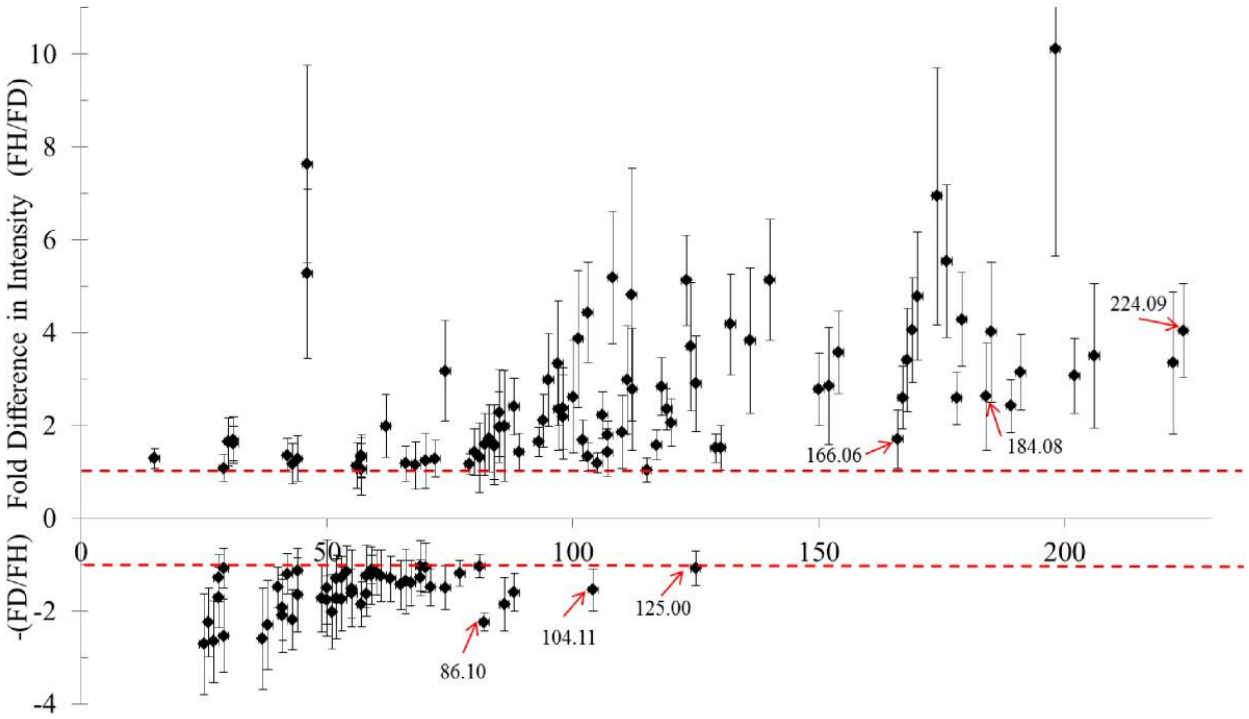

Figure 4.6. Depth profiles were acquired from cells that were freeze-dried (FD) and from those that were frozen-hydrated (FH). 137 ions were selected that were detected in the spectra of both sample types. The intensity of each ion was summed over the entire depth profile. Intensity values for each ion were averaged and normalized to the total ion dose. For a given ion, the average intensity from the FD cells was divided by the average intensity from the FH cells. If this ratio was below one, the -(FD/FH) ratio was used instead. The fold difference is plotted on the y-axis as a function of m/z. The red dotted lines signify (FH/FD) and (FD/FF) intensities of 1. Error bars signify one standard deviation. All depth profiles were acquired for 1000 seconds, with a 500 μm x 500 μm analysis area and a 700 μm x 700 μm sputter area. For the FD cells, n = 10, from four total samples and three separate data acquisition sessions. For the FH cells, n = 11, from three total samples and three separate data acquisition sessions.

The accumulated intensities of particular anions from FH cells are shown in Figure 4.5 alongside the intensities from FD and FF cells. Well-preserved, hydrated cells should have a similar amount of these species as FD cells, yet the observed SI intensities were significantly lower ($p < 0.05$) for all but OH^-. Incorporated water plays an important role in determining the yield of negatively charged monatomic species. Water ice drastically reduced the SI yields of negative ions compared to positive monatomic ions in computational studies [158, 159], and this

may explain why the SI intensities were lower in the FH cells. The insignificant decrease in the OH^- intensity was not surprising as it is a water fragment. Protons donated by the intracellular water may also combine with the anions to form neutral, undetected species.

A representative depth profile from a sample with frozen-hydrated cells is shown in Figure S.4.2C, depicting the Poisson-corrected intensity of selected secondary ions as a function of C_{60}^{++} sputter time. H_2O^+ and $H_5O_2^+$ profiles are shown in addition to the same fragment profiles shown in Figures S.4.2A and S.4.2B. As before, qualitatively the intensity profiles of the organic molecules are similar to those observed from the FD and FF cells. Although the initial normalized intensities are lower for all of the selected organic molecules, the intensity decay over time appears lower compared to the profiles in Figures S.4.2A and S.4.2B. This is consistent with a lowered damage cross section in the FH depth profile compared to the profiles of the dried cells. Unlike in Figures S.4.2A and B, in Figure S.4.2C the PC headgroup ($C_5H_{15}PNO_4^+$) molecule had a higher initial intensity than the headgroup fragments ($C_3H_8N^+$ and $C_5H_{12}N^+$). The intensity of NH_4^+ starts and remains high throughout the profile, likely from the ammonium acetate rinsing solution.

Given the data presented above, it would be interesting to further investigate the secondary ion yield increases that may be obtained by first doing chemical fixation to remove diffusible salts ions, and then cryogenic analysis for decreased damage. This experiment would help determine the relative contributions of proton donation from water versus decreased damage from cryogenic temperatures.

4.5 Conclusions

Sample preparation plays a key role in determining the information that is obtained from single cells with ToF-SIMS. The removal of excess media before analysis is necessary, but using rinsing technique that was too aggressive damaged the plasma membrane. The presence of intracellular salts reduced the secondary ion yield an average of 2.6-fold. Chemical fixation followed by rinsing removed a majority of the intracellular salts, "recovering" the positive secondary ion yields. Cl^- ion yields were highest in the freeze-dried cells and lowest in the formaldehyde-fixed cells. The data presented here is consistent with anion neutralization as the dominant mechanism for the lower ion yields. All of the organic secondary ions that were detected in the freeze-dried cells were also detected in the formaldehyde-fixed cells. Well-preserved, hydrated cells showed no increase or a decreased yield for most low mass ions, but an increased yield for higher mass fragments. This is consistent with the mechanism where a reduced damage cross section is produced by analysis at cryogenic temperatures. Numerous ions that were detected from the frozen-hydrated cells were not detected from the freeze-dried cells, however many of these ions were attributed to chemical combinations of water, salt and the ammonium acetate rinsing solution.

Future considerations regarding the optimal sample preparation for depth profiling cells would be need to be addressed in a case specific manner (e.g., for experiments that involve mapping small molecule drugs in cells). It may be beneficial (or necessary) to utilize chemical fixation or frozen-hydrated analysis to increase SI yields, but if the molecule is unbound and is removed or relocated during preparation, cryofixation would be necessary for accurate imaging.

Acknowledgements

The authors thank NIH and the NIBIB for their financial support (NIH EB-002027) to this work, as well as Dr. Liney Árnadóttir for her technical assistance with the FH sample mounting onto the cold stage. The authors also thank Dr. Buddy Ratner for use of his cell culture facility and Dr. Cecilia Giachelli for the use of her freeze drier.

Competing Interests

The authors declare that they have no competing interests.

Authors' contributions

MAR performed the experiments, analyzed the data and created the figures. MAR and DGC developed the experimental design, did the manuscript writing and editing, and approved the final manuscript.

URL: http://www.biointerphases.com/content/8/1/15

4.6 Supporting Information

Characterization of sample preparation methods of NIH/3T3 fibroblasts for ToF-SIMS analysis

Michael A. Robinson[1, 3], and David G. Castner[1-3, §]

National ESCA and Surface Analysis Center for Biomedical Problems[1] Departments of Bioengineering[2] and Chemical Engineering,[3] University of Washington, Seattle, WA 98195

§ Corresponding author

David G. Castner

1-206-543-8094 (phone)

1-206-543-3778 (fax)

castner@uw.edu (e-mail)

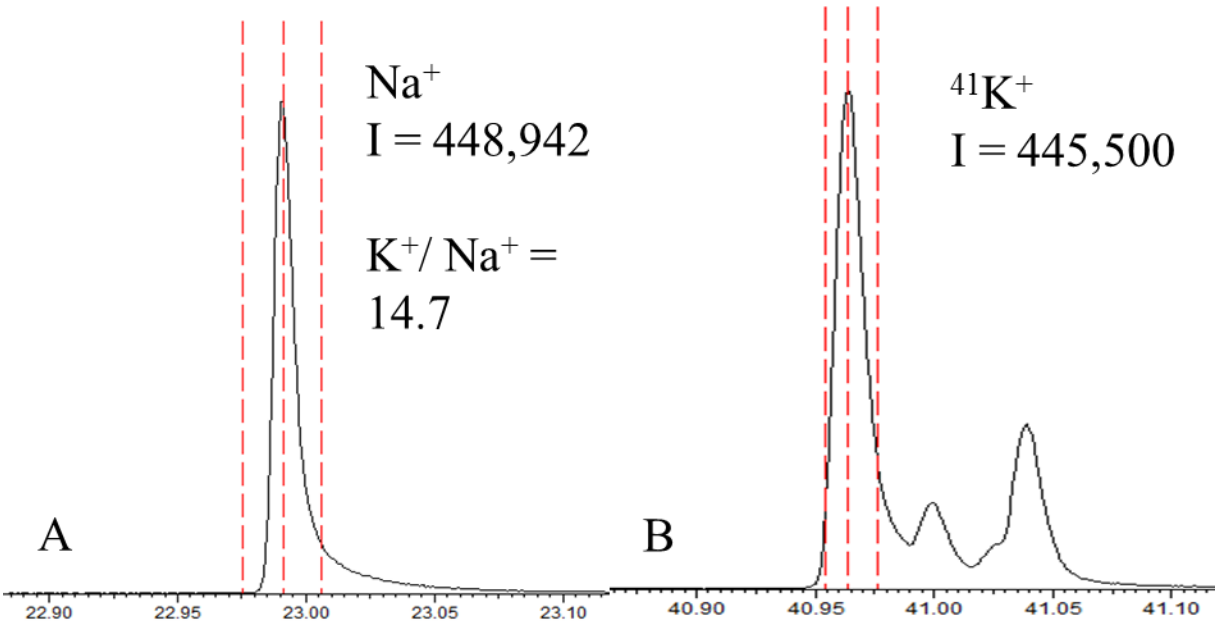

Figure S.4.1 (A) Na^+ peak and (B) $^{41}K^+$ peak from the depth profile of FH cells. The K^+/Na^+ ratio is 14.7, signifying the cells were well preserved. The $^{41}K^+$ isotope peak was used due to detector saturation of the $^{39}K^+$ isotope peak.

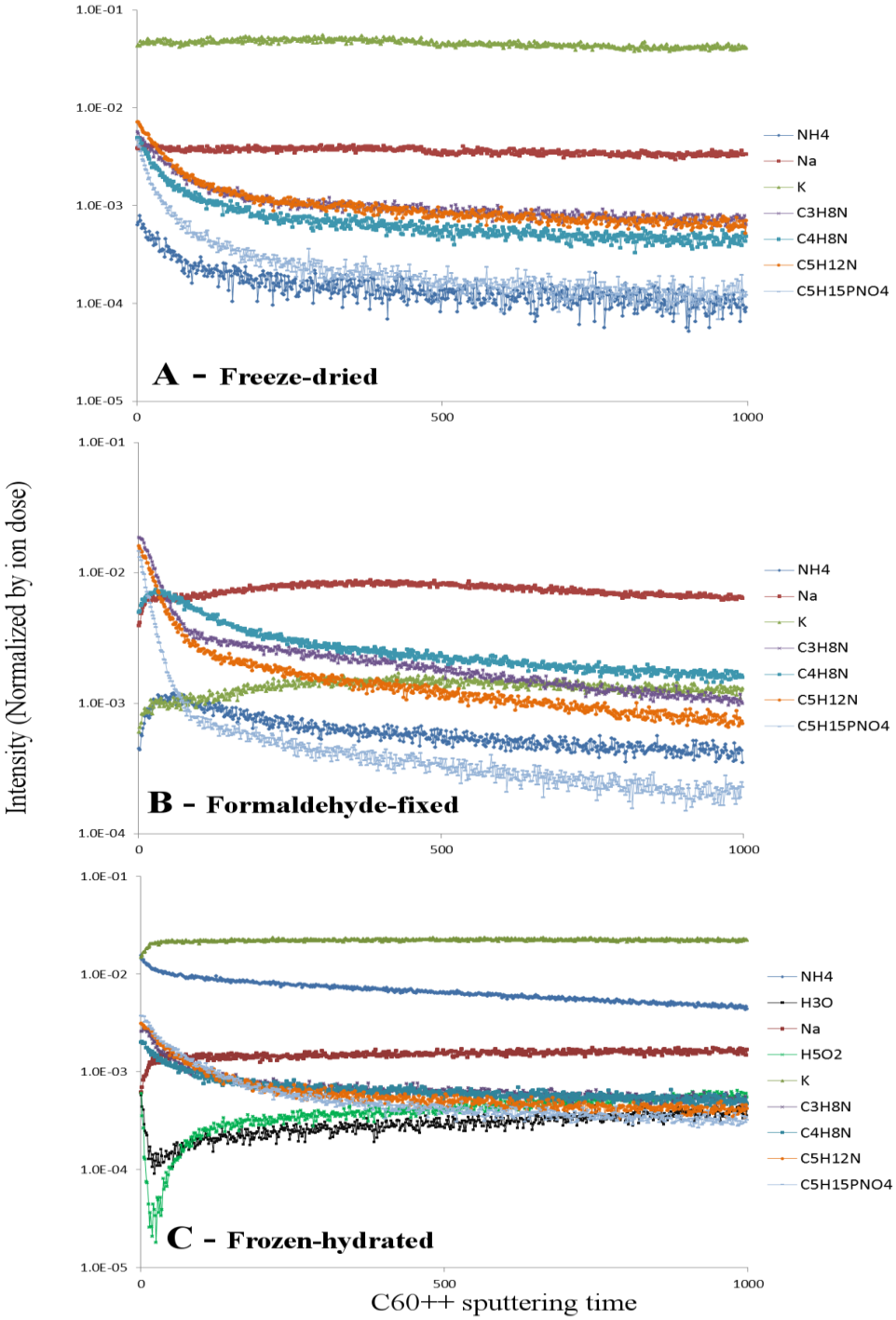

Figure S.4.2 (A) Depth profile from cells that were freeze-dried. (B) Depth profile from cells that were chemically fixed with formaldehyde. (C) Depth profile from cells that were analyzed frozen-hydrated. The depth profiles were normalized by the Bi_3^+ ion dose.

Table S.1: All positive secondary ions detected from both the FD and FF cells. Sorted by fold difference value, smallest to largest.

Mass	Fold difference	stdev	t- test	Possible composition
104.11	1.04	0.28	7.47E-01	C5H14NO
74.10	1.09	0.24	2.74E-01	C4H12N
86.10	1.18	0.24	3.08E-02	C5H12N
105.11	1.21	0.31	4.79E-02	isotope
75.10	1.22	0.23	9.20E-03	isotope
88.11	1.22	0.21	4.05E-03	C5H12N
89.11	1.30	0.25	1.45E-03	isotope
60.08	1.46	0.46	3.01E-03	
59.07	1.54	0.37	1.01E-04	
61.09	1.54	0.45	5.38E-04	
71.07	1.55	0.30	1.44E-05	
87.10	1.59	0.40	1.04E-04	
26.01	1.65	0.48	8.89E-05	
58.06	1.65	0.26	2.55E-08	C3H8N
102.09	1.66	0.28	1.59E-07	C5H12NO
58.03	1.66	0.82	4.99E-03	
118.12	1.70	0.28	3.28E-08	
16.03	1.72	0.44	5.14E-06	
16.02	1.73	0.46	3.91E-06	
103.09	1.75	0.36	2.28E-07	
16.03	1.76	0.27	1.98E-08	
71.04	1.77	0.49	1.85E-05	
125.00	1.78	0.58	4.07E-05	
15.02	1.78	0.26	1.17E-08	CH3
25.01	1.80	0.67	1.97E-04	
88.08	1.81	0.37	6.60E-08	
45.03	1.83	0.55	1.15E-05	
128.02	1.85	0.53	3.61E-06	
37.00	1.87	0.51	5.85E-06	
102.13	1.88	0.39	3.52E-08	
105.07	1.88	0.36	2.98E-05	C8H9
206.05	1.89	0.81	2.49E-04	
113.00	1.95	0.67	9.77E-04	
45.02	1.96	1.00	4.55E-04	
147.11	1.96	0.69	5.03E-05	
27.02	1.96	0.32	1.10E-10	C2H3
41.02	1.97	0.37	2.98E-08	
57.07	1.97	0.36	6.31E-06	C4H9
79.06	1.98	0.33	1.07E-08	
159.11	1.98	0.50	3.35E-04	
145.09	1.99	0.49	5.73E-04	
93.07	1.99	0.38	9.21E-06	
116.11	1.99	0.36	2.27E-10	
95.09	1.99	0.44	1.92E-04	

Phosphocholine
Hydrocarbon
Protein
$C_xH_yO_z$
Sulfur-containing

77.00	2.00	0.55	4.28E-07	
29.04	2.00	0.29	4.49E-10	C2H5
184.09	2.00	0.78	2.92E-05	C5H15NPO4
43.05	2.02	0.29	2.59E-08	C3H7
91.05	2.02	0.36	4.09E-08	C7H7
129.06	2.03	0.39	4.80E-07	
81.07	2.04	0.36	3.01E-06	
107.08	2.06	0.44	8.28E-05	
100.11	2.06	0.43	6.90E-09	
141.06	2.06	0.39	1.08E-07	
119.09	2.06	0.41	3.73E-05	
133.10	2.06	0.49	1.68E-04	
38.01	2.07	0.52	1.54E-07	
67.05	2.07	0.36	3.22E-09	C5H7
55.05	2.09	0.32	9.57E-10	C4H7
166.06	2.09	0.71	3.29E-06	C5H13NPO3
73.09	2.10	0.55	5.22E-08	
128.06	2.11	0.42	3.43E-08	
131.08	2.12	0.42	7.57E-06	
157.06	2.13	0.45	1.11E-08	
77.04	2.13	0.40	9.75E-10	C6H5
150.06	2.13	0.57	4.24E-07	C5H12SNO2?
115.05	2.15	0.43	2.02E-08	C4H7N2O2?
17.03	2.16	0.59	3.01E-08	NH3
165.05	2.16	0.46	3.33E-08	
69.07	2.16	0.39	7.77E-08	C5H9
109.10	2.16	0.52	1.51E-04	
139.01	2.17	0.80	5.75E-05	
117.06	2.17	0.42	2.62E-08	
41.04	2.19	0.37	5.14E-11	C3H5
46.07	2.19	0.71	3.69E-07	
132.08	2.19	0.57	8.77E-09	
89.08	2.20	0.54	3.79E-09	
47.04	2.20	0.84	6.26E-06	
45.05	2.23	0.52	2.81E-09	C2H7N
28.03	2.23	0.46	1.63E-10	C2H4
202.04	2.24	0.54	8.15E-08	
104.05	2.25	0.42	8.57E-10	
83.09	2.26	0.46	4.20E-07	
48.00	2.28	0.57	1.75E-08	
121.10	2.28	0.54	2.45E-05	
126.01	2.28	0.90	4.52E-05	
29.00	2.28	0.49	3.38E-10	
178.05	2.28	0.51	7.75E-08	
114.13	2.29	0.41	3.06E-11	
32.05	2.29	0.62	5.21E-09	
103.05	2.30	0.48	2.31E-09	
42.01	2.31	0.59	2.09E-08	
116.05	2.31	0.46	6.18E-09	

40.03	2.31	0.40	2.09E-11	
49.00	2.32	0.54	2.11E-09	
47.06	2.32	0.98	5.63E-06	
163.04	2.32	0.55	8.00E-08	
189.04	2.33	0.50	1.70E-08	
19.02	2.33	0.45	1.17E-08	
65.04	2.33	0.45	1.76E-10	
142.06	2.34	0.49	1.05E-08	
185.08	2.34	0.86	1.55E-06	
153.05	2.34	0.56	3.72E-08	
53.04	2.35	0.42	2.58E-10	C4H5
79.02	2.35	0.49	5.70E-10	
50.01	2.36	0.47	1.57E-10	
92.05	2.37	0.46	1.79E-10	C3H10SN
19.03	2.37	0.64	8.02E-09	
51.02	2.37	0.48	1.28E-10	C4H3
59.03	2.38	0.81	1.19E-07	
155.08	2.38	0.53	1.49E-06	
143.07	2.38	0.46	7.30E-08	C10H9N
179.06	2.41	0.57	5.05E-07	
127.05	2.41	0.55	9.32E-09	
224.10	2.41	0.93	1.56E-06	
167.06	2.43	0.63	3.89E-09	
146.09	2.43	0.54	4.15E-08	
168.03	2.44	0.84	7.35E-08	
78.05	2.44	0.46	1.52E-08	
51.01	2.45	0.55	8.89E-08	
44.99	2.45	0.73	1.34E-08	
198.09	2.46	0.89	8.50E-07	
63.02	2.46	0.48	7.60E-12	
168.07	2.47	0.77	1.42E-08	
52.03	2.47	0.50	4.44E-12	
31.02	2.49	0.48	2.33E-08	CH3O
75.02	2.49	0.69	1.27E-09	C3H7S
226.05	2.49	0.72	2.61E-09	
159.08	2.50	0.66	1.37E-08	
71.01	2.50	1.27	7.58E-06	C3H3O2
40.02	2.50	0.44	2.25E-11	
72.08	2.51	0.55	2.25E-10	
67.02	2.51	0.96	2.80E-07	
86.07	2.51	1.32	7.71E-06	
31.04	2.52	0.65	4.28E-10	CH5N
105.04	2.53	0.64	2.94E-08	
40.00	2.54	0.83	1.72E-05	
176.04	2.55	0.54	8.08E-08	
177.04	2.56	0.65	1.66E-07	
147.04	2.56	1.01	9.41E-07	
66.04	2.56	0.48	2.94E-11	
152.05	2.57	0.63	2.53E-08	

155.04	2.58	0.69	1.88E-08	
128.11	2.58	0.69	1.44E-10	
54.04	2.58	0.49	6.37E-10	
89.03	2.59	0.57	4.74E-10	
154.05	2.59	0.66	7.66E-09	
97.10	2.59	0.55	9.29E-08	
62.01	2.59	0.51	1.55E-12	
44.03	2.60	0.71	2.45E-08	CH4N2
47.01	2.64	0.78	1.30E-07	
106.06	2.64	0.56	7.04E-10	
225.10	2.64	0.84	6.42E-09	
140.04	2.64	0.65	1.35E-07	
87.02	2.66	0.55	6.95E-11	
43.02	2.67	0.56	2.74E-07	C2H3O
76.03	2.67	0.64	9.10E-10	
78.04	2.67	0.59	7.01E-12	
64.03	2.68	0.56	4.10E-10	
118.07	2.68	0.58	5.98E-10	
151.04	2.68	0.69	6.56E-08	
18.04	2.70	0.82	6.11E-09	NH4
65.01	2.70	0.69	4.03E-08	
170.09	2.70	0.77	1.51E-08	
109.22	2.71	0.61	2.82E-09	
102.04	2.72	0.70	1.98E-09	
45.04	2.72	0.70	2.81E-10	C2H5O
134.10	2.73	0.74	1.48E-07	
74.02	2.73	0.72	3.05E-09	
101.03	2.73	0.68	3.36E-09	
29.03	2.74	0.67	4.25E-09	
75.07	2.74	0.93	5.94E-09	
158.08	2.74	0.68	1.86E-09	
84.08	2.75	0.79	3.67E-10	C5H10N
156.07	2.75	0.70	1.90E-09	
139.04	2.75	0.68	1.18E-07	
87.08	2.75	0.88	1.16E-08	
180.06	2.76	0.68	1.05E-09	
106.03	2.76	0.89	4.98E-09	
42.04	2.76	0.56	6.68E-10	
111.01	2.76	1.14	2.78E-03	
130.06	2.76	0.71	1.57E-10	C9H8N
99.02	2.77	0.75	3.13E-09	
73.07	2.78	0.91	3.03E-09	C2H7N3 or C3H7NO
101.10	2.78	0.81	7.66E-10	
120.05	2.80	0.63	6.40E-10	
120.08	2.80	0.65	1.73E-09	C8H10N
204.06	2.82	0.74	2.21E-09	
57.03	2.82	0.72	9.25E-08	
57.05	2.83	0.57	3.18E-12	C3H7N
131.04	2.84	0.66	6.58E-10	C9H7O

53.02	2.84	0.66	6.30E-09	
122.10	2.84	0.63	3.22E-09	
90.04	2.84	0.63	2.02E-12	
28.02	2.85	0.59	4.76E-10	CH2N
70.07	2.85	0.76	2.56E-10	C4H8N
59.05	2.85	0.75	5.74E-10	CH5N3 or C3H7O or C2H5NO
86.01	2.85	0.62	1.54E-12	
114.05	2.86	0.83	4.56E-09	
46.03	2.86	0.78	1.98E-09	
113.03	2.87	0.69	1.46E-08	
53.00	2.87	0.66	6.55E-11	C3HO
145.06	2.88	0.72	1.40E-08	
43.04	2.89	0.59	9.10E-13	C2H5N
56.05	2.90	0.68	8.21E-11	C3H6N
67.03	2.90	0.74	1.36E-09	
144.07	2.90	0.67	1.23E-09	
44.05	2.91	0.75	7.23E-11	C2H6N
56.02	2.92	0.78	1.93E-09	
30.03	2.94	0.70	2.65E-10	CH4N
74.07	2.94	0.90	4.61E-09	C3H8NO
61.01	2.95	0.80	1.89E-11	C2H5S
54.00	2.95	1.10	3.31E-08	
108.08	2.96	0.71	6.47E-11	
126.05	2.96	0.76	1.51E-08	
133.07	2.97	0.76	5.11E-11	
87.06	2.98	0.95	3.10E-09	C3H7N2O
61.05	2.99	0.97	1.88E-09	C2H7NO
98.01	2.99	0.90	8.34E-06	
119.06	3.00	0.71	1.75E-08	
80.05	3.00	0.69	2.07E-10	
114.09	3.00	0.82	1.86E-10	
132.05	3.00	0.83	6.78E-11	
43.03	3.01	0.71	2.45E-09	CH3N2
94.06	3.01	0.72	1.89E-10	
67.04	3.01	0.66	4.10E-10	
140.10	3.02	0.90	1.53E-10	
76.02	3.03	0.72	1.48E-12	
88.04	3.03	0.74	2.23E-10	C3H6NO2
44.01	3.05	0.74	2.42E-10	CH2NO
170.05	3.05	0.96	1.94E-09	
101.07	3.06	1.01	2.62E-08	C4H9N2O
72.04	3.06	0.80	1.55E-09	C3H6NO
100.08	3.07	0.88	6.07E-10	
113.08	3.08	0.82	7.00E-10	
122.06	3.10	0.81	2.39E-10	
64.01	3.12	0.67	1.28E-12	
69.06	3.12	0.78	2.51E-11	C4H7N
127.10	3.13	0.90	2.60E-10	
119.03	3.13	0.96	1.99E-07	

60.04	3.14	0.97	6.54E-08	C2H6NO
110.07	3.14	0.99	1.78E-09	C5H8N3
60.05	3.14	0.96	2.09E-08	CH56N3
125.07	3.16	0.92	1.87E-11	
164.04	3.16	0.88	3.09E-07	
80.02	3.17	1.02	6.64E-09	
55.02	3.18	0.77	1.88E-09	C3H3O
52.01	3.18	0.69	2.84E-12	
84.05	3.19	1.00	1.47E-09	
82.05	3.19	0.86	8.96E-11	C4H6N2
100.04	3.21	1.06	1.38E-09	
72.06	3.22	0.89	4.09E-09	
95.02	3.23	0.95	2.58E-10	
107.05	3.23	0.84	1.07E-09	C7H7O
56.01	3.24	0.97	2.70E-08	
126.09	3.25	0.94	3.00E-10	
85.08	3.25	0.90	1.21E-11	
82.07	3.25	0.81	1.16E-10	
69.03	3.25	0.83	2.05E-09	C4H5O
68.05	3.25	0.81	1.13E-10	C4H6N
151.09	3.26	0.92	2.10E-11	
96.08	3.27	0.81	6.21E-10	
121.08	3.27	0.83	2.13E-10	
135.06	3.27	0.96	2.24E-10	
54.03	3.27	0.77	5.87E-11	C3H4N
57.02	3.28	0.92	5.12E-09	
99.09	3.29	0.93	3.25E-11	
70.03	3.30	0.98	4.19E-09	C3H4NO
66.03	3.30	0.76	4.19E-12	
98.09	3.31	0.86	6.36E-11	C6H12N
57.04	3.32	0.85	1.99E-10	
174.02	3.32	1.18	3.14E-08	
99.05	3.34	0.97	6.41E-10	
136.05	3.34	1.01	2.09E-07	
149.06	3.34	1.02	1.93E-10	
85.04	3.34	1.01	5.35E-09	C3H5N2O
123.06	3.36	0.98	5.40E-11	
146.05	3.36	0.97	2.40E-11	
68.02	3.37	0.90	1.46E-09	
121.04	3.37	0.91	1.38E-10	C6H5N2O
109.07	3.37	0.95	9.76E-11	
125.11	3.37	0.89	6.05E-12	
136.07	3.38	1.09	1.18E-08	C8H10NO
137.07	3.38	0.96	6.73E-10	
95.06	3.39	0.93	7.75E-10	C5H7N2
98.06	3.40	1.04	7.90E-10	C5H8NO
123.09	3.43	0.88	1.06E-10	
83.06	3.43	0.91	4.24E-10	C5H7O
68.01	3.44	1.08	1.81E-08	

97.07	3.44	0.94	1.65E-09	C6H9O
139.08	3.45	1.06	4.37E-10	
97.03	3.45	1.02	1.03E-08	
94.03	3.45	0.99	3.95E-11	
82.03	3.48	1.04	8.78E-09	C4H4NO
108.05	3.48	1.06	7.84E-10	
124.08	3.49	1.00	4.53E-10	
134.06	3.50	1.01	2.10E-10	
134.02	3.53	1.37	1.68E-07	
50.00	3.55	2.51	2.77E-03	
96.04	3.56	1.07	1.84E-09	
112.09	3.58	1.14	2.61E-11	
111.05	3.63	1.07	2.75E-09	
148.06	3.65	1.12	1.10E-08	
42.03	3.66	0.69	6.71E-15	C2H4N
124.04	3.68	1.18	9.22E-08	
110.02	3.69	1.30	3.66E-06	
111.09	3.69	1.13	4.37E-10	
81.04	3.71	0.98	8.75E-08	C4H5N2?
112.04	3.75	1.31	2.63E-07	DNA C4H6N3O
96.01	3.77	1.41	1.42E-05	
135.02	4.44	1.45	1.39E-06	

Table S.2: Positive Ions that were detected from the frozen-hydrated cells but not the freeze-dried cells, or in new very low amounts in the FD cells.

M/z	Composition	Possible structure
18.04	NH_4	NH_4
19.02	H_3O	H_3O
19.03		
19.04		
32.05	C_2H_6N	NH_4-CH_2
33.02	NH_3O	H_3O-N
33.03	CH_5O	H_3O-CH_2
33.05	N_2H_5	NH_3-NH_2
34.03	NH_4O	H_3O-NH
34.05	N_2H_6	NH_3-NH_3
35.03	NH_5O	H_3O-NH_2
35.06	N_2H_7	NH_4-NH_3
36.04	NH_6O	NH_3-H_3O
37.02	H_5O_2	H_3O-H_2O
43.02^	C2H3O	C2H3O
45.05"	CH5N2	(NH2)2-CH
47.06	CH_7N_2	$(NH_3)_2$-CH
48.04	CH_6NO	NH_3-H_2O-CH
49.08	CH_9N_2	$(NH_3)_2$-CH_3
50.06	CH_8NO	NH_4-H_2O-CH_2
52.09	N_3H_{10}	$(NH_3)_2$-NH_4
53.07	N_2H_9O	$(NH_3)_2$-H_3O
54.05	NH_8O_2	NH_3-H_5O_2
55.03	H_7O_3	H_3O-$(H_2O)_2$
55.99	KNH_3	K-NH_3
56.97	KH_2O	K-H_2O
59.01	NaH_4O_2	Na-$(H_2O)_2$
59.07^"	$C_2H_7N_2$	$(NH_3)_2$-C_2H
60.05^"	C_2H_6NO	NH_3-C_2H_3O
61.03^	$C_2H_5O_2$	$C_2H_5O_2$
61.08"	$C_2H_9N_2$	$(NH_3)_2$-C_2H_3
62.06	C_2H_8NO	NH_4-C_2H_3O-H
63.05	CH_7N_2O	$(NH_3)_2$-CHO
73.05	H_9O_4	H_3O-$(H_2O)_3$
74.01^"		
74.99	KH_4O_2	K-$(H_2O)_2$
75.06		
76.05		
76.08		
77.02	NaH_6O_3	Na-$(H_2O)_3$
77.08	CN_4H_9	$(NH_3)_3$-CN

^ Possible NH4-acetate fragment

" overlaps different peaks in dried cells

78.01		
78.06^	$C_2H_9NO_2$	NH_4-$C_2H_4O_2$
79.00		
80.00		
80.99		
83.01^	$NaC_2H_5O_2$	Na-$C_2H_5O_2$
83.99		
88.05		
89.07	$C_3H_9N_2O$	$(NH_3)_2$-C_3H_3O
90.07	$NH_{12}O_4$	NH_3-H_9O_4
92.02		
92.08^	$C_3H_{10}NO_2$	NH_4-$C_2H_5O_2$-CH
92.99	KH_3O_6	K-$(H_2O)_3$
96.07		
98.00	C_2H_5NOK	K-NH2-C2H3O
98.99	$KC_2H_4O_2$	K-$C_2H_4O_2$
99.99	$KC_2H_5O_2$	K-$C_2H_5O_2$
100.04	$C_4H_6NO_2$	C_2H_2N-$C_2H_5O_2$
101.03		
102.00		
102.06		
109.06	$H_{13}O_6$	H_3O-$(H_2O)_5$
111.00	KH_8O_4	K-$(H_2O)_4$
114.00		
114.08		
116.02		
117.00		
126.01		
126.10	$NH_{16}O_6$	NH_3-$H_{13}O_6$
127.07	$H_{15}O_7$	H_3O-$(H_2O)_6$
129.01	$KH_{10}O_5$	K-$(H_2O)_5$
137.09		
138.09		
143.03		
144.10	$NH_{18}O_7$	NH_3-$H_{15}O_7$
145.07	$H_{17}O_8$	H_3O-$(H_2O)_7$
147.02	$KH_{12}O_6$	K-$(H_2O)_6$
148.06		
152.94		
155.10		
158.03		
159.01		
160.01		
160.06		
161.00		
162.09		
163.08	$H_{19}O_9$	H_3O-$(H_2O)_8$

173.03		
174.09		
180.98		
181.09	$H_{21}O_{10}$	$H_3O\text{-}(H_2O)_9$
194.96		
195.98		
196.96		
197.08		
199.10	$H_{23}O_{11}$	$H_3O\text{-}(H_2O)_{10}$

Table S.3: All positive secondary ions detected from both the FH cells and the FD cells

Mass	Fold Difference	Stdev	t- test	Mass	Fold Difference	Stdev	t- test
15.02	1.28	0.22	1.04E-04	60.08	-1.18	0.48	2.12E-01
25.01	-2.72	1.09	4.05E-04	61.01	-1.24	0.56	1.21E-01
26.01	-2.25	0.74	1.41E-04	62.01	1.98	0.68	1.69E-04
27.02	-2.66	0.88	1.38E-08	63.02	-1.31	0.49	2.46E-02
28.02	-1.29	0.51	3.99E-02	65.04	-1.44	0.53	2.76E-03
28.03	-1.71	0.65	1.35E-04	66.03	-1.36	0.70	4.50E-02
29.00	1.07	0.29	3.92E-01	66.04	1.18	0.38	1.24E-01
29.03	-1.08	0.42	5.32E-01	67.05	-1.40	0.49	3.47E-03
29.04	-2.54	0.79	1.45E-09	68.05	1.13	0.52	3.96E-01
30.03	1.65	0.52	1.05E-04	69.04	-1.04	0.55	8.23E-01
31.02	1.61	0.38	4.87E-06	69.07	-1.28	0.40	1.21E-02
31.04	1.68	0.50	1.46E-05	70.03	1.24	0.59	1.76E-01
37.00	-2.60	1.09	3.04E-05	70.07	-1.07	0.53	6.77E-01
38.01	-2.30	0.96	1.65E-05	71.07	-1.49	0.40	3.06E-04
40.03	-1.50	0.43	1.61E-04	72.09	1.28	0.40	2.11E-02
41.02	-1.93	0.71	2.92E-06	74.07	3.17	1.08	1.81E-08
41.04	-2.11	0.79	4.13E-07	74.10	-1.50	0.47	1.25E-03
42.01	1.35	0.37	1.45E-03	77.04	-1.20	0.28	2.66E-02
42.03	-1.21	0.44	9.51E-02	79.06	1.16	0.23	2.01E-02
43.04	1.17	0.43	2.11E-01	80.05	1.42	0.50	6.69E-03
43.05	-2.19	0.65	3.82E-09	81.04	1.30	0.76	1.95E-01
44.01	-1.14	0.48	3.29E-01	81.07	-1.04	0.25	6.19E-01
44.03	-1.66	0.80	1.60E-03	82.03	-2.24	0.20	1.48E-04
44.05	1.28	0.49	5.95E-02	82.07	1.59	0.66	5.45E-03
46.03	7.62	2.13	1.40E-12	83.06	1.72	0.72	1.94E-03
46.06	5.27	1.82	2.94E-11	84.05	1.54	0.71	1.14E-02
49.00	-1.73	0.72	2.93E-04	84.09	1.58	0.86	3.04E-02
50.00	-1.51	1.04	1.22E-01	85.04	1.96	0.76	7.94E-05
50.01	-1.77	0.52	2.88E-05	85.08	2.26	0.94	1.20E-04
51.02	-2.02	0.81	8.20E-06	86.07	1.98	1.20	1.07E-03
52.01	-1.74	0.86	6.46E-04	86.10	-1.86	0.58	1.08E-05
52.03	-1.31	0.50	2.52E-02	88.08	2.41	0.61	1.07E-08
53.00	-1.29	0.47	3.13E-02	88.11	-1.60	0.40	3.42E-05
53.04	-1.75	0.69	4.31E-05	89.03	1.43	0.41	7.72E-04
54.03	-1.15	0.54	3.24E-01	93.07	1.64	0.31	2.83E-08
55.02	-1.52	0.83	1.16E-02	94.06	2.10	0.56	9.69E-09
55.05	-1.62	0.53	3.02E-05	95.09	2.98	1.00	2.98E-05
56.05	1.13	0.48	3.64E-01	97.04	3.34	1.34	4.67E-06
57.02	1.05	0.55	7.57E-01	97.07	2.34	0.88	2.07E-05
57.03	1.30	0.44	2.34E-02	98.06	2.18	0.91	8.76E-05
57.05	1.34	0.45	1.68E-02	98.10	2.36	0.87	1.25E-05
57.07	-1.86	0.49	1.64E-07	100.08	2.61	1.22	2.66E-04
58.03	-1.25	0.67	2.43E-01	101.08	3.86	1.48	2.65E-07
58.06	-1.64	0.48	1.02E-05	102.09	1.67	0.44	3.04E-05
59.05	-1.24	0.61	1.61E-01	103.05	1.32	0.31	8.14E-04
59.07	-1.11	0.31	2.50E-01	103.09	4.43	1.08	2.82E-10

Mass	Fold Difference	Stdev	t- test
104.11	-1.55	0.46	1.80E-03
105.07	1.18	0.21	6.86E-03
106.06	2.23	0.50	6.39E-11
107.05	1.41	0.51	7.19E-03
107.08	1.78	0.30	5.21E-09
108.08	5.18	1.43	7.99E-10
110.08	1.85	0.79	4.84E-04
111.06	2.98	1.17	4.22E-06
112.05	4.81	2.72	1.97E-04
112.08	2.78	1.32	1.12E-04
115.05	1.03	0.26	6.90E-01
117.06	1.58	0.32	3.71E-07
118.07	2.83	0.62	3.43E-14
119.09	2.35	0.44	5.49E-09
120.08	2.06	0.51	3.43E-09
123.09	5.12	0.98	3.76E-13
124.08	3.69	1.38	5.04E-12
125.00	-1.08	0.37	4.99E-01
125.07	2.90	1.03	2.29E-07
129.06	1.50	0.31	3.05E-06
130.06	1.52	0.48	4.22E-04
132.08	4.18	1.08	2.34E-15
136.07	3.82	1.57	4.19E-06
140.05	5.13	1.31	4.17E-10
150.06	2.78	0.78	4.87E-12
152.05	2.85	1.26	1.81E-04
154.05	3.57	0.89	1.17E-15
166.06	1.70	0.63	5.53E-05
167.06	2.60	0.68	6.30E-12
168.07	3.40	1.11	1.23E-12
169.07	4.06	1.13	8.93E-16
170.05	4.78	1.37	1.48E-16
174.02	6.94	2.77	7.62E-08
176.03	5.53	1.65	1.75E-07
178.05	2.58	0.56	2.01E-12
179.07	4.28	1.01	4.77E-11
184.08	2.62	1.16	8.37E-07
185.08	4.01	1.51	1.33E-13
189.04	2.41	0.57	9.72E-10
191.06	3.14	0.81	1.80E-10
198.10	10.10	4.46	2.72E-07
202.04	3.06	0.81	1.25E-09
206.05	3.50	1.56	3.53E-11
222.02	3.34	1.53	1.59E-06
224.10	4.03	1.01	3.06E-10

5. ToF-SIMS Depth Profiling of Cells: Z-correction, 3D Imaging, and Sputter Rate of Individual NIH/3T3 Fibroblasts

Michael A. Robinson[1,3] Daniel J. Graham[1,2] David G. Castner[1-3*]

National ESCA and Surface Analysis Center for Biomedical Problems[1] Departments of Bioengineering[2] and Chemical Engineering,[3] University of Washington, Seattle, WA 98195-1750

* Corresponding author

David G. Castner

1-206-543-8094 (phone)

1-206-543-3778 (fax)

castner@uw.edu (e-mail)

5.1 Abstract

Proper display of three-dimensional time-of-flight secondary ion mass spectrometry (ToF-SIMS) imaging data of complex, non-flat samples requires a correction of the data in the z-direction. Inaccuracies in displaying three dimensional ToF-SIMS data arise from projecting data from a non-flat surface onto a 2D image plane, as well as possible variations in the sputter rate of the sample being probed. The current study builds on previous studies by creating software written in Matlab, the ZCorrectorGUI (available at http://mvsa.nb.uw.edu/), to apply the z-correction to entire 3D data sets. Three dimensional image data sets were acquired from NIH/3T3 fibroblasts by collecting ToF-SIMS images using a dual beam approach (25 keV Bi_3^+ for analysis cycles and 20 keV C_{60}^{++} for sputter cycles). The entire data cube was then corrected using the new ZCorrectorGUI software, producing accurate chemical information from single cells in 3D. For the first time, a three dimensional corrected view of a lipid-rich subcellular region, possibly the nuclear membrane, is presented. Additionally, the key assumption of a constant sputter rate throughout the data acquisition was tested using ToF-SIMS and atomic force microscopy (AFM) analysis of the same cells. For the dried NIH/3T3 fibroblasts examined in this study, the sputter rate was found to not change appreciably in x, y or z, and the cellular material was sputtered at a rate of approximately 10 nm per 1.25×10^{13} ions C_{60}^{++}/cm^2.

5.2 Introduction

Time-of-flight secondary ion mass spectrometry (ToF-SIMS) is a powerful tool that has been previously used to study a wide range of biological materials including (but not limited to): cells and tissues, lipids, DNA, drug eluting stents, explanted biomaterials and decellularized matrix [12, 94, 96, 98, 100, 102, 123, 125, 127-130, 160-162]. The unique abilities of ToF-SIMS to acquire a full mass spectrum at high mass resolution with submicron lateral resolution [4] makes for a bright future for spectroscopic and imaging analysis of biological materials [122]. These characteristics are required to visualize sub-cellular features, which may prove powerful for analyzing drug or metabolite behavior within single cells.

In addition to creating two-dimensional chemical maps of the surface, three-dimensional imaging has become feasible with the incorporation of cluster ion sources into ToF-SIMS instruments. This has been facilitated by the increase in yield during analysis provided by primary ions such as Bi_3^+, and the ability of C_{60} sputtering to efficiently remove material while minimizing residual damage in the remaining material [8, 10, 43, 163-165]. A 3D imaging experiment with current ToF-SIMS instrumentation often requires a dual beam approach [11, 14, 34, 36], where multiple sequential analysis and sputter cycles are carried out until the feature of interest is fully consumed. This mode of analysis is becoming more widely used in the ToF-SIMS community. In 2006, Gillen *et al.* constructed 3D images of various pharmaceuticals in biocompatible polymers [166], and in 2007 Fletcher *et al*. constructed 3D images of a *Xenopus Laevis* oocyte [12]. Soon after, Breitenstein *et al.* published a view of a single cell in three dimensions [14]. Recently, Fletcher *et al.* imaged frozen-hydrated HeLa-M cells in 3D, and were able to localize the rich adenine signal from DNA within the nucleus [27]. These latter two

papers addressed an important challenge in producing realistic 3D images from ToF-SIMS depth profiles, the fact that the data matrix is inverted as the image data is acquired from a 3D object.

The correction of ToF-SIMS data to create a more accurate representation of the original sample is not new to the SIMS community. There are two distinct corrections that may be required. The first corrects a data set acquired from a sample that is three dimensional. The need for this correction is explained in more detail in the following paragraph. The second correction addresses any significant changes to the erosion rate as the sample is sputtered. This may result from non-uniform composition within the sample[167, 168], changes to the incident angle of the primary ion beam [169, 170], or sputter induced topographic damage [171, 172]. In 1982 Patkin *et al*. describe a correction to the intensity of ion images due to differential sputtering in plastic embedded plant tissue during dynamic SIMS experiments [168]. Relative sputtering rates of 1.5 and 1.2 were calculated for the cells walls and nuclei, compared to the cytoplasm. Wagter *et al.* used atomic force microscopy (AFM) to correct for initial topography and differences in the sputter rate for different materials in the dynamic SIMS depth profile data of a Zr-2.5%Nb alloy sample [173]. With this correction the SIMS data was fit to the AFM topographic maps taken before and after the acquisition of the SIMS depth profile. The AFM data was used to calibrate the z-scale of the SIMS data. This approach has been developed further in a series of papers from the Winograd group [167, 174, 175]. For example, a protocol was developed for correcting the z-axis in a 3D data set obtained from a thin trehalose film with implanted 15-keV Ga^+ ions [175]. The region damaged by the implanted Ga^+ had a much lower sputter rate that then the surrounding trehalose, which was compensated for with a similar AFM calibration of the SIMS depth profile. In instances where differential sputtering is significant,

this type of correction is necessary for the accurate 3D reconstruction and visualization of the data.

To understand the need for correcting a ToF-SIMS image stack created from a 3D object, consider a model hemisphere system. The cyclic sputtering of this sample would be analogous to the peeling of an onion, with a small "layer" of material being removed by each sputter cycle. Due to the fact that the data from this 3D surface is saved in a 2D image slice, a flat image is produced from a non-flat surface. This results in a collection of images where the ensuing "3D" image stack will be upside-down, and assuming a constant sputter rate, have the same shape as the real object. Simply rotating the data stack 180° is not sufficient since information originating from within the cell volume would not be in the correct location. A pixel shift needed to correct this problem was introduced by Breitenstein *et al.*[14]. For this correction the upside down contour of the feature being imaged is determined. This contour line is then defined as the new Z=0 line and the data is corrected accordingly. It should be noted that this correction does not take into account any horizontal shifts due to changes in the perceived beam position. However, as shown in the data provided below, these types of shifts, if present, are not significant for the samples used in this work. For an accurate z-correction, the sputter rate through the feature being profiled needs to not change significantly, otherwise an additional correction for differential sputtering must be applied.

The assumption of a constant sputter rate has been used in both of the 3D depth profiling studies of cells that corrected for the non-flat nature of those cells[14, 27]. Due to the complexity of the cellular structure, it is important to examine the validity of this assumption. Chandra *et al.* found that there was no noticeable differential sputtering effects in freeze-fractured, freeze-dried NIH/3T3 fibroblasts under dynamic bombardment using Ar^+, O_2^+ and Cs^+

primary ions[59]. It is necessary to determine if this is a valid assumption when C_{60} is used as the sputter source in ToF-SIMS studies.

The method used to prepare single cells for ToF-SIMS analysis will affect the information obtained from them, and may affect the sputtering issues that are described in this text. There are generally three methods to prepare cells: analyze frozen-hydrated after cryofixation, lyophilization after cryofixation, and chemical fixation. Frozen-hydrated analysis best maintains the native structure of the cells[27, 176], and also may increase ion yields because of protons donated by the incorporated water matrix[146, 149, 177]. Breitenstein *et al.* shows that chemical fixation is a viable method to prepare cells in many instances [70]. The two methods that yield dry cells, cryofixation followed by lyophilization, and chemical fixation with air drying are examined in this study. Dried cells were chosen for comparison of the corrected SIMS data with the AFM topography data since the AFM used in this study does not have a cryogenic stage.

In this study we explore the validity of the assumption of a constant sputter rate in depth profiles of NIH/3T3 cells utilizing C_{60}^{++} as the sputter source. Furthermore, a new visualization tool, the ZCorrectorGUI, is introduced. This applies a z-axis correction, as described by Breitenstein *et al.*[14], to entire data sets, as well as 3D visualization in the same program. Lastly, we show for the first time, a three dimensional, corrected view of a lipid-rich subcellular feature within a single cell, possibly the nuclear membrane, using ToF-SIMS imaging.

5.3 Materials and Methods

5.3.1 Cell Culture

NIH/3T3 fibroblasts were cultured on 1 cm x 1 cm silicon chips[150] that were previously cleaned by sequentially sonicating for 5 minutes, 2x each in dichloromethane, acetone and methanol. The cells were grown in Dulbecco's Modified Eagle Medium (DMEM) (Invitrogen, Carlsbad, CA) supplemented with 10% fetal bovine serum (Hyclone, Waltham, MA) and 1% antibiotic/antimyotic (Invitrogen, Carlsbad, CA). Cells were seeded at densities between 20,000-40,000 cells and allowed to grow for 24-48 hours, depending on the desired coverage.

5.3.2 Chemical Fixation

Silicon chips with seeded cells were removed from the culture media and gently rinsed for 5 seconds in 150 mM ammonium acetate (Sigma, St. Louis, MO) at pH 7.4.[136] The samples were then placed in room temperature 4% ethanol-free formaldehyde (Thermo Scientific, Erie, PA) in 1X phosphate buffered saline (PBS) (EDS Chemicals) for 30 minutes. After fixation the cells were rinsed for 5 seconds, then edges of the silicon chip were touched with a Kimwipe to remove excess media, and the samples were allowed to air dry overnight in a laminar flow hood.

5.3.3 Lyophilization

Silicon chips with seeded cells were removed from the culture media and gently rinsed for 30 seconds in 150 mM ammonium acetate at pH 7.4. Prior to cryofixation the edges of the silicon chip were touched with a Kimwipe to remove excess media. The samples were then plunge frozen in liquid ethane[178], and stored in small glass test tubes under liquid nitrogen (LN_2). The test tubes were placed into a pre-cooled lyophilization flask, with LN_2 still in the tubes, and the flask attached to the vacuum of a manifold type freeze drier (SP Scientific, Warminster, PA). The samples were lyophilized overnight.

5.3.4 Time-of-flight Secondary Ion Mass Spectrometry

ToF-SIMS experiments were performed using an ION-TOF TOF.SIMS 5-100 (ION-TOF GmbH, Münster, Germany) equipped with two ion sources. A liquid metal ion gun (LMIG) was used to generate a pulsed 25 keV Bi_3^+ beam, whereas an electron impact gun was used to generate a 20 keV C_{60}^{++} beam. Both beams hit the target at an angle of 45°. For the 3D data sets, the Bi_3^+ beam was rastered over a constant area (varies between data sets) and centered inside a 500 μm × 500 μm C_{60}^{++} crater. For the 3D data sets, a high spatial resolution (HSR) mode was used to acquire the images, while a high mass resolution bunched mode was used to acquire spectra intermittently for peak assignments. The mass resolution ($m/\Delta m$) for $C_2H_3^+$ was roughly 300 and 5000 for the imaging and spectra modes, respectively. Target currents were measured before each data set using a Faraday cup. The Bi_3^+ current was typically 0.04-0.05 pA with an 80.1 ns pulse width for the imaging mode, while the C_{60}^{++} current varied between data sets. The C_{60} sputtering time was varied, depending on the current, to achieve a constant sputter dose of 1.25 $x10^{13}$ ions/cm^2 for each sputter cycle. Analysis cycles using a Bi_3^+ sputter dose of 5.8 x 10^{11} ions/cm^2 was used to acquire images (256x256 pixels) at each slice.

5.3.5 Atomic Force Microscopy

To measure the height of the dried cells before ToF-SIMS analysis, a Dimension ICON (Bruker, Santa Barbara, CA) atomic force microscope was used in ScanAsyst® mode in air with a silicon nitride, ScanAsyst-Air tip. Raw AFM data was imported into the NanoScope Analysis software and a second order plane fit was applied to all images. No further modifications were applied to the images.

5.3.6 Data Handling/ ZcorrectorGUI

Peak intensity images from peaks known to correspond to components of cells were exported from the IONTOF Version 4 program (ION-TOF GmbH, Münster, Germany) as .bif files and saved in a folder. Those files were then imported into the ZCorrectorGUI (Dan Graham Ph.D., NESAC/BIO, University of Washington) toolbox written for MATLAB (MathWorks, Natick, MA).

The ZCorrectorGUI is a graphical user interface (GUI) for MATLAB that incorporates a similar "z-correction" pixel shift as described in[14], as well as 2D and 3D image display capabilities that allow visualization of a corrected data cube. The ZCorrectorGUI can import image files exported from the IONTOF software as .bif (Version 4) or .bif6 (Version 6) files. For non-IONTOF users, the data can be loaded from the Matlab workspace once it is imported into Matlab as properly organized data matrices (see the tutorials available at http://mvsa.nb.uw.edu/node/340). Any combination of masses can be viewed in the corrected state and examined in 3D. Three color overlays can be created in the corrected and 3D views. In addition transparency values can be varied to examine selected components within the 3D volume.

The ZcorrectorGUI shifts the pixels vertically to their correct position by first defining a new z=0 boundary, then moving every pixel to the correct location based on this new boundary. A schematic of this process is shown in Figure 5.1. Figure 5.1A shows a XZ slice through a cell depicting the m/z 58^+ peak intensities with no correction, showing the first analysis cycle at the top and the last analysis cycle at the bottom. The slice is upside-down but some sub-cellular features can be seen. To correct the z-axis of this image, the program thresholds the total counts image for a given slice (B) and finds the line at the interface defining the new z=0 (blue line) (C). The distance between the *new* z=0 line and a given pixel is measured, and after flattening of the

new z=0 line, the pixel is correctly placed at the measured distance from the flattened z=0 line (D). As a comparison, the result from simply rotating the image slice 180° can be seen in E, where the highlighted pixel (in red) is in the incorrect location. This pixel shift method is applied to all slices in the data cube, so for a data set with 10, 256x256 pixel images, the above process will occur 10 x 256 x 256 (655,360) times.

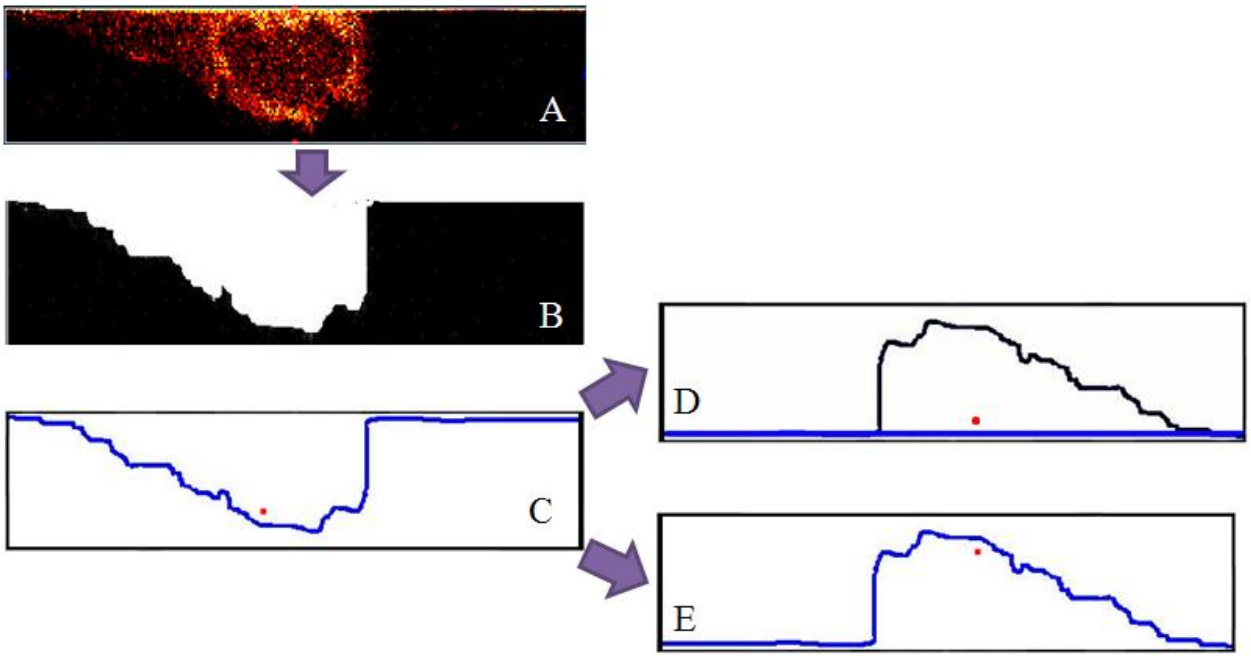

Figure 5.1: A flow diagram of the z-correction process. (A) XZ slice from a cell, showing the m/z 58^{+}peak intensities. (B) Thresholded image of the total counts image from the same data set as A. (C) An outline of the thresholded image is created. This is the new z=0 line. (D) Results when the z-correction is properly implemented. The z=0 line is flat, and the red pixel is in its proper position. (E) Results from flipping the image in C 180° without the z-correction. The location of the red pixel is wrong.

5.4 Results and Discussion

5.4.1 ZcorrectorGUI

Figure 5.2 shows data from a single 3T3 fibroblast that was chemically fixed with 4% formaldehyde and air dried. There are 56 slices in the data set, each image is 86x86 μm^2 and consists of 256x256 pixels. In 2A, the cell is visualized by plotting the intensity of the lipid peak at m/z 58^+. In Figure 2B the same data is plotted after smoothing. The data was smoothed using the Matlab 'smooth3' function using the default (3,3,3) box filter. This function uses a standard box filter to smooth the data by replacing the data in each voxel with the mean of the data within the box size chosen. These images only depict the outer lipid membrane of the cell, but there are methods that can be used to "see inside" past the plasma membrane. The first method is depicted in Figure 5.2 C-G, which shows selected corrected XY slices of the m/z 58^+ peak intensities for the same cell. These corrected slices are analogous to an x-ray computed tomography (CT) scan as they represent the information in the horizontal plane at that position. This allows the users to determine accurately where in the z-direction a target component, such as a metabolite or drug, is located. The ZcorrectorGUI is also capable of displaying the corrected data in the YZ or XZ planes. In addition, movies can be created that visualize slicing through the corrected data in any of these planes.

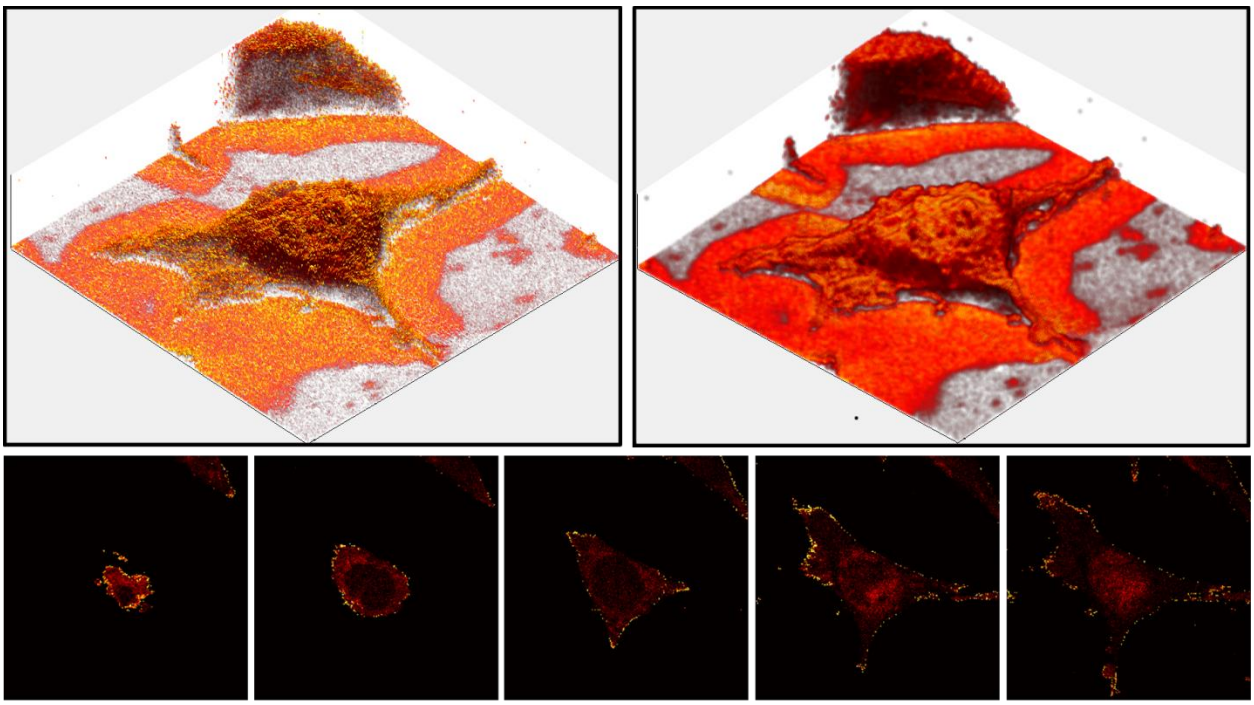

Figure 5.2: Visualization options provided by the ZcorrectorGUI. The data set consists of 56 images. Each image contained 256x256 pixels and was 86x86 μm^2 in size. (A) An image of the m/z 58^+ signals from a corrected data set of a single NIH/3T3 fibroblast. (B) The same data from A, after smoothing. (C-G) A series of corrected XY images of the m/z 58^+peak intensities. With the corrected data, one can move through the cell vertically in a similar fashion as a CT scan moves through tissue. C is at the top of the cell, while G is near the bottom of the cell.

Another way to visualize components within the cell is to use a 3-D image similar to those shown in Figures 5.2 A and B, but to make the entire data set semi-transparent. A similar method was used to map the adenine signal in HeLa-M cells recently [27]. The results using the ZcorrectorGUI can be seen in Figure 5.3, where the m/z 58^+ signal is displayed in all images. In A the data was first smoothed and then made translucent by changing the alpha value (a measure of the total opacity of the image: 0 = fully transparent, 1 = fully opaque) to 0.02. Here a lipid rich region can be seen within the nucleus, which is possibly a nucleolus. In B only the voxels with an intensity of 1-25 are displayed, and the alpha value was set to 0.04. For C, only the

voxels with an intensity of 3 are displayed, and the alpha value is 0.25. A spherical feature consisting of lipids, likely the nuclear membrane, is clearly visible. This ability to display voxels with their intensity specified by the user is useful because it allows internal features to be visualized. To our knowledge this is the first reported 3D images of a nuclear membrane-like component using a MS imaging technique.

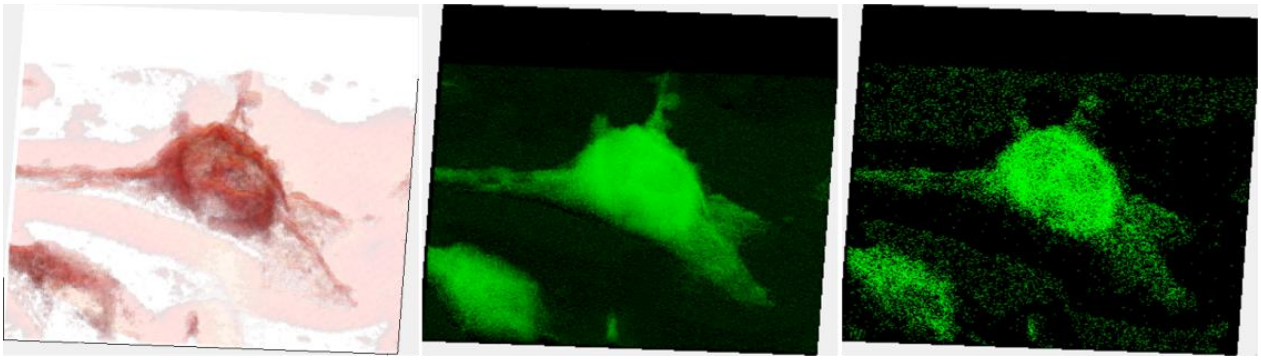

Figure 5.3: Visualization of the m/z 58^+ signal from a single NIH/3T3 fibroblast. The data was corrected in the ZcorrectorGUI and the transparency was adjusted within the GUI to allow the visualization of the sub-cellular lipid-rich feature, most likely the nuclear membrane. There are 56 images in the data set, with each image 86x86 μm^2 in size and containing 256x256 pixels. (A) m/z 58^+ image, data smoothed, 0.02 alpha value (a measure of transparency). (B) m/z 58^+ image, only the voxels with intensity values between 1-25 are plotted, alpha value 0.04. (C) m/z 58^+ image, only voxels with an intensity value of 3 are plotted, alpha value 0.25.

5.4.2 Sputter rate of single cells

The most critical assumption made when applying this z-correction to the data is that the sputter rate of the sample is homogenous throughout the sample in the x, y and z directions. A cell is a complicated biological system with many components, including organelles, the cytoskeleton network, and nucleoli. The sputter rate of these materials may be different from one another. Other assumptions include an easy to find contrast between the feature of interest

and the background, as well as a flat substrate that exhibits minimal sputtering. To determine the validity of the assumption of a constant sputter rate, AFM height profiles and corrected ToF-SIMS cross-sections of the same cell were compared. If these data do not closely agree, then differential sputtering is present, and an additional correction must be implemented to produce an accurate 3D reconstruction of the cell.

An overlay of an AFM height profile and a corrected XZ ToF-SIMS cross section of a single cryofixed, lyophilized fibroblast is shown in Figure 5.4A (This is a separate cell/dataset from the one shown in Figures 5.2 and 5.3). The AFM height profile and overlay with the corrected YZ ToF-SIMS cross section that run perpendicular to the slice in Figure 4A is shown in Figure 4B. The horizontal and vertical lines in Figure 4C define the slices used for the AFM height profiles and the ToF-SIMS corrected cross-sections seen in 4A and B. The AFM height profiles were scaled to match the corrected ToF-SIMS cross-sections. If the sputter rate were completely homogeneous throughout the data acquisition, then the AFM and ToF-SIMS data along any line should match exactly. In Figures 4A and B, there is good agreement between the AFM and ToF-SIMS data, indicating that any changes in sputter rate throughout the acquisition of the data set is small under the experimental conditions used in this study. In Figure 4A, the ZCorrectorGUI was able to appropriately correct for most of the topography, except towards the left side of the cell where the ToF-SIMS data extends out further on the left side than the AFM data, possibly due to shadowing during C_{60} sputtering. However, the excellent agreement between the ToF-SIMS and AFM profiles over the majority of the cell indicates that the assumption of a constant sputter rate is valid.

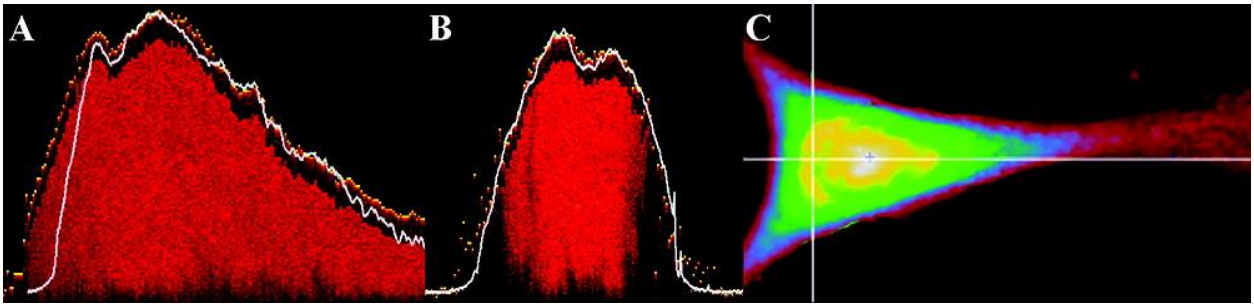

Figure 5.4: A comparison of corrected ToF-SIMS and AFM data from the same cell. (A) An overlay of a corrected slice from ToF-SIMS showing the distribution of all the detected ions and the height profile acquired with AFM along the same line (horizontal line in C). The AFM height profile is white and the ToF-SIMS data is red. (B) An overlay of a corrected slice from ToF-SIMS showing the distribution of all the detected ions and the height profile acquired with AFM along the same line (vertical line in C). The AFM height profile is white and the ToF-SIMS data is red. (C) The AFM height image. Image is 50x90 μm^2. Intensity scale changes from red to white as the height increases from 0 to 1.8 µm.

A different cell that was prepared by chemical fixation with 4% formaldehyde followed by air drying is shown in the Supplemental Information, Figure S.5.1. The AFM and ToF-SIMS results for this cell are in good agreement, similar to the results for the lyophilized cell in Figure 5.4. Thus, for both lyophilized and chemically fixed NIH 3T3 fibroblasts no significant changes to the sputter rate were noted. So the assumption of a constant sputter rate for the z-correction appears to be valid.

This agrees with data from Chandra *et al.* who used direct current Ar^+, Cs^+, and O_2^+ beams to etch freeze-dried NIH/3T3 fibroblasts and found no evidence of differential sputtering between the nucleus and cytoplasm [59]. This data is also consistent with the independence of sputter rate from density, which was shown in a recent study by Muramoto *et al.* for C_{60} sputtering during the depth profiling of thin organic films [131]. If density had a significant

effect on the sputter rate, the higher density nucleoli would be expected to have a different sputter rate compared to the less dense cytoplasm.

With some cells, as shown in Figure S.5.2, it was observed that there is a small salt residue present after all of the organic material had been removed by sputtering. This is the same data set displayed in Figure 5.4. Figure S.5.2 A-C shows the summation of the Na^+ and K^+ signal at slices 90, 132, and 141 respectively. These are raw, uncorrected images 86x86 μm^2 in size and containing 256x256 pixels. Figures S.5.2 D-F show the summation of the major lipid components at the same slices, and G-I are the total ion signal at these slices. The salt signal is still present in two small horizontal bands in slice 141, well after all of the organic material has been removed. A possible explanation for this is that this substance is underneath the cell and only becomes detectable after the cellular material above it has been etched away. The ammonium acetate rinse used on this sample is used to remove excess *surface* salts, but likely would not remove any salt crystals underneath the cells. Another explanation is that salt species may build up with increasing C_{60} dose during the profile due to the lower sputter yield of these ions compared to the organic cellular material. Based on the similarities in the overlays in Figures 5.4 and S.5.1, as well as the TOC graphic, this does not appear to be the case. The intracellular Na^+ and K^+ signals from the cell in Figure 4 were rather homogenous in x and y across all slices, and did not appear to increase with depth (data not shown). If salt accumulation was decreasing the average sputter rate with increasing C_{60} dose, and leading to the formation of the salt residue, then the residue should be present in a much larger area of the cell, not only the two small regions shown in Figure S.5.2 C. Also, any salt residue accumulation would be expected to form under the area of the tallest portion of the cell due to the most salt accumulation, which was not observed. Lastly, the cell shown in Figure 5.4 had roughly double

salt content of the cell in Figure S.5.1 (data not shown), and the average sputter rate for both cells was determined to be very similar. All of these points suggest that salt accumulation is not significantly affecting the average sputter rate of dried single cells using 20 keV C_{60}^{++} as the sputter source, and that any leftover salt residue originates from underneath the cell.

It was previously shown for organic delta-layers that the sputtering yield and depth resolution decreased with increasing C_{60} ion dose. The degradation in depth resolution was believed to be primarily caused by the development of topography on the sample surface [33]. A similar diminishment of the sputter yield may also be occurring here. However, the data in Figure 4 shows that there appears to be little change detected in the sputter rate as a function of depth. This cell type already has inherent roughness prior to sputtering, and subsequent C_{60} etch cycles do not significantly increase this native topography (See Figure S.5.3). Additionally, to minimize the damage caused the Bi analysis beam, low Bi ion doses compared to the C_{60} sputter dose were used [7].

Varying the angle of incidence of the primary ion with the surface has been shown to affect the sputter yield both experimentally[169] and computationally[170]. It follows that the sputter yield from topographically complex surfaces such as cells may also be affected. While this could play a small role in the data presented here, based on Figures 4 and S.1 as well as the TOC graphic, it does not appear to result in significant changes to the sputter rate. This could be due to the fact that the topography of the cell is sufficiently rough so any sputter rate differences are averaged out across the cell surface.

The average sputter rate of single NIH/3T3 fibroblasts can be calculated by dividing the number of sputter cycles needed to remove all of the cellular material by the maximum height of

the cell, as measured by AFM. The cell featured in Figure 5.4 was considered removed after 131 slices when the lipid signal was no longer detected, while the maximum AFM measured height of the cell was 1412 nm. This yields an average sputter rate of 10.8 nm per 1.25 $x10^{13}$ ions/cm^2 C_{60}^{++}. For the cell featured in Figure S.1, the ToF-SIMS data set consisted of 88 slices and the maximum AFM measured height was 905 nm, making the average sputter rate 10.3 nm per 1.25 $x10^{13}$ ions/cm^2 C_{60}^{++}. Although only two cells are used here, the calculated sputter rates are in good agreement. There seems to be little difference between the average sputter rates in dried cells that were prepared in two different ways.

Although the sputter rate appears to not change significantly for any x-y-z positions in these cells, this may not hold for every biological sample and every preparation method. For example, frozen-hydrated NIH/3T3 fibroblasts will probably exhibit preferential sputtering due to the large sputter yield of the ice compared to the organic material [179]. It also remains to be seen if differential sputter rates are observed in tissue sections sputtered by C_{60} bombardment. Tissue sections have a more heterogeneous microstructure than single cells which could lead to different components sputtering at distinct rates, which has been observed in plant cells [168].

5.5 Conclusion

A new GUI for MATLAB is introduced that performs a "z-correction" pixel shift on a data matrix, and allows for new visualization methods in two and three dimensions. Using this new GUI, for the first time, a three dimensional corrected view of a lipid-rich subcellular region, possibly the nuclear membrane, is presented. An important assumption for this z-correction is that sputter rate is constant within the sample. We show, on different dried cells prepared by either cryofixation with freeze drying or chemical fixation with air drying, that this is a valid

assumption. While there may be small changes in the sputter rate at any given position due to differential sputtering, they do not appear to be significant enough to warrant a further correction to the data. The average sputter rate of dried NIH/3T3 fibroblasts cells was approximately 10 nm per $1.25x10^{13}$ ions C_{60}^{++}/cm^2. The tools developed in this study provide improved visualization of target chemistries within single cells and will be useful for other biomedically relevant three dimensional systems. The ZCorrectorGUI can be downloaded for free at: http://mvsa.nb.uw.edu/

Acknowledgements

The authors gratefully acknowledge the funding and facilities provided by the National ESCA and Surface Analysis Center for Biomedical Problems (NESAC/BIO) through grant EB-002027 from the National Institutes of Health. The authors thank Prof. Buddy Ratner for the use of his cell culture facilities, as well as Prof. Cecilia Giachelli for use of the lyophilizer. The authors also thank Dr. Jim Hull for assistance with acquiring the atomic force microscopy data.

Table of Contents Graphic:

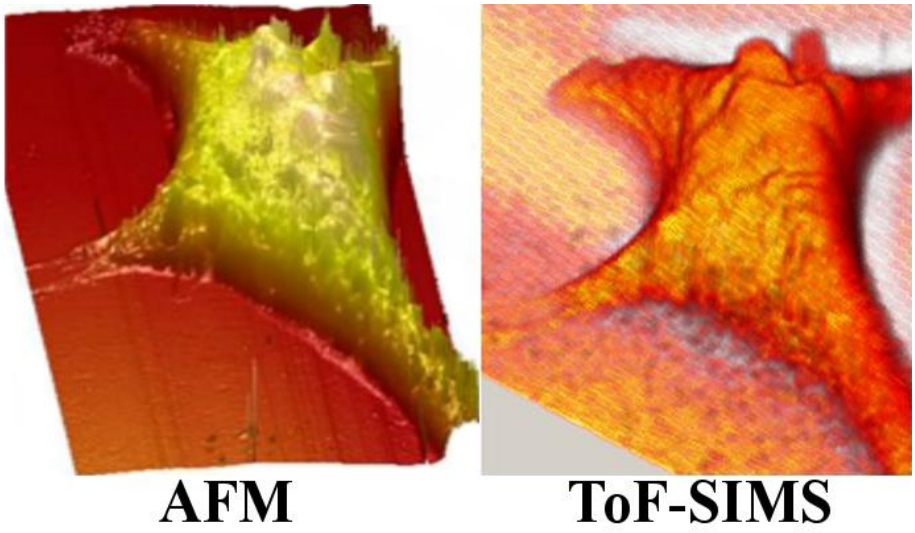

URL: http://pubs.acs.org/doi/full/10.1021/ac300480g#

5.6 Supporting Information

ToF-SIMS Depth Profiling of Cells: Z-correction, 3D Imaging, and Sputter Rate of Individual NIH/3T3 Fibroblasts

Michael A. Robinson[1,3] Daniel J. Graham[1,2] David G. Castner[1-3*]

National ESCA and Surface Analysis Center for Biomedical Problems[1] Departments of Bioengineering[2] and Chemical Engineering,[3] University of Washington, Seattle, WA 98195-1750

* Corresponding author

David G. Castner

1-206-543-8094 (phone)

1-206-543-3778 (fax)

castner@uw.edu (e-mail)

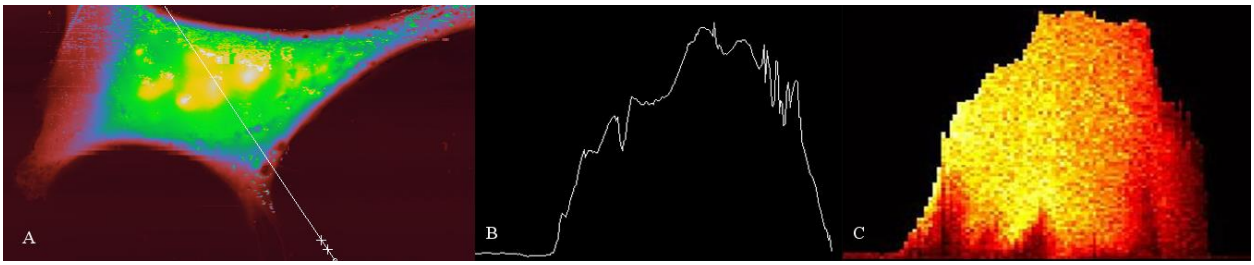

Figure S.5.1 A comparison of AFM and corrected ToF-SIMS data of a chemically fixed NIH/3T3 fibroblast. (A) An AFM topography image of a formaldehyde-fixed NIH/3T3 fibroblast. Scale bar represents height. The image is 80 µm x 50 µm. The maximum height is 905 nm. (B) The height profile across the line seen in A. The maximum height is 905 nm. (C) Corrected ToF-SIMS data of the total amount of ions from the same slice represented in B.

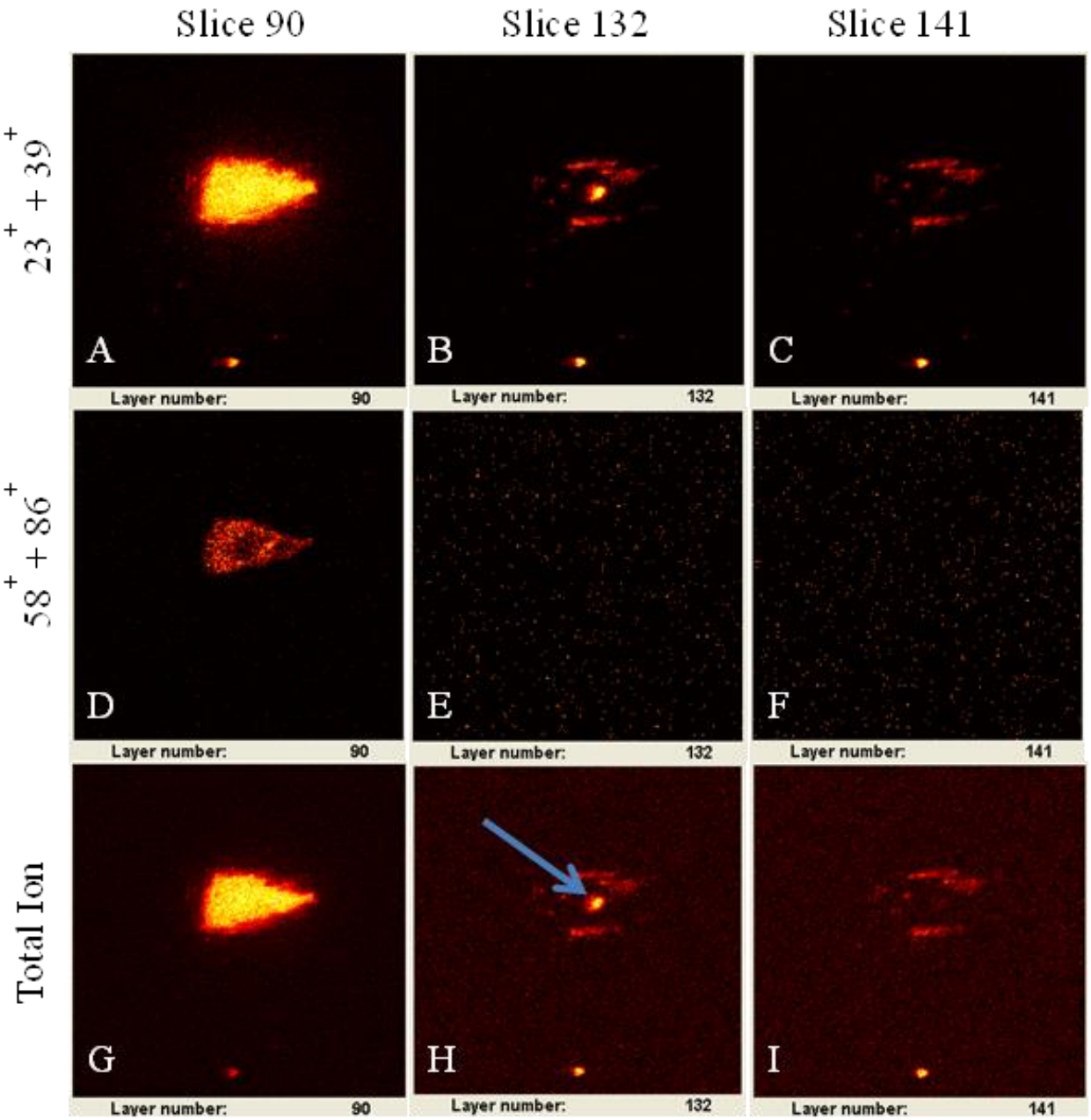

Figure S.5.2 (A-C) The summation of the salt signal from $^{+}23 + 39^{+}$ at slices 90,132, and 141, respectively. (D-F) The summation of the lipid peaks $^{+}58 + 86^{+}$ at slices 90, 132, and 141 respectively. (H-I) The total ion signal from slices 90, 132, and 141 respectively. The organic lipid peaks are totally absent at slice 132. All of the sputterable material is absent by slice 141. A salt residue still remains and is very resistant to sputtering. These are raw, uncorrected images containing256x256 pixels and are 86x86 μm^2 in size.

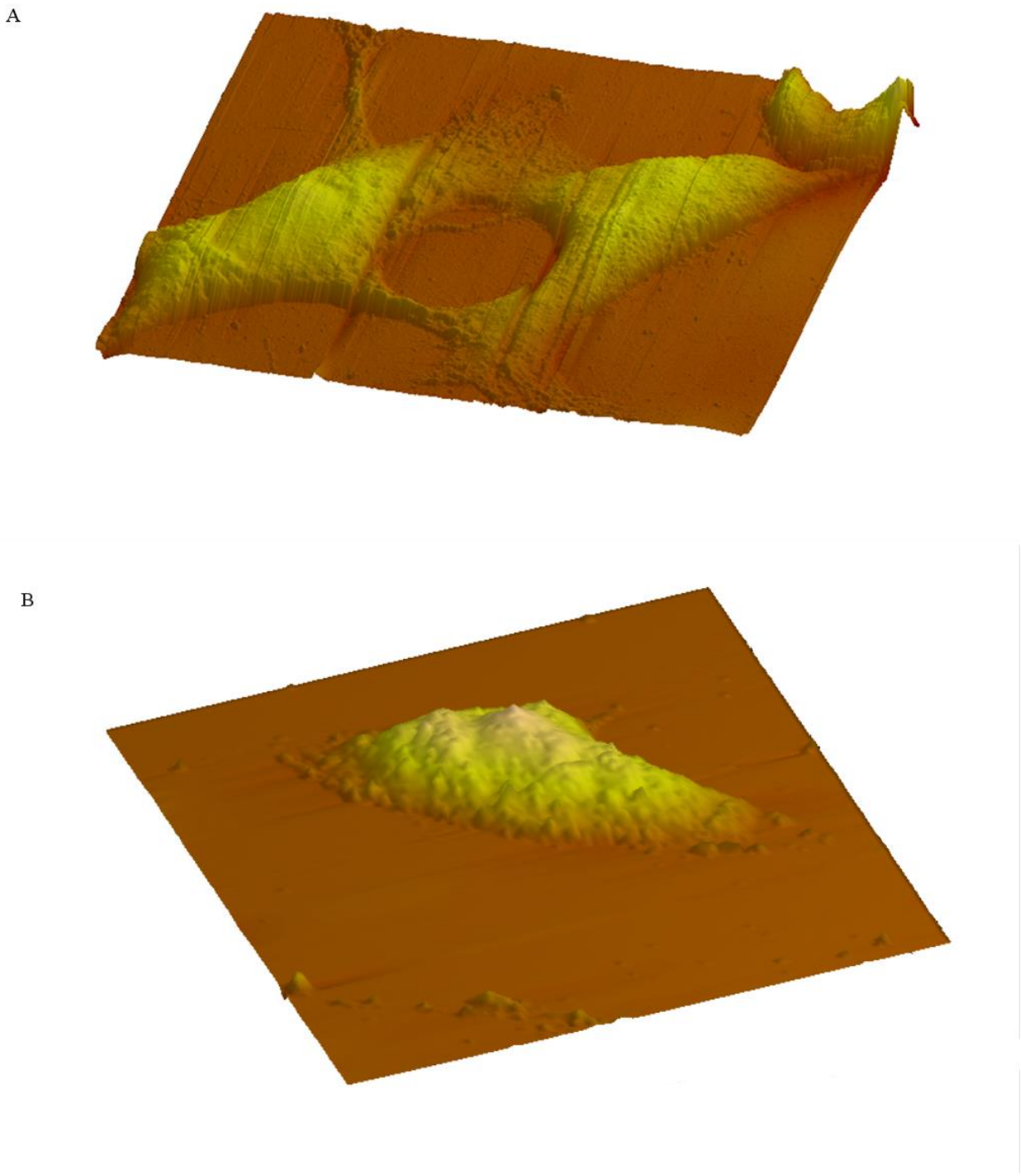

Figure S.5.3 AFM topography images of cells that were (A) Not sputtered with C_{60} and (B) sputtered with C_{60} for 400 seconds. Both images are 80 µm x 80 µm.

6. Chemical analysis of eight human breast cancer cell lines with ToF-SIMS

Michael A. Robinson[1,2], Fionnuala Morrish[3], David Hockenbery[3], Lara Gamble[1,4§]

National ESCA and Surface Analysis Center for Biomedical Problems[1], Departments of Chemical Engineering[2] and Bioengineering[4], University of Washington, Seattle, WA, 98195

Clinical Research Division[3], Fred Hutchinson Cancer Research Center, Seattle, WA, 98109

[§]Corresponding Author:

Lara Gamble

1-206-616-4173 (phone)

1-206-543-3778 (fax)

lgamble@uw.edu (e-mail)

Keywords: ToF-SIMS, cells, breast cancer, lipid, metabolism, triple negative, PCA

6.1 Abstract

Time-of-flight secondary ion mass spectrometry (ToF-SIMS) and principal component analysis (PCA) were used to determine chemical differences between eight breast cancer cell lines, which may be manifestations of unique metabolic processes. Four cell lines did not express estrogen receptor (ER), progesterone receptor (RP) or overexpress human epidermal growth factor receptor 2 (HER2), also known as triple negative (TN). Four cell lines were receptor positive (RP), that is one or more of the surface receptors were expressed. Using the spectra acquired with ToF-SIMS and PCA, the cell lines were successfully distinguished from one another. The TN cell lines displayed the most variance, where they were separated from one another on PC1 and 2 using positive secondary ions (SI). In contrast, the RP lines were partially separated from one another on PC4 using positive SIs. Using negative SIs, clear separations between both types of cell lines was observed on PC2 and 3. The molecular species that made the largest contributions to the variance were lipids, including phospholipids, mono- and diacylclycerols (MAG, DAG), fatty acids, and cholesterol. The normalized peak intensities of several key ions that were identified by PCA were plotted and compared. The plots revealed unique intensity distributions among the cell lines, particularly those based on length and saturation levels of fatty acids and the alkyl tails of MAGs and DAGs. Two peak lists which encompassed different mass ranges were investigated. For both positive and negative SIs, the best results were obtained with peak lists with the mass range m/z 200 – 850.

6.2 Introduction

Among women and cancer in 2012, breast cancer was estimated to have had the highest number of new cases and the second highest number of deaths [180]. The number of estimated breast cancer deaths has fallen annually since ~1990 [180], in part due to the improvements in targeted therapies [181] and personalized treatments [182], although the mortality rate is still unacceptably high. As mechanisms of tumor onset and growth are better understood, the number of deaths should continue to fall with an increasing pace. One broad, important mechanism that is not fully understood is tumor metabolism. An important connection between perfusion, glucose metabolism and neo-adjuvant chemotherapy resistance in tumors was established using dynamic kinetic positron emission tomography (PET) imaging with ^{15}O-H_2O and ^{18}F-fluorodeoxyglucose (FDG) [183-185]. Resistant tumors often displayed a perfusion/glucose metabolism mismatch, i.e. increased glucose consumption with respect to blood flow, and perfusion was not diminished in the resistant tumors. It was hypothesized that resistance tumors, those that displayed the perfusion/metabolism mismatch, utilized alternate metabolic pathways to satisfy the energetic needs of the tumor, labeled "metabolic flexibility". It was also hypothesized that the perfusion/metabolism mismatch is linked to tumor phenotype; that it is more severe in triple negative (TN) tumors compared to those that express estrogen receptor (ER) or overexpress human epidural growth factor receptor 2 (HER2).

Positive therapeutic results have resulted from the immunohistochemical (IHC) classification of breast tumors based on the presence of ER, progesterone receptor (PR) and HER2 [186]. If a tumor lacks ER and PR and does not overexpress HER2, it is classified as TN. TN tumors have a higher mortality rate than those that are receptor positive (RP) [187, 188]. Tumors have also been classified into molecular subtypes using gene expression arrays and

hierarchal clustering [189, 190]. Five subtypes were identified: luminal A, luminal B, HER2-enriched, basal, and normal breast like. A large majority of basal tumors are also TN by IHC, but the two classifications are not synonymous [191-193]. A recent gene expression analysis of TN breast cancer cells identified six subtypes within the TN class [194], showing that current classifications continue to be improved and expanded upon.

Lipogenesis and altered lipid metabolism are hallmarks of cancer onset and progression [195], as many cancer cell lines and tumors have a higher than normal rate of *de novo* fatty acid synthesis to support rapid proliferation [196]. Pathways involving lipid metabolism are being treated as new therapeutic targets, as knocking out the ability to rapidly produce lipids has reduced cellular viabilities [197, 198]. Lipidomic analyses are becoming more frequent as lipid metabolism is increasingly being viewed as an important component of breast cancer biology. One investigation that probed phospholipid species in breast cancer cell lines related differences in phosphatidylcholine and lysophosphatidylcholine levels to the aggressiveness of breast cancer cell lines. The same study also observed variations in the levels of several additional phospholipids could be linked to cancerous versus noncancerous cell lines [199, 200].

Time-of-flight secondary ion mass spectrometry (ToF-SIMS) has several strengths that make it an effective tool for single cell analysis. First, all secondary ions are extracted into the mass analyzer simultaneously. This is important as no information is "thrown away" by having to select only a particular subset of ions. Second, submicron spatial resolutions can be achieved in images acquired from cell and tissue samples [201], providing the capability to visualize subcellular features [27, 34, 154]. Because of this, ToF-SIMS is a natural complement to other mass spectrometry methods like matrix-assisted laser desorption ionization mass spectrometry (MALDI-MS) and desorption electrospray ionization mass spectrometry (DESI-MS). MALDI-

MS has been utilized in numerous investigations to study cancerous tissues [202, 203], and an increasing number of investigations into cancer that apply DESI-MS haven been completed [204, 205]. The surface sensitivity of ToF-SIMS is very high, on the order of 1-3 nm [206], allowing for precise control of data acquisition in depth. The difficulties interpreting ToF-SIMS spectra acquired from biological surfaces (or any other complex surfaces) arise from the large amount of fragmentation caused by the high energy primary ion impacts, and the huge variety of molecules from which these fragments may originate. In many cases, multivariate analysis (MVA) methods are utilized to aid the analysis by highlighting the largest sources of variance within the data set [121]. A recent review of lipid analysis with ToF-SIMS was written by Passarelli *et al.* [84].

Three human breast cancer cell lines were previously compared to one another with ToF-SIMS and principal component analysis (PCA) [104]. First, the cytosolic, nuclear and insoluble particulate fractions were separated from the MDA-MB-231 (TN), T47D and MCF7 (both RP) cell lines and ToF-SIMS spectra were collected. Using PCA, the fractions were successfully distinguished from one another. The insoluble particulate fractions separated from the nuclear and cytosolic components on principal component 1 (PC1). The nuclear components from the three cell lines separated from one another, as did the three cytosolic components, although some overlap was observed between the nuclear and cytosolic components. Additionally, freeze-dried, freeze-fractured cells were analyzed and compared. The RP T47D and MCF7 lines were more similar to each other than to the TN MDA-MB231 line. This study showed the potential to distinguish breast cancer cell lines based on the unique molecular signatures acquired with ToF-SIMS and PCA.

Soon after, three closely related prostate cancer cell lines were studied and distinguished from each other using discriminant function analysis (DFA) [105, 106]. Two cell lines were isolated from metastases, one from bone and one from a lymph node. The third line was a non-malignant, normal adult prostatic cell line. In these studies, discriminant function 1 (DF1) separated the bone metastasis cell line from the others, and DF2 separated the cancerous cells from the non-malignant line. All three lines were successfully separated from one another on a DF1 vs. DF2 plot. This study envisioned that ToF-SIMS may be used to discriminate individual cell types in mixed populations or even within tissue samples. Prostate cancer cell lines were also earlier studied by ToF-SIMS and synchrotron-based FT-IR [207, 208].

Barnes *et al.* then successfully identified individual cell types in mixed culture using ToF-SIMS, PCA and partial least-squares discriminant analysis (PLS-DA) [124]. Although these cells were not cancer cells, this study confirmed that ToF-SIMS is capable of classifying cell types in mixed cultures.

More recently, a series of studies that focused on several aspects of cancer were conducted using an Ionoptika J105 ToF-SIMS instrument. In one, the hypoxic core of multicellular tumor spheroids (MTSs) were found to be chemically distinct from the outer layer [209]. The second showed that differing the doxorubicin dosages on MTSs altered the mass spectra obtained from the hypoxic regions identified by PCA, providing insight into the metabolic response to chemotherapy [210]. A third reviews how ToF-SIMS may be applied to imaging metabolites in cells and tissues [211].

Gastric cancer tissue was distinguished from normal tissue using PLS-DA and a new platform to automatically identify and align peaks [212]. Additionally, network analysis showed

deregulation in amino acid metabolism. Human normal colon mucosa was compared against colon cancer tissue, and with PCA significant differences in the protein profile was observed [213]. ToF-SIMS showed that thyroid tumor cells had high cholesterol levels compared to non-cancerous pig thyrocytes [214]. A recent investigation probed choline metabolism in murine glioma, incorporating SIMS, MRI and PET imaging [215]. Another study by the same group used SIMS and MRI imaging to visualize the distribution of choline metabolites in MCF7 and MDA-MB-231 breast cancer xenograft models. Chandra *et al.* have published several studies that used dynamic SIMS imaging to map the boron distribution in single cells to study boron neutron capture therapy [216-218]. Although outside the scope of this work, these are some of the few examples of imaging the distribution of therapeutic agents using SIMS.

This paper aims to forward the previous work by comparing a larger number of breast cancer cell lines with ToF-SIMS, with a larger peak list than some examples described above. In this study, four TN and four RP lines were analyzed. As before, we show that PCA can distinguish between cell lines, but additionally the relationship between the TN and RP lines was examined, as well as between the TN lines. The differences highlighted here may be linked to future breast cancer tissue studies, where tissues are classified and treated based receptor status.

6.3 Materials and Methods

6.3.1 Cell line growth and preparation

The RP cells lines that were used in this study were MCF7, T47D, BT474, HCC1428, and the TN MDA-MB-231, BT549, HS578T and HCC1395. The cell lines are summarized in Table 6.1. All cell lines were grown in the appropriate culture media, either RPMI 1640 (Gibco, LifeSciences Technology, USA) or Dulbecco's Modified Eagle Media (DMEM, Gibco,

LifeSciences Technology, USA) supplemented with 10% fetal bovine serum (HyClone, Thermo Scientific, USA) and 1% Penicillin-Streptomycin (Gibco, LifeSciences Technology, USA). Cells were seeded onto 1 cm x 1 cm silicon chips that were previously cleaned with 2x successive sonications in dichloromethane, acetone, and methanol. The cleaned chips were dried with nitrogen and stored in a laminar flow hood until cell seeding. Prior to ToF-SIMS analysis, the silicon chips were removed from the cell growth media, briefly rinsed with 150 mM ammonium acetate [136], fixed in 4% formaldehyde for 30 minutes, then rinsed with water to remove excess buffer salts that were introduced during the fixation. The cells were dried overnight in air and analyzed the following day.

6.3.2 ToF-SIMS

ToF-SIMS experiments were performed using an ION-TOF ToF-SIMS 5-100 (ION-TOF GmbH, Münster, Germany) equipped with two ion sources. A liquid metal ion gun (LMIG) was used to generate a pulsed 25 keV Bi_3^+ beam, whereas an electron impact gun was used to generate a 20 keV C_{60}^{++} beam. Both beams hit the target at a 45° angle. The mass resolution ($m/\Delta m$) for the $C_2H_3^+$ ion was predominantly greater than 4500. Positive ion spectra were calibrated to CH_3^+, $C_2H_3^+$, $C_3H_3O^+$, $C_4H_7^+$, $C_7H_7^+$, and $C_{27}H_{45}^+$. Negative ion spectra were calibrated to CH^-, OH^-, C_2H^-, $C_{16}H_{31}O_2^-$ and $C_{18}H_{33}O_2^-$. Target currents were measured before each data set using a Faraday cup. The Bi_3^+ current was typically 0.15 pA. A Bi_3^+ dose of 5.0 x 10^{11} ions/cm^2 was used to acquire spectra that were 250 µm x 250 µm and with 128x128 pixels. A short C_{60}^{++} etching sequence was used prior to data collection to "clean" the surface of the cells as this has been previously shown to improve cell sample separation [124]. Typical C_{60}^{++} primary ion currents were between 0.5 – 1.0 nA. The C_{60}^{++} etching dose was 1.6 x10^{13} ions/cm^2. A 1.25 x 10^{13} 20 keV C_{60}^{++}/cm^2 dose density removed ~10 nm of material from

NIH/3T3 fibroblasts [154], so it is likely that a portion of the plasma membrane was removed during this 'cleaning' cycle. The C_{60} etching area was a constant 500 µm x 500 µm. Low energy electrons were flooded onto the surface of the samples to compensate for charge buildup.

6.3.3 Principal component analysis (PCA)

The data used in this study were preprocessed to put them in a form appropriate for PCA. Regions-of-interest (ROIs) were selected for each data file to exclude all areas with exposed substrate. All PCA analysis was done using the SpectraGUI (Dan Graham, NESAC/BIO, University of Washington). Peak lists were created for both positive and negative ion spectra that included all peaks whose maximum intensity was twice or more that of the average background intensity to the left and right of the peak, excluding known salt, salt adduct, inorganic and substrate peaks (as specified for each PCA figure in results section). Representative spectra from all eight cell lines were overlaid, then peaks were selected manually and integration limits for each peak were also set manually. The data were normalized to the intensities of all of the peaks in the given peak list, and then the data were square-root transformed and mean centered before PCA was applied.

6.3.4 Normalized peak intensity histograms

The normalized intensity plots were generated by dividing the intensity of the selected peak by the sum of the intensities of all of the peaks in the High Mass peak list. These values were then averaged over all of the data files for a given cell line and plotted as normalized intensities.

6.4 Results

Time-of-flight secondary ion mass spectrometry was used to generate mass spectra from eight human breast cancer cell lines. Four triple negative (TN) and four receptor positive (RP)

lines were analyzed in this study. The cell lines and their ER, PR and HER-2 receptor status are summarized in Table 6.1. PCA was used to help highlight the largest sources of variance in the spectra from the eight cell lines. For both positive and negative ion spectra two different peak lists were created for PCA analysis: “Large” and “High Mass”. The Large peak lists contained 624 peaks (positive ions) and 535 peaks (negative ions) from m/z 15 – 852. For the Large peak list, all peaks with a maximum intensity twice or greater than the average background to the left and right of the peak were selected (excluding known salt [26], salt adduct, and substrate peaks). The High Mass peak lists contained peaks from the “Large” peak list above m/z 200 resulting in 284 peaks for the positive ion list and 207 peaks for negative ion list. Peaks that were identified by the PCA analysis using the High Mass peaks lists as being a key peaks of interest are detailed in Table 6.2A (positive ions) and 6.2B (negative ions), including proposed chemical compositions and biomolecule identifications.

Table 6.1: The cell lines used in this study with ER, PR and Her2 receptor status.

	ER	PR	HER2
MCF-7	+	+	-
HCC-1428	+	+	-
BT-474	+	+	+
T47-D	+	+	-
HS-578t	-	-	-
MDA-231	-	-	-
HCC-1395	-	-	-
BT-549	-	-	-

Table 6.2A: Key positive ion m/z and fragment ID for peaks that show the largest variance in PC 1, 2 and 4.

Mass (m/z)	Composition	Possible Biomolecule	Reference
224.11	$C_8H_{19}PNO_4$	PChol. + glycerol fragment	219
237.22	$C_{16}H_{29}O$	FA, (16:0)	
263.24	$C_{18}H_{31}O$	FA, (18:1)	
311.26	$C_{19}H_{35}O_3$	MAG, (16:1)	219

313.27	**$C_{19}H_{37}O_3$**	**MAG, (16:0)**	**219**
337.27	**$C_{21}H_{37}O_3$**	**MAG, (18:2)**	
339.29	**$C_{21}H_{39}O_3$**	**MAG, (18:1)**	**219**
341.30	**$C_{21}H_{41}O_3$**	**MAG, (18:0)**	**219**
369.35	**$C_{27}H_{45}$**	**Cholesterol fragment**	**219**
495.43	**$C_{31}H_{59}O_4$**	**DAG, (28:0)**	
521.45	**$C_{33}H_{61}O_4$**	**DAG, (30:1)**	**219**
523.46	**$C_{33}H_{63}O_4$**	**DAG, 14:0 chain + 16:0 chain, (30:0)**	**219**
547.46	**$C_{35}H_{63}O_4$**	**DAG, (32:2)**	**219**
549.48	**$C_{35}H_{65}O_4$**	**DAG, (32:1)**	**219**
551.49	**$C_{35}H_{67}O_4$**	**DAG, two 16:0 chains, (32:0)**	**219**
575.49	**$C_{37}H_{67}O_4$**	**DAG, (34:2)**	**219**
577.51	**$C_{37}H_{69}O_4$**	**DAG, (34:1)**	**219**
579.53	**$C_{37}H_{71}O_4$**	**DAG, 16:0 chain + 18:0 chain, (34:0)**	
599.49	**$C_{39}H_{67}O_4$**	**DAG, (34:4)**	**219**
601.51	**$C_{39}H_{69}O_4$**	**DAG, (34:3)**	**219**
603.53	**$C_{39}H_{71}O_4$**	**DAG, (34:2)**	**219**
605.54	**$C_{39}H_{73}O_4$**	**DAG, (34:1)**	
607.55	**$C_{39}H_{75}O_4$**	**DAG, Two 18:0 chains, (36:0)**	

Table 6.2B: Key negative ion m/z and fragment ID for peaks that show the largest variance in PC 1, 2 and 3.

Mass (m/z)	Composition	Possible Biomolecule	Reference
208.07	**unknown**	**unknown**	
227.20	**$C_{14}H_{27}O_2$**	**Myristic acid, 14:0**	**123, 223**
253.22	**$C_{16}H_{29}O_2$**	**Palmitoleic acid, 16:1**	**123, 222**
255.23	**$C_{16}H_{31}O_2$**	**Palmitic acid, 16:0**	**123, 222**
259.03	**unknown**	**unknown**	
265.25	**$C_{18}H_{33}O$**	**18:0 fragment**	**123**
277.22	**$C_{18}H_{29}O_2$**	**Linolenic acid; 18:3**	**123, 222**
279.24	**$C_{18}H_{31}O_2$**	**Linoleic acid; 18:2**	**123, 222**
281.25	**$C_{18}H_{33}O_2$**	**Oleic acid; 18:1**	**123, 222**
283.26	**$C_{18}H_{35}O_2$**	**Stearic acid; 18:0**	**123, 222, 223**
299.07	**unknown**	**unknown**	
303.24	**$C_{20}H_{31}O_2$**	**Arachidonic acid; 20:4**	**222, 223**
305.25	**$C_{20}H_{33}O_2$**	**Dihomo-gamma-linolenic acid; 20:3**	**223**
307.27	**$C_{20}H_{35}O_2$**	**Eicosadienoic acid; 20:2**	**223**
309.28	**$C_{20}H_{37}O_2$**	**Eicosenoic acid; 20:1**	**223**
311.29	**$C_{20}H_{39}O_2$**	**Arachidic acid, 20:0**	
329.25	**$C_{22}H_{33}O_2$**	**Docosadienoic acid; 22:5**	
331.26	**$C_{22}H_{35}O_2$**	**Adrenic acid; 22:4**	**223**
333.27	**$C_{22}H_{37}O_2$**	**22:3**	
365.35	**unknown**	**unknown**	

385.35	**$C_{27}H_{45}O$**	**cholesterol**	**221**
393.38	**unknown**	**unknown**	
465.32	**$C_{27}H_{45}SO_4$-**	**Cholesterol Sulfate**	**80, 224**

6.4.1 Comparison of TN and RP cell lines using positive ions

PCA was used to explore the mass spectral variations between all eight breast cancer cell lines and identify the key species which produced with these variations. Principal component (PC) scores plots generated using the Positive Ion with the High Mass peak list is shown in Figure 6.1. In the PC1 vs. PC2 scores plot (top left), the four TN cell lines data (red symbols) predominantly separated from one another, with some overlap of the 95% confidence limits (circles around the symbols) of the MDA-MB-231 and BT549 cell lines. There was significantly more overlap among the RP cell lines data (gray and black symbols).

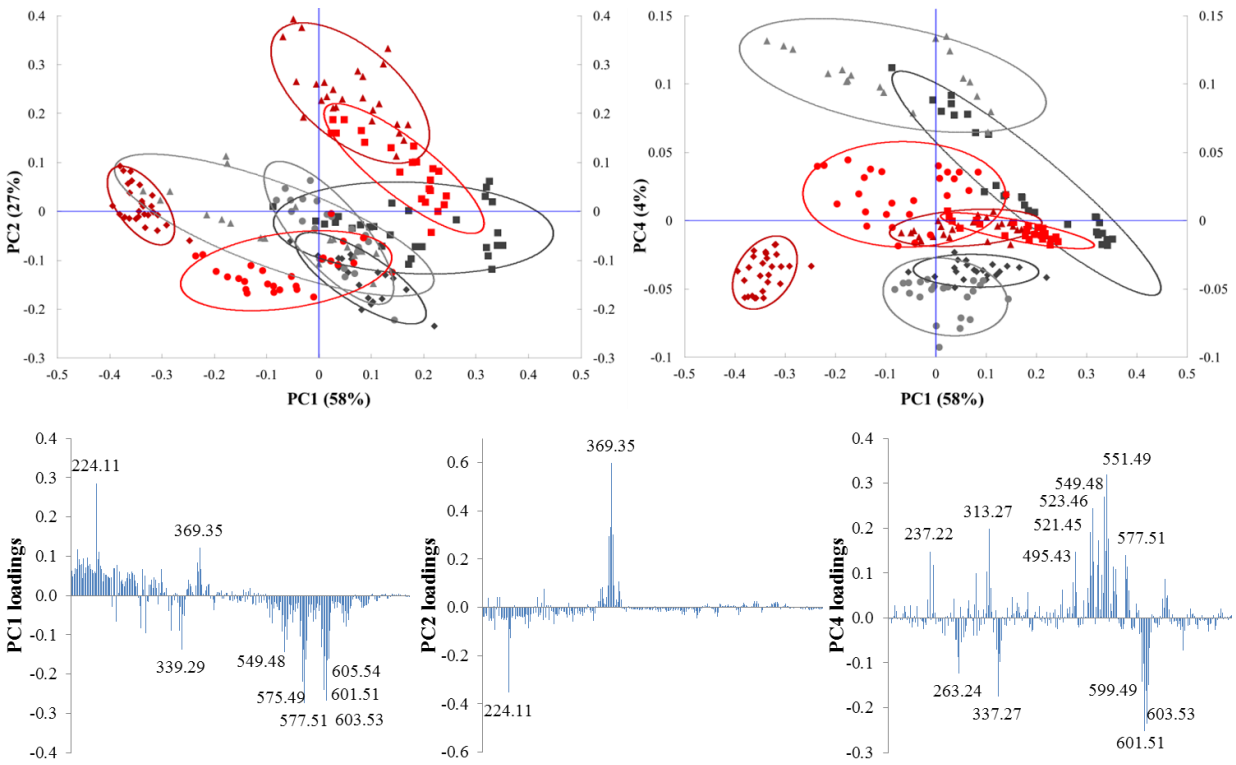

Figure 1. PCA of eight breast cancer cell lines using the High Mass peak list. Positive ions were used. (Top left) The PC 1 vs. PC 2 scores plot. The TN cell lines are colored with red and the RP cell lines are gray. (Top right) The PC 1 vs. PC 4 scores plot. The TN cell lines are colored with red and the RP cell lines are gray. (Bottom left) The loading plot for PC 1. (Bottom middle) The loading plot for PC 2. (Bottom right) The loading plot for PC 4. The cell lines are plotted with the following symbols: ■ MDA-MB-231, ▲ BT549, ● HCC1395, ♦ HS578t, ■ T47D, ▲ BT474, ♦ MCF7, ● HCC1428.

Across PC 1 (58% of the total variance) the MDA-MB-231 and most of the BT549 data points had positive scores on PC1. The phospholipid fragment (phosphocholine + C_3H_4), referred to here as Pchol. (m/z 224^+), and the cholesterol fragment (m/z 369^+) had the highest loadings in the positive direction (Figure 6.1, bottom left). All of the HS578t, and a majority of the HCC1395 spots had negative scores for PC 1, where MAGs and DAGs (m/z 339^+, 549^+, 575^+, 577^+, 601^+, 603^+, 605^+) had the highest negative loads. Specific peak identifications can be found in Table 2A which summarizes the higher loading peaks (both positive and negative loads) for the positive ion spectra.

Across PC2 (27% of the total variance), the BT549 and most of the MDA-MB231 spots had positive scores loading primarily with cholesterol which was the most significant peak in the PC2 positive loads. All of the TN HCC1395 and RP MCF7 spots had negative scores. A majority of the spots of the other three RP lines also had negative scores, although a small number from each line had positive values. Pchol. was the most significant peak in the PC2 negative loads. The HS578t line had several spots with positive scores and several spots with negative scores in PC2 putting it, on average across the center line in PC2. An ongoing area of research is the sub-classification of TN breast cancers [192-194]. In one study, TN breast tumors were classified into six different TN subtypes using gene expression analysis, and TN cell lines were found that are representative of the subtypes. The MDA-MB-231, HS578t and BT549 cell lines were identified within the "mesenchymal-like" subgroup of TN lines, while the HCC1395

line was unclassified [194]. The separation of the TN cell types across PC 2 matches the classifications of these cell lines by Lehmann *et al.* [194]

While PC1 and PC2 were useful in separating out chemical differences between the TN cell lines (cholesterol and Pchol vs. DAGs and MAGs for PC1, and cholesterol vs. Pchol for PC2), the RP cell lines were not separated well from one another using the first two PCs. They were best distinguished from one another along PC4 (4 % of total variance) when the High Mass peak list was applied. The scores plot of PC1 vs. PC4 is shown in Figure 6.1 (top right), along with the loading plot for PC4 (Figure 1, bottom right). The positive PC4 loadings were dominated by MAG and DAG fragments with very little contribution from the Pchol and cholesterol peaks. The RP BT474 and most of the T47D spots had positive scores on PC4. There was large amount of variance in the BT474 and T47D data, potentially caused by biological factors between the cells on different days of analysis, or an unintended variation in data acquisition parameters. MAG and DAG fragments containing tails with 16-carbon length or less (m/z 237^+, 313^+, 495^+, 521^+, 523^+, 549^+, 551^+, 577^+) had high loads in the positive direction (see Table 2A for fragment identification). The HCC1428 and MCF7 lines had negative scores on PC4, where the major contribution to the negative loadings were from MAG and DAG fragments containing only unsaturated 18-carbon tails (m/z 263^+, 337^+, 599^+, 601^+, 603^+). The TN HS578t spots also all had negative scores on PC4. The TN BT549 and MDA-MB-231 spots had slightly negative scores while a majority of the HCC1395 spots had positive scores.

While separation between the cell lines appears more obvious using the Positive Ion High Mass peak list, there is still some separation of the lines when including the lower molecular weight ions. The PC1 vs. PC2 scores plot, generated using the Positive Ion Large peak list, is shown in Figure S.6.1. As in Figure 6.1, the TN lines largely separated from one another while

the RP lines did not. The PC1 and PC2 loading plots are shown in S.6.1B and C, where Pchol. species had high loadings on PC1, and cholesterol and DAGs had high loadings on PC2. However, below m/z 200 there are many Pchol related fragments as well as proteins (see Table S.6.1 for identification). There are also numerous hydrocarbon fragments that may be related to different phospholipids, MAGs, DAGs, TAGs, or cholesterol. Some interesting information can be gleaned from the PCA using the Positive Ion Large peak list. However, since many of the lower mass peaks are not chemically specific (e.g. can be due to cholesterol or DAG), peaks identified in the High Mass peak lists, both positive and negative, were the focus of the remainder of the analysis discussed below.

6.4.2 Normalized peak intensities (positive ions)

To help clarify the contributions of specific molecular species to chemical differences found for the cell lines using PCA methods, the normalized intensities of the key peaks that were identified by PCA are plotted in Figure 6.2A (and Supplemental Figure S.6.2). The histograms shown in Figure 6.2A are of Pchol (top left, m/z 224^{+}), cholesterol (top right, m/z 369^{+}), DAG 32:0 (bottom left, m/z 551^{+}) and DAG 36:3 (bottom right, m/z 601^{+}). These peaks had the highest loading in PC2 (Pchol and cholesterol) and PC 4 (DAG 32:0 and DAG 36:3). As seen in Figure 6.2, they also displayed distinct intensity for different cell lines. \

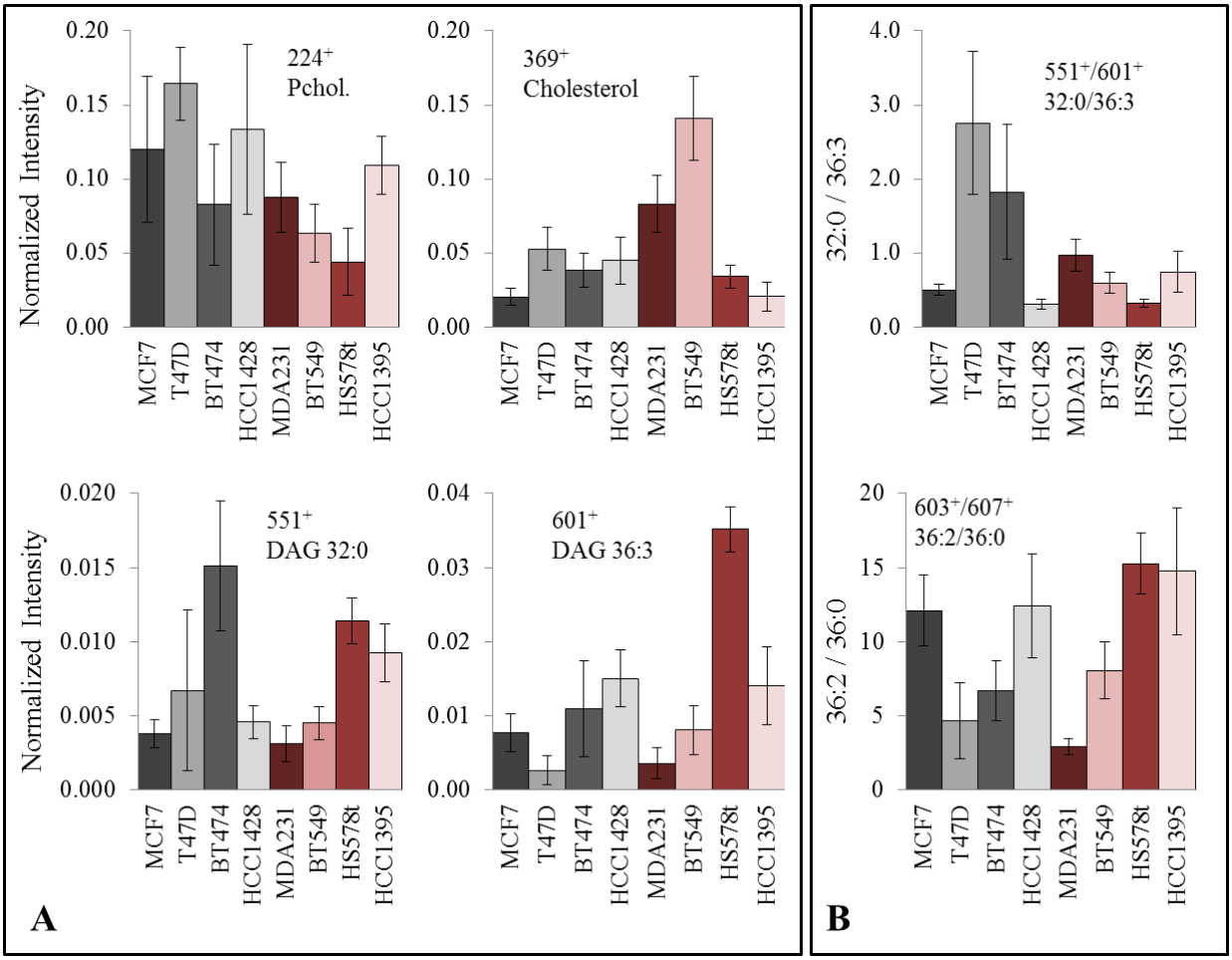

Figure 6.2. (A) Normalized intensities of selected positively charged ions. The species shown are (top left) Pchol. fragment, m/z 224^+ (top right) cholesterol, m/z 369^+ (bottom left) DAG 32:0, m/z 551^+ and (bottom right) DAG 36:3, m/z 601^+. (B) An average of the ratio of the intensities of (top) $551^+/601^+$ and (bottom) $603^+/607^+$ (m/z 603^+ represents DAG 36:2 and 607^+ represents DAG 36:0). The TN cell lines are colored red and the RP cell lines are gray. All intensities were normalized by the sum of the intensities of all of the peaks in the High Mass peak list.

The normalized intensities for the cholesterol fragment are plotted in Figure 6.2A (top right). The BT549 line had the highest relative intensities of cholesterol. In contrast the MCF7 lines had one of the lowest normalized cholesterol intensities. This is consistent with the loads identified in PC2 of Figure 6.1 where BT549 had the most positive scores (loading with cholesterol) and the MCF7 had among the most negative scores (consistent with that line having potentially less cholesterol). However, not all of the relative intensity histograms will have

obvious correlations with the PCA since PCA scores are due to a combination of information. For example cell lines with negative scores in PC2 may have more Pchol. than the lines with positive scores instead of just less cholesterol. The histogram of the normalized Pchol. intensities (6.2A, top left) can help clarify this difference. As can be seen from this histogram, the Pchol intensities overlap for many of the cell lines (within standard deviation). However, it can be see that the T47D line has a significantly higher value compared to the BT549 and HS578t lines.

The normalized intensities of the DAG 32:0 (two saturated 16-carbon alkyl tails) and DAG 36:3 (three total saturated bonds in the two alkyl tails) are shown in Figure 6.2A (bottom left and right, respectively). The intensity patterns for these two lipids are different between the cell lines, an indication that the cell lines have unique contributions from DAGs that contain alkyl tails of varying length and saturation levels. The BT474, HS578t and HCC1395 lines had high intensities of DAG 32:0. For DAG 36:3 the HS578t line had a much higher intensity any of the other lines. The DAG fragments may have originated from TAG parent molecules [123, 219, 220], but in other experiments were not correlated to TAGs [221].

Variations between the peak intensities of the DAG species with different alkyl tails chain lengths and saturation levels can also be visualized by plotting the average of the ratios of the intensities of particular species. The average of the ratios of DAG 32:0 / 36:3 is plotted in Figure 6.2B (top). A high value indicates more DAG species with saturated 16-carbon tails compared to unsaturated 18-carbon tails. The T47D and BT474 lines had the highest values, whereas the MCF7, HCC1428 and HS578t lines had the lowest. These values correlate well with the PC4 scores plot in Figure 6.1, where the T47D and BT474 data points had positive scores and the MCF7, HCC1428 and HS578t data points had negative scores. The DAG 32:0

and DAG 36:3 had the highest positive and negative loading (m/z 551^+ and 601^+ respectively) and thus are likely strong contributors to the scores explaining the good correlation.

In contrast to the DAG 32:0 / 36:3 ratio, which compared two DAGs with a different chain length and saturation level, the ratio of the intensities of DAG 36:2 / 36:0 (same chain length, different saturation levels) is shown in Figure 6.2B (bottom). The histograms for DAG 36:2 and DAG 36:0 individually are in Figure S.6.2. While the DAG 36:0 peak (m/z 607) did not have a large load in the positive PCs (PC1 – 4), unsaturated analogues (DAGs 36:2, 36:3, and 36:4) were all identified as having large loads in PC1 and PC4. It is interesting to compare the ratio of saturated vs. unsaturated species by following the ratio of the DAG 36:0 / 36:2. The histogram of these ratios shows that two of the TN lines (HS578t and HCC1395) had higher amounts of the unsaturated DAG as well as the RP MCF 7 and HCC1428 lines. Similar ratios for DAG 32:0 / 36:0, 32:1 / 32:0, and MAG 16:0 / 18:0 are shown in Figure S.6.2 in supplemental data. Each of the trends from the ratio of different DAGs is unique and emphasizes that each of these cell lines have unique lipid compositions.

The intensities of the 16:1, 16:0, 18:2, 18:1 and 18:0 MAG fragments (m/z 311^+, 313^+, 337^+, 339^+ and 341^+) are plotted in Figure S.6.2 in supplemental data. Many of the MAG fragments may have originated from a DAG parent molecule, or even that the MAG and DAG fragments originated from a common TAG molecule. This origin of the MAG fragment from the breakdown of DAGs and TAGs has been hypothesized previously in ToF-SIMS experiments [123]. Examples of this can be seen from the intensity patterns of saturated tails, such as MAG 16:0 (313^+) compared to DAG 32:0 (551^+).

6.4.3 Comparison of TN and RP cell lines using negative ions

Negative ion mass spectra were also collected from each of the cell lines. Whereas the scores plot of all eight lines and the Large peak list with positive ions (Figure S.6.1) showed some separations, especially between the TN lines, there was no clear separation between the cell lines when the Large peak list with negative ions was used (data now shown). However, using the Negative Ion High Mass peak list there was significant separation between the cell lines. The scores plot of PC1 vs. PC2 using the Negative Ion High Mass peak list is shown in Figure 6.3 (top left). The BT549, HCC1395 and HS578t spots had positively scores on PC1 (46% of the total variance). The MDA-MB-231 spots had scores in the negative direction of PC. However, in general all of the cell lines showed a broad spread across PC1 and the RP lines had both positively loading spots and negatively loading spots. Better separation in the cells lines was found in the PC2 and PC3.

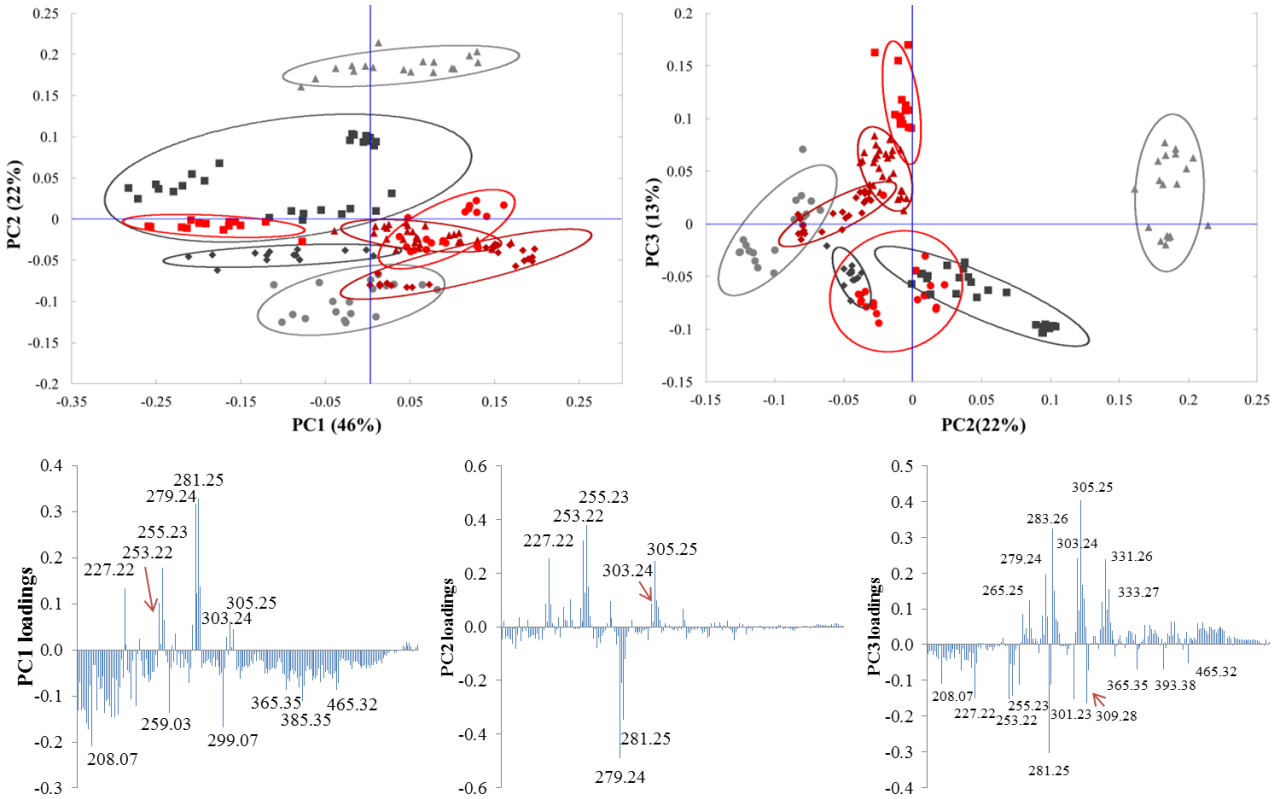

Figure 6.3. PCA of eight breast cancer cell lines using the High Mass peak list and negative ions. (Top left) The PC 1 vs. PC 2 scores plot. The TN cell lines are colored red and the RP cell

lines are gray. (Top right) The PC 2 vs. PC 3 scores plot. The TN cell lines are colored red and the RP cell lines are gray. (Bottom left) The loading plot for PC 1. (Bottom middle) The loading plot for PC 2. (Bottom right) The loading plot for PC 3. The cell lines are plotted with the following symbols: ■ MDA-MB-231, ▲ BT549, ● HCC1395, ♦ HS578t, ■ T47D, ▲ BT474, ♦ MCF7, ● HCC1428.

The scores plot of PC2 vs. PC3 is shown in Figure 6.3 (top right). PC2 (22% of the total variance) mostly separated the RP lines from one another based on the length of fatty acids. The BT474 and T47D lines had spots with positive scores, where the 14 and 16-carbon FA species (14:0, m/z 227^-; 16:1, m/z 253^-; 16:0, m/z 255^-) had high positive loadings (Figure 6.3, bottom middle), as did the 20:4 and 20:3 FA fragments at m/z 303^- [222] and 305^- [223]. The 18:2 and 18:1 FA species (18:2, m/z 279^-; 18:1, m/z 281^-) had the largest negative loadings for PC2.

The TN lines were better separated on PC3 (13% of the total variance) with loading that depended on FA saturation and length. The MDA-MB-231 and BT549 spots had positive scores. The fragments with the highest positive loadings (Figure 3, bottom right) were the 18:0 (m/z 283^-) and 18:2 fatty acids, as well as the unsaturated 20:3 and 20:4 fragments. The ions at m/z 333^-, 331^- also had high positive loadings and may be related to 22:3, 22:4 [223, 224], however these are tentative identifications. The spots of the TN HCC1395 line and RP MCF7 and T47D lines had negative scores where the 18:1 FA had the highest negative loading. The 14:0, 16:1 and 16:0, 20:1 and 20:5 FAs also had high negative loadings. The m/z 465^- fragment, tentatively identified as cholesterol sulfate [78, 225], had a weak negative loading, along with the unidentified peaks at m/z 208^-, 365^- and 393^-. Interestingly, the m/z 385^- cholesterol fragment had a weak positive loading (not labeled), while cholesterol sulfate loaded in the opposite direction. In other ToF-SIMS imaging experiments, these two molecules did not co-locate on tissue samples from patients with Fabry disease [78].

6.4.4 Normalized peak intensities (negative ions)

The normalized intensities of selected negatively charged ions are shown in Figure 6.4A (and Supplemental Figure S.6.3). Many of the fragments attributed to FAs displayed distinct intensity patterns, an indication that the cell lines contained unique contributions from these species. For 16:0 (6.4A, top left), the RP T47D and BT474 lines had higher intensities than the other two RP lines. Among the TN lines, MDA-MB-231 was lower than the other TN lines. Average normalized intensities of FA 18:1 (Figure 6.4A, top right) and 18:0 (6.4A, bottom left) are also shown. Obvious trends can be seen such as the MDA-MB-231 line displayed lowest intensity of 18:1 and the highest intensity of 18:0. Some of these trends can be emphasized by looking at a ratio of the fragments (such as saturated vs. unsaturated 18:1/18:0 ratio (6.4B, bottom). Here the MDA231 line clearly shows the lowest ratio of 18:1/18:0 FAs. In contrast, the HCC1395 line can also be more easily seen to have the highest 18:1/18:0 ratio. Similarly another interesting comparison is the FA 18:2 / 18:1 ratio (6.44A, top right) which better illustrates the average normalized intensity differences between these two different saturated fragments. The TN MDA231, BT549, and HS578t lines had a higher value for this ratio along with the RP HCC1428 line.

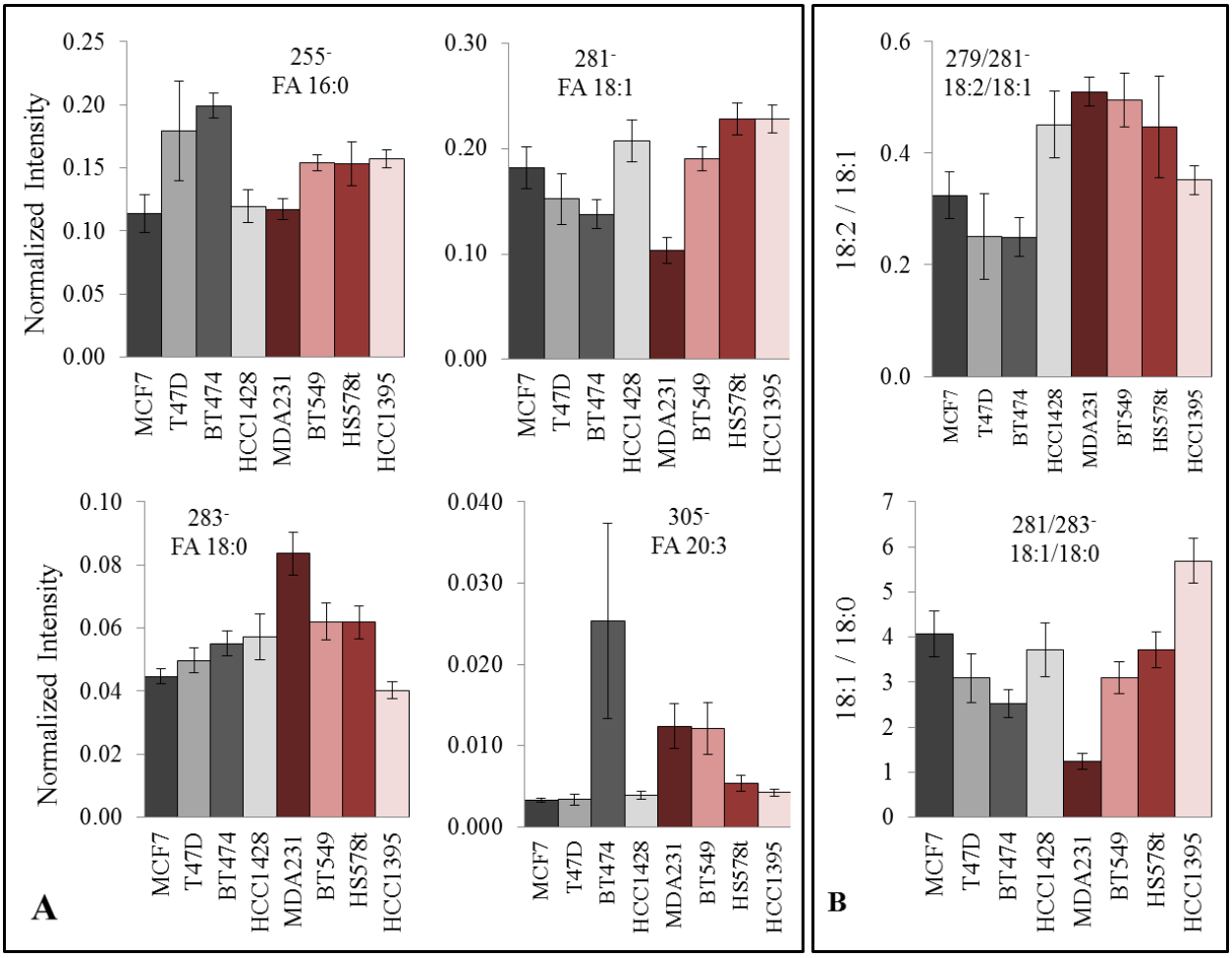

Figure 6.4. (A) Normalized intensities of selected negatively charged ions. The species shown are (top left) FA 16:0, m/z 255^- (top right) FA 18:1, m/z 281^- (bottom left) FA 18:0, m/z 283^- and (bottom right) FA 20:3, m/z 305^-. (B) An average of the ratio of the intensities of (top) $279^-/281^-$ and (bottom) $281^-/283^-$. The TN cell lines are colored red and the RP cell lines are gray. All intensities were normalized by the sum of the intensities of all of the peaks in the High Mass peak list.

The FA 20:3 (Figure 6.4A, bottom right) species showed a unique intensity pattern compared to the 16- and 18-carbon FAs. Two of the four TN lines and the RP BT474 line had the highest values. Additionally, the normalized intensities of the 20:5, 20:4, 20:2, 20:1 and 20:0 fatty acids are shown in Figure S.3 (m/z , 305^-, 307^-, 309^-, 311^-) many with unique patterns. These 20-carbon species had high loadings in PCs 2 and 3 (Figure 3).The intensity pattern of the

18:3 fatty acid (m/z 277$^-$) and cholesterol sulfate fragments are shown in S.3. For cholesterol sulfate, the intensity pattern is different compared to the non-sulfate cholesterol (Figure 2).The negative secondary ion data suggest that fatty acid metabolism, particularly focused on elongation and saturations pathways [226] , are varied between the cell lines.

6.5 Conclusion

Eight human breast cancer cell lines were compared with ToF-SIMS and PCA. Many of the cell lines were successfully distinguished from one another. The TN cell lines displayed the largest separation when positive ions were used, whereas the RP lines showed much less. PCA identified phospholipids, cholesterol, fatty acids, MAGs and DAGs as the largest sources of variance that caused the separations of the cell lines from another. Both the length and saturation levels of fatty acids and akyl tails of MAGs and DAGs were sources of variance. The differences in the normalized intensities of the key secondary ions identified by indicate variations in lipid metabolism. Using positive secondary ions, some separation was achieved when a peak list with the mass range m/z 15-852 was used. No separation was achieved using negative secondary ions and a peak list with a similar mass range. When the peak list was truncated to m/z 200 – 852, a better separation was produced for both positive and negative secondary ion data.

Acknowledgements

This research was supported by NIH grants CA1-38293 and EB-002027.

6.6 Supporting Information

Chemical Analysis of eight human breast cancer cell lines with ToF-SIMS

Michael A. Robinson[1,2], Fionnuala Morrish[3], David Hockenbery[3], Lara Gamble[1,4§]

National ESCA and Surface Analysis Center for Biomedical Problems[1], Departments of Chemical Engineering[2] and Bioengineering[4], University of Washington, Seattle, WA, 98195

Clinical Research Division[3], Fred Hutchinson Cancer Research Center, Seattle, WA, 98109

[§]Corresponding Author:

Lara Gamble

1-206-616-4173 (phone)

1-206-543-3778 (fax)

lgamble@uw.edu (e-mail)

Keywords: ToF-SIMS, cells, breast cancer, lipid, metabolism, triple negative, PCA

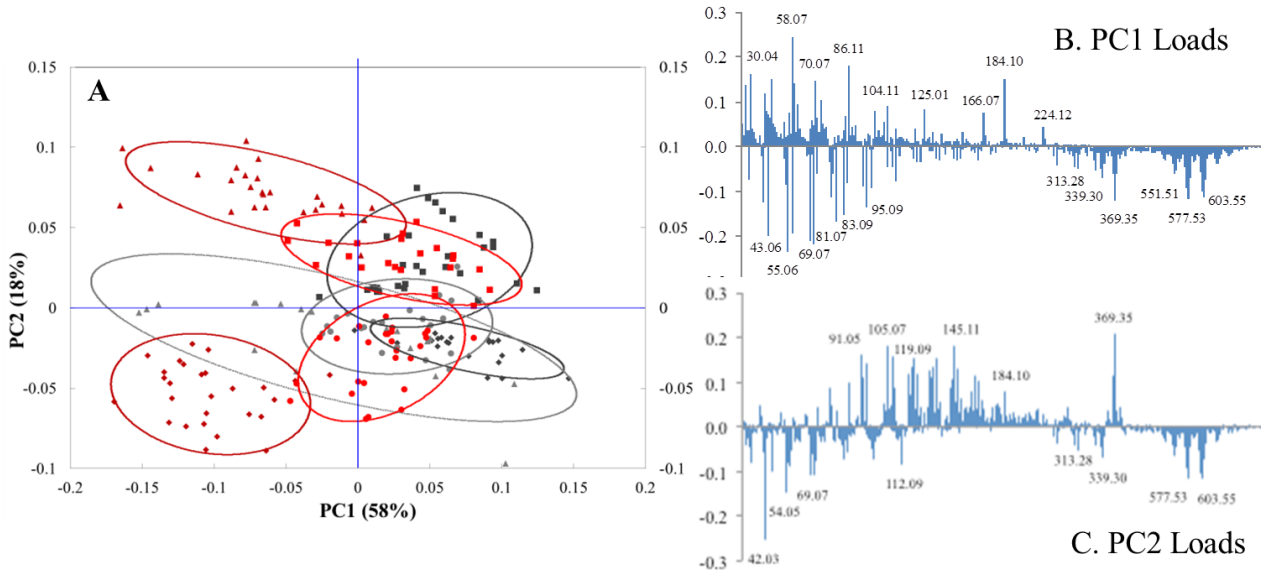

Figure S.6.1. PCA of eight breast cancer cell lines using the Large Positive Ion peak list. (A) PC 1 vs. PC 2 scores plot. The TN cell lines are colored with red and the RP cell lines are gray. (B) Loadings plot for PC 1. (C) Loadings plot for PC 2. The cell lines are plotted with the following symbols: ■ MDA-MB-231, ▲ BT549, ● HCC1395, ♦ HS578t, ■ T47D, ▲ BT474, ♦ MCF7, ● HCC1428.

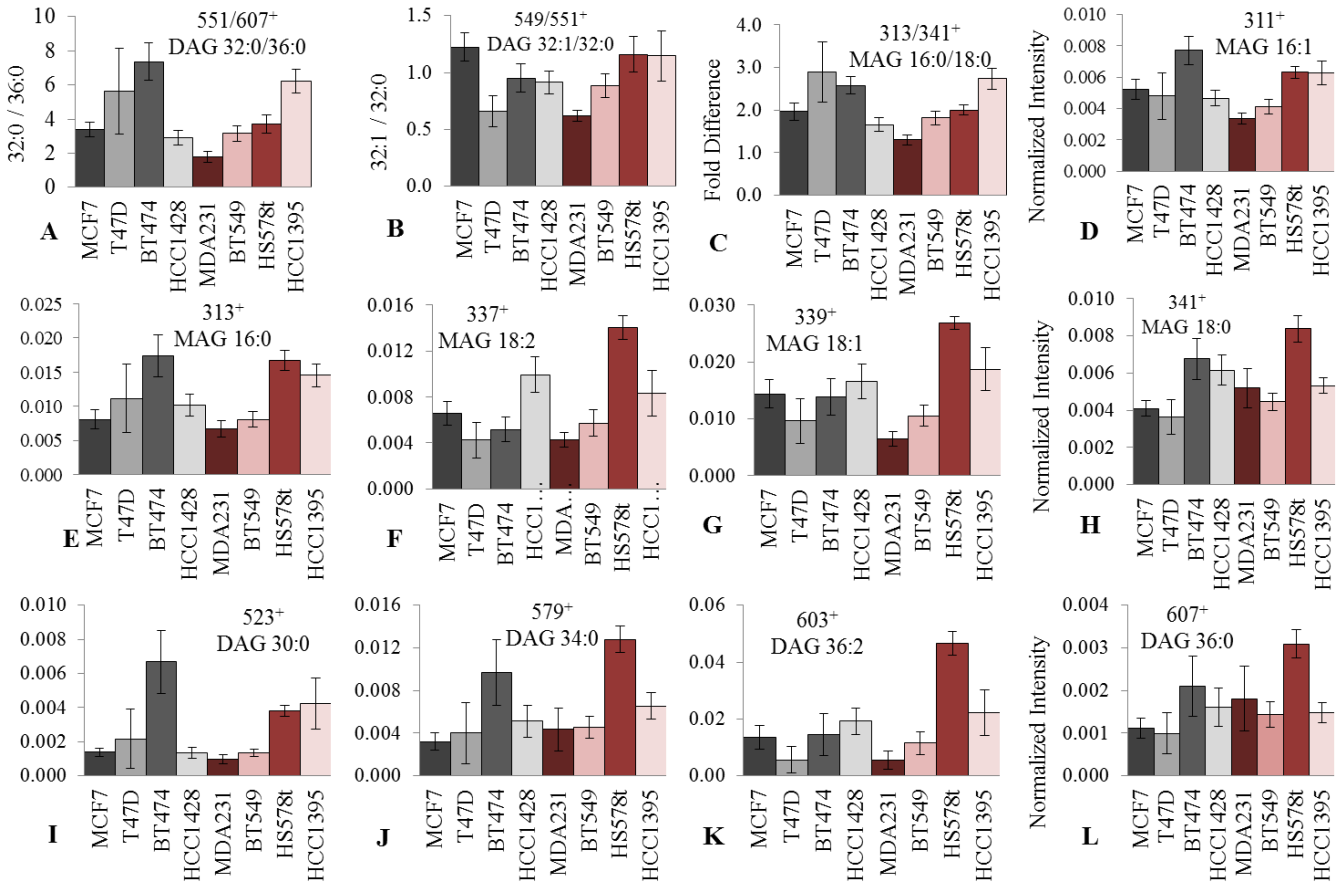

Figure S.6.2. Normalized intensities of selected positively charged ions. The species shown are (A) An average of the ratio of the intensities of $551^{+}/607^{+}$ (B) An average of the ratio of the intensities of $549^{+}/551^{+}$ (C) An average of the ratio of the intensities of $313^{+}/341^{+}$ (D) MAG 16:1, m/z 311^{+} (E) MAG 16:0, 313^{+} (F) MAG 18:2, 337^{+} (G) MAG 18:1, 339^{+} (H) MAG 18:0, 341^{+} (I) DAG 28:0, 523^{+} (J) DAG 34:0, 579^{+} (K) DAG 36:2, m/z 603^{+} and (L) DAG 36:0, 607^{+}. The TN cell lines are colored red and the RP cell lines are gray. All intensities were normalized by the sum of the intensities of all of the peaks in the High Mass peak list.

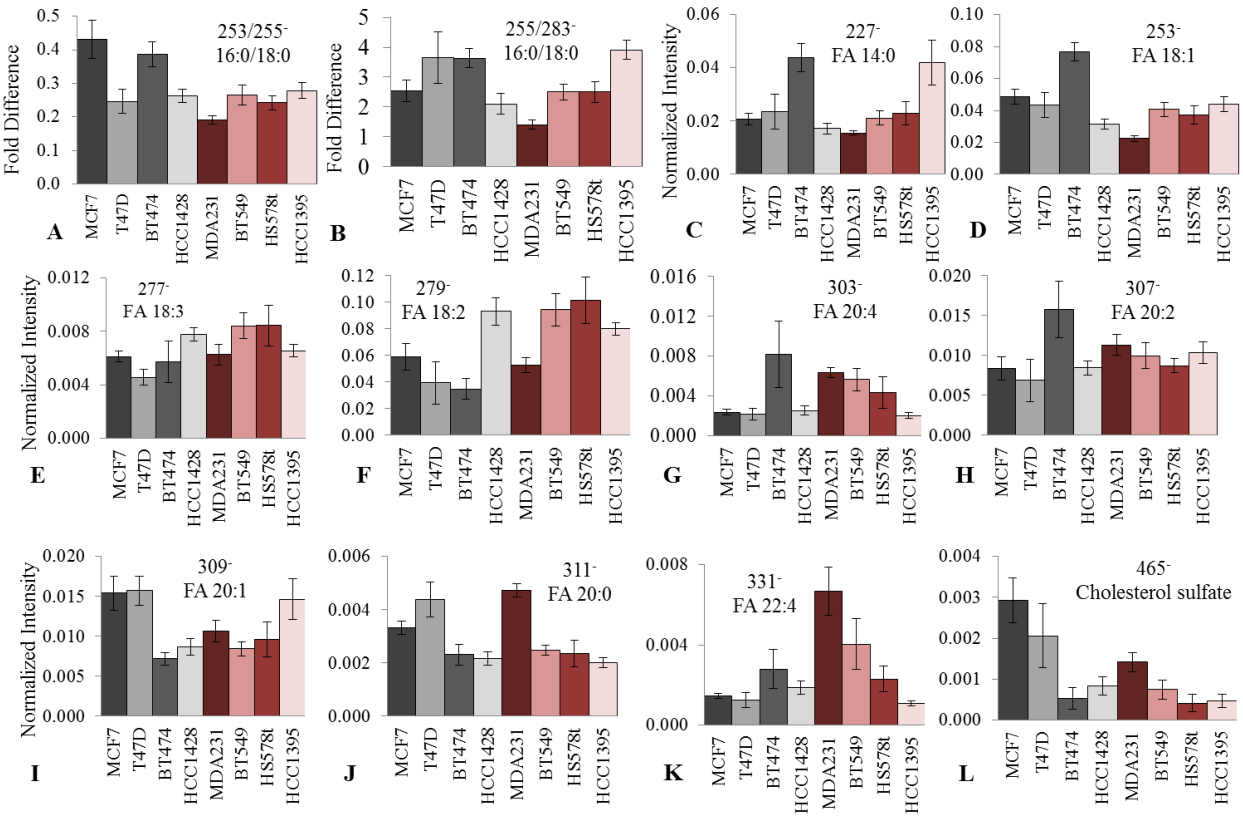

Figure S.6.3. Normalized intensities of selected negatively charged ions. The species shown are (A) An average of the ratio of the intensities of $253^-/255^-$ (B) An average of the ratio of the intensities of $279^-/281^-$ (C) FA 14:0, m/z 227^- (D) FA 16:1, m/z 253^- (E) FA 18:3, m/z 277^- (F) FA 18:2, m/z 279^- (G) FA 20:4, m/z 303^- (H) FA 20:2, m/z 307^- (I) FA 20:1, m/z 309^- (J) FA 20:0, m/z 311^- (K) FA 22:4, m/z 331^- and (L) Cholesterol sulfate, m/z 465^-. The TN cell lines are colored red and the RP cell lines are gray. All intensities were normalized by the sum of the intensities of all of the peaks in the High Mass peak list.

7. Analysis of Breast Cancer Tumors with ToF-SIMS

Michael Robinson[1,2], Blake Bluestein[1,3], Peggy Porter[4], Lara Gamble[1,3]

[1]National ESCA and Surface Analysis Center for Biomedical Problems,

Departments of Chemical Engineering[2] and Bioengineering[3], University of Washington, Seattle, WA 98195

[4]Fred Hutchison Cancer Research Center

[§]Corresponding Author:

Lara Gamble

National ESCA and Surface Analysis Center for Biomedical Problems

Department of Bioengineering

Box 351750

Seattle, WA 98195

1-206-543-8094 (phone)

1-206-543-3778 (fax)

lgamble@uw.edu (e-mail)

7.1 Abstract

Breast cancer is a hetergeneous malignincy whose mechanisms are not fully understood. Previous work has established a link beteween glucose metabolism/perfusion and chemotherapeutic resistance. In this work, ToF-SIMS imaging was applied to samples from four separate tumor tissues. Data was acquired from multiple samples from two tissue blocks to establish the repeatability of the results. For one tissue block, the two samples provided very similar results. Principal component analysis (PCA) was applied in two different capacities: first it was applied to the spectral data obtained from the tissues, and second it was applied to the image data. The four tissue blocks were successfully distinguished from another using PCA, for both positive and negative secondary ions. Imaging PCA revealed several domains on the tissue surface, several of which were identifiable in the hemotoxylin and eosin (H&E) stained adjecent tissue slice. Imaging PCA also revealed several domains that were not visible in the H&E stained sections. Unique fatty acid distributions were observed for each of the four tissue blocks that may relate to tumor phenotype and chemotherapeutic resistance.

7.2 Introduction

The mechanisms underlying breast cancer onset [227], progression [228], metabolism [229] and chemoresistance [230] are not fully understood. An important link between glucose metabolism, perfusion and neo-adjuvant chemotherapy resistance in breast cancer tumors was established using dynamic kinetic positron emission tomography (PET) imaging with ^{15}O-H_2O and ^{18}F-fluorodeoxyglucose (FDG) [183-185]. A perfusion/glucose metabolism mismatch, i.e. increased glucose consumption with respect to blood flow, was displayed often in resistant tumors, and perfusion was generally not diminished in the resistant tumors. It was hypothesized that resistance tumors, those that displayed the perfusion/metabolism mismatch, utilized alternate metabolic pathways to satisfy the energetic needs of the tumor, labeled "metabolic flexibility". It was also hypothesized that tumor phenotype is connected to the perfusion/metabolism mismatch; that it is more severe in triple negative (TN) tumors compared to those that express estrogen receptor (ER) or overexpress human epidural growth factor receptor 2 (HER2).

To better understand the link between chemoresistance, metabolism and tumor phenotype, ToF-SIMS chemical imaging was employed. Typical histological techniques provide a great deal of information about the tumor but are insufficient to gain a full understanding. A recent ToF-SIMS imaging study examined multicellular tumor spheroids (MTSs), and found that the hypoxic cores were chemically distinct from the outer oxygenated layer [209]. Another study showed that differing the doxorubicin dosages on MTSs altered the mass spectra obtained from the hypoxic regions identified by principal component analysis (PCA), providing insight into the metabolic response to chemotherapy [210]. A third reviewed ToF-SIMS imaging of metabolites in cells and tissues [211]. PCA was recently applied to help interpret the data

acquired from a large area analysis of normal and osteoarthritic cartilage tissue. Unique lipid profiles were determined that distinguished the healthy tissue from the arthritic tissue [231].

The objective of the Seattle Breast Cancer Specialized Project of Research Excellence (SPORE) is to positively impact breast cancer prevention, detection and care of women with the disease. The work presented here is within a projectthe goal to predict poor prognosis and poor response to neoadjuvant chemotherapy, using the framework of metabolic flexibility. The goal of this work continues to be to determine if the information obtained from ToF-SIMS spectra acquired from breast cancer tumors could be linked to differences in metabolic processes, specifically those involved in neoadjuvant chemotherapy resistance. The ToF-SIMS information, combined with gene expression array analysis, and PET and MRI imaging may be used to help predict chemotherapeutic resistance and more fully understand its underlying mechanisms.

7.3 Materials and methods

7.3.1 Tissue preparation

Slices of human breast cancer tumor tissues were cut at the Fred Hutchison Cancer Research Center (FHCRC) and transported to the University of Washington for analysis with ToF-SIMS. The time from cutting to analysis was not more than 90 minutes for any sample.

Tissues slices were cut from tissue blocks that were embedded in optimum cutting temperature (OCT) compound, cryopreserved using liquid nitrogen (LN_2) and stored in a -80 °C freezer. The blocks were removed from the freezer and sectioned inside of a cryostat-microtome held at -23 °C. Five µm thick slices were cut and placed onto 1 cm x 1 cm silicon chips that were previously cleaned with 2x successive sonications in dichloromethane, acetone, and

methanol. The silicon chips were placed in a petri dish and transported to the ToF-SIMS where the data were immediately acquired.

7.3.2 ToF-SIMS

ToF-SIMS experiments were performed using an ION-TOF TOF.SIMS 5-100 (ION-TOF GmbH, Münster, Germany) equipped with two ion sources. A liquid metal ion gun (LMIG) was used to generate a pulsed 25 keV Bi_3^+ beam, whereas an electron impact gun was used to generate a 20 keV C_{60}^{++} beam. Both beams hit the target at an angle of 45°. A high mass resolution (HMR) mode was used to acquire spectra in the positive and negative ion modes. The mass resolution (m/Δm) for the $C_2H_3^+$ ion was predominantly greater than 4500 and the spatial resolution was five µm. Positive ion spectra were calibrated to CH_3^+, $C_2H_3^+$, $C_3H_3O^+$, $C_4H_7^+$, $C_7H_7^+$ and $C_{27}H_{45}^+$. Negative ion spectra were calibrated to CH^-, OH^-, C_2H^-, $C_{16}H_{31}O_2^-$ and $C_{18}H_{33}O_2^-$. Target currents were measured before the acquisition of each data set using a Faraday cup. The Bi_3^+ current in the HMR was set to 0.15 pA. A high spatial resolution (HSR) imaging mode was used to acquire images with submicron spatial resolution [201]. The HSR had nominal mass resolution and a primary ion current of 0.05 pA. Low energy electrons were flooded onto the samples to compensate for any charge buildup.

Spectra were acquired from several 1 mm x 1 mm "patches" on each tissue, the positions of which are shown in Figure 7.1. Each patch contained 25 200 µm x 200 µm "tiles". On one particular tissue slice, the patches were 1.2 mm x 1.2 mm and contained 36 200 µm x 200 µm tiles. The Bi_3^+ dose was limited to 5.0 x 10^{11} ions/cm^2 for each tile in both the positive and negative ion modes, thus a total Bi_3^+ dose of 1 x 10^{12} ions/cm^2 was reached for each tile. All tiles had 256 x 256 pixels, giving the patches a total pixel count of 1280 x 1280. The patches

that measured 1.2 mm x 1.2 mm (only one tissue slice) contained 1536 x 1536 pixels. In all cases, HMR positive ion data was acquired followed immediately by HMR negative ion data on the same area. X and Y coordinates were saved in the software to ensure that data from the same area were acquired for positive and negative ions. There were some slight differences in the position of the areas when positive and negative ions were collected, but these were not greater than ~20 μm. Once the negative ion data was acquired, positive ion data from a new patch was acquired. HSR resolution images were obtained from each patch after all HMR spectra were finished.

The SurfaceLab 6 software (ION-TOF GmbH, Münster, Germany) was used for all analyses.

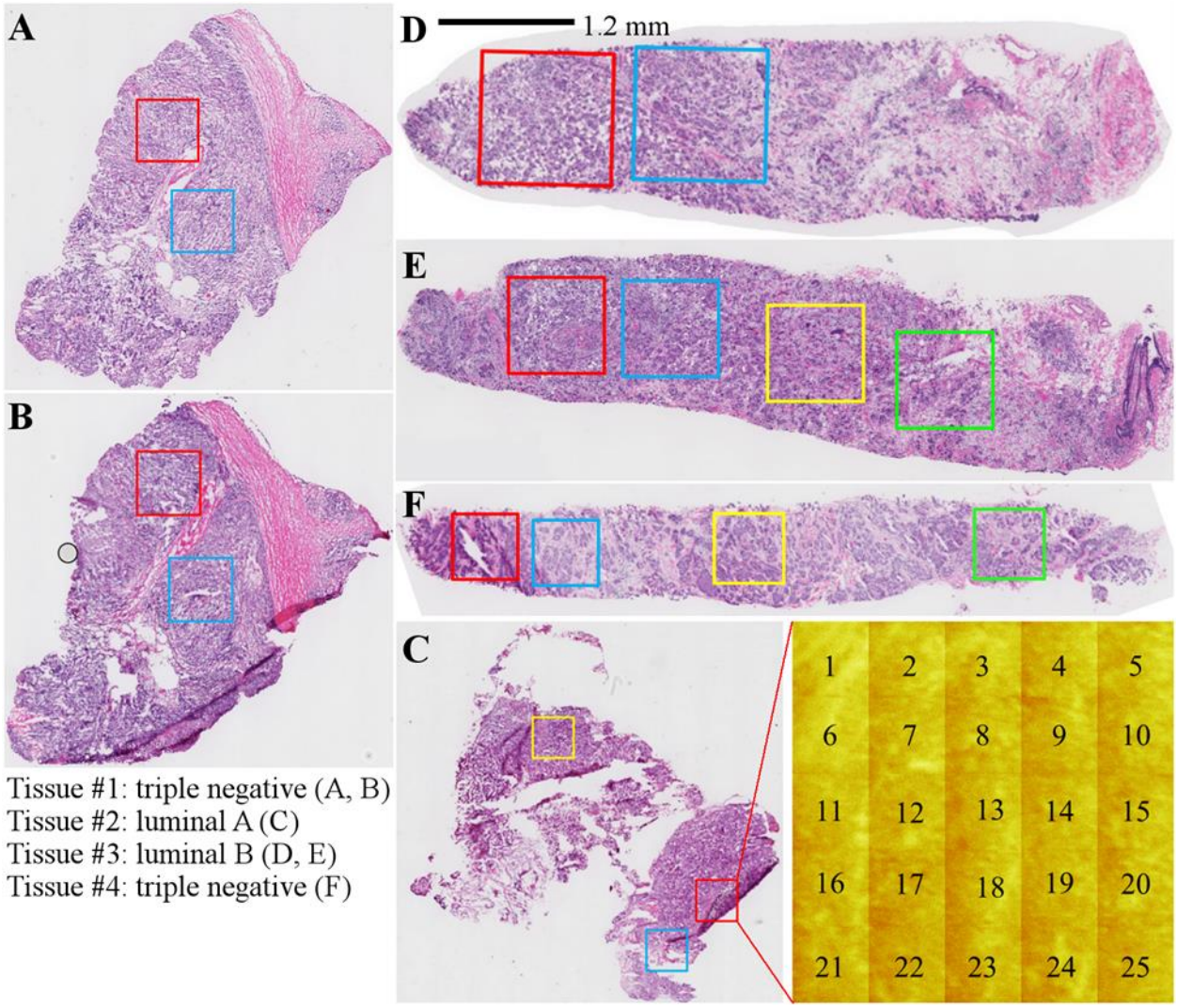

Figure 7.1 (A-F) Optical images of the H&E stained tissue slices that were used in this work. The H&E images and ToF-SIMS data were adjacent sections. The boxes represent the patches where data was acquired, where the colors represent the order the data was acquired. In order from first to last: red, blue, yellow, green. All analysis patches were 1 mm x 1 mm except those in D, which measured 1.2 mm x 1.2 mm. The scale bar applies only to D. An example patch is shown in the bottom right which shows the 25 200 x 200 µm tiles. The tissue slices are identified as follows: (A) tissue #1, slice #1; (B) tissue #1, slice #2; (C) tissue #2; (D) tissue #3, slice #1; (E) tissue #3, slice #2; (F) tissue # 4. Molecular designations of these tissue are found below.

7.3.3 Principal component analysis

Principal component analysis (PCA) was applied to the ToF-SIMS data in two separate ways. In the first, PCA was applied to the spectra acquired from all of the tissues. In the second, PCA was applied to the image data of individual patches.

The data used in this study were preprocessed to put them in a form appropriate for PCA. Regions of exposed substrate and regions of OCT (m/z 332.24^{+}) were excluded from all analyses by applying a threshold to the pixels with a silicon signal (m/z 27.98^{+}) and OCT.. All PCA was done using the freely available SpectraGUI and ImageGUI programs (Dan Graham, NESAC/BIO, University of Washington) that run within Matlab (Mathworks, Natick, MA). Several peak lists were created for positive and negative ions and are discussed in more detail below. In all cases, peaks were chosen whose maximum intensity was twice or more that of the average background intensity to the left and right of the peak. The spectra from all tissues were overlaid, then peaks were selected manually and integration limits for each peak were also set manually.

For the PCA applied to the spectra, Poisson-corrected peak intensities were exported as .txt files from the SurfaceLab 6 software and imported into the SpectraGUI software. Known salt, salt adduct, and substrate peaks were excluded from the peak lists. The data were normalized to the sum of the intensities of all of the peaks in the peak list, square-root transformed and mean centered prior to PCA.

For the PCA applied to the image data, .bif6 files were exported from SurfaceLab 6. With one exception, no peaks were excluded from these data. For the two patches with 36 tiles (Figure 1D), peaks had to be excluded to reduce the size of the .bif6 to avoid memory limitations within Matlab. PCA could not be completed within the SpectraGUI if the .bif6 file was above ~ 8 GB. The .bif6 files which were exported from the patches with 1536 x 1536 pixels reached 8

GB when they contained ~800 peaks, whereas the .bif6 files that were exported from the patches that contained 1280 x 1280 pixels were 6 GB with ~1300 peaks. Peaks to the left of .00 of a mass (e.g. m/z 78.92) with low intensity were excluded until a suitable file size was reached. For all analyses, no normalization was applied, and the data were Poisson scaled and mean centered before PCA.

7.4 Results

To simplify the complexity and aid in the interpretation of the ToF-SIMS data, PCA was applied using two different methods. First, it was applied to the spectra acquired from the tissues to attempt to distinguish one tissue from another and determine the largest sources of variance. PCA was also applied to the image data of individual patches to determine the largest sources of variance within a patch.

7.4.1 PCA applied to spectra acquired from tissue slices

Data from a total of 17 patches were acquired from four different tissue blocks. PCA was applied to all of the spectra that were obtained the tissues to determine if the tissues could be distinguished from one another. PCA also determined the peaks that were the largest sources of variance. Since the results from PCA are dependent on the set of peaks that were chosen as an input, it is important to choose the correct peak list. In this work, three different peak lists were investigated, the results of which are presented below. First, all peaks within the mass range m/z 0 – 920 were selected, excluding known salt, salt adduct, substrate and inorganic peaks. 794 and 621 peaks were chosen from the positive and negative ion modes, respectively. These peaks lists were named the “Large” Positive or Negative Ion peak lists. Second, the Large peak lists were truncated at m/z 200, such that only peaks above m/z 200 were included. 378 and 279

peaks were chosen positive and negative ions, respectively. These peak lists were named the "High Mass" peak lists. Third, the peak lists that were created during the analysis of eight human breast cancer cell lines (see Chapter 6, [232]) were used to test whether the tumor sections could be related to the cell lines. 284 and 207 peaks were chosen in the positive and negative ion modes, respectively. These peak lists were named the "High Mass (cell)" peak lists.

The major results from the PCA are shown below. Figure 7.2 shows the PC1 vs. PC2 (top left) and PC 2 vs. PC 3 (bottom left) scores plots created using the Large Negative Ion Peak list. The ovals surrounding the data points indicate 95% confidence intervals. The corresponding loading plots are shown to the right. Using the Large peak list, all four tissues were mostly separated from another. The needle biopsies (tissues #3 and 4, red, yellow, green) were distinguished from the excised (non-needle biopsied) tumor tissue samples (#1 and 2, purple, dark blue, light blue) on the plot of PC1 vs. PC2. The TN tissues (#1 and 4) were largely separated from the RP tissues (#2 and 3) across PC3. The peaks with consistently high loadings were fatty acids 14:0, 16:1, 16:0, 18:2, 18:1, 18:0 (m/z 227^-, 253^-, 255^-, 279^-, 281^-, 283^-, 305^-), vitamin E (m/z 163^-, 429^-), and fragments related to proteins (m/z 26^- and 42^-).

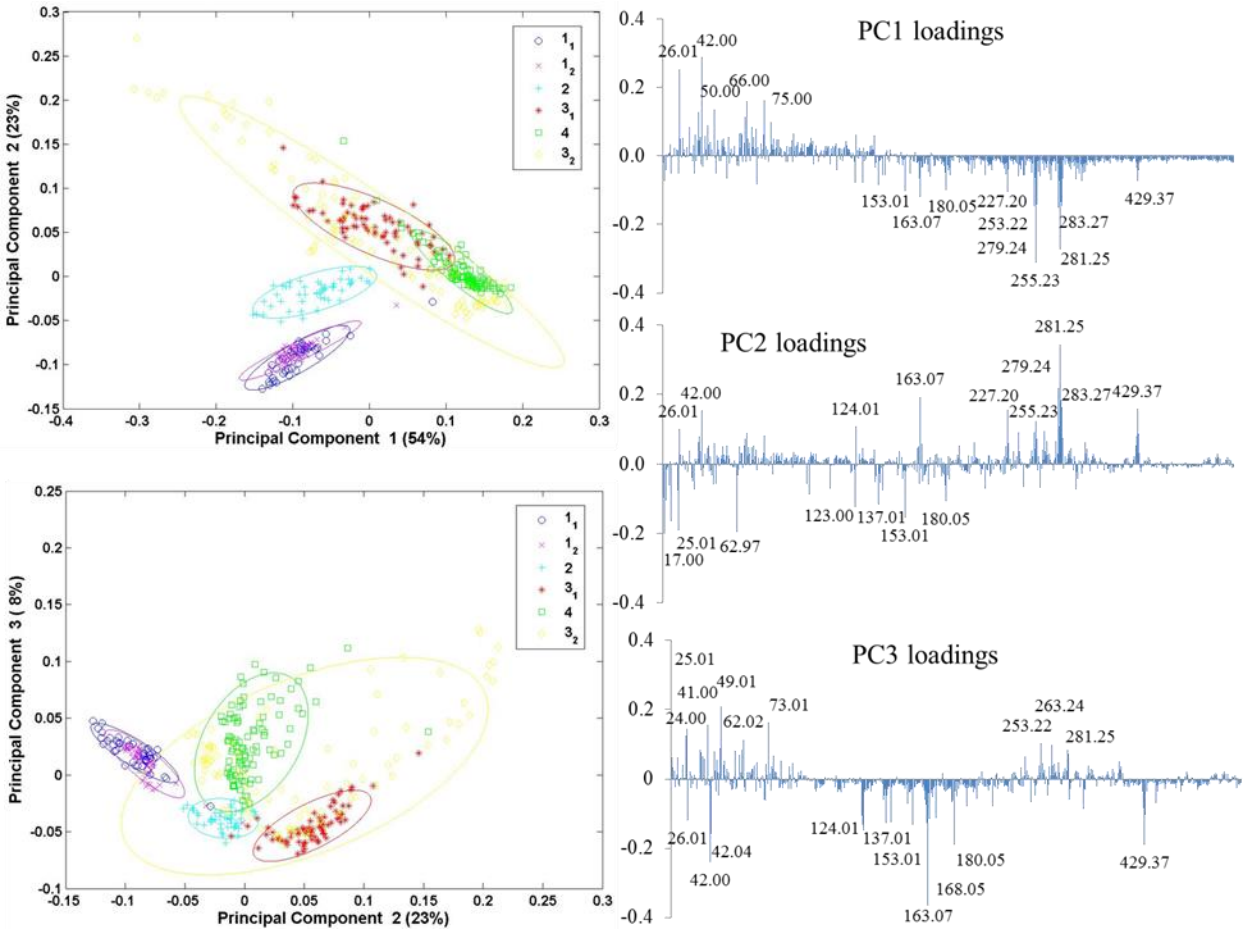

Figure 7.2 The PC1 vs. PC2 (top left) and PC2 vs. PC3 (bottom left) scores plots created using the Large Negative Ion peak list. The corresponding loading plots are on the right. The labeled secondary ions are shown in Table 7.1. Tissue #1: TN, dark blue and purple; tissue #2: luminal A, light blue; tissue #3: luminal B, red and yellow; tissue #4: TN, green.

To test the variability from slice to slice, data was acquired from multiple slices for tissues #1 and 3. These slices are labeled with subscripts (e.g. 1_1 and 1_2) in the legends in the scores plots. For tissue #1, the data from the separate slices were largely overlapping. In contrast, there was a larger difference between the two slices from tissue #3. Because the spread of the data points of the second tissue #3 slice (yellow) was much larger than any of the other slices, in many cases it overlapped with the data points from multiple other tissues. There are several possible explanations for the cause of the greater variability in the data from this slice.

As additional samples are sliced from the tissue block, more and more tumor tissue is removed and eventually normal breast tissue will be reached. It is possible that the second slice that was analyzed from tissue #3 was nearing normal breast tissue, and thus had a higher amount of lipids and more variability in the data compared to the other samples. Another explanation involves tumor structure. From Figure 7.1, it can be seen that tissues #3 and 4, the needle biopsied tissues, have more connective tissue and structures other than the "cancerous nests" when compared to tissues #1 and 2. Using regions of interest to select only cancer cell areas, either by using a single chemical image or PCA, it may be possible to reduce the amount of variability in the ToF-SIMS analysis.

To test whether the tissues studied in this work could be compared to the breast cancer cell lines studied previously [232], the peak lists that were created to analyze the cell lines were applied to the tissue data. The PC1 vs. PC2 scores plots created using the High Mass and High Mass (cell) peak lists are compared in Figure 7.3. The plots are quite similar, although tissues #2 and #4 were better separated from one another with the (cell) peak list. The similarity is not surprising since the peaks with the highest loadings from the High Mass peak list are also present in the High Mass (cell) list. The loading plots, shown below the scores plots, are also quite similar. With the (cell) peak list, the TN tissues (#1 and 4) were separated across PC 2, where the FA 16:0, 16:1 and 20:3 (m/z 305^-) peaks had high positive loadings and FA 18:0 and vitamin E peaks had high negative loadings.

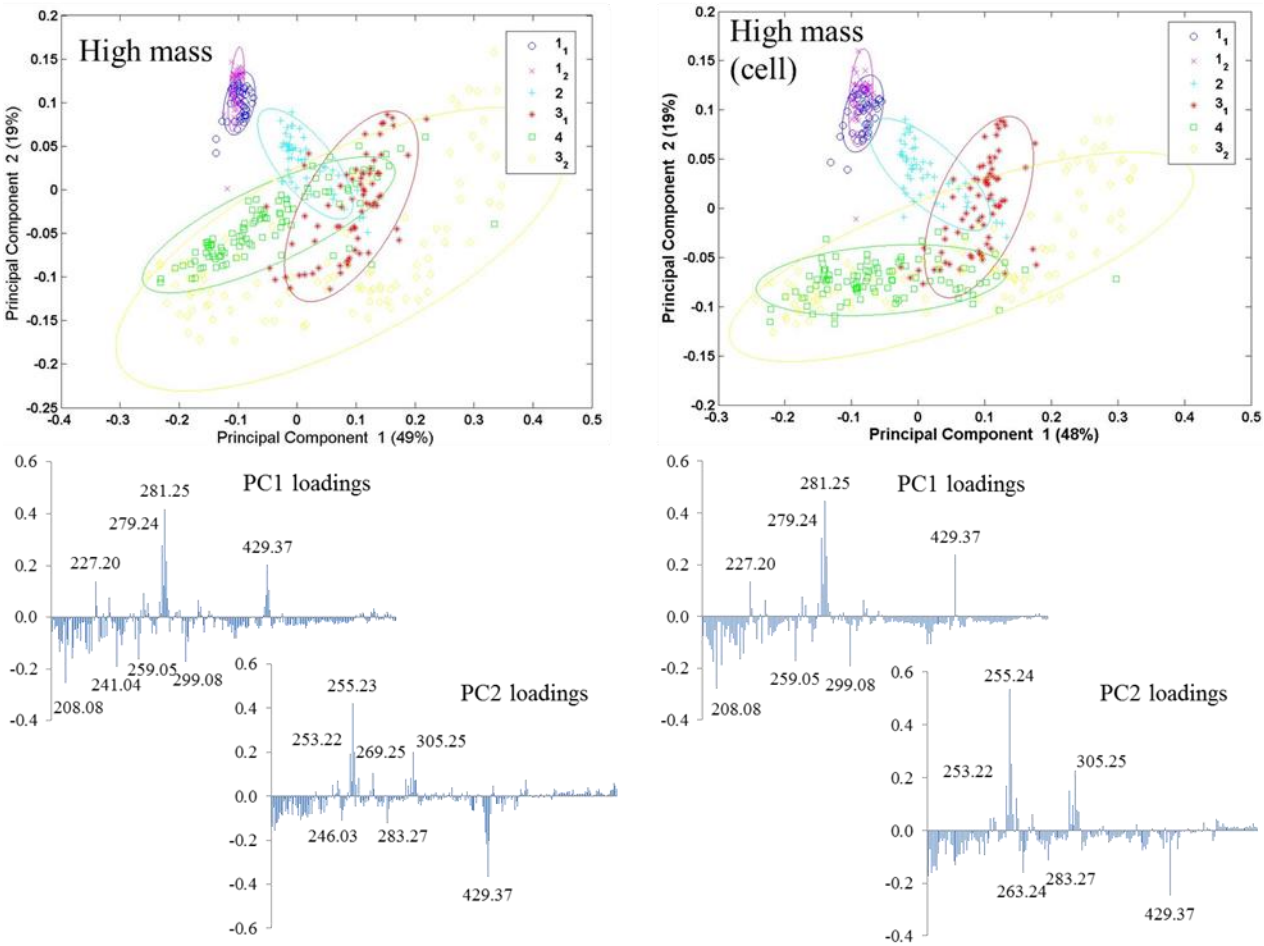

Figure 7.3 A comparison of the PC1 vs. PC2 scores plots when the High Mass peak list was used (top left) versus when the High Mass (cell) peak list was used (top right) with negative secondary ions. The corresponding loading plots are found below the scores plots. Details regarding the peak lists can be found in the Results section. The labeled secondary ions are shown in Table 7.1. Tissue #1: TN, dark blue and purple; tissue #2: luminal A, light blue; tissue #3: luminal B, red and yellow; tissue #4: TN, green.

Using the High Mass (cell) Negative Ion peak list, the TN tissues (#1 and 4) separated from one another on PC 2. On the contrary, the TN overlapped with one another in the PC 1 vs. PC 3 scores plot shown in Figure 7.4. The RP tissues also best separate form one another using PCs 1 and 3.

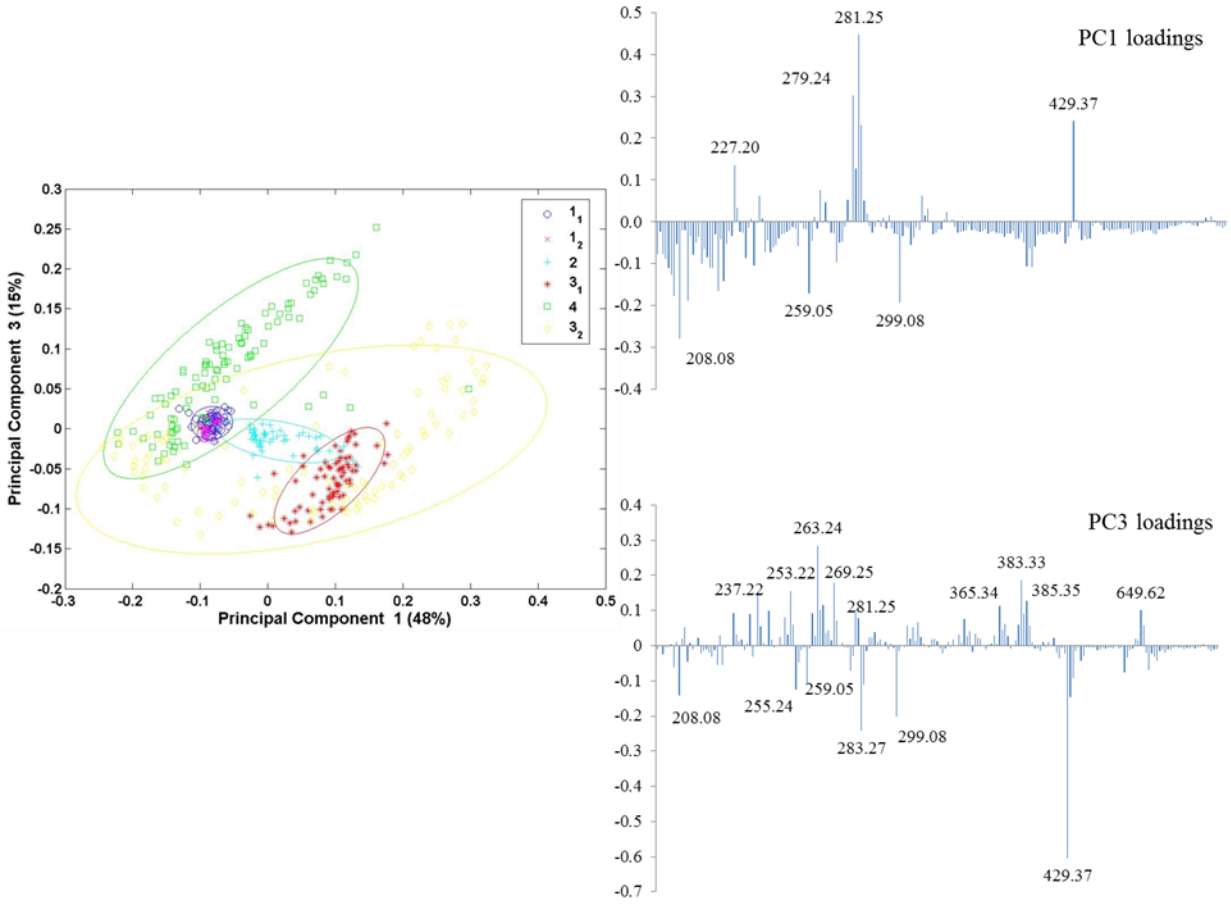

Figure 7.4 The PC1 vs. PC3 scores and loading plots when High Mass (cell) Negative Ion peak list was used. The labeled secondary ions are listed in Table 7.1. Tissue #1: TN, dark blue and purple; tissue #2: luminal A, light blue; tissue #3: luminal B, red and yellow; tissue #4: TN, green.

The PC1 vs. PC2 scores plot and corresponding loading plots that resulted from using the High Mass (cell) Positive Ion peak list are shown in Figure 7.5. The TN tissues separated from the RP tissues on PC 1, where the highest positively loading peaks were diacylglycerol (DAG, m/z 523^+, 549^+, 551^+, 575^+, 577^+, 579^+, 601^+, 603^+, 605^+, 607^+) and vitamin E (m/z 165^+, 430^+) species, and the highest negatively loading peak was cholesterol (m/z 369^+). Although the TN tissues were not completely separated on PC2, all of the data points for tissue #1 had positive scores and a majority of the data points for tissue #4 had negative scores. A phosphocholine

peak (m/z 224^{+}) had the highest positive loading, while cholesterol, DAGs and vitamin E peaks had negative loadings. The labeled peaks are compiled in Table 7.2.

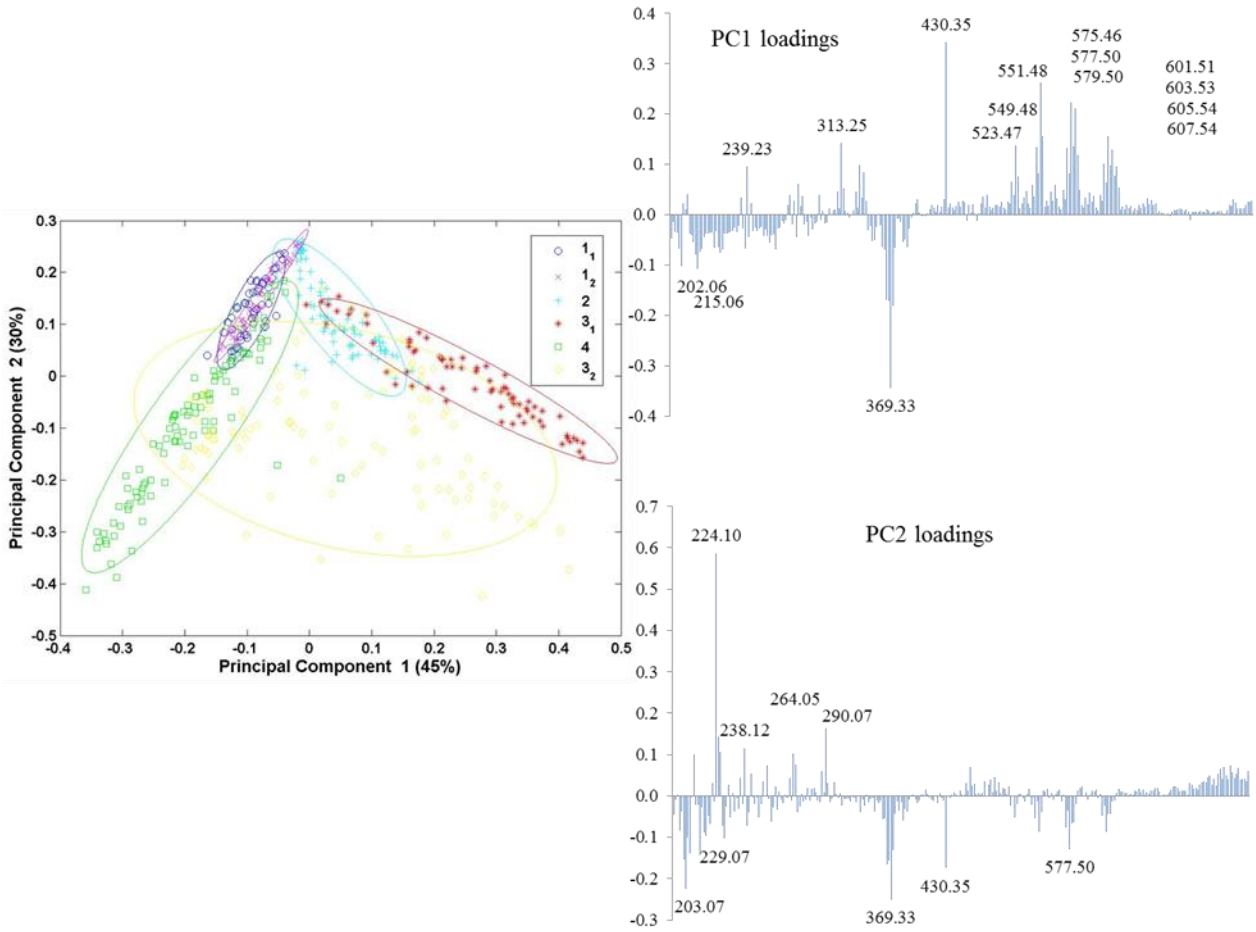

Figure 7.5 The PC1 vs. PC2 scores and corresponding loading plots when the High Mass (cell) Positive Ion peak list was used. The labeled secondary ions are shown in Table 7.2. Tissue #1: TN, dark blue and purple; tissue #2: luminal A, light blue; tissue #3: luminal B, red and yellow; tissue #4: TN, green.

7.4.2 PCA applied to images acquired from tissue slices

PCA was applied to the image data of each patch to not only highlight the largest sources of variance within a patch, but also relate the variance to biological structures. In many cases PCA produced scores with XY distributions that matched structured visible in the adjacent H&E-stained sections, but it was also able to produce scores with distributions that were not visible the

optical images. Examples of the results form PCA when it was applied to image data are shown in Figures 7.6 and 7.7. Figure 7.6 shows the positive and negative scores, plotted separately, of PC1-5 for the positive secondary ions, while the results for the negative secondary ions are shown in Figure 7.7.

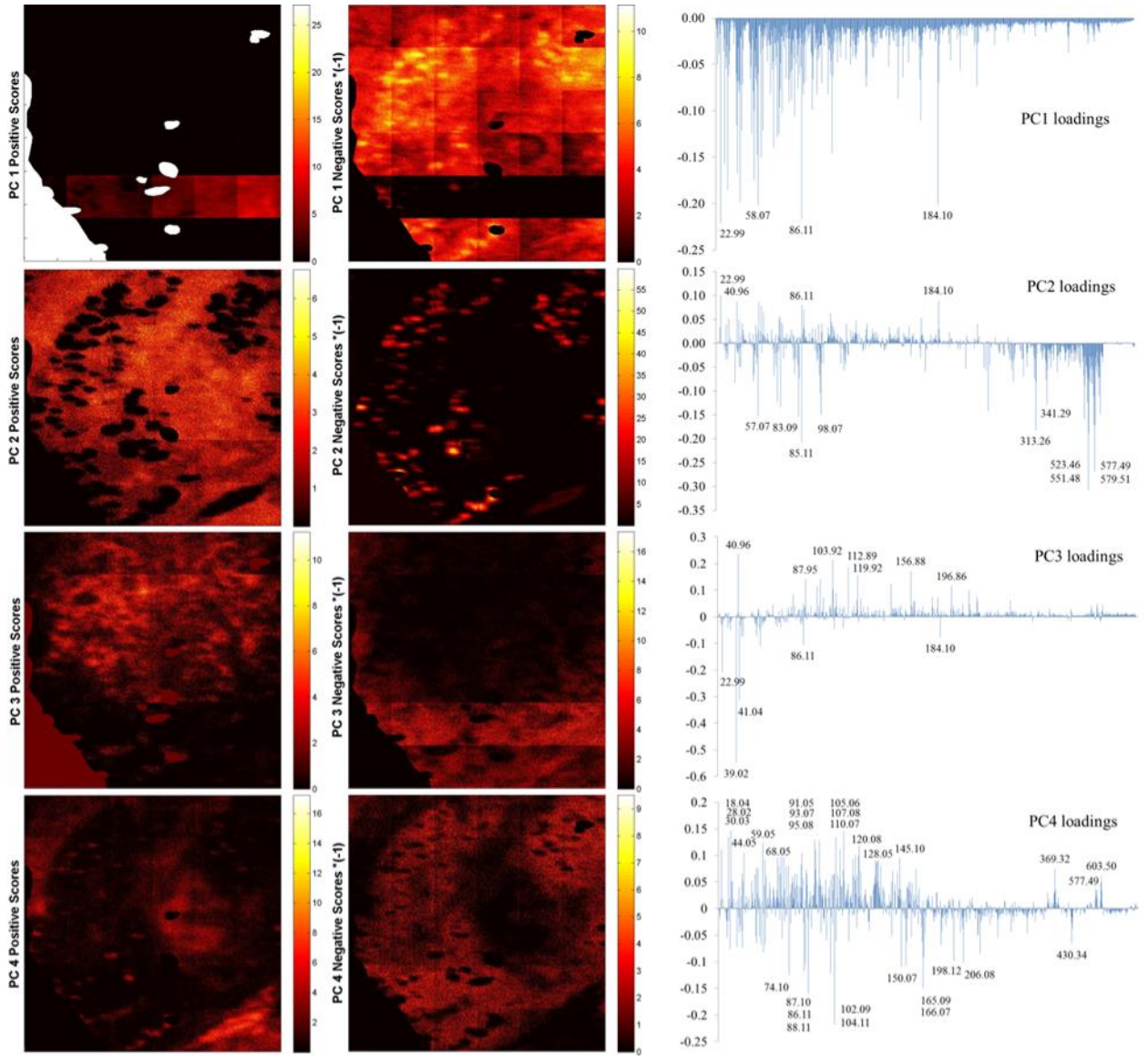

Figure 7.6 PCA imaging scores and loading plots for PC1-4 (top to bottom) when positive secondary ions were used. See the Methods section for details on the peak list. The patch was from tissue #3, the red square in Figure 7.1D. The scores are plotted as the positive (left column, i.e. $PC1^{+}$) and negative (right column, i.e. $PC1^{-}$) maps. For example, $PC1^{+}$ corresponds to the positive loadings in PC1, and $PC1^{-}$ corresponds to the negative loadings in PC1. The ions listed

in the loading plots are shown in Table 7.2. The area analyzed was 1.2 mm x 1.2 mm and contained 36 200 µm x 200 µm individual tiles.

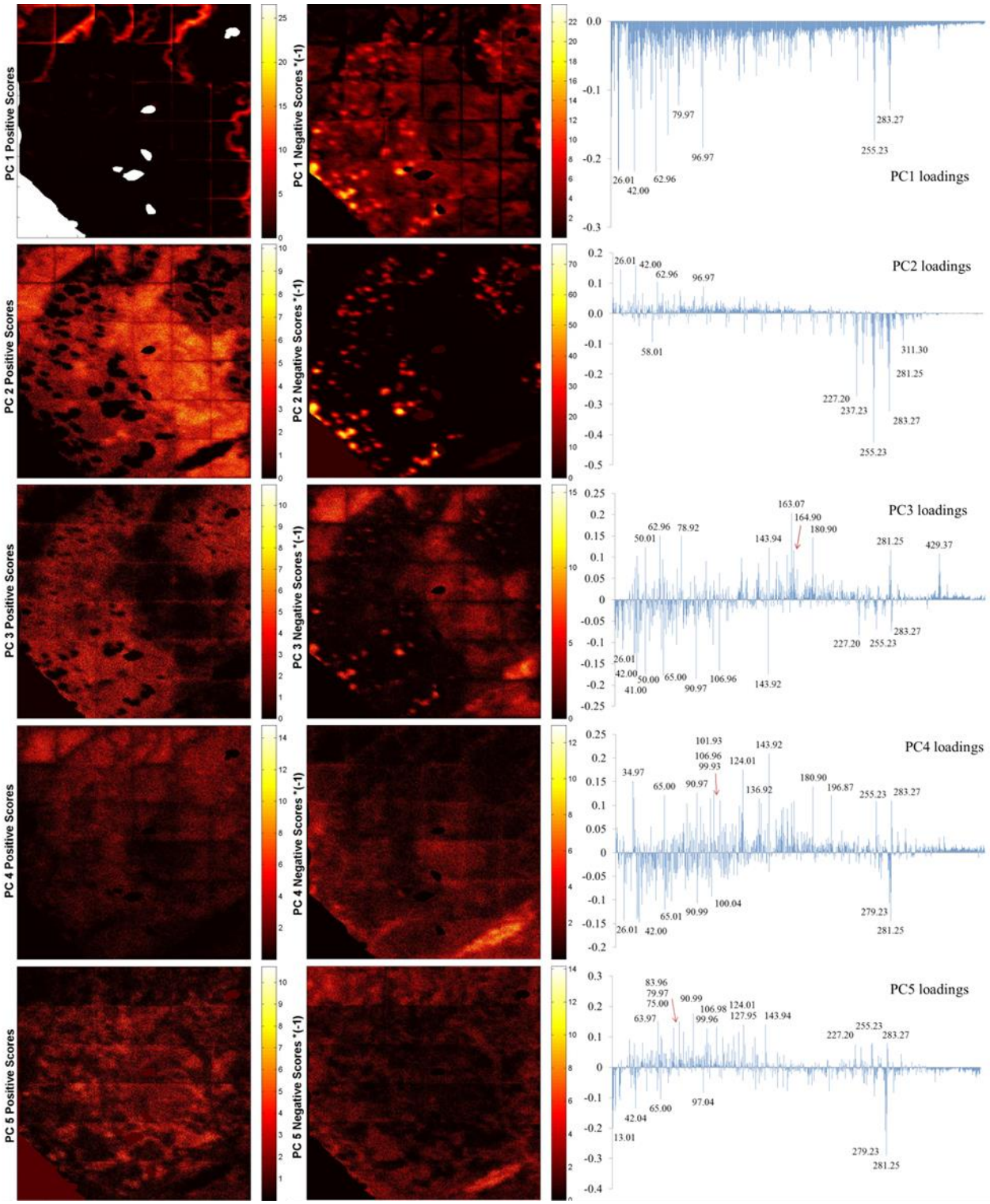

Figure 7.7 PCA imaging scores and loading plots for PC1-5 (top to bottom) when negative secondary ions were used. See the Methods section for details on the peak list. The patch was from tissue #3, the red square in Figure 7.1D. The scores are plotted as the positive (left column, i.e. $PC1^+$) and negative (right column, i.e. $PC1^-$) maps. For example, $PC1^+$ corresponds to the positive loadings in PC1, and $PC1^-$ corresponds to the negative loadings in PC1. The ions listed in the loading plots are shown in Table 7.1. The area analyzed was 1.2 mm x 1.2 mm and contained 36 200 µm x 200 µm individual tiles.

The pixels that were excluded from the analysis because of either exposed substrate or OCT were captured in $PC1^+$ (first row) of both the positive and negative ion data. This is reflected in the loading plots, as there are no peaks that load in the positive direction in either case. During the acquisition of the positive ion data, the Bi_3^+ analysis beam current appeared to gradually decrease with time starting in the fourth row. This is reflected as a region of higher intensity in the positive scores on PC1 and low intensity in the negative scores. This may be prevented by normalization of the data before PCA, but memory limitations prevented this normalization. A different artifact was captured in $PC1^+$ of the negative ion data, shown by regions of high intensity. This artifact may have been caused by charging effects, causing peaks to shift into or out of the selected integration limits. In all cases, charging effects were more pronounced during the acquisition of negative ion data compared to positive data.

What appear to be lipid droplets were highlighted in the $PC2^-$ scores image (second row) in both the positive and negative ion data. The lipid droplets are also visible in the optical image of the H&E-stained section (Figure 7.1). Phosphocholine fragments (m/z 86^+, 166^+, 184^+, 224^+) and the protein fragments CN^- and CNO^- (m/z 26^-, 42^-) had positive loadings in the positive and negative data, respectively, and spanned the area of the tissue that excluded the lipid droplets. Monoacylglycerol (MAG, m/z 313^+, 341^+) and DAG (523^+, 551^+, 577^+, 579^+, 607^+) fragments had the highest negative loadings in the positive ion data, while fatty acid fragments (m/z 225^-,

227^-, 253^-, 255^-, 281^-, 283^-) had the highest negative loadings for the negative ion data. The MAG, DAG and fatty acid peaks are lipids that would be expected to be present in high concentrations in lipid droplets.

A vitamin E-rich domain was observed from both the positive ($PC4^-$, fourth row) and negative ($PC3^+$, third row) secondary ion data. The dominant vitamin E peaks are m/z 430^+, 165^+, 429^- and 163^-. This domain covers a large portion of the tissue and has near zero intensities in the locations of the lipid droplets. A more subtle relationship was observed between this domain ($PC3^+$, negative ion data) and the domain shown in PC 2^+ (negative ion data). They appear to be largely inverse images of each other, where regions of high intensity on one correspond to regions of low intensity on the other. $PC3^-$ (negative ion data) pulled out a domain that includes what may be sulphur-containing species and the 14:0, 16:0 and 18:0 fatty acids (see Table 7.1 for peak identifications). An interesting feature highlighted by high loadings of unsaturated 18-carbon containing DAG (m/z 603^+, 577^+) and fatty acid (m/z 279^-, 281^-) species is visible in the bottom right of the images produced from positive ($PC4^+$, fourth row) and negative ($PC4^-$, fourth row) data.

A high salt domain dominated by K^+-containing species was captured in $PC3^+$ in the positive ion data. $PC3^-$ showed a domain high in phosphocholine fragments (m/z 86^+, 184^+), as well as, surprisingly, Na^+ (m/z 23^+). A similar domain was observed in $PC5^+$ of the negative data that appears to be localized to the center of the image. Many of the highest loading peaks in this domain may be phosphate-containing species (see Table 7.1 for peak identifications). It is difficult to distinguish between many of the sulfate and phosphate species due to the very similar masses many of these species have, but it is possible. For example, a mass resolution of ~9000 is needed to completely distinguish between HSO_3^- (calculated mass m/z 80.965) and $H_2PO_3^-$

(calculated mass m/z 80.974). However, the sulphate peaks often appear as shoulders on the left side of the phosphate peaks, and can be selected as individual peaks.

Comparable domains were captured by $PC4^+$ and $PC3^-$ in the positive and negative secondary ion data, respectively. This domain appears to be the opposite of the vitamin E-rich domain discussed above. Cholesterol (m/z 369^+), DAGs containing unsaturated 18-carbon alkyl tails (m/z 577^+ and 603^+), hydrocarbon fragments (m/z 91^+, 93^+, 95^+, 105^+, 107^+, 110^+) likely originating from cholesterol) and small nitrogen-containing fragments (m/z 18^+, 30^+, 44^+) had high loadings in the positive data. The negatively charged ions with the highest loadings were saturated 14, 16 and 18-carbon fatty acids (m/z 227^-, 255^-, 283^-), what are likely sulphur-containing species (m/z 91^-, 107^-, 144^-), and small nitrogen-containing fragments (m/z 26^-, 42^-). The discrepancy in the saturated and unsaturated fatty acids comes from the oval feature in the bottom right corner of the images. This feature is composed of unsaturated fatty acids, which is clear in $PC4^+$ (positive data) and $PC4^-$ (negative data) and in Section 7.4.4 below. In $PC3^-$ (negative data), the lipid droplets are displayed a moderate intensity, explaining the loading of the saturated fatty acids in this direction.

7.4.3 Relating chemical images to biological structures

Specific structures in the H&E-stained tissue section were also observed in the ToF-SIMS chemical images. Lipid droplets are visible in $PC2^+$ (positive data) and $PC2^-$ (negative data) in Figures 7.6 and 7.7, and in the H&E section in Figure 7.1D. Connective tissue, or stroma, is visible in $PC3^+$ of tissue #4 in Figure 7.8 (top left), while "cancer cell "nests" are visible in $PC3^-$ (Figure 7.8, top middle). The loading plot for PC3 is shown in Figure 7.8, top right. The stroma and cancerous nests are visible in the H&E image (Figure 7.8, bottom left) and

the optical image acquired from the ToF-SIMS analytical chamber (7.8, bottom middle). The larger box represents the 1 mm x 1 mm analysis area, whereas the smaller box represents the area from which a depth profile was acquired. A 400 µm x 400 µm summed depth profile overlay image is shown in Figure 7.8 (bottom right) where green represents the PO_2^- + PO_3^- and red represents CN^- + CNO^-. To create this image, a depth profile was acquired and time images from individual slices were summed. This is an effective strategy to create an image with increased secondary ion intensities, as well as create an image that better resembles an image of an H&E-stained tissue. The summed image confirms that the structures highlighted by $PC3^+$ and $PC3^-$ are connective tissue and cells, respectively. Single cells were also observed in the HSR images from additional tissues, by the K^+, CN^- and CNO^- distributions (data not shown).

Relating chemical signals to real structures is an important piece moving forward. As the tumors are heterogeneous, the current method of PCA is using the signal from all of the structures. Using PCA to pick out specific structures, like cancerous cell nests, and transforming those areas into regions-of-interest may change the separation between the tissue slices in the PCA shown above.

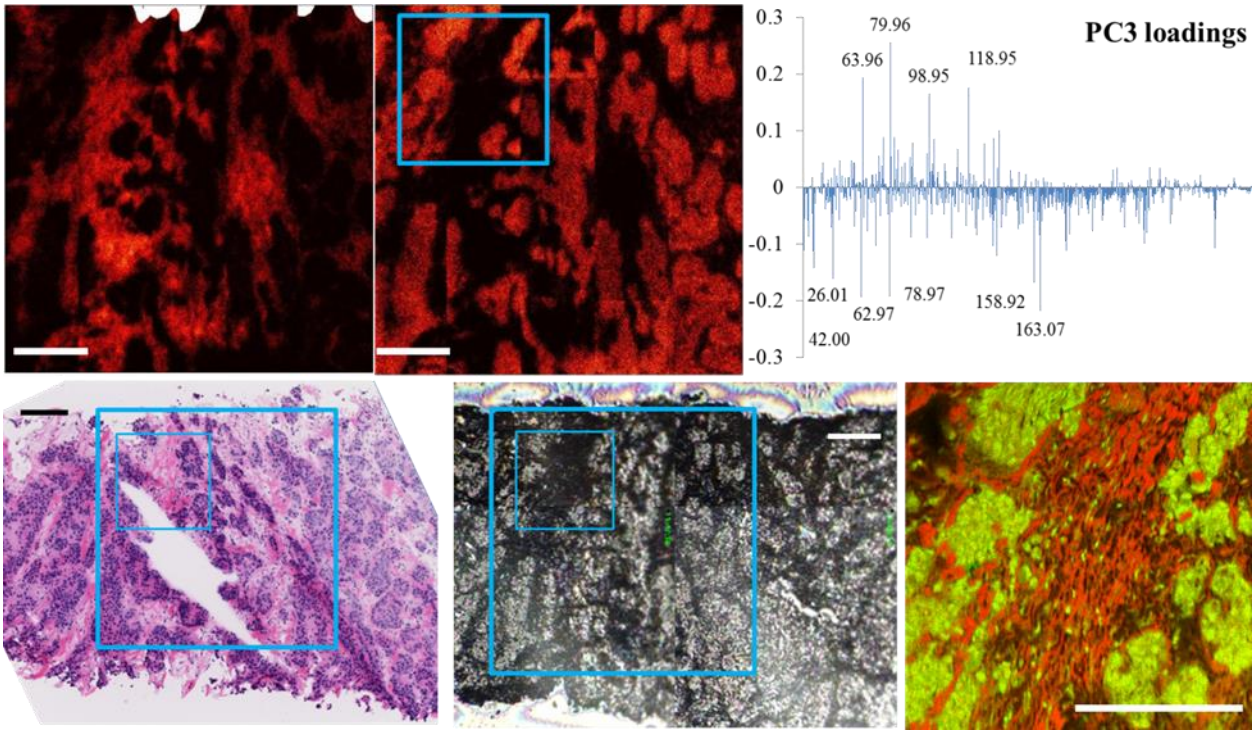

Figure 7.8 Top left: $PC3^+$ (positive ions); top middle: $PC3^-$ (positive ions); top right: scores for PC3 (positive ions); bottom left: Image of adjacent H&E-stained slice; bottom middle: optical image from within theToF-SIMS analytical chamber; bottom right: Overlay of the 400 µm x 400 µm depth profile. Red represens CN^- + CNO^-, green represents PO_2^- + PO_3^-. The larger boxes represents the 1 mm x 1 mm analysis area. The smaller boxes represents the 400 µm x 400 µm depth profile. All scale bars except bottom right are 100 µm. Bottom right scale bar is 200 µm.

7.4.4 Mapping unique distribution of fatty acids

Lipogenesis is an important component of cancer onset and progression , and lipid metabolism has gained increased attention as a vital mechanism for breast cancer [198, 233]. The distributions of saturated and unsaturated fatty acids in patches from each of the tissue blocks are shown in Figure 7.9. The 16:0 + 18:0 species are depicted in red and the 18:1 and 18:2 fragments are displayed in green. Not only are there unique distributions of these molecules within a tissue patch, there is a difference between the tissues. The lipid droplets in tissue #3 (top left) were composed of mostly unsaturated 18-carbon fatty acids, while the lipid droplets from tissue #4 (top right) were larger and contained a majority of saturated fatty acids. In tissue

#3, a large amount of the tissue surrounding the lipid droplets had a high intensity of unsaturated fatty acids, while a large portion of tissue #4 had a high intensity of saturated fatty acids. Tissue #2 (bottom left) contained fewer lipid droplets than either tissue #3 or 4, and the droplets that were present were comprised of mostly unsaturated fatty acids. There were no lipid droplets on the areas that were analyzed on tissue #1. The surrounding area in the selected area of tissue #2 had distinct regions dominated by unsaturated fatty acids and regions with higher saturated fatty acid intensity. The selected area in tissue #1 appeared to have a single region made up of a relatively uniform mixture of saturated and unsaturated fatty acids.

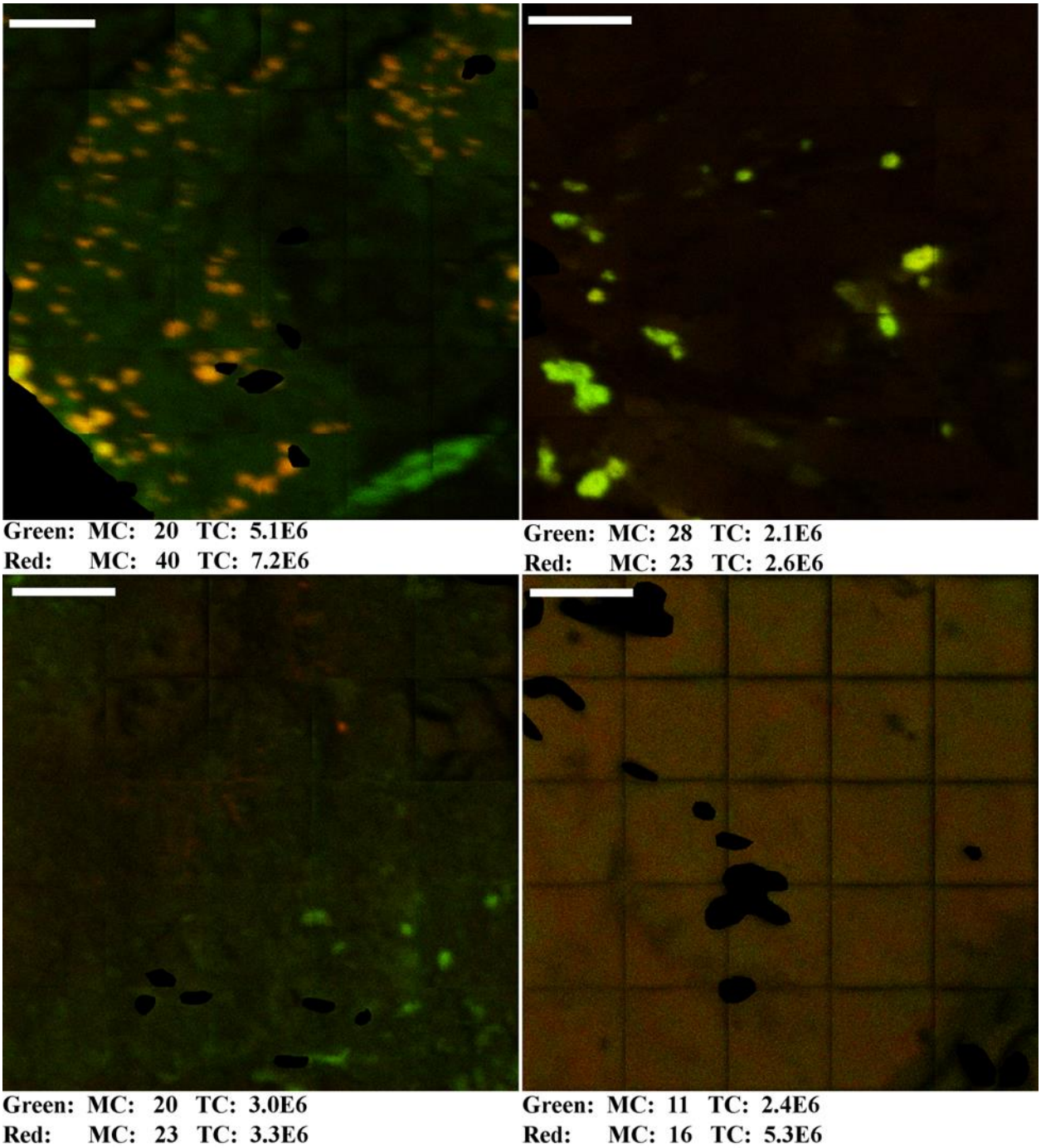

Figure 7.9 A red/green overlay of a patch from each of the four tissue blocks showing the distributions of the saturated fatty acids 16:0 + 18:0 (red) and the unsaturated fatty acids 18:1 + 18:2 (green). Scale bars are 200 µm. The max counts per pixel (MC) and total counts of the species mapped (TC) are displayed for each image. Top left: tissue #3; top right: tissue #4; bottom left: tissue #2; bottom right: tissue #1.

7.5 Conclusion

Breast cancer tumors were analyzed with ToF-SIMS imaging and PCA. Four different tumors were succesfully separated from one another using the spectra obtained from multiple 1 mm x 1mm patches. Imaging PCA revealed several domains on the surface of the tissues, several of which were also idenfiable in the image of the adjacent H&E-stained tissue slice, and several that were not. Differing fatty acid profiles were observed for the four tissues. Two tissues had a higher quantity, and larger lipid droplets than the other two. The lipid droplets contained a majority of either saturated or unsaturated fatty acids, as did the surrounding tissue area. Future work will involve using imaging PCA to extract ROI's related to specific structures, i.e. cellular nests or stroma. The separation of the tissue sections may change depending on the areas that are selected for PCA

Acknowledgements

This work was supported by NIH grants CA1-38293 and EB-002027.

Table 7.1 Key negatively charged secondary ions from PCA analysis

Mass	Possible Composition	Biomolecule
17	OH	
24	C2	
25.01	C2H	
26.01	CN	
34.97	Cl	
41	C2HO	
42	CNO	
42.04	C2H4N	
49.01	C4H	
50	C3N	
50.01		
58.01	C2H2O2	
62.02	C5H2 or C3H3Na	

62.97	PO2	
65	C4HO	
66	C3NO	
73.01	C6H	
75		
78.92		
79.97	HPO3	
83.96	CHSONa	
90.97	C2H3S2	
96.97	H2PO4	
99.93		
101.93		
106.96	C2H3S2O	
123		
124.01		
136.92		
137.01		
143.92	S2O5	
143.94	H2P2O5	
153.01		
163.07	C10H11O2	Vitamin E
164.9		
180.05		
180.9		
196.87	K2NaSO4	
208.08		
227.2	C14H27O2	FA 14:0
237.22	C16H29O	
241.01		
246.03		
253.22	C16H29O2	FA 16:1
255.23	C16H31O2	FA 16:0
259.05		
263.24	C18H31O	
269.25	C17H33O2	
279.24	C18H31O2	FA 18:2
281.25	C18H33O2	FA 18:1
283.27	C18H35O2	FA 18:0
299.08		
305.25	C20H33O2	FA 20:3
311.3	C20H39O2	FA 20:0

365.34		
383.33		
385.35	C27H45O	cholesterol
429.37	C29H49O2	Vitamin E
649.62		

Table 7.2 Key positively charged secondary ions from PCA analysis

Mass	Possible Composition	Biomolecule
18.04	NH4	
22.99	Na	
28.02	CH2N	
30.03	CH4N	
39.02	C3H3	
40.96	41^K	
41.04	C3H5	
44.05	C2H6N	
57.07	C4H9	
58.07	C3H8N	PC
59.05		
68.05	C5H8	
74.1	C4H12N	
83.09	C6H11	
85.11	C6H13	
86.11	C5H12N or C6H14	PC
87.1		
87.95	CNKNa	
88.11	C5H14N	
91.05	C5H8Na or C7H7	
93.07	C5H10Na or C7H9	
95.08	C7H11	
98.07	C4H8N3 or C6H10O	
102.09	C5H12NO	PC
103.92	CNK2	
104.11	C5H14NO	PC
105.06	C8H9	
107.08	C8H11	
110.07	C5H8N3 or C7H10O	

112.89	K2Cl	
119.92	CNOK2	
120.08	C8H10N	
128.05	C6H8O3	
145.1	C11H13	
150.07	C5H13NPO2	PC
156.88	K2PO3	
165.09	C10H13O2	Vitamin E
166.07	C5H13NPO3	PC
184.1	C5H13NPO4	PC
196.86	K2NaSO4 or Na4Cl3	
198.12	C5H12NPO3Na	
206.08	C5H14NPO4Na	PC
313.26	C19H37O3	MAG 16:0
341.29	C21H39O3	MAG 18:0
369.32	C27H45	Cholesterol
430.34	C29H50O2	Vitamin E
523.46	C33H63O4	DAG (30:0)
551.48	C35H67O4	DAG (32:0)
577.49	C37H69O4	DAG (34:1)
579.51	C37H71O4	DAG (34:0)
603.5	C39H71O4	DAG (36:2)

8. Conclusions and future directions

8.1 Conclusions

The data presented in this dissertation showed that biological cells and tissues can be successfully analyzed with time-of-flight secondary ion mass spectrometry (ToF-SIMS). A portion of the work focused on the development and characterization of methods for analyzing cells and tissues. The other portion of the work applied ToF-SIMS to determine answers to important biological problems.

For example, eight human breast cancer cell lines were largely distinguished from one another on the basis of the unique mass spectra obtained from each line. Key secondary ions were identified using principal component analysis (PCA) and related to important pathways in cellular metabolism. A majority of the key ions were related to lipids, specifically fatty acids, cholesterol, phospholipids, and mono- and diacylglycerols. This result was not totally surprising since single cells have a large amount of lipid material and ToF-SIMS has a propensity to probe lipids, even being described as a "lipid microscope" [234].

Tumor samples from four different breast cancer patients were analyzed with ToF-SIMS. Using PCA, the four tumors were successfully distinguished from one another. Several chemically distinct domains were identified with imaging PCA, some of which were related to structures observed in the H&E stains, and others which were not. A more directed PCA approach would involve using some of the principal component images as regions of interest to include like structures from each of the tissue samples. Unique distributions of saturated and unsaturated fatty acids were mapped for each of the tissues.

In another chapter, the sputter rates of individual NIH/3T3 fibroblasts were determined to be uniform in x, y and z. This is important to 3D imaging applications and it was the key assumption in a previously invented "z-correction" pixel shift [14]. With this assumption validated, the z-correction becomes a reliable method to produce 3D reconstructions that contain a more accurate distribution of secondary ions.

Several methods to prepare NIH/3T3 fibroblasts were investigated. It was determined that chemical fixation followed by rinsing removed a majority of chloride ions, but not other anions, and this resulted in increased yields of all most organic, positively charged secondary ions. This is consistent with a mechanism where anions are combining with cations to form undetectable, neutral molecules. When the cells were analyzed frozen-hydrated, the yield of larger ($m/z > \sim125$) positively charged secondary ions was higher compared to freeze-dried cells, but lower molecular weight ions ($m/z < \sim125$) exhibited nearly the same or lower yields. This result is consistent with a mechanism where cryogenic temperatures lower the damage cross sections of the impinging primary ions.

8.2 Future directions

There are many questions that can be asked that expand on the work presented here and would be worth exploring.

For the breast cancer cell (Chapter 6) and tumor tissue (Chapter 7) studies, only principal component analysis (PCA) was utilized. PCA is a useful tool used in conjunction with ToF-SIMS data, but there are other, more complex multivariate analysis methods that can provide further insight. For example, it may be possible using partial least squares discriminant analysis (PLS-DA) and PCA to build a model using the cell line data and project the tissue data onto that

model, potentially classifying the tissue types based on the cell line data. Furthermore, additional information may be extracted from the images of the tumor tissues with maximum autocorrelation factor (MAF).

Chapter 6 attempted to distinguish eight breast cancer cell types from one another and link the largest sources of variance to biological mechanisms. A similar approach may be taken that investigates the effect that different stressors have on a subset of the cell lines. A stressor may be a chemotherapeutic agent, hypoxia, or glucose deprivation. Given any of these, it is expected that the characteristic ToF-SIMS spectra change compared to the "normal" spectra for those cell lines.

It has been shown in several studies that subcellular imaging of native and non-native species is possible with ToF-SIMS. One possible, important study could focus on attempting to image the 3D, intracellular distribution of chemotherapeutics in single breast cancer cells. Platinum-containing drugs are especially intriguing because the platinum secondary ion signal would be easier to detect than a characteristic fragment that contained only carbon, oxygen and nitrogen. It is known that certain drugs are effective against certain cell types, and ineffective against others [194]. These types of studies probe at which concentration of a drug where half of cells are eradicated, but offer little insight into mechanisms of resistance. Large argon clusters may also play a useful role here, potentially preserving more molecular signal during 3D data acquisition than the C_{60} sputtering beams that were used in this work. This would be important to retain platinum signal, but would be very important for preserving the molecular signal from non-platinum-containing drugs and signals from native intracellular structures.

There are several natural next steps to the 3D imaging work presented in Chapter 5. First, a similar set of experiments could be run using large argon clusters as the sputter source to determine if the sputter rate of NIH/3T3 fibroblasts is uniform. Additional cell types could also be studied, similar to the plant cell shown in Section B.2. Many complex biological samples may *not* have the uniform sputter rates described in Chapter 5, samples like plant cells, tumor tissues, or samples with multiple polymer layers, like organic light emitting diodes. In these cases, in addition to correcting the position of pixels in the z-axis, differential sputter rates, and sputter rates that change with time would need to be accounted for to reconstruct a more accurate 3D image. The sputter rate of a material is dependent on the position of the material in a multilayer sample [235]. There are also models that describe damage accumulation with increased etching ion dose [165, 236]. It would be possible to include these types of information and equations into the ZcorrectorGUI so that more accurate reconstructions may be produced. The user may have to input certain parameters that were determined experimentally, but eventually with enough experiments, general rules may be developed that describe these phenomena and input into the GUI.

Appendix

Appendix A. ToF-SIMS 3D Imaging of HeLa Cells

Jeremy Brison,[1,3*γ] Michael A. Robinson,[1,2γ] Danielle S.W. Benoit,[3†] Shin Muramoto,[1,2°] Patrick S. Stayton,[3] David G. Castner [1,2,3§]

[γ]These authors contributed equally to this work.

National ESCA and Surface Analysis Center for Biomedical Problems[1],

Departments of Chemical Engineering[2] and Bioengineering[3], University of Washington, Seattle, WA 98195-1653

[*]Current affiliation: IBA Medical Accelerators Solutions, Belgium

[†]Current affiliation: Departments of Biomedical Engineering and Chemical Engineering, University of Rochester, Rochester, New York 14627

°Current affiliation: National Institute of Standards and Technology, Gaithersburg, Maryland 20899

[§]Corresponding Author:

David G. Castner

1-206-543-8094 (phone)

1-206-543-3778 (fax)

castner@uw.edu (e-mail)

A.1 Abstract

In this study a non-native chemical species, bromodeoxyuridine (BrdU), was imaged within single HeLa cells using time-of-flight secondary ion mass spectrometry (ToF-SIMS). Z-corrected 3D images were reconstructed that accurately portray the distribution of intracellular BrdU as well as other intracellular structures. Additionally, important parameters influencing the quality of the HeLa cell 3D images were investigated. Atomic force microscopy measurements revealed that the HeLa cells were sputtered at a rate of approximately 4 nm per 10^{13} C_{60}^{+} ions/cm^2 at 10 keV and a 45° incident angle. Optimal 3D images were acquired using a Bi_3^{+} liquid metal ion gun (LMIG) operating in the simultaneous high mass and spatial resolution mode. Operating the Bi_3^{+} LMIG in the high mass resolution mode only was sufficient to show BrdU was successfully localized to the cell nuclei, but the visualization of other sub-micron cellular features required operating the Bi_3^{+} LMIG at high mass and spatial resolutions.

A.2 Introduction

Time-of-flight secondary ion mass spectrometry (ToF-SIMS) is increasingly used in the life sciences to characterize complex biological samples and biomedical devices [237-244]. This rapid expansion coincides with the advent of polyatomic ion sources, which have fundamentally changed the way ToF-SIMS data is acquired [245-247]. Compared to their monoatomic counterparts, cluster ions such as Bi_3^{q+} [5, 248], C_{60}^{q+} [8] and gas cluster ion beam (GCIB) Ar [9, 249] provide higher secondary ion yields for high mass molecular fragments which results in extended mass range and enhanced sensitivity. The concerted action of cluster atoms during impact with the surface also results in higher sputter yields[250], causing less residual chemical damage during analysis [50, 251] due to the formation of a lower damage volume from shallower implantation depths [131]. Because of this capability, cluster ions have demonstrated a remarkable aptitude for molecular depth profiling organic and biological materials [166, 251, 252]. Numerous examples of successful molecular depth profiles have been reported in the literature for polymers and biological samples (See reference [253] for a recent review).

The use of cluster ion sources in ToF-SIMS has demonstrated a great potential for molecular 3D imaging of single biological cells [27, 54, 154, 254-259]. Its sub-micron spatial resolution [4, 260], combined with its parallel detection capability and molecular specificity give the instrument the ability to detect all elements without the need for selective markers, making it a complementary tool to methods such as matrix-assisted laser desorption ionization (MALDI) mass spectrometry [215] and fluorescence microscopy [261]. Particularly intriguing is the prospect of mapping the intracellular distributions of small molecule therapeutics in single cells with ToF-SIMS, now a possibility given the advances described above. An important criterion

to achieve this is a data acquisition mode that provides simultaneous high spatial and mass resolutions.

A significant number of 2D images of cells and tissues have been published in literature, but few full molecular 3D images have been reported to date. Obtaining 2D and 3D images of single cells is still challenging [240], with the main reasons stemming from the extreme surface sensitivity of the technique, low secondary ion yields (especially after prolonged sputter times) and the necessity to perform the experiment in an ultra-high vacuum environment.

Cluster ions offer new opportunities for analysis of biological samples because they allow depth profiling with low ion induced chemical damage [240, 262]. They can be used to "clean up" the sample surface [124, 132, 258] and to reach specific depths within the cells, which offers the opportunity to more easily control the depth analyzed in a cell than the freeze-fracture method. However, since a biological cell is a highly heterogeneous volume, it is essential to obtain a detailed and a fundamental understanding of "cluster ions – biological matter" interactions so that the optimal sample preparation (chemical fixation, freeze-dried, frozen-hydrated, freeze-fracture, etc.) and cluster cleaning can be selected to produce optimal 3D imaging. For example, the ion induced chemical damage and the etching rates in biological matter are still an area of active investigation [11, 27, 154]. Also, it is not clear if these parameters are constant through depth profiling and for all species present in all sample types. The sputter rate of NIH/3T3 fibroblasts using C_{60}^{++} was shown to be largely uniform throughout an entire depth profile [154], although the ion yields of many secondary ions decreased in NIH/3T3 fibroblasts [25] with increasing primary ion dose. In rat brain tissue samples the secondary ion yield of cholesterol, phospholipid and protein fragments did not decrease

substantially with increasing sputter dose when the tissue was held at -120 °C, although the sputter yield was not measured [26].

Other groups have identified the importance of improving the mass resolution for ToF-SIMS, as well as acquiring data with both high mass and spatial resolutions. Two examples include a modified commercial MALDI instrument with a C_{60} primary ion source [52, 263], and Ionoptika's J105 instrument [54, 256]. Both of these instruments utilize a direct current instead of a pulsed primary ion beam and incorporate orthogonal mass analyzers with objective of acquiring data at both high spatial and mass resolutions. Due to other instrument constraints, the modified MALDI instrument was not able to achieve high spatial resolution images. A C_{60} primary ion beam was recently added to a Fourier transform ion cyclotron resonance mass spectrometer to achieve mass resolving powers greater than 3,000,000 [264, 265]. Although the spatial resolution demonstrated by this instrument was not as good as the spatial resolution used in typical ToF-SIMS imaging experiments, the mass resolving power is unparalleled. New combined high mass and spatial resolution imaging modes have been recently introduced by PHI [266] and IONTOF [267]. Thus, imaging with simultaneous high mass and spatial resolution is now receiving significant interest in the ToF-SIMS community.

In this study we investigate the 2D and 3D ToF-SIMS images of human HeLa cells acquired in the dual beam mode [7] (*i.e.*, Bi_3^+ for imaging and C_{60}^+ for etching) with the sputter depth calibrated using atomic force microscopy (AFM). The Bi_3^+ liquid metal ion gun (LMIG) was operated at different conditions (high mass resolution, high spatial resolution, simultaneous high mass and spatial resolutions) to assess the effectiveness of the LMIG operating mode for imaging the HeLa cells. The HeLa cells used in these experiments were treated with

bromodeoxyuridine (BrdU), a well-known nuclear marker[268], to help identify and delimit the nuclei during 3D imaging.

A.3 Materials and Methods

A.3.1 Time-of-Flight Secondary Ion Mass Spectrometry

ToF-SIMS experiments were performed using an ION-TOF TOF.SIMS 5-100 (ION-TOF GmbH, Münster, Germany) equipped with a Bi LMIG and a C_{60} electron impact source. A pulsed 25 keV Bi_3^+ analysis beam and a 10 kV C_{60}^{q+} (q = 1, 2) sputter beam were used for this study. Both beams struck the target at an angle of 45º. The Bi LMIG gun was used in a high current, high mass resolution (HMR) mode and in two types of high spatial resolution (HSR) modes. An example spectrum for each at m/z 81^- is plotted in Figure A.1. The two types of HSR modes are "burst alignment" where the ion beam has a long pulse width (higher current but nominal mass, top spectrum) and "burst" mode, where the ion beam has a series of short pulses (high mass resolution but lower target current, middle spectrum). In the burst mode, the long pulses (170 ns in this study) are cut into a burst of successive short ion pulses by a sine blanker operating at 40 MHz (i.e., 6 pulses of 2 ns every 25 ns). In the burst alignment mode, the ion beam is not bunched to avoid the energy dispersion that causes the degradation of the spatial resolution. In contrast, the short pulses in the burst mode provide simultaneous high mass and spatial resolutions with a low, but useable, primary ion current (see below). Six peaks resulting from these short pulses were summed together to increase the signal intensity, providing increased sensitivity.

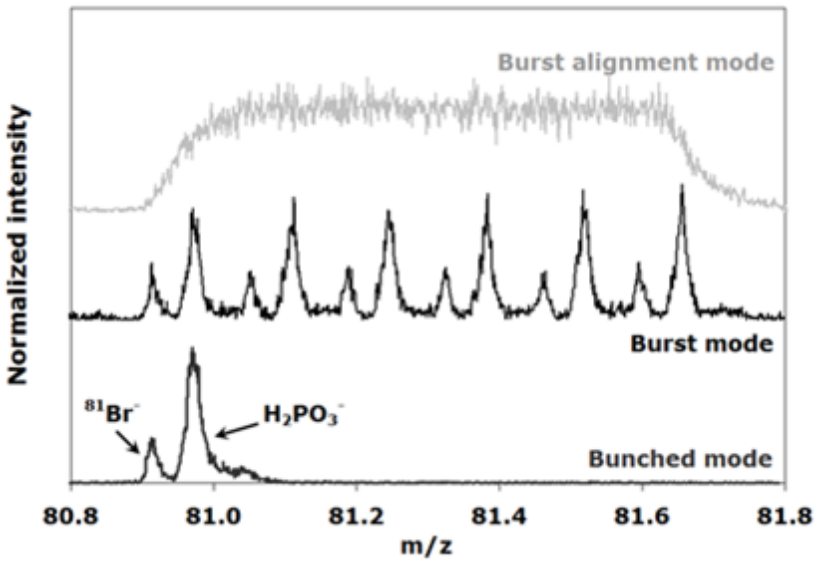

Figure A.1: Three Bi_3^+ analysis modes used for ToF-SIMS analysis of HeLa cells treated with BrdU generate different spectra. Top spectrum: HSR "burst alignment" mode. Middle spectrum: "burst" mode with both high mass and spatial resolutions. Bottom spectrum: HMR "bunched" mode. Additional details of the analysis modes are provided in the experimental section.

To acquire secondary ion images, Bi_3^+ was typically rastered over a 200 × 200 μm^2 area, centered inside a 500 × 500 μm^2 C_{60}^{q+} crater. Target currents were measured separately before each measurement, with Bi_3^+ at 0.2 pA in the HMR mode, 0.08 pA in burst alignment, less than 0.01 pA in the burst mode, and C_{60}^{q+} between 0.15 nA and 1 nA. The spatial and mass resolutions (measured at *m/z* 27) were typically 5 μm and >8,000 (HMR mode), <1 μm and nominal (burst alignment mode), and <1 μm and >5,000 (burst mode). Low energy electrons were flooded onto the sample to compensate for charge buildup.

For the burst mode data set, 14 2D images (referred to as "slices") were acquired. This data was collected in the "non-interlaced" mode, where the analysis and sputter beams are active in different ToF-cycles. This operation mode is necessary to produce images with sufficient

secondary ion intensities. The total Bi_3^+ accumulated ion dose for each slice was less than 7.5 x 10^{10} ions/cm^2. The total C_{60}^+ ion dose per slice was 1.3 x 10^{14} ions/cm^2, which corresponds to the removal of ~52 nm of material per slice (see below). For the HMR data set, 244 2D images were acquired. The data was collected with the Bi_3^+ and C_{60}^+ ion beams operated in the same ToF cycle (referred to as "interlaced" mode [269]). The total Bi_3^+ accumulated ion dose for each slice was 2.0 x 10^{10}, and the total C_{60}^+ ion dose per slice was 1.3 x 10^{13} C_{60}^+ ions/cm^2.

A.3.2 Data Handling/3D Image Reconstruction

ToF-SIMS data were reconstructed in 3D using the ZcorrectorGUI [154] (Dan Graham Ph.D., NESAC/Bio, University of Washington), a free GUI that runs in Matlab (MathWorks, Natick, MA). First, peak intensity images were plotted in the SurfaceLab 6 software (ION-TOF GmbH, Münster, Germany), and then exported as .bif3D files. The .bif3D files were imported into the ZcorrectorGUI to create the 3D reconstructions.

For the 3D reconstruction of the burst mode images each 2D Bi_3^+ image from the 14 slices was split into two 2D images, resulting in 28 slices and effectively doubling the height of the cells in the image. For the 3D HMR image, the initial 244 2D images were reconstructed by plotting 24 slices, where each new reconstructed slice was the summation of 10 2D images from the raw data. The last four slices were excluded from the reconstruction.

A.3.3 Atomic Force Microscopy

AFM (Dimension 3100, Veeco Metrology Inc., Santa Barbara, CA) was used to measure the height of the cells and their morphology before and after sputtering with differing C_{60}^{q+} doses. The AFM was equipped with a 315 kHz, 42 N/m PointProbe Plus silicon tip (Nanosensors, Neuchâtel, Switzerland), and operated in the intermittent contact mode in air. At

least four locations of each cell at a particular area were scanned to determine the average height. These measurements were used to calibrate the depth scale of molecular depth profiles. As a first approximation, the cells nuclei and cytoplasm were considered as flat areas and their thickness was averaged over the selected regions.

A.3.4 HeLa Cells and Sample Preparation

HeLa cells, human cervical carcinoma cells (ATCC CCL-2), were maintained in minimum essential media (MEM) containing L-glutamine (Gibco), 1% penicillin-streptomycin (Gibco), and 10% fetal bovine serum (FBS, Invitrogen) at 37 °C and 5% CO_2. After trypsinizing, the HeLa cells (12,000 cells/cm^2) were seeded onto Si surfaces that had been cleaned by sequential sonications in DI water, dichloromethane, acetone, and methanol. Then the cells were allowed to adhere overnight to the Si surface. The cells were then prepared for ToF-SIMS analysis in the following ways:

1. Figure 2: Cells were washed in ammonium acetate (AA), and either air dried (top row) or dried with a gentle stream of nitrogen (bottom row).
2. Figures (3-6): Cells were washed in AA, fixed in 4% phosphate-buffered paraformaldehyde, rinsed with double distilled H_2O (ddH_2O), and dried with N_2. Cells were also incubated in the presence of 20 μM BrdU for 48 hours prior to seeding. BrdU, which is incorporated into DNA during cell division, is a good label for cell depth profiling. BrdU can be detected using the $^{81}Br^-$ signal ($^{79}Br^-$ overlaps with PO_3^-), as well as $C_4H_2N_2O_2Br^-$ at m/z 189 and 191 ($^{79}Br^-$ and $^{81}Br^-$ isotopes).

A.4 Results and Discussion

A.4.1 C_{60} etching to reveal subcellular structures

Obtaining the ideal ToF-SIMS image of a biological cell is challenging. Complexities from many factors can affect the quality of the acquired image. Sample preparation is one of these factors and numerous studies have focused on optimizing sample preparation procedures for analyzing cells with ToF-SIMS [27, 136, 270, 271]. The general conclusion is that no single preparation procedure is optimal for all experiments, since even a small change in the preparation methods can change the quality of the information obtained from single cells. For example, Figure A.2 shows positive secondary ion images of HeLa cells imaged with Bi_3^+ for two slightly different preparation protocols [136, 270]: one rinsed in AA for 30 seconds and then dried in air (top row); the other rinsed in AA for the same time but dried using a gentle stream of N_2 (bottom row).

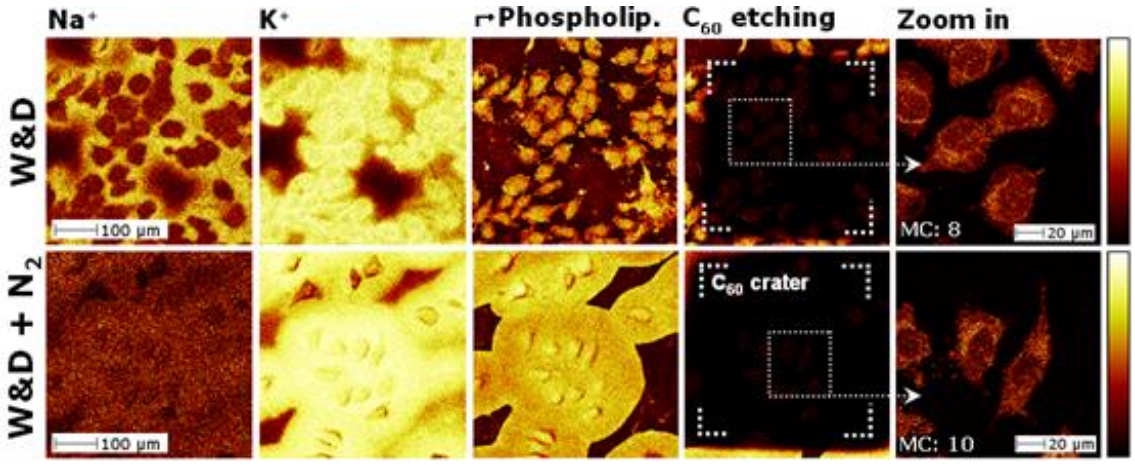

Figure A.2: Positive burst alignment (HSR) ion images of the HeLa cells prepared by a simple wash-and-dry method. The cells were rinsed with AA and then dried in air (top row) or with a gentle flow of N_2 (bottom row). Etching was performed using C_{60}^{++} at 20 keV with a dose of 1.0×10^{14} C_{60}^{++} ions/cm^2.

The sum of phospholipid signals (See Table A.S.1) in the third column shows that the plasma membranes of the cells dried in air retained the native cell shape better than those dried

with a N_2 stream. The images in the bottom row show that the Na^+, K^+ and phospholipid signals are not specifically localized outside or inside the cells, indicating extensive damage to the plasma membrane, and therefore leakage of some internal contents for samples dried with a N_2 stream.

One way to overcome the problem of damage or smearing introduced by the sample preparation method is to use C_{60} cluster ion etching to remove contaminants or damaged regions from the sample surface, allowing higher quality ToF-SIMS images to be acquired [124, 132, 258]. ToF-SIMS images of HeLa cells after C_{60}^{++} etching are also shown in Figure A.2. In the fifth column, acquired after C_{60}^{++} etching, a subcellular feature of the cells is now visible: the perinuclear enriched phospholipid regions that delimit the cells' nuclei. Smaller phospholipid spots within the nucleus suggest positions of nucleoli. The intracellular structures for both preparation methods after C_{60}^{++} etching appear similar, independent of which drying method was used. In both cases, the growth medium residues and the material located around the cells from leakage are quickly removed by the etching, revealing subcellular features. Thus, C_{60} etching is a useful tool to reveal intracellular structures by removing the surface damage caused by non-optimal, sample preparation methods. It is interesting that the phospholipid rich regions observed in Figure 2 and in Brison *et al.*[34] are similar to those obtained with a NanoSIMS instrument for HeLa cells fixed in gluteraldehyde and treated with an isotopically labeled peptide [272], as well as ToF-SIMS images of cells fixed with gluteraldehyde [70, 257] and formaldehyde [154].

A.4.2 Burst mode and 3D imaging of single cells

Another factor that determines the quality of the ToF-SIMS image is sample morphology. Features such as surface roughness, chemical complexity, and heterogeneous structure of the sample can play a significant role in acquiring high resolution images. Recent reviews have highlighted that the nominal mass resolution resulting from not bunching the LMIG analysis beam in the HSR mode strongly limits the capabilities of ToF-SIMS to detect specific biomolecules due to poor mass resolution, especially those ions with inherently low intensities [256]. For example, imaging the $BrdU^-$ molecules in the HSR imaging mode is impossible because their peaks in the mass spectrum cannot be discriminated from the PO_3^- and $H_2PO_3^-$ phosphate peaks. Similarly, phospholipid, amino acid, nucleic acid and carbohydrate peaks strongly interfere with each other in spectra obtained using the HSR mode. To collect an image representative of a particular species when the analysis is done at nominal mass resolution, that species of interest must be the dominant peak at the selected nominal mass. While this happens on occasion, this is usually not the case. On the other hand, the main advantage of the ToF-SIMS technique over other imaging modalities such as MALDI mass spectrometry is its sub-micrometer spatial resolution. Preserving the mass, spatial and depth resolutions is essential for optimal 3D chemical analysis of single cells with ToF-SIMS.

In this investigation, we use burst mode (see Methods section) to acquire ToF-SIMS images of single cells with both high mass and spatial resolutions to produce a more accurate representation of those cells. An example of negative ToF-SIMS spectra obtained with 25 keV Bi_3^+ using three different analysis modes are shown in Figure A.1 for *m/z* 81^-. The figure shows that the $^{81}Br^-$ signal cannot be resolved in the HSR burst alignment mode (top spectrum), making accurate mapping of the BrdU molecule impossible. If this peak were chosen to construct an image, any signal produced by the $^{81}Br^-$ ion would be overwhelmed by the more intense $H_2PO_3^-$

peak. Conversely, the spectrum obtained in HMR bunched mode (bottom spectrum) allows the discrimination of the $^{81}Br^-$ peak from the $H_2PO_3^-$ peak, but the images produced would have poor spatial resolution. Lastly, the spectrum acquired in burst mode (middle spectrum) allows the proper identification of both species while preserving the spatial resolution provided by the HSR imaging mode (see below). The intensity of the $^{81}Br^-$ peak is obtained by summing the intensities of the 6 peaks created in the burst mode (see Methods section for details).

Figure A.3 compares the images obtained in the HMR and burst modes (top and bottom rows, respectively) from the same sample of chemically-fixed HeLa cells. The data recorded in 3D (alternate cycles of imaging with Bi_3^+ and etching with C_{60}^+) but are displayed as the sum of selected 2D images. For the burst mode data, the first 2D image slice was excluded, equating to about 52 nm of material (see below). This was done to decrease the contribution from surface contamination. For the HMR data, slices 50-130 were summed and displayed to best emphasize the $C_xH_yO_z^-$ intracellular features.

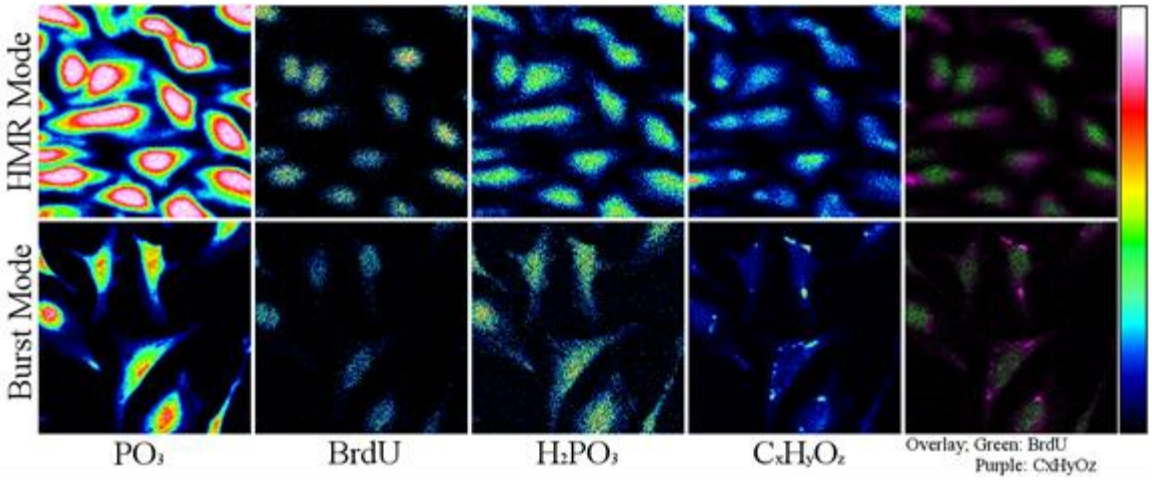

Figure A.3: ToF-SIMS images (Left to right: PO_3^-, $BrdU^-$, $H_2PO_3^-$, $C_xH_yO_z^-$ and an overlay of $BrdU^-$ and $C_xH_yO_z^-$) of HeLa cells acquired from the same sample in HMR mode (top row) and burst mode (bottom row). The images were reconstructed by summing multiple images from the

3D data stack. The images in the top row are 202 x 202 μm^2 and the images in the bottom row are 165 x 165 μm^2.

The advantage of using the burst mode instead of the HMR mode is clearly demonstrated in Figure A.3. In the HMR mode, the secondary ion signals outline the general shape of the cells, however the exact localization of specific chemical species is difficult to visualize. The $BrdU^-$ signal is detected inside the cell nuclei using both operating modes, although with higher spatial resolution in the burst mode. Comparing the $C_xH_yO_z^-$ images (See Table A.S.1 for details of the peaks included in these images) obtained using HMR and burst modes highlight the need for high spatial resolution for optimal ToF-SIMS imaging. The images acquired in the burst mode show the $C_xH_yO_z^-$ fragments are located outside of the cells' nuclei in tightly packed bundles (bottom row, fourth column). The 16-84% line scan across one of these features, shown in Figure A.4, reveals that the spatial resolution in the burst mode is capable of truly sub-micron (~900 nm) imaging in biological cells. In contrast, these structures are largely blurred out in the HMR images. In several cells almost the entire cytoplasmic region appears to contain significant $C_xH_yO_z^-$ signal. In the burst mode, there are multiple small cavities in the PO_3^- image where the phosphate content is significantly lower than in the surrounding area, consistent with a NanoSIMS study that resolved cytoplasmic regions with very low P^- intensity and high CN^- intensity [272]. The sum of $C_xH_yO_z^-$ signals is detected around the cells nuclei and is largely located within these cavities. These cavities are not visible in the HMR images. When compared to fluorescence images from the literature, the $C_xH_yO_z^-$ enriched regions seem to correspond to the Golgi apparatus of the HeLa cells [272]. As Golgi are composed of stacks of membranous cisternae, it is possible that the $C_xH_yO_z^-$ species are fragments of the fatty acids from these cisternae [125]. However, this assignment of the $C_xH_yO_z^-$ species to the Golgi is speculative

since no labeling was used to detect and identify the Golgi locations. Further experiments using labels would be necessary to confirm this identification.

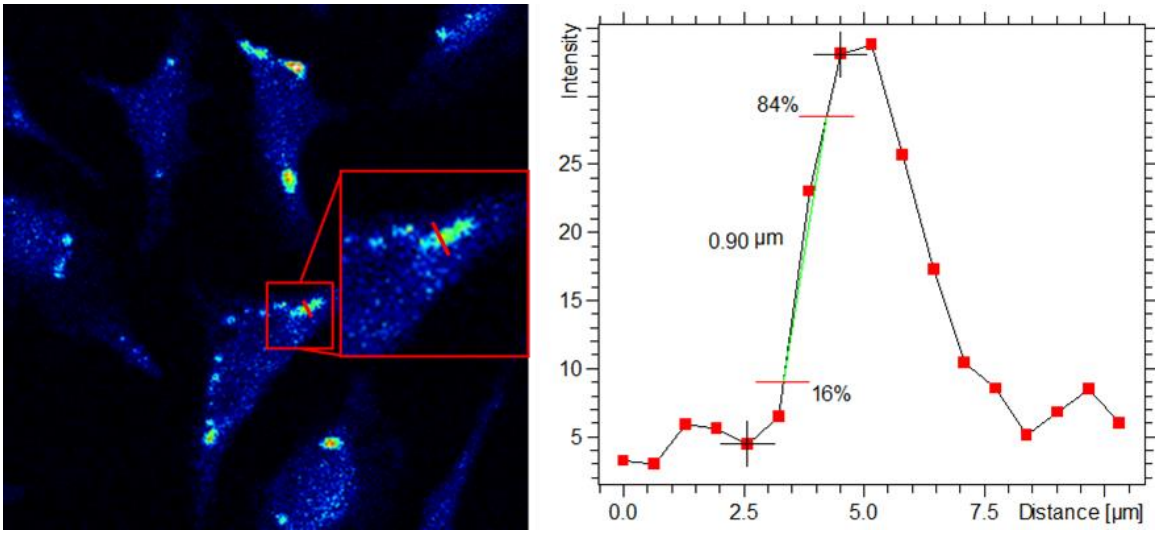

Figure A.4: Left image: Burst mode image of the summed $C_xH_yO_z^-$ species from Figure 3. Inset: Blow up of the portion in the red box. Right image: Line scan across the red line in the left image. The line scan shows that sub-micrometer spatial resolution was achieved using burst mode to collect data from single HeLa cells.

The $C_xH_yO_z^-$-rich domains may also be due to a fixation artifact as paraformaldehyde molecules could be "trapped" inside the HeLa cells during fixation. Paraformaldehyde is also composed of oxygen, carbon and hydrogen ($OH(CH_2O)_nH$ with n = 8 - 100). A $BrdU^-$ (green) and $C_xH_yO_z^-$ (purple) overlay is shown on the far right of Figure 3. It is clear from the burst mode overlay that the structures depicted by the $C_xH_yO_z^-$ signals do not extend to large regions of the cytoplasmic space, as is depicted in the HMR overlay. This suggests that these signals arise from a particular type of organelle and not a species common to the entire cytoplasm.

AFM images of the HeLa cells were also acquired before and after etching (separate data set) with well-defined C_{60}^{q+} dose densities. An example of these AFM images is shown in

Supplemental Figure A.S.1. These images were used to calibrate the depth scale of the corresponding 3D reconstructions and to determine average etching rates. By dividing the thicknesses measured by AFM and correlating the data with C_{60}^{q+} dose density, an estimation of the sputter rate could be obtained. Supplemental Figure A.S.2 shows a similar sputter rate for both paraformaldehyde-fixed and freeze-dried cells when using C_{60}^{+} at 10 keV. Linear fits to data gave a sputter rate of 4 nm per $1x10^{13}$ C_{60}^{+}ions/cm^2 at 10 keV and 9.5 nm per 10^{13} C_{60}^{++} ions/cm^2 at 20 keV throughout the cells. By using these estimated sputter rates, the C_{60} dose density can be converted to approximately 52 nm removed per C_{60} sputter cycle in the burst mode imaging experiments. Some the cells in the 3D burst mode images are completely etched away after 10 cycles. The maximum height of these cells can then be estimated as 520 nm, which is in good agreement with the values found in Supplemental Figure 2 and those in Robinson *et al.* [154]. For other cells the maximum height is estimated to be larger than 520 nm because more than 10 cycles were needed to completely etch the cellular material. It is interesting to note that the C_{60} etching rates of the HeLa cells used here and NIH/3T3 fibroblasts are quite similar (both ~9 nm per 10^{13} C_{60}^{++} ions/cm^2 at 20 keV), despite being different cell types, and data from both studies indicate that there is little difference in the sputter rate between freeze-dried and chemically fixed cells.

Each voxel of the 3D data sets presented in Figure 3 contains a full mass spectrum, meaning that the data set contains $9.2x10^5$ spectra, making it challenging to extract relevant information. This is especially true when all of the stacks are summed and presented in two dimensions. Other ways to present this data are illustrated in Figure A.5. The 3D image in the bottom left of Figure A.5 shows that the first layer, acquired before C_{60}^{+} etching, has a much more intense total ion signal than the rest of the slices. It may be that this is due to surface

contamination or residual cell growth media that was removed by the initial C_{60} etching cycle. The apparent size of the cells decreases as the C_{60}^+ dose increases, indicating that a portion of the cell is removed with each successive C_{60} etching sequence. This decrease partially explains why many signals decline slowly with the increasing C_{60}^+ dose during the full depth profiles of cells in Brison *et al.*[34]. Further identification of sub-cellular features in the 3D image of Figure 5 is difficult. An alternative way to present the data for specific ion signals is to show a z-corrected XZ or YZ vertical cross-section, first demonstrated by Breitenstein *et al.* [70, 257]. A similar method was later applied to HeLa cells where the cells were reconstructed in 3D and the nucleus was discerned from the cytoplasm using DNA molecular signals and PCA [27]. The z-correction is a simple, yet important transformation that displays the mass spectral distribution of non-flat samples more accurately. The major assumption of this correction is that the sputter rate of the sample remains uniform throughout the acquisition, as is shown in this work and by others[154]. The result of this approach is shown in the right part of Figure 5 for the total negative ion signal, the sum of the $C_xH_yO_z^-$ signals, the sum of the $BrdU^-$ signals, and the Si^- signal from the substrate. Based on the values given above, each cross section is approximately 520 nm high and 165 μm long.

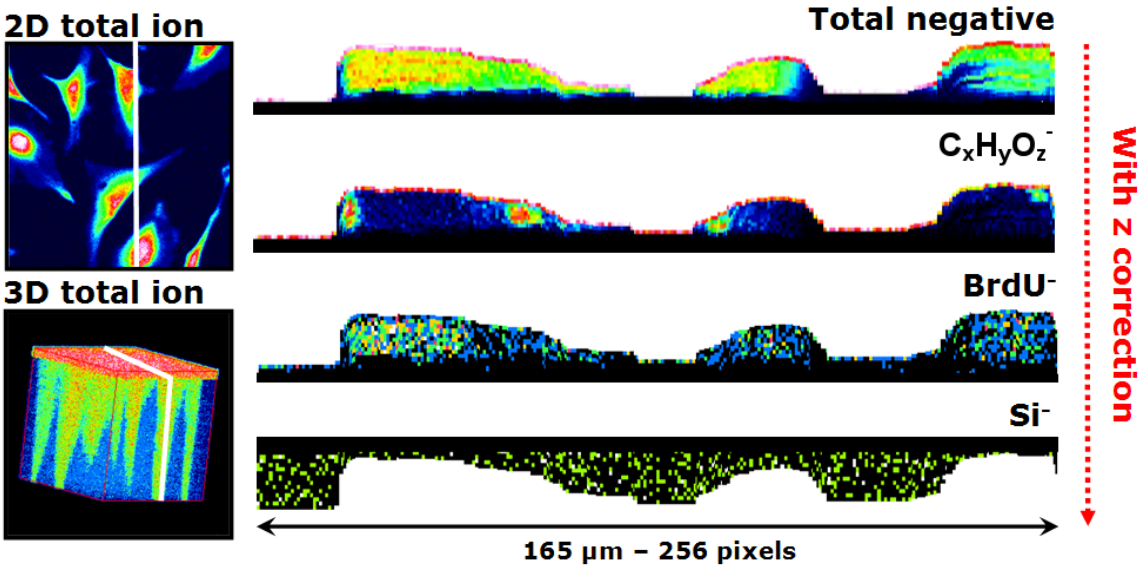

Figure A.5: Negative ToF-SIMS images of HeLa cells**.** Top left: 2D image (total ion) obtained by summing the images from all 14 slices. Bottom left: 3D total negative ion image showing the 14 analysis/etching cycles. This 3D image was not z-corrected. Right: vertical cross-sections for specific ion signals after the z-correction. The position of the vertical cross-section is shown by the white lines in the 2D and 3D images.

The nuclei of the HeLa cells, indicated by the higher intensity of BrdU, are clearly defined. They are surrounded by voxels with lower BrdU intensity that are interpreted as the cytoplasm. The thickness of the cells then decreases gradually outside of the nuclear region. At its outermost extremity, the cytoplasm is approximately 100 nm thick. High $C_xH_yO_z^-$ signals are detected in regions outside of the cells' nuclei. A low intensity region is observed between the area with high $C_xH_yO_z^-$ signal and the nucleus of some cells. This may be the perinuclear region that is rich in phospholipids, observed with positive secondary ions (Figure A.2). Similar cytoplasmic lipid-rich regions have also been observed previously[154, 257] and may be a result of highly membranous organelles surrounding the nucleus.

A comparison of three dimensional, z-corrected images reconstructed from the burst and HMR imaging modes is shown in Figure A.6. An overlay of the $BrdU^-$ and $C_xH_yO_z^-$ fragments from the HMR mode is shown in the bottom left image. Here, the BrdU is easily visualized and localized to the nucleus, but as before, the $C_xH_yO_z^-$ features are not discernible. In the top left a burst mode image plotting the sum of the CN^- and CNO^- fragments clearly shows the location and shape of each cell. In the top right is the burst mode image showing the sum of $C_xH_yO_z^-$ fragments, where the majority of the $C_xH_yO_z^-$ signal is confined to the regions also observed in Figures A.3 and A.5. In the bottom right is the burst mode image of the $BrdU^-$ signal, which is localized to the nuclei. For the burst mode images, the first slice was excluded for clarity. No smoothing or transparency was applied to the images shown in Figure A.6. To accurately visualize the distributions of the $C_xH_yO_z^-$ and $BrdU^-$ species simultaneously, burst mode was required. In the HMR mode, the $BrdU^-$ was localized to the nuclei, but the $C_xH_yO_z^-$ species could not be well discerned. In the HSR imaging mode, the $C_xH_yO_z^-$ fragments were visible, but the $BrdU^-$ fragments could not be separated from the phosphate peaks.

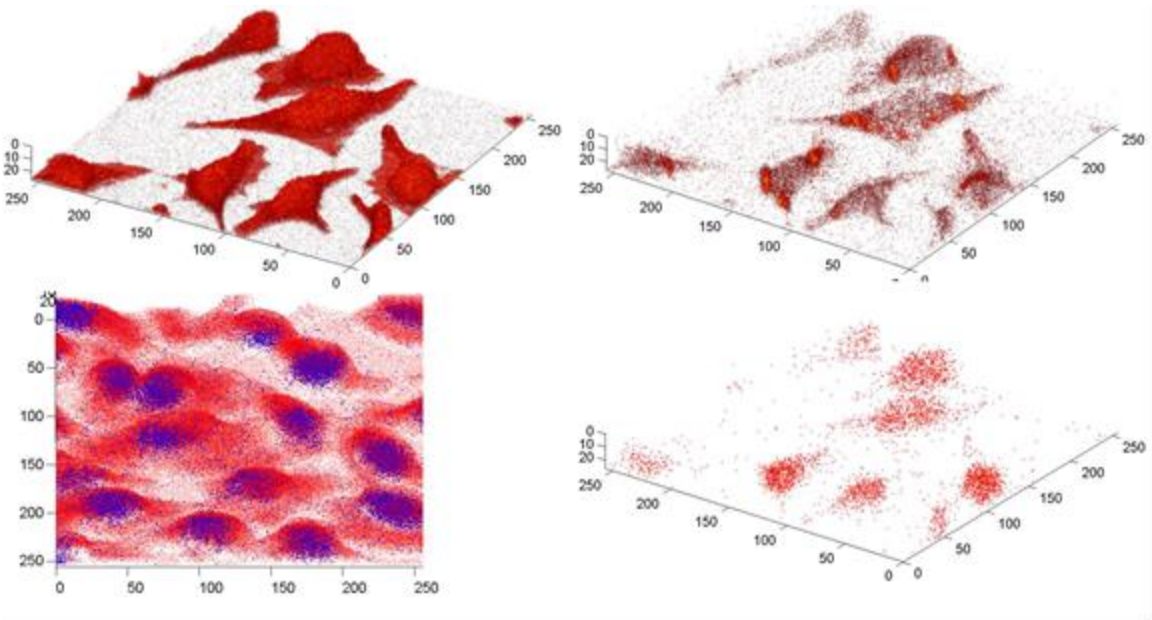

Figure A.6: Z-corrected 3D images of BrdU localized within cells using two different LMIG operating modes. In the bottom left overlay is obtained from the HMR bunched mode with the $BrdU^-$ signal shown in blue and the sum of the $C_xH_yO_z^-$ signals in red. The other three images are burst mode images. The top left: $CN^- + CNO^-$; top right: $\Sigma C_xH_yO_z^-$; bottom right: $\Sigma BrdU^-$. The bottom left image is 202 x 202 μm^2 and contains 24 slices. The burst mode images are 165 x 165 μm^2, and contain 26 slices.

This work has shown the benefit of doing analysis with simultaneous high mass and spatial resolution (burst mode), however this mode is limited in everyday use because the primary ion current is very low. A typical current for the burst alignment mode is 0.05 pA, which can produce images with sufficient chemical contrast in a few minutes. For the burst mode, this current is reduced to less than 0.01 pA. Acquisition times increase dramatically with such a low current.

A.5 Conclusions

In this study important parameters influencing the quality of ToF-SIMS images of biological cells were investigated. 3D ToF-SIMS data sets of HeLa cells with incorporated BrdU and subcellular spatial resolution were described. High-resolution spectra and images of the HeLa cells were acquired in different LMIG operating modes and were compared. The results show that images acquired with both high mass and spatial resolutions are necessary to properly assign secondary ion species and to image subcellular regions. When using the "burst mode" where the Bi_3^+ beam is not bunched, but contains bursts of short pulses, BrdU-rich nuclei and subcellular regions with high concentration of oxygen containing fragments (i.e., $C_xH_yO_z^-$) were observed. The BrdU and $C_xH_yO_z^-$ regions were also observed in the high mass resolution mode (low spatial resolution), but visualization of their specific location inside the cells was difficult. The sputter rate was observed to be constant during the C_{60}^+ depth profiling of the cells, allowing

a depth scale to be applied to the 3D data cubes, more accurately revealing the locations of the cells' nuclei and of other intracellular species of the HeLa cells.

Acknowledgment

This research was supported by NIH grants EB-002027 and EB-006163. The AFM measurements were done at the University of Washington Nanotechnology User Facility, a member of the NSF National Nanotechnology Infrastructure Network. JB was supported by the National Fund for Scientific Research (FRS-FNRS) and DB was supported as a Merck Fellow of the Damon Runyon Cancer Research Foundation (#DRG 1948-07).

This manuscript was submitted to *Analytical Chemistry* on July 24, 2013.

A.6 Supplemental Information

ToF-SIMS 3D Imaging of HeLa Cells

Jeremy Brison,[1,3*γ] Michael A. Robinson,[1,2γ] Danielle S.W. Benoit,[3†] Shin Muramoto,[1,2°] Patrick S. Stayton,[3] David G. Castner[1,2,3§]

[γ]These authors contributed equally to this work.

National ESCA and Surface Analysis Center for Biomedical Problems[1],

Departments of Chemical Engineering[2] and Bioengineering[3], University of Washington, Seattle, WA 98195-1653

[*]Current affiliation: IBA Medical Accelerators Solutions, Belgium

[†]Current affiliation: Departments of Biomedical Engineering and Chemical Engineering, University of Rochester, Rochester, New York 14627

°Current affiliation: National Institute of Standards and Technology, Gaithersburg, Maryland 20899

[§]Corresponding Author:

David G. Castner

1-206-543-8094 (phone)

1-206-543-3778 (fax)

castner@uw.edu (e-mail)

Supplementary material

Table A.S.1: The list of positive and negative secondary ions used in Figures 3, 4, 5. The peaks and assignments were taken from [273, 274].

Positive mode	*Ion*	*m/z*	*Origin*
Phospholipids	$C_3H_8N^+$	58.06	Phosphocholine head group
	$C_5H_{12}N^+$	86.10	PC HG
	$C_2H_6PO_4^+$	125.00	PC HG
	$C_5H_{13}NPO_3^+$	166.06	PC HG
	$C_5H_{15}NPO_4^+$	184.07	PC HG
	$C_8H_{19}NPO_4^+$	224.08	PC HG
Negative mode	*Ion*	*m/z*	*Origin*
BrdU	$^{81}Br^-$	80.93	Bromodeoxyuridine
	$C_4H_2N_2O_2{}^{79}Br^-$	188.93	Bromodeoxyuridine
	$C_4H_2N_2O_2{}^{81}Br^-$	190.93	Bromodeoxyuridine
$C_xH_yO_z^-$	C_2HO^-	41.00	
	$C_2H_3O^-$	43.02	
	CHO_2^-	45.00	
	$C_3H_3O^-$	55.02	
	$C_2H_2O_2^-$	58.00	
	$C_2H_3O_2^-$	59.01	
	$C_3HO_2^-$	69.00	
	$C_3H_3O_2^-$	71.02	
	$C_4H_3O_2^-$	83.03	

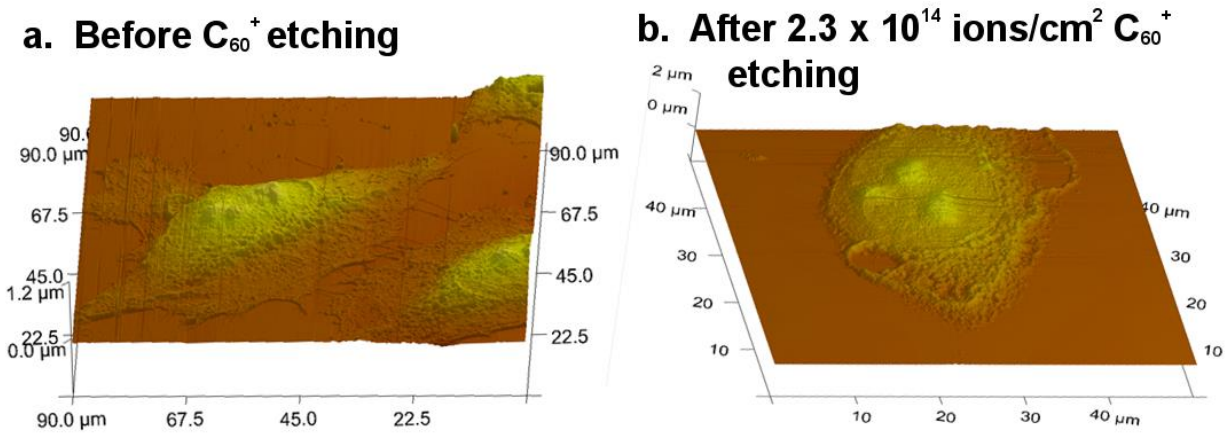

Figure A.S.1: AFM topography images of HeLa cells fixed in 4% paraformaldehyde (a) before C_{60}^+ etching and (b) after etching with 2.3 x 10^{14} ions/cm^2 of C_{60}^+.

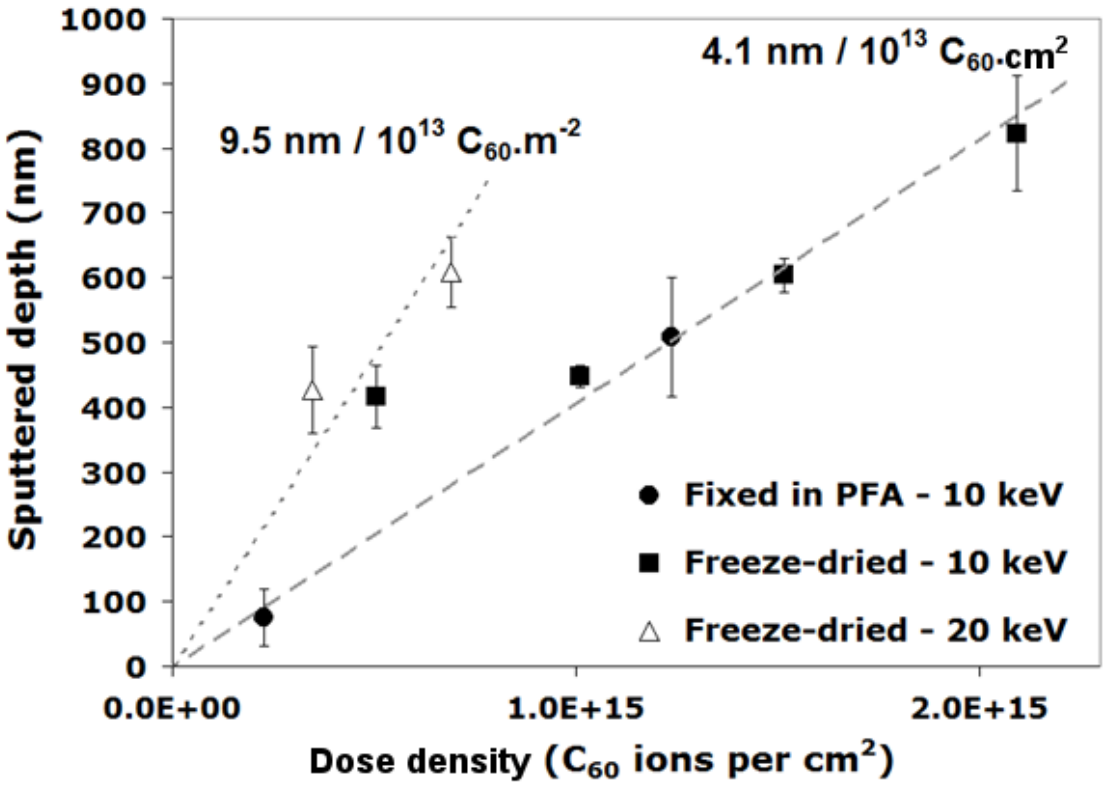

Figure A.S.2: Etching rates of HeLa cells by 10 keV and 20 keV C_{60}^{q+} ions at an incident angle of 45°. The cells were rinsed with ammonium acetate and either fixed in paraformaldehyde (n=6) for freeze-dried (n=14). The thicknesses of several cells, before and after etching, were measured using AFM.

Appendix B. Miscellaneous projects/work

B.1 3D Imaging of AuNPs in NIH/3T3 fibroblasts

Michael Robinson, Sirne Techane

B.1.1 Background

Gold nanoparticles (AuNPs) are increasing in popularity as possible diagnostic and therapeutic agents for a variety of illnesses [275]. AuNPs have been reproducibly synthesized with diameters of single nanometers to microns with low polydispersities [276]. They are readily functionalized with a variety of ligands, ranging from polyethylene glycol (PEG) to entire proteins [174].

AuNPs of a range of sizes and functional groups are readily taken up by many cells types, including tumor cells [277, 278]. Imaging is necessary to determine the location of the AuNPs as they are taken up, if they are taken up at all. For many applications AuNPs have specific targets, whether that be a particular cell types or region with a cell [279]. Transmission electron microscopy (TEM) [280] and confocal microscopy [281] have been used to localize AuNPs in cells or tissues. TEM can provide organizational information of the area around the AuNPs, but it cannot provide additional molecular information. AuNP detection using confocal microscopy can be quantitative [282], although this method also does not provide any additional chemical information.

Recently, confocal Raman microscopy was used to map the location of AuNPs within single cells after various incubation times [167]. The organic material from the cell was readily distinguished by imaging the C-H stretches and the gold was visible due to its unique

photoluminescence peak. While 3D representations were successfully constructed, little supplementary information about the cell was obtained. ToF-SIMS may have the ability to produce accurate 3D images that localize AuNPs in single cells and provide chemical information regarding a cell's biological reaction to the AuNPs. To that end, a recent study used confocal Raman spectroscopy to map silver nanoparticles in single cells, and used Laser-SNMS also saw signs of oxidative stress in the plasma membranes of the dosed cells in the ToF-SIMS data [283].

The goal of this work was to use ToF-SIMS depth profiling capabilities to successfully create an accurate 3D reconstruction of AuNPs within single NIH/3T3 fibroblasts. This data could then be compared with previous data sets of the same cell line to potentially determine stresses on the cell upon AuNP uptake, in addition to the localization information particles.

B.1.2 Experimental

B.1.2.1 AuNP synthesis

24.2 +/- 4.3 nm AuNPs were synthesized using the procedure in Techane *et al.* [284]. Briefly, the method developed by Niidome *et al.* [285] was used to produce C2 NH_2-SAM-AuNPs, and then the AuNPs were functionalized with C11 NH_2-thiols through a ligand-exchange process.

B.1.2.2 Cell growth and preparation for ToF-SIMS analysis

NIH/3T3 fibroblasts were grown on 1 cm x 1cm silicon chips that were previously cleaned with 2x five minute successive sonications in dichloromethane, acetone and methanol. Cells were seeded and allowed to grow for 24 hours, then AuNPs were introduced into the

growth media at a concentration of approximately $2x10^{13}$ AuNPs/ml. 100 µL of AuNPs in water was added to 900 µL of cell media, and the mixture replaced the previous media. The cells were grown for an additional 24 hours. At 48 hours, the samples were rinsed with 150 mM ammonium acetate (AA), fixed in 4% formaldehyde for 30 minutes, rinsed again with AA and air dried overnight. The samples were loaded into the ToF-SIMS instrument the following morning.

B.1.2.3 ToF-SIMS

Negative secondary ion spectra were collected with an ION-TOF TOF SIMS 5-100 instrument (ION-TOF, Münster, Germany), using a pulsed 25 keV Bi_3^+ primary ion beam in the high spatial resolution mode. Samples were sputtered with a 20 keV C_{60}^{++} beam. Both the Bi and C_{60} beams are oriented 45° normal to the surface. The Bi_3^+ current was 0.04-0.05 pA and had an 80.1 ns pulse width. The C_{60}^{++} current was 0.35 nA and the sputter dose varied. Negative spectra were mass calibrated using the CH^-, OH^-, Au^- peaks. Secondary ions were collected over a range of 0–850 m/z. The high spatial resolution mode had nominal mass resolution. Low energy electrons were flooded onto the sample to compensate for charge buildup on the surface. All data was collected and analyzed using the IONTOF Surface Lab 6 software.

The data was collected for the 3D images using the dual beam approach. Analysis slices used a Bi_3^+ dose of $2.3x10^{11}$ ions/cm^2. A C_{60}^{++} dose of 2.5×10^{13} ions/cm^2 was used to sputter material in between analysis cycles, removing roughly 20 nm of organic material per cycle (See Chapter 5).

3D images were created by first doing a z-correction to the data stack using the ZcorrectorGUI (Dan Graham, NESAC/BIO, University of Washington) within MATLAB, then

every image slice in the corrected stack was exported as a .png file. The .png files were imported into ImageSurfer 1.27 (Computer Integrated Systems for Microscopy and Manipulation, University of North Carolina), and the two-color 3D images were created.

B.1.3 Results

B.1.3.1 2D image of AuNPs within NIH/3T3 fibroblasts

A 2D ToF-SIMS image of AuNPs localized within single cells is shown in Figure B.1. The green color represents the Cl^- signal and is indicative of cellular material. The purple color represents the summation of gold related peaks (m/z Au^-, Au_2^-, Au_2CN^-, Au_3^-). This image was acquired after a C_{60}^{++} dose of $6.4x10^{14}$ ions/cm^2, which removed an estimated 600 nm of organic material prior to this image acquisition.

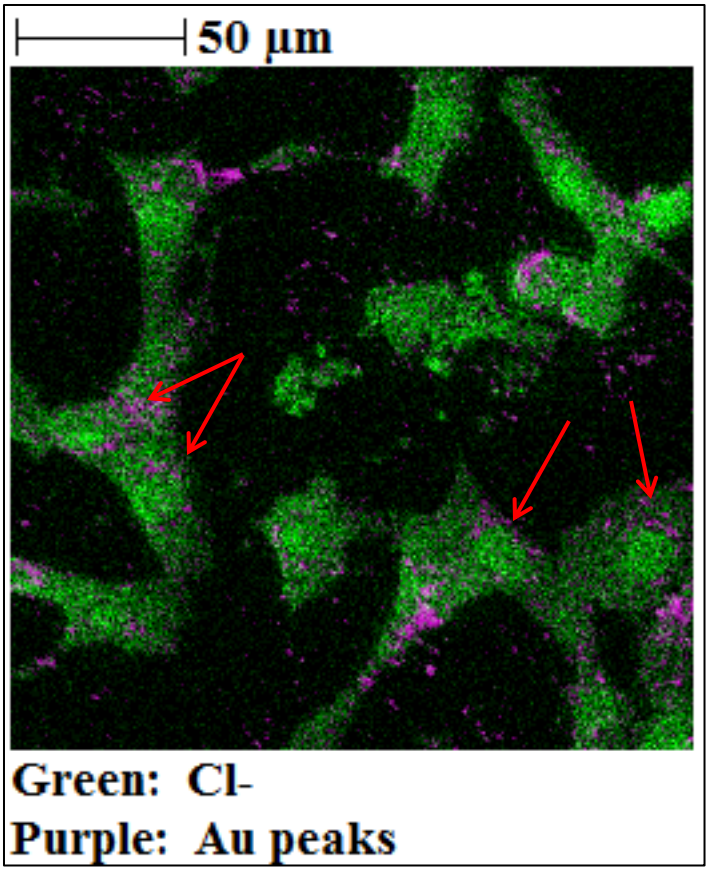

Figure B.1 AuNPs imaged within NIH/3T3 fibroblasts by ToF-SIMS. The green color represents Cl^- and the purple color represents a summation of the Au peaks. The image is 203 µm x 203 µm and contains 256 x 256 pixels. The image was acquired after a total C_{60}^{++} dose of $6.4x12^{14}$ ions/cm^2, which removed an estimated 600 nm of organic material.

In Figure B.1, the red arrows indicate regions of perinuclear localization, which has been previously shown with intracellular AuNPs [286]. It is possible that some of the AuNPs are simply sitting on top of the plasma membrane of cells and are not removed during sputtering. There is some Au signal originating from regions outside of the cellular material, which are likely AuNPs on the substrate that were not removed during the rinsing steps.

B.1.3.2 3D reconstruction of AuNPs within NIH/3T3 fibroblasts

A 3D reconstruction was attempted using dual beam depth profiling and the ZcorrectorGUI software, and the results are shown in Figure B.2 A and B. The green color represents the PO_3^- signal intensity and is indicative of cellular material. The red color represents the location of Au-related peaks. A C_{60}^{++} sputter dose of $2.5x10^{13}$ ions/cm^2 was used in between analysis cycles, which removed roughly 20 nm of organic material per sputter cycle. On this particular spot, no gold signal was detected outside of the cells. The cells in Figure B.2 were on the same sample as in Figure B.1.

During the depth profile experiment, gold was revealed when the organic material above it was sputtered away. From Figure B.2 B, it is clear that 20 keV C_{60}^{++} is inefficient when attempting to remove these gold nanoparticles. In the 2D images (not shown), it is clear that no signals arising from the gold disappear with successive sputter cycles, although new gold signals do appear.

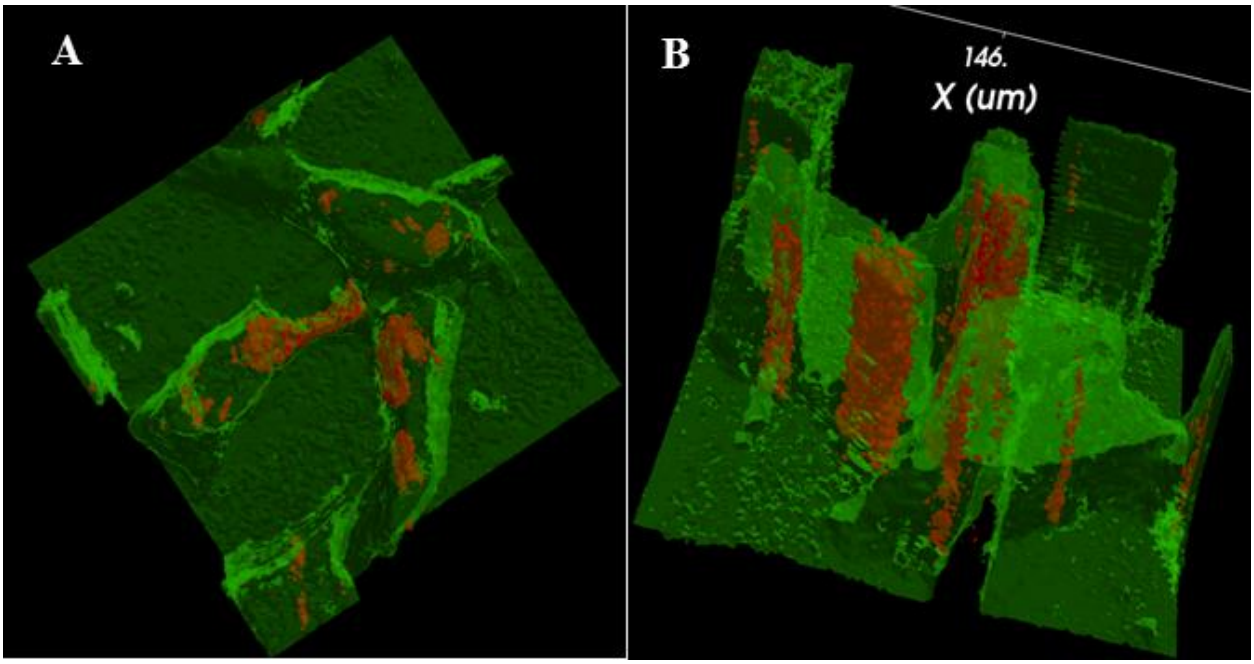

Figure B.2 A 3D reconstruction of AuNPs within NIH/3T3 fibroblasts, imaged by ToF-SIMS dual-beam depth profiling. Green represents PO_3^-, red representation a summation of Au-related peaks. The PO_3^- channel was made semi-transparent in order to better visualize the intracellular AuNP signal. Images are 100 µm x 100 µm. The image stack consists of 55 slices, with a Bi_3^+ dose of $2x10^{11}$ ions/cm^2 used for each analysis slice. A dose of $2.5x10^{13}$ C_{60}^{++} ions/cm^2 was used for each sputtering cycle, which removed roughly 20 nm of organic material per cycle.

B.1.4 Current hurdles and future experiments

The major hurdle to successfully reconstructing a 3D image of intracellular AuNPs is that 20 keV C_{60}^{++} is not efficient at removing the AuNPs. A recent study shows that an ion dose of $5x10^{18}$ ions C_{60}^{++}/cm^2 removed 20 nm of AuNP material on a silicon substrate [287], which is about 20x larger than the sputter rate of the organic cellular materials. There are several alternatives that may remedy this problem in the future.

The first is to use a NanoSIMS instrument (dynamic SIMS), which should be able to etch through AuNPs. The primary ion source is a Cs^+ beam, which outputs a DC ion beam for analysis. Most molecular information is destroyed when a DC beam like this is used, but this should be able to localize the AuNPs within a cell, and maintain depth information. ToF-SIMS could be done on the same sample (different cell) to acquire additional molecular information.

A second alternative is to use a higher energy C_{60} beam, which may be able to sputter the AuNPs more efficiently. This would be the ideal solution because it reduces the complexity of the experiment and requires one instrument instead of two.

A third option is to try adding a lower concentration of AuNPs to the media, so that less AuNPs enter the cell. The less intracellular gold material there is in the cell, the lower the

sputtering dose must be used to remove it. Since C_{60}^{++} has been shown to be able to remove AuNPs, it is worth trying the experiment again using higher C_{60}^{++} ion doses.

B.2 3D imaging of complex materials with non-uniform sputter rates: onion skin cell

Michael Robinson

B.2.1 Background

For the continuation of the 3D imaging work in Chapter 5, the next logical step for the ZcorrectorGUI is to add the capability to correct for the heterogeneous sputter rates. A sample was required that contained several regions with different sputter rates. A plant cell was chosen because of a previous dynamic SIMS study that showed the cell wall and nucleus had 1.5x and 1.2x lower sputter rates compared to the cytoplasm, respectively [173]. This is not surprising, as the function of the cell wall is to provide rigidity to the plant cell. It is composed of the complex polysaccharides cellulose and xylan, and also contains lignin. An onion cell was chosen because there is a straightforward method to peel off a monolayer of cells from the onion.

B.2.2 Experimental methods

B.2.2.1. Cell preparation

A monolayer of onion cells was peeled off of a red onion and placed onto a 1 cm x 1cm silicon substrate. A monolayer of cells may be peeled on the back of a piece of onion. The sample was rinsed in 150 mM ammonium acetate and then fixed in 4% formaldehyde in 1X PBS for 30 minutes. Pieces of the monolayers of cells tend to roll up, but when placed in the rinsing solutions flatten and float on the top of the liquid. After fixation, the sample was rinsed very

gently in 150 mM ammonium acetate. The sample was dried in air overnight in a laminar flow hood and placed into the ToF-SIMS instrument the following morning.

B.2.2.2 ToF-SIMS

See Section B.1.2.3 for ToF-SIMS instrument details.

Data was collected in the dual beam mode. Bi_3^+ in the high spatial resolution mode was used for analysis and C_{60}^{++} was used for sputtering. The Bi_3^+ current was 0.04 pA and the C_{60}^{++} current was 0.5 nA. Analysis cycles used a $4x10^{11}$ Bi_3^+ ions/cm^2 dose, while the sputtering cycles used a $7.5x10^{13}$ C_{60}^{++} ions/dose. Based on previous experiments with NIH/3T3 fibroblasts, 10 nm of material was removed with a C_{60}^{++} sputter dose of $1.25x10^{13}$ ions/cm^2 (see Chapter 5). The analysis size was 100 µm x 100 µm, and the sputter area was 300 µm x 300 µm. Low energy electrons were flooded onto the surface to compensate for charge buildup.

B.2.2.3 AFM

To measure the height of the dried cells before ToF-SIMS analysis, a Dimension ICON (Bruker, Santa Barbara, CA) AFM was used in ScanAsyst® mode in air with a silicon nitride, ScanAsyst-Air tip. Raw AFM data was imported into the NanoScope Analysis software and a second order plane fit was applied to all images. No further modifications were applied to the images.

B.2.3 Results

B.2.3.1 Finding the same cell in the AFM and ToF-SIMS instruments

The same cell was located in both the AFM and ToF-SIMS. An Optical image from the AFM is shown in Figure B.3 A and one from the ToF-SIMS is shown in B.3 B. The red arrows indicate the nucleus of the same cell in the images.

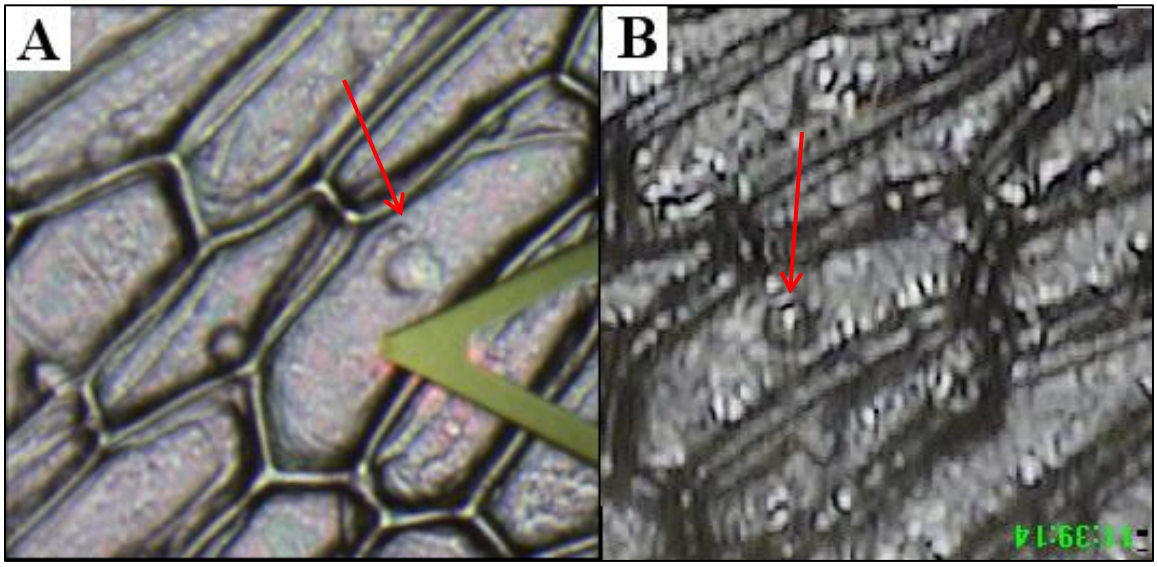

Figure B.3 Optical images of the same cell from (A) the AFM instrument, and (B) the ToF-SIMS instruments. The images in A and B are estimated to be 225 µm x 225 µm. The red arrows indicate the nucleus of the same cell in both images.

B.2.3.2 AFM and ToF-SIMS comparison

A 3D topography map of a portion of the onion cell seen in Figure B.3 is shown in Figure B.4 A. A portion of the cell wall is captured (green/white area), as well as the nucleus (blue) and cytoplasm (red). The height ranges from 0 to 5.5 µm as the color changes from red to white. The nucleus is 1.8 µm at the highest point, while the green area of the cell wall is 3.7 µm tall. A 3D reconstruction of the ToF-SIMS data is shown in B.4 B. The images in A and B are oriented the same direction. The nucleus is visible in both in both images, and the portion that overlaps is

the area above the nucleus. The 3D reconstruction shows that C_{60}^{++} was able to successfully sputter through a large portion of the onion's cell wall. There was some leftover material at the end of the data acquisition period which had very high Na^+ and K^+ signals, as well as very low organic signals. This has been attributed to the inability to remove all of the buffer salts after the chemical fixation, due to the very gentle rinsing used

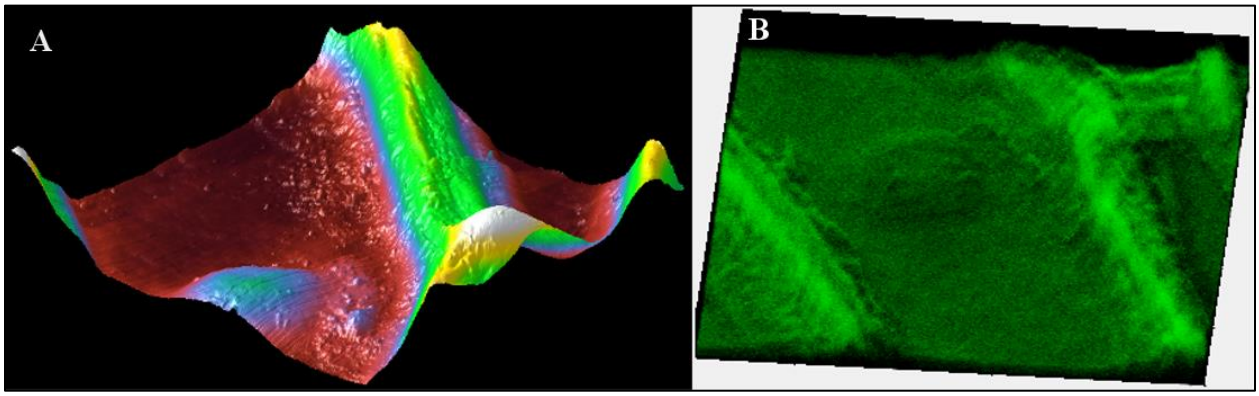

Figure B.4 (A) This is a three dimensional topography image of a portion of a single onion cell, produced by AFM. The cell was fixed in formaldehyde for 30 minutes and air dried. The height ranges from 0 to 6 µm as the color moved from red to white. (B) Corrected ToF-SIMS 3D data stack. m/z 81^+ is displayed. Pixels with the intensities 3-10 are displayed, and made semitransparent. There are 187 images in the ToF-SIMS data stack, all of which are 100 µm x 100 µm. The AFM image is 80 µm x 80 µm.

Figure B.5 shows the ToF-SIMS corrected data and AFM height profile from two perpendicular slices of the cell. In A and C are the corrected ToF-SIMS data slice and corresponding AFM height profile, respectively. B is the corrected ToF-SIMS data from a separate slice, and D is its corresponding AFM height profile. The inset in A shows the locations of the plotted slices. The slice in A and C is for the section of cell wall separating two adjacent cells, or the "ridge". The slice shown in B and D is oriented 90° to the previous line and includes the nucleus. The mass fragment $C_5H_3^+$ is plotted in A and C.

The cross-section in A qualitatively matches the shape of the height profile in C. The two relative maximums in the cell wall ridge, visible in Figures B.4 A and B.5 C are also visible in the ToF-SIMS corrected slice in B.5 A. On the left side of A, which is the cytoplasmic region of the cell, 3 layers are visible. The top layer is rich in $C_5H_3^+$, the middle layer is thinner and depleted of $C_5H_3^+$, and the bottom layer also contains relatively high amounts this fragment. Most of the ridge section also displays a high intensity of $C_5H_3^+$, which could be indicative of the cell wall. Since a cell should be totally surrounded by the cell wall, it is not surprising to see it above and below the "void" space of the cytoplasm. It is expected that a unique signal from the cell wall would also be intense throughout sections that line the sides of the cell. The rigidity of these areas is retained after dehydration, and the subsequent reduction in height is not as severe as in the cytoplasm.

The slice displayed in B and D goes through the nucleus, but not a cell wall ridge. At a glance, the shape of the AFM height profile in D matches the ToF-SIMS data. In B, the 3 layer pattern is again visible in the cytoplasmic region. Within the nucleus there is a larger region depleted of $C_5H_3^+$, further suggesting that this ion is indicative of the cell wall.

Without further experiments, it is difficult to determine if the sputter rate is constant throughout the data acquisition. It is not expected to be constant in the regions that transition from cell wall to cytoplasm, but the sputter rate may be constant for the cell wall ridges, as they do not encounter these transitions.

The cell wall ridge is being sputtered, on average, at a slower rate than the nucleus. The cytoplasm is removed after about 50 cycles in regions near both the nucleus and the ridge. Once this "baseline" is removed, it take 40 cycles to remove the rest of the nucleus and 100 scans to

remove the rest of the ridge. The heights of the nucleus and ridge are 1.8 and 2.7 µm, respectively. Thus, the nucleus is removed at a rate of 45 nm/ sputter cycle and the ridge is removed at 37 nm/ sputter cycle, an 18% difference. Interestingly, this is very near same sputtering rate difference found with dynamic SIMS experiments of radish root tip cells [168].

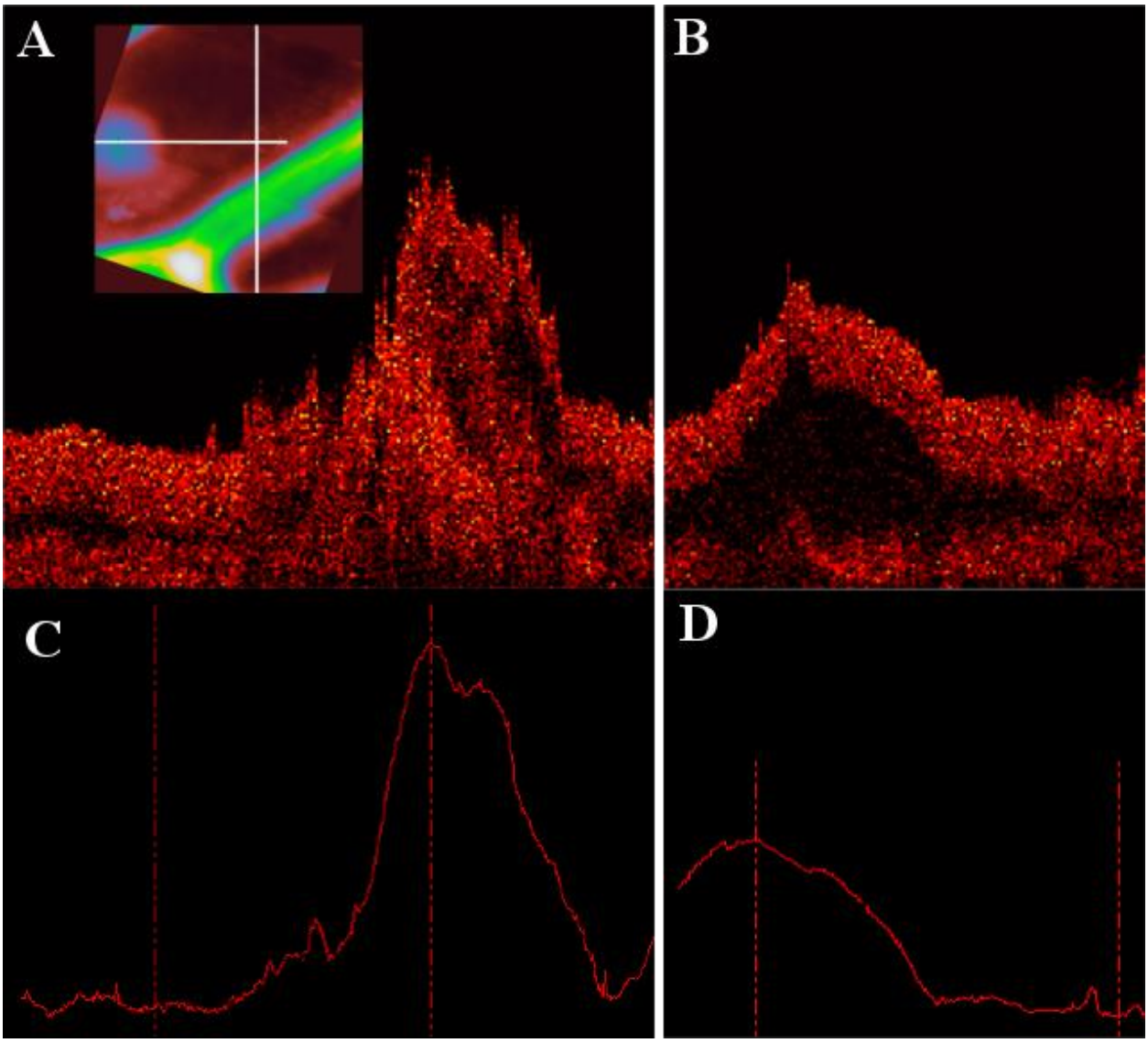

Figure B.5 A comparison of ToF-SIMS corrected data and AFM height profiles across two perpendicular lines. The mass fragment $C_5H_3^+$ is plotted in A and C. The inset in A shows the locations of the slices. There are 187 slices in the ToF-SIMS data stack. (A) ToF-SIMS

corrected data. (B) ToF-SIMS corrected data, perpendicular to the line from A. (C) AFM height profile from the same line as A. The maximum height is 3.7 μm. (D) AFM height profile from the same line as B. The maximum height is 1.8 μm.

B.2.4 Current hurdles and future experiments

An improved rinsing procedure must be developed to remove salt material encountered during the acquisition (the fixing buffer contains NaCl), a better rinsing procedure should be developed to remove these.

Additional experiments with multiple AFM scans are necessary to determine the sputtering rate of the cell wall and cytoplasm. An initial AFM scan would provide the topography of the cell with respect to the flat section of the cell. Then, after enough sputter cycles to completely remove this material, a second AFM scan could provide the height of that section.

B.3 Chemical mapping of lactating mouse breast tissue

Michael Robinson

B.3.1 Background

To our knowledge, the distribution of molecular species has not yet been mapped in lactating mouse breast tissue. The mouse tissue is a simpler "model" system compared to human breast tumor samples.

B.3.2 Materials and Methods

B.3.2.1 Tissue preparation

A Frozen mouse tissue block, stores in a -80 °C was sectioned using a cryomicrotome. See Section 5.2.1 for details on the cryomicrotome. Four μm thick slices were placed onto

previously cleaned silicon substrates and air dried. An adjacent section was sliced and was stained with hematoxylin and eosin (H&E).

B.3.2.2 ToF-SIMS

See Section B.1.2.3 for ToF-SIMS instrument details.

HMR and HSR data were collected. A 3.2 mm x 4 mm large area raster "patch" was collected in the HSR mode. The patch contained 80 total tiles. Each tile was 400 µm x 400 µm and contained 256 x 256 pixels. 100 analysis scans were collected for each tile. The total acquisition time of the patch was 52,429 seconds (14.6 hours). The patch had 2560 x 2048 pixels. The approximate analysis area of the patch is shown in Figure B.6, represented by the box drawn on the adjacent H&E stained tissue slice.

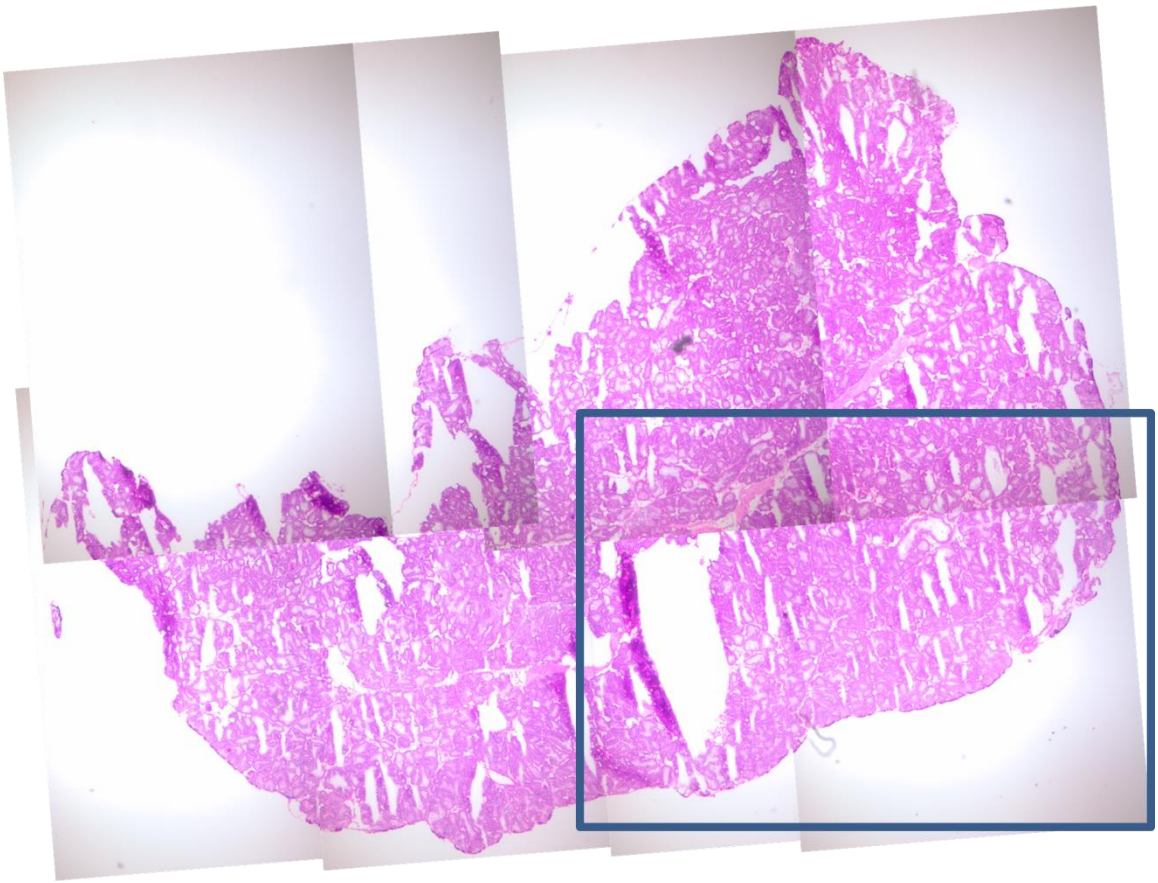

Figure B.6 Approximate analysis area of the large patch on the lactating mouse breast tissue. The H&E stained tissue was an adjacent slice. Box measures approximately 3.2 mm x 4 mm.

B.3.3 Results

Three color overlays of the tissue slice are shown in Figures B.7 and B.8. Unique distributions of phosphocholine, cholesterol, and DAGs were observed. In both Figures, the blue (m/z 579^+ and 607^+) and green (m/z 439^+, 465^+, 495^+ and 523^+) colors represent two different groups of DAGs. In Figure B.7, the red color represents phosphocholine (m/z 184^+), whereas in Figure B.8 red represent cholesterol (m/z 369^+). Peak identifications are found in Table B.1.

There are four distinct regions displayed in the image overlays. Two regions contained separate DAG profiles. The first, colored green, contained DAGs with shorter 10, 12 and 14 carbon length alkyl chains. These regions may be milk generating ducts. The second region, colored blue, contains mostly DAGs with longer 18 carbon length alkyl chains. These regions may be representative of adipocytes. A zoomed-in view of these regions is shown in Figure B.9. The structures visible in the chemical image are also visible in the adjacent H&E-stained section. Figure B.10 shows the spectra from three different regions-of-interest (ROI) from an area on the same tissue slice as the large patch, but not within the patch. The ROI's were chosen to match the color scheme in Figure B.7. The "red" region is rich in phospholipids, the "green" region rich in DAGs with short alkyl chains, and the "blue" region is rich in DAGs with longer alkyl chains.

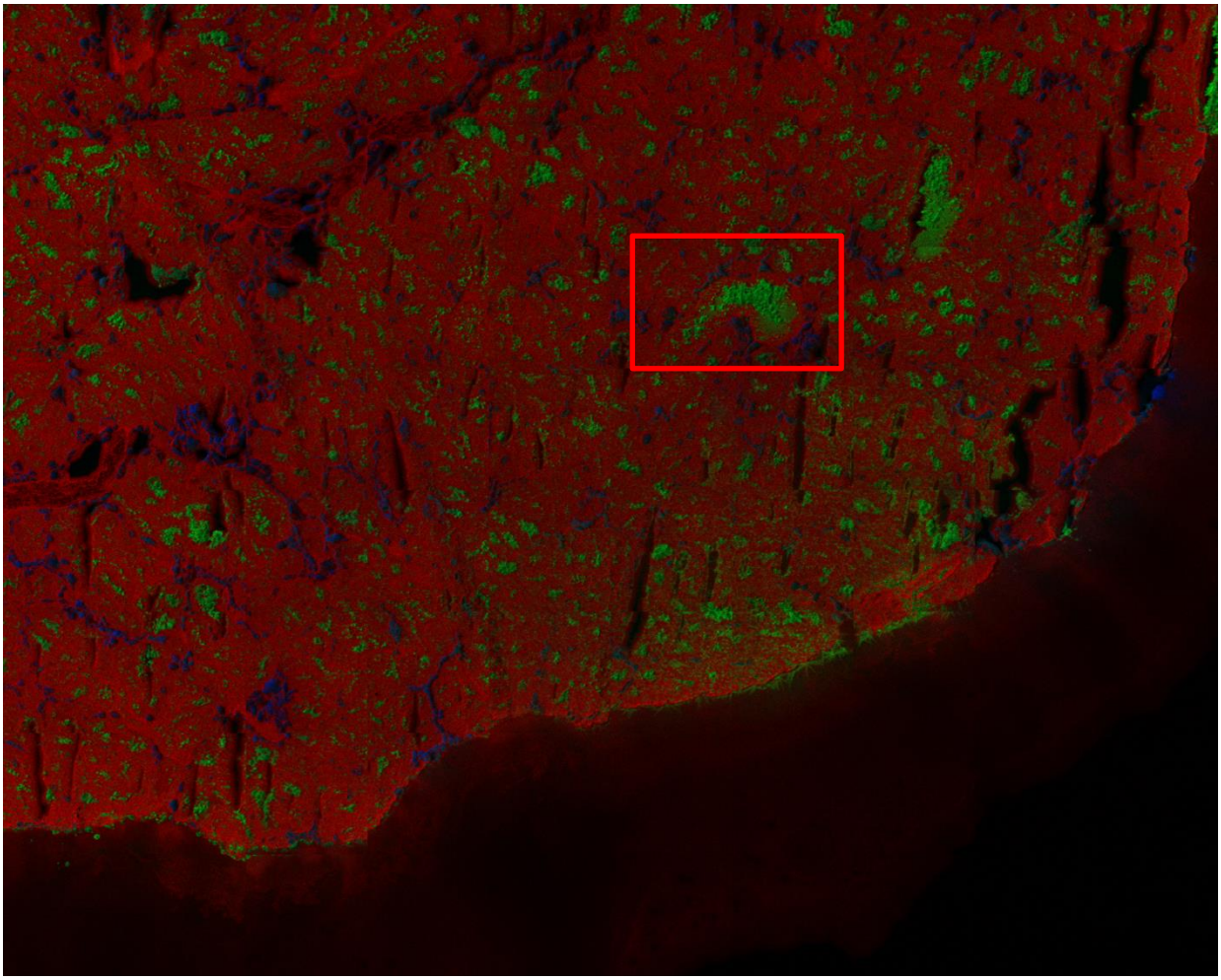

Figure B.7 Three color overlay of lactating mouse breast tissue. Image is 3.2 mm x 4.0 mm. Red: Phosphocholine, m/z 184^{+}; green: DAGs 22:0. 24:0. 26:0, 28:0 at m/z 439^{+}, 465^{+}, 495^{+} and 523^{+}; blue: DAGs 34:0 and 36:0 at m/z 579^{+} and 607^{+}. The image is 3.2 mm x 4.0 mm and contains 80 (8 x 10) 400 µm x 400 µm tiles.

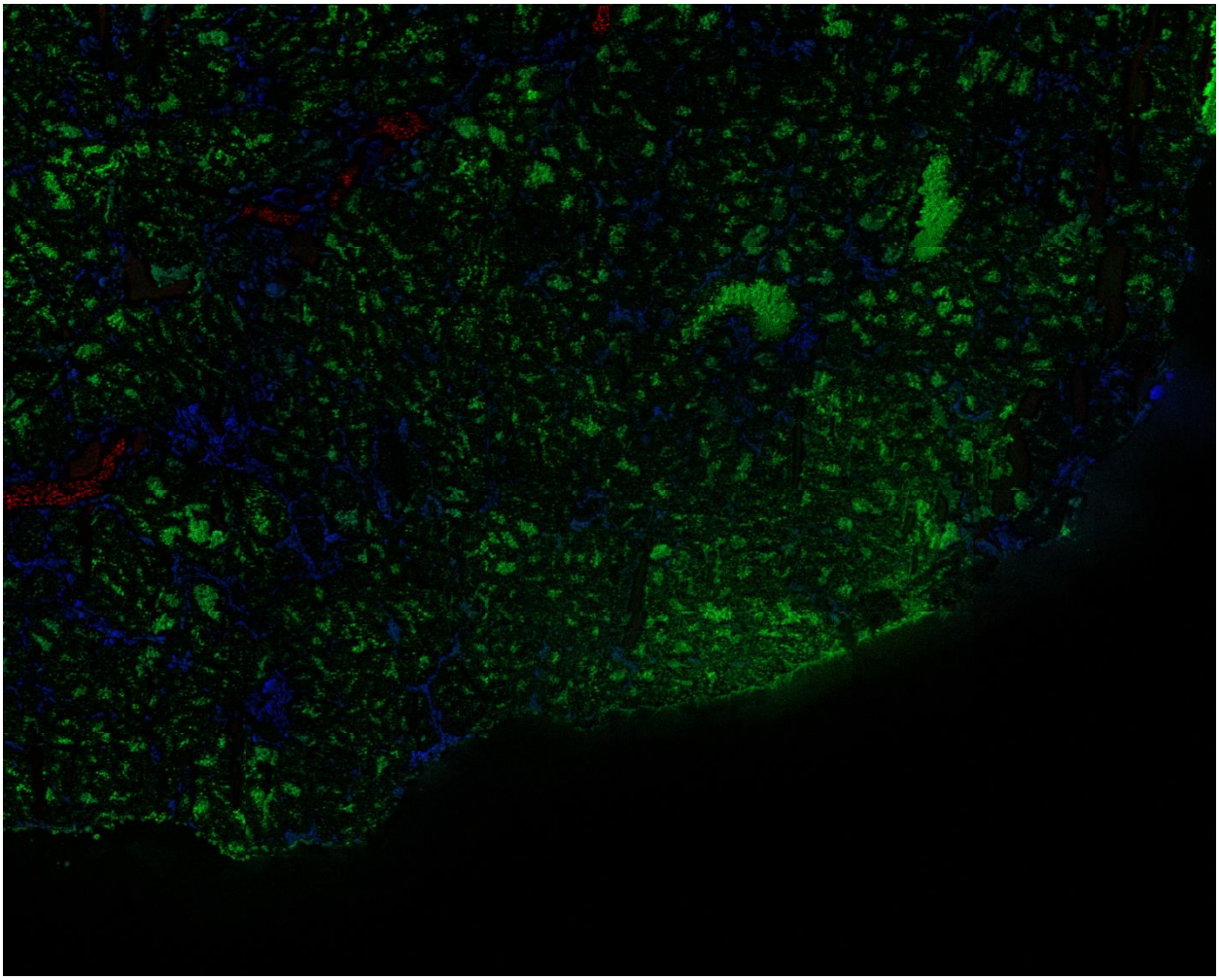

Figure B.8 Three color overlay of lactating mouse breast tissue. Red: cholesterol, m/z 369^{+}; green: DAGs 22:0. 24:0. 26:0, 28:0 at m/z 439^{+}, 465^{+}, 495^{+} and 523^{+}; blue: DAGs 34:0 and 36:0 at m/z 579^{+} and 607^{+}. The image is 3.2 mm x 4.0 mm and contains 80 (8 x 10) 400 µm x 400 µm tiles.

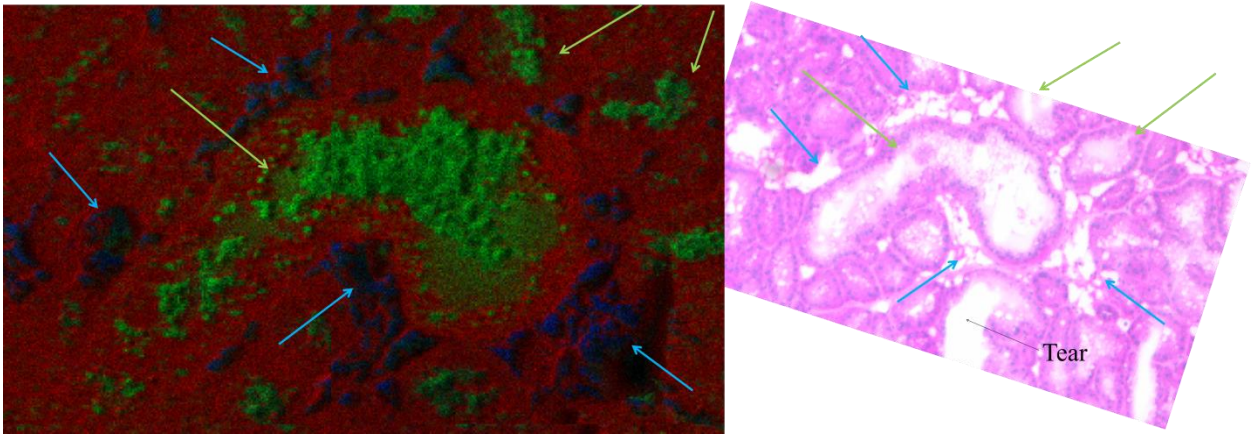

Figure B.9 Three color overlay of lactating mouse breast tissue. Image is approximately 0.4 mm x 0.7 mm. Red: Phosphocholine, m/z 184^+; green: DAGs 22:0. 24:0. 26:0, 28:0 at m/z 439^+, 465^+, 495^+ and 523^+; blue: DAGs 34:0 and 36:0 at m/z 579^+ and 607^+. The area shown is approximately the area within the red box in Figure B.7. The arrows on the chemical image and H&E-stained image show the same structures visualized in the two images.

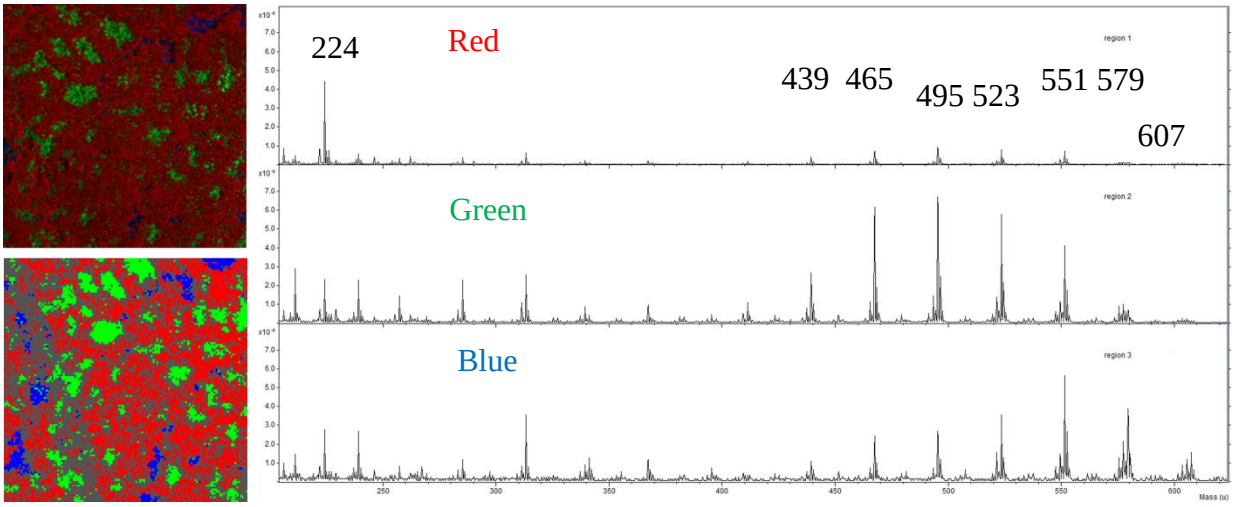

Figure B.10 Top image: HSR three color overlay of a spot on the lactating mouse breast tissue slice. Red: phosphocholine fragment, m/z 224^+; green: DAGs 22:0. 24:0. 26:0, 28:0 at m/z 439^+, 465^+, 495^+ and 523^+; blue: DAGs 34:0 and 36:0 at m/z 579^+ and 607^+. Bottom image: Regions of interest from approximately the same area, shown by the red, green and blue regions. HMR spectra were extracted from these regions. The colors correspond to the regions plotted with the same colors in the left image. Both images are 500 µm x 500 µm.

Bibliography

1. Wilt, B.A., L.D. Burns, E.T. Wei Ho, K.K. Ghosh, E.A. Mukamel, and M.J. Schnitzer, *Advances in Light Microscopy for Neuroscience.* Annual Review of Neuroscience, 2009. **32**(1): p. 435-506.
2. Schroeder, J.L., M. Bakalar, T.J. Pohida, and R.S. Balaban, *Rapid overlapping-volume acquisition and reconstruction (ROVAR): automated 3D tiling for high-resolution, large field-of-view optical microscopy.* Journal of Microscopy, 2011. **243**(1): p. 103-110.
3. Gan, L. and G.J. Jensen, *Electron tomography of cells.* Quarterly Reviews of Biophysics, 2011: p. 1-30.
4. Gunnarsson, A., F. Kollmer, S. Sohn, F. Hook, and P. Sjovall, *Spatial-Resolution Limits in Mass Spectrometry Imaging of Supported Lipid Bilayers and Individual Lipid Vesicles.* Analytical Chemistry, 2010. **82**(6): p. 2426-2433.
5. Touboul, D., F. Kollmer, E. Niehuis, A. Brunelle, and O. Laprevote, *Improvement of biological time-of-flight-secondary ion mass spectrometry imaging with a bismuth cluster ion source.* Journal of the American Society for Mass Spectrometry, 2005. **16**(10): p. 1608-1618.
6. Davies, N., D.E. Weibel, P. Blenkinsopp, N. Lockyer, R. Hill, and J.C. Vickerman, *Development and experimental application of a gold liquid metal ion source.* Applied Surface Science, 2003. **203–204**(0): p. 223-227.
7. Brison, J., S. Muramoto, and D.G. Castner, *ToF-SIMS Depth Profiling of Organic Films: A Comparison between Single-Beam and Dual-Beam Analysis.* Journal of Physical Chemistry C, 2010. **114**(12): p. 5565-5573.
8. Weibel, D., S. Wong, N. Lockyer, P. Blenkinsopp, R. Hill, and J.C. Vickerman, *A C-60 primary ion beam system for time of flight secondary ion mass spectrometry: Its development and secondary ion yield characteristics.* Analytical Chemistry, 2003. **75**(7): p. 1754-1764.
9. Lee, J.L.S., S. Ninomiya, J. Matsuo, I.S. Gilmore, M.P. Seah, and A.G. Shard, *Organic Depth Profiling of a Nanostructured Delta Layer Reference Material Using Large Argon Cluster Ions.* Analytical Chemistry, 2010. **82**(1): p. 98-105.
10. Wong, S.C.C., R. Hill, P. Blenkinsopp, N.P. Lockyer, D.E. Weibel, and J.C. Vickerman, *Development of a C60+ ion gun for static SIMS and chemical imaging.* Applied Surface Science, 2003. **203-204**: p. 219-222.
11. Muramoto, S., J. Brison, and D.G. Castner, *ToF-SIMS depth profiling of trehalose: The effect of analysis beam dose on the quality of depth profiles.* Surface and Interface Analysis, 2011. **43**(1-2): p. 58-61.
12. Fletcher, J.S., N.P. Lockyer, S. Vaidyanathan, and J.C. Vickerman, *TOF-SIMS 3D Biomolecular Imaging of Xenopus laevis Oocytes Using Buckminsterfullerene (C60) Primary Ions.* Analytical Chemistry, 2007. **79**(6): p. 2199-2206.
13. Chait, B.T. and K.G. Standing, *Time-of-flight mass spectrometer for measurement of secondary ion mass spectra.* International Journal of Mass Spectrometry and Ion Physics, 1981. **40**(2): p. 185-193.
14. Breitenstein, D., C.E. Rommel, R. Mollers, J. Wegener, and B. Hagenhoff, *The chemical composition of animal cells and their intracellular compartments reconstructed from 3D mass spectrometry.* Angewandte Chemie International Edition, 2007. **46**(28): p. 5332-5335.

15. Muramoto, S., J. Brison, and D.G. Castner, *Exploring the Surface Sensitivity of TOF-Secondary Ion Mass Spectrometry by Measuring the Implantation and Sampling Depths of Bin and C60 Ions in Organic Films.* Analytical Chemistry, 2011. **84**(1): p. 365-372.
16. Vickerman, J., *ToF-SIMS: Surface Analysis by Mass Spectrometry*, J.C. Vickerman, Editor 2001, IM Publications and Surface Spectra Limited. p. 3.
17. Sigmund, P., *Correction.* Physical Review, 1969. **187**(2): p. 768.
18. Sigmund, P., *Theory of Sputtering I. Sputtering Yields of Amorphous and Polycrystalline Targets.* Physical Review, 1969. **184**(2): p. 383-&.
19. Benninghoven, A. *Molecular Secondary Ion Emission*. in *SIMS II*. 1982. Stanford, CA: Springer-Verlag.
20. Delcorte, A., B.G. Segda, B.J. Garrison, and P. Bertrand, *Inferring ejection distances and a surface energy profile in keV particle bombardment experiments.* Nuclear Instruments and Methods in Physics Research Section B: Beam Interactions with Materials and Atoms, 2000. **171**(3): p. 277-290.
21. Jones, E.A., N.P. Lockyer, J. Kordys, and J.C. Vickerman, *Suppression and enhancement of secondary ion formation due to the chemical environment in static-secondary ion mass spectrometry.* Journal of the American Society for Mass Spectrometry, 2007. **18**(8): p. 1559-1567.
22. Douglas, M.A. and P.J. Chen, *Quantitative trace metal analysis of silicon surfaces by ToF-SIMS.* Surface and Interface Analysis, 1998. **26**(13): p. 984-994.
23. Brison, J., N. Mine, S. Poisseroux, B. Douhard, R.G. Vitchev, and L. Houssiau, *Measurement and modeling of work function changes during low energy cesium sputtering.* Surface Science, 2007. **601**(6): p. 1467-1472.
24. Piwowar, A.M., N.P. Lockyer, and J.C. Vickerman, *Salt Effects on Ion Formation in Desorption Mass Spectrometry: An Investigation into the Role of Alkali Chlorides on Peak Suppression in Time-of-Flight-Secondary Ion Mass Spectrometry.* Analytical Chemistry, 2009. **81**(3): p. 1040-1048.
25. Robinson, M.A. and D.G. Castner, *Characterization of sample preparation methods of NIH/3T3 fibroblasts for ToF-SIMS analysis.* Biointerphases, 2013. **8**(1): p. 1-12.
26. Jones, E.A., N.P. Lockyer, and J.C. Vickerman, *Depth profiling brain tissue sections with a 40 keV C-60(+) primary ion beam.* Analytical Chemistry, 2008. **80**(6): p. 2125-2132.
27. Fletcher, J.S., S. Rabbani, A. Henderson, N.P. Lockyer, and J.C. Vickerman, *Three-dimensional mass spectral imaging of HeLa-M cells - sample preparation, data interpretation and visualisation.* Rapid Communications in Mass Spectrometry, 2011. **25**(7): p. 925-932.
28. Krantzman, K.D., E.L. Cook, A. Wucher, and B.J. Garrison, *A statistical analysis of the lateral displacement of Si atoms in molecular dynamics simulations of successive bombardment with 20-keV C(60) projectiles.* Nuclear Instruments & Methods in Physics Research Section B-Beam Interactions with Materials and Atoms, 2011. **269**(14): p. 1591-1594.
29. Postawa, Z., L. Rzeznik, R. Paruch, M.F. Russo, N. Winograd, and B.J. Garrison, *Depth profiling by cluster projectiles as seen by computer simulations.* Surface and Interface Analysis, 2011. **43**(1-2): p. 12-15.
30. Seliger, R.L., J.W. Ward, V. Wang, and R.L. Kubena, *High-intensity scanning ion probe with submicrometer size.* Applied Physics Letters, 1979. **34**(5): p. 310-312.

31. Prewett, P.D. and E.M. Kellogg, *Liquid metal ion sources for FIB microfabrication systems — recent advances.* Nuclear Instruments and Methods in Physics Research Section B: Beam Interactions with Materials and Atoms, 1985. **6**(1–2): p. 135-142.
32. Yamada, I., J. Matsuo, N. Toyoda, and A. Kirkpatrick, *Materials processing by gas cluster ion beams.* Materials Science and Engineering: R: Reports, 2001. **34**(6): p. 231-295.
33. Shard, A.G., F.M. Green, P.J. Brewer, M.P. Seah, and I.S. Gilmore, *Quantitative Molecular Depth Profiling of Organic Delta-Layers by C60 Ion Sputtering and SIMS.* Journal of Physical Chemistry B, 2008. **112**: p. 2596-2605.
34. Brison, J., D.S.W. Benoit, S. Muramoto, M. Robinson, P.S. Stayton, and D.G. Castner, *ToF-SIMS imaging and depth profiling of HeLa cells treated with bromodeoxyuridine.* Surface and Interface Analysis, 2011. **43**(1-2): p. 354-357.
35. Kersting, R., B. Hagenhoff, F. Kollmer, R. Möllers, and E. Niehuis, *Influence of primary ion bombardment conditions on the emission of molecular secondary ions.* Applied Surface Science, 2004. **231–232**(0): p. 261-264.
36. Brison, J., S. Muramoto, and D.G. Castner, *ToF-SIMS Depth Profiling of Organic Films: A Comparison between Single-Beam and Dual-Beam Analysis* The Journal of Physical Chemistry C, 2010(Article ASAP).
37. Wucher, A., J. Cheng, and N. Winograd, *Molecular Depth Profiling Using a C60 Cluster Beam: The Role of Impact Energy.* Journal of Physical Chemistry C, 2008. **112**: p. 16550-16555.
38. Kurczy, M.E., P.D. Piehowski, C.T. Van Bell, M.L. Heien, N. Winograd, and A.G. Ewing, *Mass spectrometry imaging of mating Tetrahymena show that changes in cell morphology regulate lipid domain formation.* Proceedings of the National Academy of Sciences, 2010. **107**(7): p. 2751-2756.
39. Fletcher, J.S., X.A. Conlan, E.A. Jones, G. Biddulph, N.P. Lockyer, and J.C. Vickerman, *TOF-SIMS analysis using C-60- effect of impact energy on yield and damage.* Analytical Chemistry, 2006. **78**(6): p. 1827-1831.
40. Hamraoui, K. and A. Delcorte, *Effects of Molecular Orientation and Size in Sputtering of Model Organic Crystals.* Journal of Physical Chemistry C, 2010. **114**(12): p. 5458-5467.
41. Postawa, Z., B. Czerwinski, M. Szewczyk, E.J. Smiley, N. Winograd, and B.J. Garrison, *Microscopic insights into the sputtering of Ag{111} induced by C-60 and Ga bombardment.* Journal of Physical Chemistry B, 2004. **108**(23): p. 7831-7838.
42. Smith, R. and R.P. Webb, *Energetic Fullerene Interactions with a Graphite Surface.* Proceedings: Mathematical and Physical Sciences, 1993. **441**(1913): p. 495-499.
43. Gillen, G. and S. Roberson, *Preliminary evaluation of an SF5+ polyatomic primary ion beam for analysis of organic thin films by secondary ion mass spectrometry.* Rapid Communications in Mass Spectrometry, 1998. **12**(19): p. 1303-1312.
44. Delcorte, A. and B.J. Garrison, *keV fullerene interaction with hydrocarbon targets: Projectile penetration, damage creation and removal.* Nuclear Instruments & Methods in Physics Research Section B-Beam Interactions with Materials and Atoms, 2007. **255**(1): p. 223-228.
45. Ninomiya, S., Y. Nakata, K. Ichiki, T. Seki, T. Aoki, and J. Matsuo, *Measurements of secondary ions emitted from organic compounds bombarded with large gas cluster ions.* Nuclear Instruments and Methods in Physics Research Section B: Beam Interactions with Materials and Atoms, 2007. **256**(1): p. 493-496.

46. Ninomiya, S., K. Ichiki, H. Yamada, Y. Nakata, T. Seki, T. Aoki, and J. Matsuo, *Molecular depth profiling of multilayer structures of organic semiconductor materials by secondary ion mass spectrometry with large argon cluster ion beams.* Rapid Communications in Mass Spectrometry, 2009. **23**(20): p. 3264-3268.
47. Green, F.M., A.G. Shard, I.S. Gilmore, and M.P. Seah, *Analysis Of The Interface And Its Position In C-60(n+) Secondary Ion Mass Spectrometry Depth Profiling.* Analytical Chemistry, 2009. **81**(1): p. 75-79.
48. Rabbani, S., A.M. Barber, J.S. Fletcher, N.P. Lockyer, and J.C. Vickerman, *TOF-SIMS with Argon Gas Cluster Ion Beams: A Comparison with C(60)(+).* Analytical Chemistry, 2011. **83**(10): p. 3793-3800.
49. Fletcher, J.S., S. Rabbani, A.M. Barber, N.P. Lockyer, and J.C. Vickerman, *Comparison of C60 and GCIB primary ion beams for the analysis of cancer cells and tumour sections.* Surface and Interface Analysis, 2012: p. n/a-n/a.
50. Mahoney, C.M., *Cluster secondary ion mass spectrometry of polymers and related materials.* Mass Spectrometry Reviews, 2010. **29**(2): p. 247-293.
51. Carado, A., J. Kozole, M. Passarelli, N. Winograd, A. Loboda, J. Bunch, J. Wingate, J. Hankin, and R. Murphy, *Biological tissue imaging with a hybrid cluster SIMS quadrupole time-of-flight mass spectrometer.* Applied Surface Science, 2008. **255**(4): p. 1572-1575.
52. Carado, A., J. Kozole, M. Passarelli, N. Winograd, A. Loboda, and J. Wingate, *Cluster SIMS with a hybrid quadrupole time-of-light mass spectrometer.* Applied Surface Science, 2008. **255**(4): p. 1610-1613.
53. Guerquin-Kern, J.L., T.D. Wu, C. Quintana, and A. Croisy, *Progress in analytical imaging of the cell by dynamic secondary ion mass spectrometry (SIMS microscopy).* Biochimica Et Biophysica Acta-General Subjects, 2005. **1724**(3): p. 228-238.
54. Rabbani, S., J.S. Fletcher, N.P. Lockyer, and J.C. Vickerman, *Exploring subcellular imaging on the buncher-ToF J105 3D chemical imager.* Surface and Interface Analysis, 2011. **43**(1-2): p. 380-384.
55. Moller, J., A. Beumer, D. Lipinsky, and H.F. Arlinghaus, *Introduction of a cryosectioning-ToF-SIMS instrument for analysis of non-dehydrated biological samples.* Applied Surface Science, 2006. **252**(19): p. 6709-6711.
56. Lanekoff, I., M.E. Kurczy, K.L. Adams, J. Malm, R. Karlsson, P. Sjovall, and A.G. Ewing, *An in situ fracture device to image lipids in single cells using ToF-SIMS.* Surface and Interface Analysis, 2011. **43**(1-2): p. 257-260.
57. Lanekoff, I., M.E. Kurczy, R. Hill, J.S. Fletcher, J.C. Vickerman, N. Winograd, P. Sjövall, and A.G. Ewing, *Time of Flight Mass Spectrometry Imaging of Samples Fractured In Situ with a Spring-Loaded Trap System.* Analytical Chemistry, 2010. **82**(15): p. 6652-6659.
58. Chandra, S., M.T. Bernius, and G.H. Morrison, *Intracellular localization of diffusible elements in frozen-hydrated biological specimens with ion microscopy.* Analytical Chemistry, 1986. **58**(2): p. 493-496.
59. Chandra, S., W.A. Ausserer, and G.H. Morrison, *Evaluation of matrix effects in ion microscopic analysis in freeze-fractured, freeze-dried cultured cells.* Journal of Microscopy (Oxford), 1987. **148**: p. 223-239.

60. Ausserer, W.A., S. Chandra, and G.H. Morrison, *Morphological and elemental integrity of freeze-fractured, freeze-dried culctured cells during ion microscopic analysis.* Journal of Microscopy-Oxford, 1989. **154**: p. 39-57.
61. Mentre, P., *Preservation of the diffusible cations for SIMS microscopy I. A problem related to the state of water in the cell.* Biology of the Cell, 1992. **74**(1): p. 19-30.
62. Fragu, P., C. Briançon, C. Fourré, J. Clerc, O. Casiraghi, J. Jeusset, F. Omri, and S. Halpern, *SIMS microscopy in the biomedical field.* Biology of the Cell, 1992. **74**: p. 5-18.
63. Fragu, P., J. Clerc, C. Briancon, C. Fourre, J. Jeusset, and S. Halpern, *Recent development in medical applications of SIMS microscopy.* Micron, 1994. **25**(4): p. 361-370.
64. Clerc, J., C. Fourre, and P. Fragu, *SIMS microscopy: Methodology, problems and perspectives in mapping drugs and nuclear medicine compounds.* Cell Biology International, 1997. **21**(10): p. 619-633.
65. Fragu, P. and E. Kahn, *Secondary ion mass spectrometry (SIMS) microscopy: A new tool for pharmacological studies in humans.* Microscopy Research and Technique, 1997. **36**(4): p. 296-300.
66. Colliver, T.L., C.L. Brummel, M.L. Pacholski, F.D. Swanek, A.G. Ewing, and N. Winograd, *Atomic and molecular imaging at the single-cell level with ToF-SIMS.* Analytical Chemistry, 1997. **69**(13): p. 2225-2231.
67. Pacholski, M.L., D.M. Cannon, A.G. Ewing, and N. Winograd, *Static time-of-flight secondary ion mass spectrometry imaging of freeze-fractured, frozen-hydrated biological membranes.* Rapid Communications in Mass Spectrometry, 1998. **12**(18): p. 1232-1235.
68. Pacholski, M.L., D.M. Cannon, A.G. Ewing, and N. Winograd, *Imaging of Exposed Headgroups and Tailgroups of Phospholipid Membranes by Mass Spectrometry.* Journal of the American Chemical Society, 1999. **121**(19): p. 4716-4717.
69. Ostrowski, S.G., C.T. Van Bell, N. Winograd, and A.G. Ewing, *Mass spectrometric imaging of highly curved membranes during tetrahymena mating.* Science, 2004. **305**(5680): p. 71-73.
70. Breitenstein, D., C.E. Rommel, J. Stolwijk, J. Wegener, and B. Hagenhoff, *The chemical composition of animal cells reconstructed from 2D and 3D ToF-SIMS analysis.* Applied Surface Science, 2008. **255**(4): p. 1249-1256.
71. Ostrowski, S.G., M.E. Kurczy, T.P. Roddy, N. Winograd, and A.G. Ewing, *Secondary ion MS imaging to relatively quantify cholesterol in the membranes of individual cells from differentially treated populations.* Analytical Chemistry, 2007. **79**(10): p. 3554-3560.
72. John, C.M. and R.W. Odom, *Static secondary ion mass spectrometry (SSIMS) of biological compounds in tissue and tissue-like matrices.* International Journal of Mass Spectrometry and Ion Processes, 1997. **161**(1-3): p. 47-67.
73. Mains, J., C.G. Wilson, and A. Urquhart, *ToF-SIMS Analysis of Dexamethasone Distribution in the Isolated Perfused Eye.* Investigative Ophthalmology & Visual Science, 2011. **52**(11): p. 8413-8419.
74. Mains, J., C. Wilson, and A. Urquhart, *ToF-SIMS analysis of ocular tissues reveals biochemical differentiation and drug distribution.* European Journal of Pharmaceutics and Biopharmaceutics, 2011. **79**(2): p. 328-333.

75. Malmberg, P., K. Borner, Y. Chen, P. Friberg, B. Hagenhoff, J.E. Mansson, and H. Nygren, *Localization of lipids in the aortic wall with imaging TOF-SIMS.* Biochimica Et Biophysica Acta-Molecular and Cell Biology of Lipids, 2007. **1771**(2): p. 185-195.
76. Amaya, K.R., E.B. Monroe, J.V. Sweedler, and D.F. Clayton, *Lipid imaging in the zebra finch brain with secondary ion mass spectrometry.* International Journal of Mass Spectrometry, 2007. **260**(2-3): p. 121-127.
77. Aranyosiova, M., A. Chorvatova, D. Chorvat, Jr., C. Biro, and D. Velic, *Analysis of cardiac tissue by gold cluster ion bombardment.* Applied Surface Science, 2006. **252**(19): p. 6782-6785.
78. Touboul, D., S. Roy, D.P. Germain, P. Chaminade, A. Brunelle, and O. Laprevote, *MALDI-TOF and cluster-TOF-SIMS imaging of Fabry disease biomarkers.* International Journal of Mass Spectrometry, 2007. **260**(2-3): p. 158-165.
79. Tahallah, N., A. Brunelle, S. De La Porte, and O. Laprevote, *Lipid mapping in human dystrophic muscle by cluster-time-of-flight secondary ion mass spectrometry imaging.* Journal of Lipid Research, 2008. **49**(2): p. 438-454.
80. Magnusson, Y., P. Friberg, P. Sjovall, F. Dangardt, P. Malmberg, and Y. Chen, *Lipid imaging of human skeletal muscle using TOF-SIMS with bismuth cluster ion as a primary ion source.* Clinical Physiology and Functional Imaging, 2008. **28**(3): p. 202-209.
81. Tokareva, E.N., P. Fardim, A.V. Pranovich, H.P. Fagerholm, G. Daniel, and B. Holmbom, *Imaging of wood tissue by ToF-SIMS: Critical evaluation and development of sample preparation techniques.* Applied Surface Science, 2007. **253**(18): p. 7569-7577.
82. Mazel, V., P. Richardin, D. Touboul, A. Brunelle, P. Walter, and O. Laprevote, *Chemical imaging techniques for the analysis of complex mixtures: New application to the characterization of ritual matters on African wooden statuettes.* Analytica Chimica Acta, 2006. **570**(1): p. 34-40.
83. Zhou, C., Q. Li, V.L. Chiang, L.A. Lucia, and D.P. Griffis, *Chemical and Spatial Differentiation of Syringyl and Guaiacyl Lignins in Poplar Wood via Time-of-Flight Secondary Ion Mass Spectrometry.* Analytical Chemistry, 2011. **83**(18): p. 7020-7026.
84. Passarelli, M.K. and N. Winograd, *Lipid imaging with time-of-flight secondary ion mass spectrometry (ToF-SIMS).* Biochimica Et Biophysica Acta: Molecular and Cell Biology of Lipids, 2011. **1811**(11): p. 976-990.
85. Vaezian, B., C.R. Anderton, and M.L. Kraft, *Discriminating and Imaging Different Phosphatidylcholine Species within Phase-Separated Model Membranes by Principal Component Analysis of TOF-Secondary Ion Mass Spectrometry Images.* Analytical Chemistry, 2010. **82**(24): p. 10006-10014.
86. Prinz, C., F. Hook, J. Malm, and P. Sjovall, *Structural effects in the analysis of supported lipid bilayers by time-of-flight secondary ion mass spectrometry.* Langmuir, 2007. **23**(15): p. 8035-8041.
87. Mantus, D.S., B.D. Ratner, B.A. Carlson, and J.F. Moulder, *Static secondary ion mass spectrometry of adsorbed proteins.* Analytical Chemistry, 1993. **65**(10): p. 1431-1438.
88. Lhoest, J.B., M.S. Wagner, C.D. Tidwell, and D.G. Castner, *Characterization of adsorbed protein films by time of flight secondary ion mass spectrometry.* Journal of Biomedical Materials Research, 2001. **57**(3): p. 432-440.
89. Kulp, K.S., E.S.F. Berman, S.L. Fortson, K.J.J. Wu, M.G. Knize, L. Wu, R.D. White, R. Gandour-Edwards, D.B. Seligson, L.D. Goodglick, D. Chia, S. Tze, and J.S. Felton, *Using time-of-flight secondary ion mass spectrometry (ToF-SIMS) for sensitive cell type*

differentiation and analysis of paraffin-embedded bladder and prostate tissue sections: Applications for cancer prognosis. Proceedings of the American Association for Cancer Research Annual Meeting, 2007. **48**: p. 751-752.
90. Saleem, M. and H.-J. Galla, *Surface view of the lateral organization of lipids and proteins in lung surfactant model systems—A ToF-SIMS approach.* Biochimica et Biophysica Acta (BBA) - Biomembranes, 2010. **1798**(4): p. 730-740.
91. Sanni, O.D., M.S. Wagner, D. Briggs, D.G. Castner, and J.C. Vickerman, *Classification of adsorbed protein static ToF-SIMS spectra by principal component analysis and neural networks*, 2002. p. 715-728.
92. Muramoto, S., D.J. Graham, M.S. Wagner, T.G. Lee, D.W. Moon, and D.G. Castner, *ToF-SIMS Analysis of Adsorbed Proteins: Principal Component Analysis of the Primary Ion Species Effect on the Protein Fragmentation Patterns.* Journal of Physical Chemistry C, 2011. **115**(49): p. 24247-24255.
93. Wagner, M.S., M. Shen, T.A. Horbett, and D.G. Castner, *Quantitative analysis of binary adsorbed protein films by time of flight secondary ion mass spectrometry.* Journal of Biomedical Materials Research Part A, 2003. **64A**(1): p. 1-11.
94. Wagner, M.S., T.A. Horbett, and D.G. Castner, *Characterization of the Structure of Binary and Ternary Adsorbed Protein Films Using Electron Spectroscopy for Chemical Analysis, Time-of-Flight Secondary Ion Mass Spectrometry, and Radiolabeling.* Langmuir, 2003. **19**(5): p. 1708-1715.
95. Wagner, M.S., T.A. Horbett, and D.G. Castner, *Characterizing multicomponent adsorbed protein films using electron spectroscopy for chemical analysis, time-of-flight secondary ion mass spectrometry, and radiolabeling: capabilities and limitations.* Biomaterials, 2003. **24**(11): p. 1897-1908.
96. Baio, J.E., F. Cheng, D.M. Ratner, P.S. Stayton, and D.G. Castner, *Probing orientation of immobilized humanized anti-lysozyme variable fragment by time-of-flight secondary-ion mass spectrometry.* Journal of Biomedical Materials Research, 2011. **97A**(1).
97. Baio, J.E., T. Weidner, G. Interlandi, C. Mendoza-Barrera, H.E. Canavan, R. Michel, and D.G. Castner, *Probing albumin adsorption onto calcium phosphates by x-ray photoelectron spectroscopy and time-of-flight secondary ion mass spectrometry.* Journal of Vacuum Science & Technology B, 2011. **29**(4).
98. May, C.J., H.E. Canavan, and D.G. Castner, *Quantitative X-ray photoelectron spectroscopy and time-of-flight secondary ion mass spectrometry characterization of the components in DNA.* Analytical Chemistry, 2004. **76**(4): p. 1114-1122.
99. Lee, C.Y., P.C.T. Nguyen, D.W. Grainger, L.J. Gamble, and D.G. Castner, *Structure and DNA hybridization properties of mixed nucleic acid/maleimide-ethylene glycol monolayers.* Analytical Chemistry, 2007. **79**(12): p. 4390-4400.
100. Lee, C.Y., G.M. Harbers, D.W. Grainger, L.J. Gamble, and D.G. Castner, *Fluorescence, XPS, and TOF-SIMS surface chemical state image analysis of DNA microarrays.* Journal of the American Chemical Society, 2007. **129**(30): p. 9429-9438.
101. Graf, N., T. Gross, T. Wirth, W. Weigel, and W.E.S. Unger, *Application of XPS and ToF-SIMS for surface chemical analysis of DNA microarrays and their substrates.* Analytical and Bioanalytical Chemistry, 2009. **393**(8): p. 1907-1912.
102. Wagner, M.S. and D.G. Castner, *Characterization of Adsorbed Protein Films by Time-of-Flight Secondary Ion Mass Spectrometry with Principal Component Analysis.* Langmuir, 2001. **17**(15): p. 4649-4660.

103. Jungnickel, H., E.A. Jones, N.P. Lockyer, S.G. Oliver, G.M. Stephens, and J.C. Vickerman, *Application of TOF-SIMS with chemometrics to discriminate between four different yeast strains from the species Candida glabrata and Saccharomyces cerevisiae.* Analytical Chemistry, 2005. **77**(6): p. 1740-1745.
104. Kulp, K.S., E.S.F. Berman, M.G. Knize, D.L. Shattuck, E.J. Nelson, L.G. Wu, J.L. Montgomery, J.S. Felton, and K.J. Wu, *Chemical and biological differentiation of three human breast cancer cell types using time-of-flight secondary ion mass spectrometry.* Analytical Chemistry, 2006. **78**(11): p. 3651-3658.
105. Baker, M.J., M.D. Brown, E. Gazi, N.W. Clarke, J.C. Vickerman, and N.P. Lockyer, *Discrimination of prostate cancer cells and non-malignant cells using secondary ion mass spectrometry.* Analyst, 2008. **133**(2): p. 175-179.
106. Baker, M.J., E. Gazi, M.D. Brown, N.W. Clarke, J.C. Vickerman, and N.P. Lockyer, *ToF-SIMS PC-DFA analysis of prostate cancer cell lines.* Applied Surface Science, 2008. **255**(4): p. 1084-1087.
107. Michael Becker, M.S., Detlev Suckau, Soren Deininger, *MALDI Imaging of Proteins ar 20 μm Resolution on the ultrafleXtreme*, Bruker Daltonik: Bremen.
108. Richards, A.L., C.B. Lietz, J.B. Wager-Miller, K. Mackie, and S. Trimpin, *Imaging mass spectrometry in transmission geometry.* Rapid Communications in Mass Spectrometry, 2011. **25**(6): p. 815-820.
109. Zavalin, A., E.M. Todd, P.D. Rawhouser, J. Yang, J.L. Norris, and R.M. Caprioli, *Direct imaging of single cells and tissue at sub-cellular spatial resolution using transmission geometry MALDI MS.* Journal of Mass Spectrometry, 2012. **47**(11): p. 1473-1481.
110. Main Andersson, P.A., Richard M. Caproli, *MALDI Imaging and Profiling Mass Spectrometry in neuroproteomics*, in *Neuroproteomics*, A. O, Editor 2010, CRC Press: Boca Raton.
111. Schober, Y., S. Guenther, B. Spengler, and A. Römpp, *Single Cell Matrix-Assisted Laser Desorption/Ionization Mass Spectrometry Imaging.* Analytical Chemistry, 2012. **84**(15): p. 6293-6297.
112. Hammond, J.S., *Comparison of SIMS and MALDI for Mass Spectrometric Imaging*, M. Setou, Editor 2010, Springer Japan. p. 235-257.
113. Benabdellah, F., A. Seyer, L. Quinton, D. Touboul, A. Brunelle, and O. Laprévote, *Mass spectrometry imaging of rat brain sections: nanomolar sensitivity with MALDI versus nanometer resolution by TOF–SIMS.* Analytical and Bioanalytical Chemistry, 2010. **396**(1): p. 151-162.
114. Takáts, Z., J.M. Wiseman, and R.G. Cooks, *Ambient mass spectrometry using desorption electrospray ionization (DESI): instrumentation, mechanisms and applications in forensics, chemistry, and biology.* Journal of Mass Spectrometry, 2005. **40**(10): p. 1261-1275.
115. Laskin, J., B.S. Heath, P.J. Roach, L. Cazares, and O.J. Semmes, *Tissue Imaging Using Nanospray Desorption Electrospray Ionization Mass Spectrometry.* Analytical Chemistry, 2012. **84**(1): p. 141-148.
116. Hallett, J.E., C.R. Ferreira, L.S. Eberlin, and R.G. Cooks, *Lipid fingerprinting of oocytes and pre-implantation mouse embryos by DESI.* Reproduction Fertility and Development, 2012. **24**(1): p. 163-163.
117. Yin, Z., H. Hao, and C. Weibo, *Imaging with Raman Spectroscopy.* Current Pharmaceutical Biotechnology, 2010. **11**(6): p. 654-661.

118. Willets, K., *Surface-enhanced Raman scattering (SERS) for probing internal cellular structure and dynamics.* Analytical and Bioanalytical Chemistry, 2009. **394**(1): p. 85-94.
119. Krafft, C., B. Dietzek, and J. Popp, *Raman and CARS microspectroscopy of cells and tissues.* Analyst, 2009. **134**(6).
120. Keren, S., C. Zavaleta, Z. Cheng, A. de la Zerda, O. Gheysens, and S.S. Gambhir, *Noninvasive molecular imaging of small living subjects using Raman spectroscopy.* Proceedings of the National Academy of Sciences, 2008. **105**(15): p. 5844-5849.
121. Graham, D. and D. Castner, *Multivariate Analysis of ToF-SIMS Data from Multicomponent Systems: The Why, When, and How.* Biointerphases, 2012. **7**(1): p. 1-12.
122. Fletcher, J.S., *Cellular imaging with secondary ion mass spectrometry.* Analyst, 2009. **134**(11): p. 2204-2215.
123. Sjovall, P., B. Johansson, D. Belazi, P. Stenvinkel, B. Lindholm, J. Lausmaa, and M. Schalling, *TOF-SIMS analysis of adipose tissue from patients with chronic kidney disease.* Applied Surface Science, 2008. **255**(4): p. 1177-1180.
124. Barnes, C.A., J. Brison, M. Robinson, D.J. Graham, D.G. Castner, and B.D. Ratner, *Identifying Individual Cell Types in Heterogeneous Cultures Using Secondary Ion Mass Spectrometry Imaging with C60 Etching and Multivariate Analysis.* Analytical Chemistry, 2011. **84**(2): p. 893-900.
125. Magnusson, Y.K., P. Friberg, P. Sjovall, J. Malm, and Y. Chen, *TOF-SIMS Analysis of Lipid Accumulation in the Skeletal Muscle of ob/ob Mice.* Obesity, 2008. **16**(12): p. 2745-2753.
126. Dubey, M., J. Brison, D.W. Grainger, and D.G. Castner, *Comparison of Bi(1)(+), Bi(3)(+) and C(60)(+) primary ion sources for ToF-SIMS imaging of patterned protein samples.* Surface and Interface Analysis, 2011. **43**(1-2): p. 261-264.
127. Fisher, G.L., A.M. Belu, C.M. Mahoney, K. Wormuth, and N. Sanada, *Three-Dimensional Time-of-Flight Secondary Ion Mass Spectrometry Imaging of a Pharmaceutical in a Coronary Stent Coating as a Function of Elution Time.* Analytical Chemistry, 2009. **81**(24): p. 9930-9940.
128. Belu, A., C. Mahoney, and K. Wormuth, *Chemical imaging of drug eluting coatings: Combining surface analysis and confocal Raman microscopy.* Journal of Controlled Release, 2008. **126**(2): p. 111-121.
129. Klerk, L.A., P.Y.W. Dankers, E.R. Popa, A.W. Bosman, M.E. Sanders, K.A. Reedquist, and R.M.A. Heeren, *TOF-Secondary Ion Mass Spectrometry Imaging of Polymeric Scaffolds with Surrounding Tissue after in Vivo Implantation.* Analytical Chemistry, 2010. **82**(11): p. 4337-4343.
130. Barnes, C.A., J. Brison, R. Michel, B.N. Brown, D.G. Castner, S.F. Badylak, and B.D. Ratner, *The surface molecular functionality of decellularized extracellular matrices.* Biomaterials, 2011. **32**(1): p. 137-143.
131. Muramoto, S., J. Brison, and D.G. Castner, *Exploring the Surface Sensitivity of TOF-Secondary Ion Mass Spectrometry by Measuring the Implantation and Sampling Depths of Bi(n) and C(60) Ions in Organic Films.* Analytical Chemistry, 2012. **84**(1): p. 365-372.
132. Kurczy, M.E., P.D. Piehowsky, D. Willingham, K.A. Molyneaux, M.L. Heien, N. Winograd, and A.G. Ewing, *Nanotome Cluster Bombardment to Recover Spatial Chemistry After Preparation of Biological Samples for SIMS Imaging.* Journal of the American Society for Mass Spectrometry, 2010. **21**(5): p. 833-836.

133. Kurczy, M.E., P.D. Piehowski, S.A. Parry, M. Jiang, G. Chen, A.G. Ewing, and N. Winograd, *Which is more important in bioimaging SIMS experiments-The sample preparation or the nature of the projectile?* Applied Surface Science, 2008. **255**(4): p. 1298-1304.
134. Chandra, S., *Imaging intracellular elemental distribution and ion fluxes in cultured cells using ion microscopy: a freeze-fracture methodology.* Journal of Microscopy, 1986. **144**(Pt 1): p. 15-37.
135. Roddy, T.P., D.M. Cannon, S.G. Ostrowski, N. Winograd, and A.G. Ewing, *Identification of Cellular Sections with Imaging Mass Spectrometry Following Freeze Fracture.* Analytical Chemistry, 2002. **74**(16): p. 4020-4026.
136. Berman, E.S.F., S.L. Fortson, K.D. Checchi, L. Wu, J.S. Felton, K.J.J. Wu, and K.S. Kulp, *Preparation of single cells for imaging/profiling mass spectrometry.* Journal of the American Society for Mass Spectrometry, 2008. **19**(8): p. 1230-1236.
137. Nygren, H., C. Eriksson, P. Malmberg, H. Sahlin, L. Carlsson, J. Lausmaa, and P. Sjovall, *A cell preparation method allowing subcellular localization of cholesterol and phosphocholine with imaging TOF-SIMS.* Colloids and Surfaces B: Biointerfaces, 2003. **30**(1-2): p. 87-92.
138. Malm, J., D. Giannaras, M.O. Riehle, N. Gadegaard, and P. Sjovall, *Fixation and Drying Protocols for the Preparation of Cell Samples for Time-of-Flight Secondary Ion Mass Spectrometry Analysis.* Analytical Chemistry, 2009. **81**(17): p. 7197-7205.
139. Passarelli, M.K. and N. Winograd, *Characterizing in situ Glycerophospholipids with SIMS and MALDI Methodologies.* Surface and Interface Analysis, 2011. **43**(1-2): p. 269-271.
140. Fartmann, M., C. Kriegeskotte, S. Dambach, A. Wittig, W. Sauerwein, and H.F. Arlinghaus, *Quantitative imaging of atomic and molecular species in cancer cultures with TOF-SIMS and Laser-SNMS.* Applied Surface Science, 2004. **231**: p. 428-431.
141. Kellenberger, E., *The Response of Biological Macromolecules and Supramolecular Structures to the Physics of Specimen Cryopreparation*, in *Cryotechniques in Biological Electron Microscopy*, R.A. Steinbrecht and K. Zierold, Editors. 1987, Springer-Verlag: Berlin. p. 35-63.
142. Frisz, J.F., K. Lou, H.A. Klitzing, W.P. Hanafin, V. Lizunov, R.L. Wilson, K.J. Carpenter, R. Kim, I.D. Hutcheon, J. Zimmerberg, P.K. Weber, and M.L. Kraft, *Direct chemical evidence for sphingolipid domains in the plasma membranes of fibroblasts.* Proceedings of the National Academy of Sciences, USA, 2013.
143. Mahoney, C.M., A.J. Fahey, G. Gillen, C. Xu, and J.D. Batteas, *Temperature-controlled depth profiling of poly(methyl methacrylate) using cluster secondary ion mass spectrometry. 2. Investigation of sputter-induced topography, chemical damage, and depolymerization effects.* Analytical Chemistry, 2007. **79**(3): p. 837-845.
144. Mahoney, C.M., A.J. Fahey, and G. Gillen, *Temperature-controlled depth profiling of poly(methyl methacrylate) using cluster secondary ion mass spectrometry. 1. Investigation of depth profile characteristics.* Analytical Chemistry, 2007. **79**(3): p. 828-836.
145. Piwowar, A.M., J.S. Fletcher, J. Kordys, N.P. Lockyer, N. Winograd, and J.C. Vickerman, *Effects of Cryogenic Sample Analysis on Molecular Depth Profiles with TOF-Secondary Ion Mass Spectrometry.* Analytical Chemistry. **82**(19): p. 8291-8299.

146. Piehowski, P.D., M.E. Kurczy, D. Willingham, S. Parry, M.L. Heien, N. Winograd, and A.G. Ewing, *Freeze-etching and vapor matrix deposition for ToF-SIMS imaging of single cells.* Langmuir, 2008. **24**(15): p. 7906-7911.
147. Lewis, K.B. and B.D. Ratner, *Observation of Surface Rearrangement of Polymers Using ESCA.* Journal of Colloid and Interface Science, 1993. **159**(1): p. 77-85.
148. Ratner, B.D.W., P. K.; Hoffman, A. S.; Kelly, M.A.; Scharpen, L. H., *Radiation-Grafted Hydrogels for Biomaterial Applications as Studied by the ESCA Technique.* Journal of Applied Polymer Science, 1978. **22**: p. 643-664.
149. Lanekoff, I., M.E. Kurczy, R. Hill, J.S. Fletcher, J.C. Vickerman, N. Winograd, P. Sjovall, and A.G. Ewing, *Time of Flight Mass Spectrometry Imaging of Samples Fractured In Situ with a Spring-Loaded Trap System.* Analytical Chemistry. **82**(15): p. 6652-6659.
150. Wittig, A., M. Wiemann, M. Fartmann, C. Kriegeskotte, H.F. Arlinghaus, K. Zierold, and W. Sauerwein, *Preparation of cells cultured on silicon wafers for mass spectrometry analysis.* Microscopy Research and Technique, 2005. **66**(5): p. 248-258.
151. Piwowar, A.M., S. Keskin, M.O. Delgado, K. Shen, J.J. Hue, I. Lanekoff, A.G. Ewing, and N. Winograd, *C60-ToF SIMS imaging of frozen hydrated HeLa cells.* Surface and Interface Analysis, 2013. **45**(1): p. 302-304.
152. Altelaar, A.F.M., I. Klinkert, K. Jalink, R.P.J. de Lange, R.A.H. Adan, R.M.A. Heeren, and S.R. Piersma, *Gold-Enhanced Biomolecular Surface Imaging of Cells and Tissue by SIMS and MALDI Mass Spectrometry.* Analytical Chemistry, 2005. **78**(3): p. 734-742.
153. Castner, D.G. and B.D. Ratner, *Biomedical surface science: Foundations to frontiers.* Surface Science, 2002. **500**(1–3): p. 28-60.
154. Robinson, M.A., D.J. Graham, and D.G. Castner, *ToF-SIMS Depth Profiling of Cells: z-Correction, 3D Imaging, and Sputter Rate of Individual NIH/3T3 Fibroblasts.* Analytical Chemistry, 2012. **84**(11): p. 4880-4885.
155. Fletcher, J.S., N.P. Lockyer, and J.C. Vickerman, *Developments in molecular SIMS depth profiling and 3D imaging of biological systems using polyatomic primary ions.* Mass Spectrometry Reviews, 2011. **30**(1): p. 142-174.
156. Sostarecz, A.G., D.M. Cannon, C.M. McQuaw, S. Sun, A.G. Ewing, and N. Winograd, *Influence of Molecular Environment on the Analysis of Phospholipids by Time-of-Flight Secondary Ion Mass Spectrometry.* Langmuir, 2004. **20**(12): p. 4926-4932.
157. Conlan, X.A., N.P. Lockyer, and J.C. Vickerman, *Is proton cationization promoted by polyatomic primary ion bombardment during time-of-flight secondary ion mass spectrometry analysis of frozen aqueous solutions?* Rapid Communications in Mass Spectrometry, 2006. **20**(8): p. 1327-1334.
158. Wojciechowski, I.A., U. Kutliev, S. Sun, C. Szakal, N. Winograd, and B.J. Garrison, *Emission of ionic water clusters from water ice films bombarded by energetic projectiles.* Applied Surface Science, 2004. **231–232**(0): p. 72-77.
159. Wojciechowski, I.A., S. Sun, C. Szakal, N. Winograd, and B.J. Garrison, *Ion Emission from Water Ice Due to Energetic Particle Bombardment†.* Journal of Physical Chemistry A, 2004. **108**(15): p. 2993-2998.
160. Jones, E.A., N.P. Lockyer, and J.C. Vickerman, *Mass spectral analysis and imaging of tissue by ToF-SIMS - The role of buckminsterfullerene, C-60(+), primary ions.* International Journal of Mass Spectrometry, 2007. **260**(2-3): p. 146-157.

161. Baker, M.J., L. Zheng, N. Winograd, N.P. Lockyer, and J.C. Vickerman, *Mass Spectral Imaging of Glycophospholipids, Cholesterol, and Glycophorin A in Model Cell Membranes.* Langmuir, 2008. **24**(20): p. 11803-11810.
162. Lee, C.Y., L.J. Gamble, D.W. Grainger, and D.G. Castner, *Mixed DNA/oligo (ethylene glycol) functionalized gold surfaces improve DNA hybridization in complex media.* Biointerphases, 2006. **1**(2): p. 82-92.
163. Benguerba, M., A. Brunelle, S. Della-Negra, J. Depauw, H. Joret, Y. Le Beyec, M.G. Blain, E.A. Schweikert, G.B. Assayag, and P. Sudraud, *Impact of slow gold clusters on various solids: nonlinear effects in secondary ion emission.* Nuclear Instruments and Methods in Physics Research Section B: Beam Interactions with Materials and Atoms, 1991. **62**(1): p. 8-22.
164. Boussofiane-Baudin, K., G. Bolbach, A. Brunelle, S. Della-Negra, P. Hakansson, and Y. Le Beyec, *Secondary ion emission under cluster impact at low energies (5-60 KeV), influence of the number of atoms in the projectile*, 1994, HAL - CCSd - CNRS.
165. Cheng, J., A. Wucher, and N. Winograd, *Molecular depth profiling with cluster ion beams.* Journal of Physical Chemistry B, 2006. **110**(16): p. 8329-8336.
166. Gillen, G., A. Fahey, M. Wagner, and C. Mahoney, *3D molecular imaging SIMS.* Applied Surface Science, 2006. **252**(19): p. 6537-6541.
167. Wucher, A., J. Cheng, L. Zheng, D. Willingham, and N. Winograd, *Three-dimensional molecular imaging using mass spectrometry and atomic force microscopy.* Applied Surface Science, 2008. **255**(4): p. 984-986.
168. Patkin, A.J., S. Chandra, and G.H. Morrison, *Differential sputtering correction for ion microscopy with image depth profiling.* Analytical Chemistry, 1982. **54**(14): p. 2507-2510.
169. Ryan, K.E., E.J. Smiley, N. Winograd, and B.J. Garrison, *Angle of incidence effects in a molecular solid.* Applied Surface Science, 2008. **255**(4): p. 844-846.
170. Kozole, J. and N. Winograd, *Controlling energy deposition during the C(60)(+) bombardment of silicon: The effect of incident angle geometry.* Applied Surface Science, 2008. **255**(4): p. 886-889.
171. Fisher, G.L., M. Dickinson, S.R. Bryan, and J. Moulder, *C60 sputtering of organics: A study using TOF-SIMS, XPS and nanoindentation.* Applied Surface Science, 2008. **255**(4): p. 819-823.
172. Shard, A.G., F.M. Green, P.J. Brewer, M.P. Seah, and I.S. Gilmore, *Quantitative molecular depth profiling of organic delta-layers by C-60 ion sputtering and SIMS.* Journal of Physical Chemistry B, 2008. **112**(9): p. 2596-2605.
173. Wagter, M.L., A.H. Clarke, K.F. Taylor, P.A.W. vanderHeide, and N.S. McIntyre, *Topographic correction of 3D SIMS images.* Surface and Interface Analysis, 1997. **25**(10): p. 788-789.
174. Wucher, A., J. Cheng, L. Zheng, and N. Winograd, *Three-dimensional depth profiling of molecular structures.* Analytical and Bioanalytical Chemistry, 2009. **393**(8): p. 1835-1842.
175. Wucher, A., J. Cheng, and N. Winograd, *Protocols for three-dimensional molecular imaging using mass spectrometry.* Analytical Chemistry, 2007. **79**(15): p. 5529-5539.
176. Fletcher, J.S. and J.C. Vickerman, *A new SIMS paradigm for 2D and 3D molecular imaging of bio-systems.* Analytical and Bioanalytical Chemistry. **396**(1): p. 85-104.

177. Roddy, T.P., D.M. Cannon, S.G. Ostrowski, A.G. Ewing, and N. Winograd, *Proton transfer in time-of-flight secondary ion mass spectrometry studies of frozen-hydrated dipalmitoylphosphatidylcholine.* Analytical Chemistry, 2003. **75**(16): p. 4087-4094.
178. Steinbrecht, R.Z., K., *Cryotechniques in Biological Electron Microscopy*1987.
179. Russo, M.F., C. Szakal, J. Kozole, N. Winograd, and B.J. Garrison, *Sputtering Yields for C60 and Au3 Bombardment of Water Ice as a Function of Incident Kinetic Energy.* Analytical Chemistry, 2007. **79**(12): p. 4493-4498.
180. Siegel, R., D. Naishadham, and A. Jemal, *Cancer statistics, 2012.* CA: A Cancer Journal for Clinicians, 2012. **62**(1): p. 10-29.
181. Higgins, M.J., J. Baselga, and xE, *Targeted therapies for breast cancer.* The Journal of Clinical Investigation, 2011. **121**(10): p. 3797-3803.
182. Collins, I. and P. Workman, *New approaches to molecular cancer therapeutics.* Nature Chemical Biology, 2006. **2**(12): p. 689-700.
183. Dunnwald, L.K., J.R. Gralow, G.K. Ellis, R.B. Livingston, H.M. Linden, J.M. Specht, R.K. Doot, T.J. Lawton, W.E. Barlow, B.F. Kurland, E.K. Schubert, and D.A. Mankoff, *Tumor Metabolism and Blood Flow Changes by Positron Emission Tomography: Relation to Survival in Patients Treated With Neoadjuvant Chemotherapy for Locally Advanced Breast Cancer.* Journal of Clinical Oncology, 2008. **26**(27): p. 4449-4457.
184. Mankoff, D.A., L.K. Dunnwald, J.R. Gralow, G.K. Ellis, E.K. Schubert, J. Tseng, T.J. Lawton, H.M. Linden, and R.B. Livingston, *Changes in Blood Flow and Metabolism in Locally Advanced Breast Cancer Treated with Neoadjuvant Chemotherapy.* Journal of Nuclear Medicine, 2003. **44**(11): p. 1806-1814.
185. Mankoff, D.A., L.K. Dunnwald, J.R. Gralow, G.K. Ellis, A. Charlop, T.J. Lawton, E.K. Schubert, J. Tseng, and R.B. Livingston, *Blood Flow and Metabolism in Locally Advanced Breast Cancer: Relationship to Response to Therapy.* Journal of Nuclear Medicine, 2002. **43**(4): p. 500-509.
186. Bauer, K.R., M. Brown, R.D. Cress, C.A. Parise, and V. Caggiano, *Descriptive analysis of estrogen receptor (ER)-negative, progesterone receptor (PR)-negative, and HER2-negative invasive breast cancer, the so-called triple-negative phenotype.* Cancer, 2007. **109**(9): p. 1721-1728.
187. Onitilo, A.A., J.M. Engel, R.T. Greenlee, and B.N. Mukesh, *Breast Cancer Subtypes Based on ER/PR and Her2 Expression: Comparison of Clinicopathologic Features and Survival.* Clinical Medicine & Research, 2009. **7**(1-2): p. 4-13.
188. Lin, N.U., A. Vanderplas, M.E. Hughes, R.L. Theriault, S.B. Edge, Y.-N. Wong, D.W. Blayney, J.C. Niland, E.P. Winer, and J.C. Weeks, *Clinicopathologic features, patterns of recurrence, and survival among women with triple-negative breast cancer in the National Comprehensive Cancer Network.* Cancer, 2012. **118**(22): p. 5463-5472.
189. Sørlie, T., C.M. Perou, R. Tibshirani, T. Aas, S. Geisler, H. Johnsen, T. Hastie, M.B. Eisen, M. van de Rijn, S.S. Jeffrey, T. Thorsen, H. Quist, J.C. Matese, P.O. Brown, D. Botstein, P.E. Lønning, and A.-L. Børresen-Dale, *Gene expression patterns of breast carcinomas distinguish tumor subclasses with clinical implications.* Proceedings of the National Academy of Sciences, 2001. **98**(19): p. 10869-10874.
190. Perou, C.M., T. Sorlie, M.B. Eisen, M. van de Rijn, S.S. Jeffrey, C.A. Rees, J.R. Pollack, D.T. Ross, H. Johnsen, L.A. Akslen, O. Fluge, A. Pergamenschikov, C. Williams, S.X. Zhu, P.E. Lonning, A.-L. Borresen-Dale, P.O. Brown, and D. Botstein, *Molecular portraits of human breast tumours.* Nature, 2000. **406**(6797): p. 747-752.

191. Rakha, E., I. Ellis, and J. Reis-Filho, *Are Triple-Negative and Basal-Like Breast Cancer Synonymous?* Clinical Cancer Research, 2008. **14**(2): p. 618.
192. Prat, A., B. Adamo, M.C.U. Cheang, C.K. Anders, L.A. Carey, and C.M. Perou, *Molecular Characterization of Basal-Like and Non-Basal-Like Triple-Negative Breast Cancer.* The Oncologist, 2013. **18**(2): p. 123-133.
193. Perou, C.M., *Molecular Stratification of Triple-Negative Breast Cancers.* The Oncologist, 2011. **16**(suppl 1): p. 61-70.
194. Lehmann, B.D., J.A. Bauer, X. Chen, M.E. Sanders, A.B. Chakravarthy, Y. Shyr, and J.A. Pietenpol, *Identification of human triple-negative breast cancer subtypes and preclinical models for selection of targeted therapies.* The Journal of Clinical Investigation, 2011. **121**(7): p. 2750-2767.
195. Zhang, F. and G. Du, *Dysregulated lipid metabolism in cancer.* World Journal of Biological Chemistry, 2012. **3**(8): p. 167-174.
196. Kuhajda, F.P., *Fatty Acid Synthase and Cancer: New Application of an Old Pathway.* Cancer Research, 2006. **66**(12): p. 5977-5980.
197. Mashima, T., H. Seimiya, and T. Tsuruo, *De novo fatty-acid synthesis and related pathways as molecular targets for cancer therapy.* British Journal of Cancer, 2009. **100**: p. 1369-1372.
198. Hilvo, M., C. Denkert, L. Lehtinen, B. Müller, S. Brockmöller, T. Seppänen-Laakso, J. Budczies, E. Bucher, L. Yetukuri, S. Castillo, E. Berg, H. Nygren, M. Sysi-Aho, J.L. Griffin, O. Fiehn, S. Loibl, C. Richter-Ehrenstein, C. Radke, T. Hyötyläinen, O. Kallioniemi, K. Iljin, and M. Orešič, *Novel Theranostic Opportunities Offered by Characterization of Altered Membrane Lipid Metabolism in Breast Cancer Progression.* Cancer Research, 2011. **71**(9): p. 3236-3245.
199. Dória, M.L., Z. Cotrim, B. Macedo, C. Simões, P. Domingues, L. Helguero, and M.R. Domingues, *Lipidomic approach to identify patterns in phospholipid profiles and define class differences in mammary epithelial and breast cancer cells.* Breast Cancer Research and Treatment, 2012. **133**(2): p. 635-648.
200. Dória, M.L., C.Z. Cotrim, C. Simões, B. Macedo, P. Domingues, M.R. Domingues, and L. Helguero, *Lipidomic analysis of phospholipids from human mammary epithelial and breast cancer cell lines.* Journal of Cellular Physiology, 2012: p. n/a-n/a.
201. Brison, J., M. Robinson, D.S.W. Benoit, S. Muramoto, P.S. Stayton, and D.G. Castner, *ToF-SIMS 3D Imaging of HeLa Cells.* Analytical Chemistry, 2013. ***Submitted***.
202. Norris, J.L. and R.M. Caprioli, *Analysis of Tissue Specimens by Matrix-Assisted Laser Desorption/Ionization Imaging Mass Spectrometry in Biological and Clinical Research.* Chemical Reviews, 2013. **113**(4): p. 2309-2342.
203. Meding, S., U. Nitsche, B. Balluff, M. Elsner, S. Rauser, C. Schöne, M. Nipp, M. Maak, M. Feith, M.P. Ebert, H. Friess, R. Langer, H. Höfler, H. Zitzelsberger, R. Rosenberg, and A. Walch, *Tumor Classification of Six Common Cancer Types Based on Proteomic Profiling by MALDI Imaging.* Journal of Proteome Research, 2012. **11**(3): p. 1996-2003.
204. Eberlin, L.S., I. Norton, D. Orringer, I.F. Dunn, X. Liu, J.L. Ide, A.K. Jarmusch, K.L. Ligon, F.A. Jolesz, A.J. Golby, S. Santagata, N.Y.R. Agar, and R.G. Cooks, *Ambient mass spectrometry for the intraoperative molecular diagnosis of human brain tumors.* Proceedings of the National Academy of Sciences, 2013.

205. Eberlin, L.S., I. Norton, A.L. Dill, A.J. Golby, K.L. Ligon, S. Santagata, R.G. Cooks, and N.Y.R. Agar, *Classifying Human Brain Tumors by Lipid Imaging with Mass Spectrometry.* Cancer Research, 2012. **72**(3): p. 645-654.
206. Muramoto, S.B., J. Castner D. G., *Exploring the Surface Sensitivity of ToF-SIMS: Measuring the Implantation Depths and Sampling Depths of Bi and C60 Ion Sources in Organic Films.* In Review, 2011.
207. Gazi, E., N.P. Lockyer, J.C. Vickerman, P. Gardner, J. Dwyer, C.A. Hart, M.D. Brown, N.W. Clarke, and J. Miyan, *Imaging ToF-SIMS and synchrotron-based FT-IR micro spectroscopic studies of prostate cancer cell lines.* Applied Surface Science, 2004. **231**: p. 452-456.
208. Gazi, E., J. Dwyer, N. Lockyer, P. Gardner, J.C. Vickerman, J. Miyan, C.A. Hart, M. Brown, J.H. Shanks, and N. Clarke, *The combined application of FTIR microspectroscopy and ToF-SIMS imaging in the study of prostate cancer.* Faraday Discussions, 2004. **126**: p. 41-59.
209. Armitage, E.G., H.L. Kotze, J.S. Fletcher, A. Henderson, K.J. Williams, N.P. Lockyer, and J.C. Vickerman, *Time-of-flight SIMS as a novel approach to unlocking the hypoxic properties of cancer.* Surface and Interface Analysis, 2012: p. n/a-n/a.
210. Kotze, H.L., E.G. Armitage, J.S. Fletcher, A. Henderson, K.J. Williams, N.P. Lockyer, and J.C. Vickerman, *ToF-SIMS as a tool for metabolic profiling small biomolecules in cancer systems.* Surface and Interface Analysis, 2013. **45**(1): p. 277-281.
211. Armitage, E.G., H.L. Kotze, and N.P. Lockyer, *Imaging of metabolites using secondary ion mass spectrometry.* Metabolomics, 2012: p. 1-8.
212. Yun, S.J., J.-W. Park, I.J. Choi, B. Kang, H.K. Kim, D.W. Moon, T.G. Lee, and D. Hwang, *TOFSIMS-P: A Web-Based Platform for Analysis of Large-Scale TOF-SIMS Data.* Analytical Chemistry, 2011. **83**(24): p. 9298-9305.
213. Park, J.-W., H.K. Shon, B.C. Yoo, I.H. Kim, D.W. Moon, and T.G. Lee, *Differentiation between human normal colon mucosa and colon cancer tissue using ToF-SIMS imaging technique and principal component analysis.* Applied Surface Science, 2008. **255**(4): p. 1119-1122.
214. Nygren, H., P. Malmberg, M. Nilsson, C. Kriegeskotte, and H.F. Arlinghaus, *The cytochemistry of anaplastic thyroid tumour cells and differentiated thyrocytes analyzed by TOF-SIMS and depth profiling.* Applied Surface Science, 2008. **255**(4): p. 1285-1288.
215. Wehrl, H.F., J. Schwab, K. Hasenbach, G. Reischl, G. Tabatabai, L. Quintanilla-Martinez, F. Jiru, K. Chughtai, A. Kiss, F. Cay, D. Bukala, R.M.A. Heeren, B.J. Pichler, and A.W. Sauter, *Multimodal Elucidation of Choline Metabolism in a Murine Glioma Model Using Magnetic Resonance Spectroscopy and 11C-Choline Positron Emission Tomography.* Cancer Research, 2013. **73**(5): p. 1470-1480.
216. Chandra, S., W. Tjarks, D.R. Lorey Li, and R.F. Barth, *Quantitative subcellular imaging of boron compounds in individual mitotic and interphase human glioblastoma cells with imaging secondary ion mass spectrometry (SIMS).* Journal of Microscopy, 2008. **229**(1): p. 92-103.
217. Chandra, S. and D.R. Lorey Ii, *SIMS ion microscopy imaging of boronophenylalanine (BPA) and 13C15N-labeled phenylalanine in human glioblastoma cells: Relevance of subcellular scale observations to BPA-mediated boron neutron capture therapy of cancer.* International Journal of Mass Spectrometry, 2007. **260**(2-3): p. 90-101.

218. Lorey, D.R., G.H. Morrison, and S. Chandra, *Dynamic secondary ion mass spectrometry analysis of boron from boron neutron capture therapy drugs in co-cultures: Single-cell imaging of two different cell types within the same ion microscopy field of imaging.* Analytical Chemistry, 2001. **73**(16): p. 3947-3953.
219. Brunelle, A. and O. Laprévote, *Lipid imaging with cluster time-of-flight secondary ion mass spectrometry.* Analytical and Bioanalytical Chemistry, 2009. **393**(1): p. 31-35.
220. Debois, D., M.-P. Bralet, F.o. Le Naour, A. Brunelle, and O. Laprévote, *In Situ Lipidomic Analysis of Nonalcoholic Fatty Liver by Cluster TOF-SIMS Imaging.* Analytical Chemistry, 2009. **81**(8): p. 2823-2831.
221. Malmberg, P., H. Nygren, K. Richter, Y. Chen, F. Dangardt, P. Friberg, and Y. Magnusson, *Imaging of lipids in human adipose tissue by cluster ion TOF-SIMS.* Microscopy Research and Technique, 2007. **70**: p. 828-835.
222. Touboul, D., A. Brunelle, F. Halgand, S. De La Porte, and O. Laprevote, *Lipid imaging by gold cluster time-of-flight secondary ion mass spectrometry: application to Duchenne muscular dystrophy.* Journal of Lipid Research, 2005. **46**(7): p. 1388-1395.
223. Amaya, K.R., J.V. Sweedler, and D.F. Clayton, *Small molecule analysis and imaging of fatty acids in the zebra finch song system using time-of-flight-secondary ion mass spectrometry.* Journal of Neurochemistry, 2011. **118**(4): p. 499-511.
224. Campbell, D., C. Ferreira, L. Eberlin, and R.G. Cooks, *Improved spatial resolution in the imaging of biological tissue using desorption electrospray ionization.* Analytical and Bioanalytical Chemistry, 2012. **404**(2): p. 389-398.
225. Eberlin, L.S., A.L. Dill, A.B. Costa, D.R. Ifa, L. Cheng, T. Masterson, M. Koch, T.L. Ratliff, and R.G. Cooks, *Cholesterol Sulfate Imaging in Human Prostate Cancer Tissue by Desorption Electrospray Ionization Mass Spectrometry.* Analytical Chemistry, 2010. **82**(9): p. 3430-3434.
226. Mathias, R.A., C. Vergara, L. Gao, N. Rafaels, T. Hand, M. Campbell, C. Bickel, P. Ivester, S. Sergeant, K.C. Barnes, and F.H. Chilton, *FADS genetic variants and ω-6 polyunsaturated fatty acid metabolism in a homogeneous island population.* Journal of Lipid Research, 2010. **51**(9): p. 2766-2774.
227. Amir, E., O.C. Freedman, B. Seruga, and D.G. Evans, *Assessing Women at High Risk of Breast Cancer: A Review of Risk Assessment Models.* Journal of the National Cancer Institute, 2010. **102**(10): p. 680-691.
228. Bombonati, A. and D.C. Sgroi, *The molecular pathology of breast cancer progression.* The Journal of Pathology, 2011. **223**(2): p. 308-318.
229. Tennant, D.A., R.V. Duran, and E. Gottlieb, *Targeting metabolic transformation for cancer therapy.* Nature Reviews Cancer, 2010. **10**(4): p. 267-277.
230. Andre, F., N. Berrada, and C. Desmedt, *Implication of tumor microenvironment in the resistance to chemotherapy in breast cancer patients.* Current Opinion in Oncology, 2010. **22**(6): p. 547-551 10.1097/CCO.0b013e32833fb384.
231. Cillero-Pastor, B., G. Eijkel, A. Kiss, F.J. Blanco, and R.M.A. Heeren, *Time-of-Flight Secondary Ion Mass Spectrometry-Based Molecular Distribution Distinguishing Healthy and Osteoarthritic Human Cartilage.* Analytical Chemistry, 2012. **84**(21): p. 8909-8916.
232. Robinson, M., F. Morrish, D. Hockenbery, and L. Gamble, *Chemical analysis of eight human breast cancer cell lines with ToF-SIMS.* In Preparation, 2013.
233. Hilvo, M. and M. Orešič, *Regulation of lipid metabolism in breast cancer provides diagnostic and therapeutic opportunities.* Clinical Lipidology, 2012. **7**(2): p. 177-188.

234. Touboul, D., A. Brunelle, and O. Laprévote, *Mass spectrometry imaging: Towards a lipid microscope?* Biochimie, 2011. **93**(1): p. 113-119.
235. Mouhib, T., A. Delcorte, C. Poleunis, and P. Bertrand, *C(60) molecular depth profiling of bilayered polymer films using ToF-SIMS.* Surface and Interface Analysis, 2011. **43**(1-2): p. 175-178.
236. Wucher, A., *A simple erosion dynamics model of molecular sputter depth profiling.* Surface and Interface Analysis, 2008. **40**: p. 1545–1551.
237. Belu, A.M., D.J. Graham, and D.G. Castner, *Time-of-flight secondary ion mass spectrometry: techniques and applications for the characterization of biomaterial surfaces.* Biomaterials, 2003. **24**(21): p. 3635-3653.
238. Brunelle, A., D. Touboul, and O. Laprevote, *Biological tissue imaging with time-of-flight secondary ion mass spectrometry and cluster ion sources.* J. Mass Spectrom. , 2005. **40**: p. 985–999.
239. Castner, D.G. and B.D. Ratner, *Biomedical surface science: Foundations to frontiers.* Surf Sci, 2002. **500**: p. 28-60.
240. Fletcher, J.S., A. Henderson, G.X. Biddulph, S. Vaidyanathan, N.P. Lockyer, and J.C. Vickerman, *Uncovering new challenges in bio-analysis with ToF-SIMS.* Appl. Surf. Sci., 2008. **255**: p. 1264-1270.
241. Vickerman, J.C., *Molecular SIMS - A journey from single crystal to biological surface studies.* Surface Science, 2009. **603**(10-12): p. 1926-1936.
242. Ostrowski, S.G., C.T. Van Bell, N. Winograd, and A.G. Ewing, *Mass Spectrometric Imaging of Highly Curved Membranes During Tetrahymena Mating.* Science, 2004. **305**: p. 71-73.
243. Frisz, J.F., J.S. Choi, R.L. Wilson, B.A.C. Harley, and M.L. Kraft, *Identifying Differentiation Stage of Individual Primary Hematopoietic Cells from Mouse Bone Marrow by Multivariate Analysis of TOF-Secondary Ion Mass Spectrometry Data.* Analytical Chemistry, 2012. **84**(10): p. 4307-4313.
244. Tucker, K., Z. Li, S. Rubakhin, and J. Sweedler, *Secondary Ion Mass Spectrometry Imaging of Molecular Distributions in Cultured Neurons and Their Processes: Comparative Analysis of Sample Preparation.* Journal of the American Society for Mass Spectrometry, 2012. **23**(11): p. 1931-1938.
245. Appelhans, A.D. and J.E. Delmore, *Comparison of Polyatomic and Atomic Primary Beams for Secondary Ion Mass Spectrometry of Organics.* Anal. Chem., 1989. **61**: p. 1087-1093.
246. Winograd, N., *The magic of cluster SIMS.* Anal. Chem., 2005. **77**: p. 142-149.
247. Winograd, N. and J. Garrison, *Biological Cluster Mass Spectrometry.* Annu. Rev. Phys. Chem., 2010. **61**: p. 305-322.
248. Kollmer, F., *Cluster primary ion bombardment of organic materials.* Applied Surface Science, 2004. **231-232**: p. 153-158.
249. Mochiji, K., M. Hashinokuchi, K. Moritani, and N. Toyoda, *Matrix-free detection of intact ions from proteins in argon-cluster secondary ion mass spectrometry.* Rapid Communications in Mass Spectrometry, 2009. **23**(5): p. 648-652.
250. Fuoco, E.R., G. Gillen, M.B.J. Wijesundara, W.E. Wallace, and L. Hanley, *Surface Analysis Studies of Yield Enhancements in Secondary Ion Mass Spectrometry by Polyatomic Projectiles†.* Journal of Physical Chemistry B, 2001. **105**(18): p. 3950-3956.

251. Gillen, G. and S. Roberson, *Preliminary evaluation of an SF5 polyatomic primary ion beam for analysis of organic thin films by secondary ion mass spectrometry.* Rapid Commun. Mass Spectrom., 1998. **12**: p. 1303–1312.
252. Shard, A.G., R. Havelund, M.P. Seah, S.J. Spencer, I.S. Gilmore, N. Winograd, D. Mao, T. Miyayama, E. Niehuis, D. Rading, and R. Moellers, *Argon Cluster Ion Beams for Organic Depth Profiling: Results from a VAMAS Interlaboratory Study.* Analytical Chemistry, 2012. **84**(18): p. 7865-7873.
253. Mahoney, C., *Cluster secondary ion mass spectrometry of polymers and related materials.* Mass Spectrom. Rev., 2010. **29**(2): p. 247–293.
254. Fletcher, J.S., N.P. Lockyer, S. Vaidyanathan, and J.C. Vickerman, *TOF-SIMS 3D Biomolecular Imaging of Xenopus laevis Oocytes Using Buckminsterfullerene (C60) Primary Ions.* Anal. Chem., 2007. **79**: p. 2199-2206.
255. Nygren, H., B. Hagenhoff, P. Malmberg, M. Nilsson, and K. Richter, Micros. Res. Tech., 2007. **70**: p. 969-974.
256. Fletcher, J.S., S. Rabbani, A. Henderson, P. Blenkinsopp, S.P. Thompson, N.P. Lockyer, and J.C. Vickerman, *A New Dynamic in Mass Spectral Imaging of Single Biological Cells.* Anal. Chem., 2008. **80**: p. 9058-9064.
257. Breitenstein, D., C.E. Rommel, R. Möllers, J. Wegener, and B. Hagenhoff, *The Chemical Composition of Animal Cells and Their Intracellular Compartments Reconstructed from 3D Mass Spectrometry* Angew. Chem. Int. Ed., 2007. **46**(28): p. 5332-5335.
258. Fletcher, J.S., A. Henderson, G.X. Biddulph, S. Vaidyanathan, N.P. Lockyer, and J.C. Vickerman, *Uncovering new challenges in bio-analysis with ToF-SIMS.* Applied Surface Science, 2008. **255**(4): p. 1264-1270.
259. Fletcher, J.S. and J.C. Vickerman, *Secondary Ion Mass Spectrometry: Characterizing Complex Samples in Two and Three Dimensions.* Analytical Chemistry, 2012. **85**(2): p. 610-639.
260. Kollmer, F., W. Paul, M. Krehl, and E. Niehuis, *Ultra high spatial resolution SIMS with cluster ions — approaching the physical limits.* Surface and Interface Analysis, 2013. **45**(1): p. 312-314.
261. McDonnel, L.A. and R.M.A. Heeren, *Imaging Mass Spectrometry*. Mass Spectrom. Rev., 2006. **26**: p. 606-643.
262. Kurczy, M.E., P.D. Piehowski, S.A. Parry, M. Jiang, G. Chen, A.G. Ewing, and N. Winograd, *Which is more important in bioimaging SIMS experiments--The sample preparation or the nature of the projectile?* Appl. Surf. Sci., 2008. **255**(4): p. 1298-1304.
263. Carado, A., M.K. Passarelli, J. Kozole, J.E. Wingate, N. Winograd, and A.V. Loboda, *C-60 Secondary Ion Mass Spectrometry with a Hybrid-Quadrupole Orthogonal Time-of-Flight Mass Spectrometer.* Analytical Chemistry, 2008. **80**(21): p. 7921-7929.
264. Smith, D., A. Kiss, F. Leach, III, E. Robinson, L. Paša-Tolić, and R.A. Heeren, *High mass accuracy and high mass resolving power FT-ICR secondary ion mass spectrometry for biological tissue imaging.* Analytical and Bioanalytical Chemistry, 2013. **405**(18): p. 6069-6076.
265. Smith, D.F., E.W. Robinson, A.V. Tolmachev, R.M.A. Heeren, and L. Paša-Tolić, *C60 Secondary Ion Fourier Transform Ion Cyclotron Resonance Mass Spectrometry.* Analytical Chemistry, 2011. **83**(24): p. 9552-9556.
266. Bryant, S., Annual Workshop on SIMS, 2013. **Annapolis, MD**.
267. Havercroft, N., Annual Workshop on SIMS, 2013. **Annapolis, MD**.

268. Taupin, P., *BrdU immunohistochemistry for studying adult neurogenesis: Paradigms, pitfalls, limitations, and validation.* Brain Research Reviews, 2007. **53**(1): p. 198-214.
269. Zhu, Z., V. Shutthanandan, and M. Engelhard, *An investigation of hydrogen depth profiling using ToF-SIMS.* Surface and Interface Analysis, 2012. **44**(2): p. 232-237.
270. Malm, J., D. Giannaras, M.O. Riehle, N. Gadegaard, and P. Sjövall, *Fixation and Drying Protocols for the Preparation of Cell Samples for Time-of-Flight Secondary Ion Mass Spectrometry Analysis.* Anal. Chem., 2009. **81**(17): p. 7197-7205.
271. Robinson, M. and D. Castner, *Characterization of sample preparation methods of NIH/3T3 fibroblasts for ToF-SIMS analysis.* Biointerphases, 2013. **8**(1): p. 15.
272. Römer, W., T.-D. Wu, P. Duchambon, M. Amessou, D. Carrez, L. Johannes, and J.-L. Guerquin-Kern, *Sub-cellular localisation of a 15N-labelled peptide vector using NanoSIMS imaging.* Appl. Surf. Sci., 2006. **252**(19): p. 6925-6930.
273. Berman, E.S.F., K.S. Kulp, M.G. Knize, L. Wu, E.J. Nelson, D.O. Nelson, and K.J. Wu, *Distinguishing Monosaccharide Stereo- and Structural Isomers with TOF-SIMS and Multivariate Statistical Analysis.* Anal. Chem., 2006. **78**: p. 6497-6503.
274. May, C.J., H.E. Canavan, and D.G. Castner, *Quantitative X-ray Photoelectron Spectroscopy and Time-of-Flight Secondary Ion Mass Spectrometry Characterization of the Components in DNA.* Anal. Chem., 2004. **76**: p. 1114-1122.
275. Khlebtsov, N. and L. Dykman, *Biodistribution and toxicity of engineered gold nanoparticles: a review of in vitro and in vivo studies.* Chemical Society Reviews, 2011. **40**(3): p. 1647-1671.
276. Alexandridis, P., *Gold Nanoparticle Synthesis, Morphology Control, and Stabilization Facilitated by Functional Polymers.* Chemical Engineering & Technology, 2011. **34**(1): p. 15-28.
277. Chithrani, B.D., A.A. Ghazani, and W.C.W. Chan, *Determining the size and shape dependence of gold nanoparticle uptake into mammalian cells.* Nano Letters, 2006. **6**(4): p. 662-668.
278. Wedlock, L.E., M.R. Kilburn, J.B. Cliff, L. Filgueira, M. Saunders, and S.J. Berners-Price, *Visualising gold inside tumour cells following treatment with an antitumour gold(i) complex.* Metallomics, 2011. **3**(9).
279. Popovtzer, R., A. Agrawal, N.A. Kotov, A. Popovtzer, J. Balter, T.E. Carey, and R. Kopelman, *Targeted Gold Nanoparticles Enable Molecular CT Imaging of Cancer.* Nano Letters, 2008. **8**(12): p. 4593-4596.
280. Sardar, R. and J.S. Shumaker-Parry, *Spectroscopic and Microscopic Investigation of Gold Nanoparticle Formation: Ligand and Temperature Effects on Rate and Particle Size.* Journal of the American Chemical Society, 2011. **133**(21): p. 8179-8190.
281. He, H., C. Xie, and J. Ren, *Nonbleaching Fluorescence of Gold Nanoparticles and Its Applications in Cancer Cell Imaging.* Analytical Chemistry, 2008. **80**(15): p. 5951-5957.
282. Klein, S., S. Petersen, U. Taylor, D. Rath, and S. Barcikowski, *Quantitative visualization of colloidal and intracellular gold nanoparticles by confocal microscopy.* Journal of Biomedical Optics, 2010. **15**(3): p. 036015.
283. Haase, A., H.F. Arlinghaus, J. Tentschert, H. Jungnickel, P. Graf, A. Mantion, F. Draude, S. Galla, J. Plendl, M.E. Goetz, A. Masic, W. Meier, A.F. Thünemann, A. Taubert, and A. Luch, *Application of Laser Postionization Secondary Neutral Mass Spectrometry/Time-of-Flight Secondary Ion Mass Spectrometry in Nanotoxicology:*

Visualization of Nanosilver in Human Macrophages and Cellular Responses. ACS Nano, 2011. **5**(4): p. 3059-3068.
284. Techane, S.D., L.J. Gamble, and D.G. Castner, *X-ray photoelectron spectroscopy characterization of gold nanoparticles functionalized with amine-terminated alkanethiols.* Biointerphases, 2011. **6**(3): p. 98-104.
285. Niidome, T., K. Nakashima, H. Takahashi, and Y. Niidome, *Preparation of primary amine-modified gold nanoparticles and their transfection ability into cultivated cells.* Chemical Communications, 2004(17).
286. Rivolta, I., A. Panariti, M. Collini, B. Lettiero, L. D'Alfonso, L. Sironi, G. Miserocchi, and G. Chirico, *A biophysical model of intracellular distribution and perinuclear accumulation of particulate matter.* Biophysical Chemistry, 2011. **158**(2–3): p. 134-140.
287. Yang, L., M.P. Seah, E.H. Anstis, I.S. Gilmore, and J.L.S. Lee, *Sputtering Yields of Gold Nanoparticles by C60 Ions.* The Journal of Physical Chemistry C, 2012. **116**(16): p. 9311-9318.